High-Frame-Rate Ultrasound Matrix Transducers for Quantifying Blood Flow

Fool, F.

DOI
10.4233/uuid:90b26d72-be4d-47d4-a437-49b5574636f8

Publication date
2024

Document Version
Final published version

Citation (APA)
Fool, F. (2024). *High-Frame-Rate Ultrasound Matrix Transducers for Quantifying Blood Flow*. [Dissertation (TU Delft), Delft University of Technology]. https://doi.org/10.4233/uuid:90b26d72-be4d-47d4-a437-49b5574636f8

Important note
To cite this publication, please use the final published version (if applicable).
Please check the document version above.

High-Frame-Rate Ultrasound Matrix Transducers for Quantifying Blood Flow

Proefschrift

ter verkrijging van de graad van doctor
aan de Technische Universiteit Delft,
op gezag van de Rector Magnificus prof. dr. ir. T.H.J.J. van der Hagen,
voorzitter van het College voor Promoties,
in het openbaar te verdedigen op
vrijdag 20 december 2024 om 12:30 uur

door

Fabian FOOL

Ingenieur in Technische Natuurkunde,
Technische Universiteit Delft, Delft, Nederland
geboren te Vlaardingen, Nederland.

Dit proefschrift is goedgekeurd door de promotoren.

Samenstelling promotiecommissie:

Rector Magnificus	Voorzitter
Dr. ir. M.D. Verweij	Technische Universiteit Delft, *promotor*
Prof. dr. ir. N. de Jong	Technische Universiteit Delft, *promotor*
Dr. ir. H.J. Vos	Erasmus MC, *promotor*
Onafhankelijke leden:	
Prof. dr. ing. S. Kenjereš	Technische Universiteit Delft
Prof. dr. S. Cochran	University of Glasgow, United Kingdom
Prof. dr. G. van Soest	Erasmus MC
Dr. ir. A.E.C.M. Saris	Radboudumc
Prof. dr. ir. J.P. Hoogenboom	Technische Universiteit Delft, *reservelid*

The research of this thesis is part of the MIFFY project (15293) of the OTP research program financed by the Dutch Research Council (NWO).

Keywords:	ultrasound imaging, matrix transducer array, 3D, high-frame-rate, application-specific integrated circuit, beamforming, vector flow imaging, carotid artery, brain
Printed by:	Gildeprint
Cover:	Fabian Fool. Includes images adapted from those generated by Microsoft Copilot.

ISBN 978-94-6384-692-9

An electronic version of this dissertation is available at
https://repository.tudelft.nl.

Contents

Summary

Medical ultrasound, also known as echography and ultrasonic imaging, is a crucial imaging modality in modern healthcare. The advent of high-frame-rate imaging has broadened its applications, enabling the measurement of both high blood velocities over large fields-of-view, and slow-moving blood. High temporal resolution is essential, but accurate flow measurements also require high spatial resolution in all three orthogonal directions. This necessitates the use of matrix transducers, which face several challenges depending on the application. For monitoring the brains of preterm-born babies, the main challenges include designing a application-specific integrated circuit (ASIC)-integrated matrix that meets clinical requirements and achieving the necessary data reduction to minimize the number of cables, ensuring that contact between mother and child remains unrestricted. For atherosclerosis screening, challenges involve sensor-ASIC integration, developing a high-frame-rate data acquisition scheme for the ASIC-integrated matrix, including data processing for volumetric flow quantification, and addressing the high side-lobe level of a sparse matrix. The objective of this thesis is to address these challenges and develop the necessary technology to enable the use of ultrasound matrix transducers for quantifying blood flow and detecting physiologically abnormal flow patterns and velocities in the two mentioned applications.

Chapter 1 contains an introduction to the development of medical ultrasound, reviews potential applications for flow measurement, and identifies problems encountered in these applications. It also presents the research aim and objectives.

Chapter 2 provides an overview of designing a new ultrasound ASIC-integrated matrix for preterm brain monitoring. It discusses clinical requirements, acoustical design parameters, and electronic considerations. Our proposal is a 15 mm × 15 mm matrix with a 9.2 MHz centre frequency and 100 µm pitch. The prototypes revealed that the electronics needed for the proposed design are too large to fit beneath the elements. Therefore, the current technology and/or design are insufficient to achieve the desired performance.

Chapter 3 introduces an second generation ultrasound transceiver ASIC for carotid artery imaging, featuring a technique to reduce switching artefacts that negatively affected image quality. The enhanced switch controller addresses clock feedthrough and charge injection issues, reducing imaging artefacts by 20 dB.

Chapter 4 details the development of an ASIC-integrated matrix transducer for carotid artery imaging. The prototype was designed to have 7680 elements on 8 tiled ASICs and included an attenuating layer between the PZT and ASIC to combat crosstalk. On average, individual transducer elements exhibited a transmit efficiency of 30 Pa/V at 200 mm, a −6 dB bandwidth of 45 %, and a receive dynamic range of 81 dB. Overall, the characterization results are promising and encourage further up-scaling by fabricating a larger transducer with 10 tiled ASICs with about 10 000 elements.

Chapter 5 describes a computationally efficient frequency domain two-stage beamforming approach for polar geometry, allowing significant data reduction in-probe while

retaining a high-quality image. The method is verified through simulations and measurements, showing that the method requires no trade-off between resolution and artifacts compared to an alternative method that uses time-of-flight for the second stage.

Chapter 6 evaluates an electronically-translatable linear-array imaging scheme with the ASIC-integrated matrix from **Chapters 3 and 4** for carotid pulse wave imaging, which measures the stiffness of the wall using its displacement. After optimization, the results show a point spread function that is twice as wide at −6 dB, and a 4 dB higher clutter level compared to an imaging scheme that achieves high image quality but not the required frame rate for this application. The proposed scheme could be beneficial for generating 3D maps of carotid artery stiffness, providing valuable information regarding cardiovascular risk.

Chapter 7 applies the same imaging scheme and transducer from **Chapter 6** to vector flow imaging of blood in the carotid, which requires higher frame rates. The impact of four imaging scheme parameters on velocity estimation accuracy and precision is assessed through simulations of a straight-tube phantom with a 150 cm/s parabolic flow profile. The number of sub-apertures had the largest effect on performance. With 5 sub-apertures, a frame rate of 4 kHz was achieved, resulting in a relative error of 13 % and a standard deviation of 9 %. Too few sub-apertures worsened the results due to the lower resolution, while too many led to underestimation at high velocities because of the reduced frame rate. Results show the feasibility of measuring the high velocities in the carotid using this setup, provided the appropriate trade-offs are made.

Chapter 8 presents an adaptive array clutter filter to improve blood flow estimation. By basing the filter on the measured dominant Doppler frequencies in each sub-volume and temporal window, this approach circumvents the drawback of conventional compounding, which has a trade-off between image quality and the ability to measure high velocities. Simulations with a straight-tube phantom and a parabolic flow profile demonstrate that the adaptive filter can achieve a similar relative error as conventional compounding with a pulse repetition frequency at least twice as low. Additionally, it can adapt to both spatial and temporal variations in velocities. Thereby, it can aid with blood flow estimation using sparse arrays.

Chapter 9 summarizes the thesis results, discusses how well the challenges with matrix transducers were addressed, and provides recommendations for future research.

Samenvatting

Echografie, het gebruik van ultrageluid voor medische doeleinden, is van grote waarde in de gezondheidszorg. De opkomst van beeldvorming met hoge beeldfrequentie heeft de toepassingen ervan verbreed, zoals het meten van hoge bloedsnelheden in een groot volume of juist langzame bloedsnelheden. Het accuraat schatten van de snelheid vereist zowel een hoge temporele als ruimtelijke resolutie, waardoor matrixtransducers noodzakelijk zijn, maar de toepassing wordt verhinderd door verschillende uitdagingen. Bij hersenmonitoring van te vroeg geboren baby's zijn de belangrijkste uitdagingen het ontwerp van een application-specific integrated circuit (ASIC)-geïntegreerde matrix die voldoet aan alle klinische eisen en de benodigde datareductie om het aantal kabels te minimaliseren, zodat het contact tussen moeder en kind onbelemmerd blijft. Voor atherosclerose screening omvatten de uitdagingen de integratie van sensor-ASIC, de ontwikkeling van een afbeeldingsmethode met hoge beeldfrequentie voor een ASIC-geïntegreerde matrix, inclusief gegevensverwerking voor volumetrische stromingskwantificatie, en het aanpakken van beeldvervuiling met een sparse matrix. Dit proefschrift richt zich op deze uitdagingen en de ontwikkeling van technologie om met ultrasone matrixtransducers bloedstroming te kunnen kwantificeren en het detecteren van fysiologisch abnormale stromingspatronen en snelheden voor de twee genoemde toepassingen.

Hoofdstuk 1 beschrijft de ontwikkeling van echografie, bespreekt potentiële toepassingen voor stromingsmetingen en identificeert problemen die zich voordoen bij deze toepassingen. Het presenteert ook het onderzoeksdoel en de doelstellingen.

Hoofdstuk 2 bevat een overzicht van het ontwerpproces van een nieuwe ASIC-geïntegreerde matrix voor hersenmonitoring bij te vroeg geboren baby's. Het bespreekt klinische vereisten, akoestische ontwerpparameters en elektronische overwegingen. Ons voorstel is een matrix van 15 mm × 15 mm met een centrale frequentie van 9.2 MHz en een pitch van 100 µm. De prototypes toonden aan dat de benodigde elektronica voor het voorgestelde ontwerp te groot is om onder de elementen te passen. De huidige technologie en/of het ontwerp zijn dus onvoldoende om de gewenste prestaties te bereiken.

Hoofdstuk 3 introduceert een tweede generatie ASIC voor beeldvorming van de halsslagader, met een techniek om schakelartefacten te verminderen die de beeldkwaliteit negatief beïnvloedden. De verbeterde schakelcontroller pakt het niet-ideale gedrag van de transistoren aan, waardoor beeldartefacten met 20 dB worden verminderd.

Hoofdstuk 4 geeft de ontwikkeling weer van een ASIC-geïntegreerde matrix voor beeldvorming van de halsslagader. Het prototype was ontworpen met 7680 elementen verspreid over 8 ASIC's en bevatte een dempende interposerlaag tussen de PZT en ASIC om overspraak via de ASIC te bestrijden. Gemiddeld had elk element een zendefficiëntie van 30 Pa/V op 200 mm, een −6 dB bandbreedte van 45 %, en in ontvangst een dynamisch bereik van 81 dB. Over het algemeen zijn de resultaten veelbelovend en moedigen ze verdere opschaling aan door een grotere transducer te fabriceren met ongeveer 10 000 elementen verspreid over 10 ASIC's.

Hoofdstuk 5 presenteert een rekenkundig efficiënte tweetraps afbeeldingsmethode in poolcoördinaten die gebruik maakt van de golfvergelijking in de tweede trap, waardoor significante gegevensreductie in de transducer zelf mogelijk is terwijl een hoge beeldkwaliteit behouden blijft. De methode is geverifieerd door middel van simulaties en metingen, waarbij werd aangetoond dat de methode geen compromis vereist tussen resolutie en artefacten in vergelijking met een alternatieve methode die *time-of-flight* gebruikt in de tweede trap.

Hoofdstuk 6 evalueert een elektronisch verplaatsbare lineair-array afbeeldingsmethode met ASIC-geïntegreerde matrix uit **Hoofdstuken 3 en 4** voor het meten van pulsgolven die over de halsslagader lopen. Aan de hand van verplaatsing van de wand door pulsgolven kan de stijfheid van de wand worden gemeten. Na optimalisatie tonen de resultaten een twee keer bredere puntspreidingsfunctie bij −6 dB, en een 4 dB hoger niveau van ruis vergeleken met een beeldvormingsschema dat een hoge beeldkwaliteit bereikt, maar niet de vereiste beeldsnelheid voor deze toepassing. Het voorgestelde schema kan nuttig zijn om een 3D-kaart van de stijfheid van de halsslagader te genereren, wat waardevolle informatie kan bieden bij de beoordeling van hart- en vaatziekten.

Hoofdstuk 7 past dezelfde afbeeldingsmethode en transducer uit **Hoofdstuk 6** toe op het meten van bloedstroming in de halsslagader, wat een hogere beeldfrequentie vereist. De impact van vier parameters van het beeldvormingsschema op de nauwkeurigheid en precisie van snelheidsinschatting wordt beoordeeld door middel van simulaties van een recht-buis fantoom met een parabolisch stromingsprofiel van 150 cm/s. Het aantal sub-aperturen had de grootste invloed op de prestaties. Met 5 sub-aperturen werd een beeldsnelheid van 4 kHz bereikt, wat resulteerde in een relatieve fout van 13 % en een standaarddeviatie van 9 %. Te weinig sub-aperturen verslechterden de resultaten door de lagere resolutie, terwijl te veel sub-aperturen een onderschatting veroorzaakten bij hoge snelheden door de verminderde beeldfrequentie. Resultaten tonen de haalbaarheid van het meten van de hoge snelheden in de halsslagader met deze opstelling, mits de juiste afwegingen worden gemaakt.

Hoofdstuk 8 stelt een adaptieve filter voor die beeldvervuiling afkomstig van de transducer zelf vermindert om bloedstroming beter te kunnen meten. Door de filter te baseren op de gemeten dominante Doppler-frequenties in elk subvolume en tijdvenster, omzeilt deze benadering het nadeel van de conventionele methode om beeldvervuiling te verminderen door middel van het coherent combineren van afbeeldingen, wat een compromis heeft tussen beeldkwaliteit en het vermogen om hoge snelheden te meten. Simulaties met een recht-buis fantoom en een parabolisch stromingsprofiel tonen aan dat de adaptieve filter een vergelijkbare relatieve fout kan bereiken als de conventionele methode met een pulsherhalingsfrequentie die minstens twee keer zo laag is. Bovendien kan het zich aanpassen aan zowel ruimtelijke als temporele variaties in snelheden. Hiermee kan het bijdragen aan betere bloedstroominschatting met sparse arrays.

Hoofdstuk 9 vat de resultaten van dit proefschrift samen, bespreekt hoe goed de uitdagingen met matrixtransducers werden aangepakt, en geeft aanbevelingen voor toekomstig onderzoek.

1

Introduction

1

1.1 Medical ultrasound

Medical ultrasound, also known as echography and ultrasonic imaging, has become an invaluable imaging modality in modern healthcare. Echography uses high-frequency sound waves, i.e. ultrasound with frequencies usually higher than 1 MHz, to image the insides of the human body by emitting a pulse and measuring the echo [1], [2]. The time taken until an echo is measured can be converted to depth using the speed of sound, while amplitude indicates the acoustic contrast of the medium. Since its inception in the late 1940s [3], [4], echography has relied on these principles, though imaging techniques and devices have evolved significantly over time, driven by advancements in electronics and computational power.

Early ultrasound systems relied on single-element transducers mechanically moved around the patient, often with large water baths to ensure sufficient coupling between the transducer and the human body. One example of such a system is the large water bath scanner developed in the 1960s for fetal imaging [5], as shown in Figure 1.1a. At the time, the images were effectively purely black-and-white, without any gray levels, and only appeared after the scan was completed [1]. Due to this, mainly tissue interfaces and boundaries were visible and the imaging process took a long time. This eventually transformed into real-time gray-scale imaging using an array of transducers connected to a portable machine in the 1970s, allowing for better visualization of soft tissue structures. A modern version of this system is shown in Figure 1.1b. The general imaging method using these arrays involves transmitting a narrow focused beam and then translating it, as depicted in Figure 1.2a. The received signals from a transmitted beam contribute to a single line in the image, hence the term ”line-by-line” imaging. While the use of arrays and electronically translated beams resulted in much faster imaging than the previous mechanical translation, frame rates remained insufficient for certain applications, such as real-time blood flow imaging across a large field of view.

To achieve a high frame rate over a large field of view, a wide beam, such as a plane or diverging beam, can be transmitted. This approach offers the potential to image everything at once and achieve frame rates two orders of magnitude higher. However, despite the feasibility of real-time line-by-line imaging in the 1970s, it was not until the 2000s that technology capable of processing the vast amount of data from a wide field of view became available [6].

Using a wide beam to receive signals from a large field of view also presents challenges. Both lateral resolution and contrast are compromised compared to line-by-line imaging. The lack of a focused transmit beam limits the ability to distinguish scatterers, and the increased number of reflections from the wide transmission results in more clutter. However, this can be mitigated by transmitting multiple, different wide beams, such as from different transmission directions, and combining the low-quality images from each transmission into a single high-quality image [7], as illustrated in Figure 1.2b. While this increases the time required to create a single image, far fewer transmissions are needed compared to line-by-line imaging to achieve comparable image quality, thus still achieving frame rates an order of magnitude higher [7]. This “High-frame-rate” or “Ultrafast” imaging has expanded the scope of medical ultrasound to various new applications, including measuring high blood velocities over a large field of view, such as in the heart [8], and measuring slow-moving blood [9], [10].

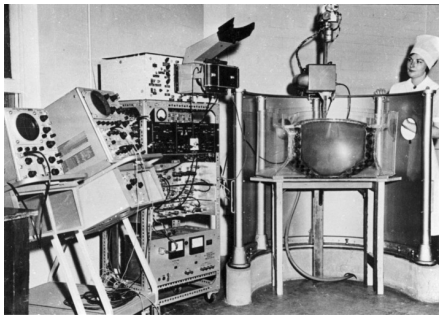

(a)

(b)

Figure 1.1: (a) Experimental water-bath ultrasound scanner for obstetrics, designed in 1960. Reproduced from Gill [11], published in Australasian Journal of Ultrasound in Medicine, Under CC-BY 3.0 license. (b) A modern cart-based scanner: Mindray Resona I9 [12].

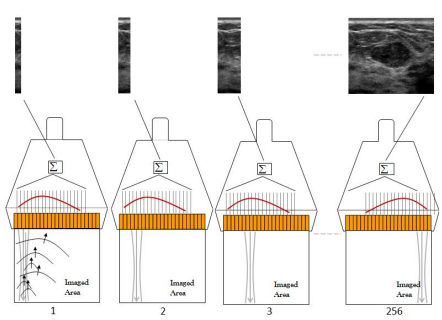

(a)

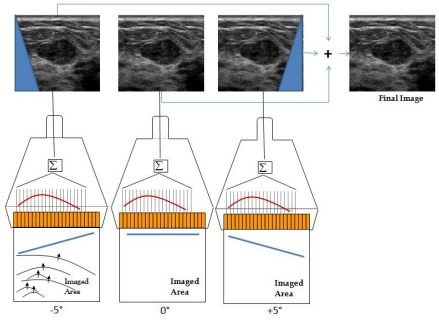

(b)

Figure 1.2: (a) Conventional image formation, where the image is formed ”line-by-line”. (b) ”High-frame-rate” compound imaging, where multiple low-quality images are combined into a single high-quality image. Reproduced from Bercoff [6], published in Ultrafast Ultrasound Imaging - Medical applications, Under CC BY-NC-SA 3.0 license.

1.2 Applications of echography

Medical ultrasound is used in various applications. It is most well known for its use in obstetrics, as nearly all pregnant women are examined by ultrasound [1]. Other applications include echocardiography [8], [13], such as measuring blood flow in the heart, and oncological fields, such as the detection and characterization of liver tumors [14]. This thesis focuses on two specific applications of medical ultrasound where high-frame-rate imaging is beneficial: brain vascularity imaging for babies to monitor their blood perfusion in the early days after preterm birth, and vascular flow imaging in the carotid bifurcation to assess atherosclerosis in larger adult cohorts.

1.2.1 Preterm Brain Monitoring

Each year, over 15 million children worldwide, about 10% of the total, are born preterm [15], [16]. Neuro-developmental problems are not uncommon in preterms and may lead to

further health issues during adulthood [17]. The main cause is inadequate brain perfusion due to underdeveloped autoregulation of the brain [18], and haemorrhages that most likely occur within the first three days after birth and tend to rapidly escalate in severity [19]–[22]. Brain monitoring during these critical early days can reduce or even prevent damage from brain injuries in these preterms by enabling quick application of treatment after detecting an abnormality, potentially preventing further neuro-developmental problems.

In order to detect an abnormality in the brain early, it could be monitored via multiple modalities. Monitoring vital parameters, such as blood pressure and oxygenation levels, can provide some information, but these are global values and do not directly inform about the brain. Magnetic Resonance Imaging (MRI) can detect changes in the brain, but MRI machines are typically not portable due to their high magnetic field strengths. Transporting critically ill neonates to the MRI is risky and therefore not an option, as they may not be stable enough for scanning [23]. Recently, portable low-field MRI machines have been introduced that still provide high-quality images [24], [25], so MRI could be used for monitoring without transport in the future. Near-infrared spectroscopy (NIRS) and amplitude-integrated electroencephalography (aEEG) are already used to constantly monitor the brain, but they can only provide localized readings and might not directly reflect the state of perfusion or miss small perfusion defects [26]–[28]. Each modality thus provides incomplete information about the brain's state. A solution that integrates all monitoring modalities to provide sufficient information could help [29]. However, even combined, these modalities do not provide sufficient information about brain abnormalities.

Cranial ultrasound could supplement other modalities to provide a more complete reading of the brain. Usually, the skull hinders the application of ultrasound to the brain [30], [31], but in newborns, the fontanelles provide an ideal acoustic window. Ultrasound has the potential to monitor haemodynamic changes across the entire brain and offer localized readings [9], [32]. This has been made possible by high-frame-rate imaging, which, due to the high number of frames, allows for much more efficient separation of tissue and blood signals [9], [10]. Ultrasound is used daily or when there is visible unease in a preterm infant in the Neonatal Intensive Care Unit (NICU) in Utrecht. However, such scans must be performed by a sonographer and cannot be done continuously. The issue is that ultrasound probes are generally quite large and are connected to the imaging system with a thick cable, making integration with other head-mounted sensors difficult. Furthermore, current probes do not provide 3D imaging, which is required to image all points of interest and ensure resilience against probe movement and placement errors. A currently existing ultrasound device that can be used for monitoring is the NeoDoppler [33], but it only provides a single scan line and cannot provide localization beyond the depth of the signal. Currently, no device exists that can provide whole-brain monitoring using ultrasound.

1.2.2 Atherosclerosis screening

Atherosclerosis is a disease characterized by the formation of abnormalities in the walls of arteries, affecting virtually all elderly people [34]. Over time, fatty deposits, known as plaques, build up in the arterial walls, leading to the narrowing of blood vessels. In the carotid artery, which supplies the head and brain with oxygen and nutrients, this condition is called carotid artery disease and usually occurs near the carotid bifurcation [35]. The

narrowing of the carotid artery, known as stenosis, or plaque rupture is a frequent cause of stroke [36], [37], a medical emergency that occurs when the blood supply to the brain is interrupted or significantly reduced. Clinical studies [38]–[41] have shown that coronary and carotid artery disease are strongly related, and the presence of plaques in the carotid artery can indicate a higher risk of a heart attack. The exact cause of plaque build-up is unknown [42], and initially, it presents no symptoms [43]. However, certain risk factors, such as obesity and smoking, increase the likelihood of developing atherosclerosis [44]. Therefore, screening high-risk populations could help prevent various negative outcomes.

Several diagnostic modalities can detect atherosclerosis in the carotid artery. Computed tomography angiography (CTA) is fast and relatively operator-independent but requires the injection of an iodine contrast medium and uses radiation [45]. MRI can also detect carotid stenosis and, unlike CTA, does not involve radiation and does not necessarily require contrast agents [46], [47]. However, MRI is expensive and less readily available, making both methods unsuitable for large-scale screening.

Ultrasound is a non-invasive, safe, and inexpensive technique that allows direct visualization of plaque morphology and blood flow in the carotid bifurcation [48], [49], both of which can be used to assess the risk of adverse events. It is therefore an ideal modality for screening and is generally the first modality used for patients with suspected carotid stenosis [50]. However, there are several problems with its application to screening, as clinical practice typically uses 2D ultrasound. First, the plaque is a 3D structure, and quantitative estimation of its shape and size from 2D ultrasound is prone to error [51]. Second, reproducing imaging planes at a later date for follow-up studies is difficult, as variations in the patient's anatomical situation may hinder access to the same imaging planes [52]. Third, measuring velocities to assess wall stiffness or haemodynamics is hampered by the presence of out-of-plane components, which reduce accuracy [53]–[57]. These issues hinder the application of 2D ultrasound for this monitoring application.

1.3 3D ultrasound

For both mentioned applications, perfusion monitoring of the preterm brain and atherosclerosis screening of the carotid artery, there are several issues with the application of 2D ultrasound, but 3D ultrasound would solve these issues. There are two distinct ways of achieving that: scanned array transducers and matrix transducers.

1.3.1 Scanned array transducer

An array transducer has multiple elements placed along a line and can form 2D images. By moving this array around, either mechanically or by hand, the separate 2D images made at different positions can be stitched together to form a 3D dataset [51], [52]. However, this method of forming 3D images has several limitations that make it unsuitable for the mentioned applications. For monitoring the carotid bifurcation, high volume rates are required to measure the high velocities in all three spatial directions. This cannot be achieved with this method, as the required motion of the 1D array only allows for relatively low volume rates. For monitoring the preterm brain, a small and lightweight device is needed that can move automatically. Mechanically swept transducers are not applicable as they are bulkier and heavier due to the additional mechanical parts in the housing or

external fixtures to move the transducer around [58]. Manually moving a smaller 1D array by hand is also not feasible as it requires constant movement by an operator. Therefore, this type of 3D imaging is not suitable for the applications in this thesis.

1.3.2 Matrix transducer

A matrix array has elements placed in two dimensions, forming a matrix of elements. It does not have the same downsides as a scanned array transducer, but it comes with its own set of challenges. These challenges are mainly due to the complexity of signal data capture in such probes, as the number of elements scales quadratically with aperture size, instead of linearly compared to the original array transducers. For example, covering an area of just 10 mm × 10 mm already requires more than 1000 elements for a 3 MHz matrix [59], while a 10 mm wide array only requires about 32 elements. Although producing matrices with 1000 elements has been shown feasible in research and clinical practice, the relatively small aperture will severely limit the lateral resolution. While constructing an array with even more elements is possible to increase resolution and contrast, it is a formidable challenge to create electrical connections to each element [60], and to control them, as typical systems can only handle 64 to 256 elements [61]. Therefore, the number of elements that can be addressed is limited.

There are four different approaches to matrix arrays that deal with the limited number of available channels differently by trading off lateral resolution, side-lobe level, frame rate, operational flexibility, and signal-to-noise ratio (SNR) against each other. A *fully-populated matrix*, as discussed before, is the most flexible type. All of its elements are densely packed and can be addressed individually, allowing them to be operated similarly to conventional 1D arrays. The downside is that this severely limits the aperture, as the element pitch should preferably be limited to half a wavelength in both directions to avoid grating lobes [1]. This kind of matrix thus has limited lateral resolution but otherwise performs like a 1D array. A *sparse matrix* has elements that sparsely populate a larger aperture [61]. Compared to the fully-populated array with the same number of elements, the larger aperture results in higher resolution, but the sparsity results in a higher side-lobe level, severely reducing contrast, and a lower SNR, which limits the imaging depth. The side-lobe level can be controlled [61], for example by basing the element positions on the Fermat Spiral [62], but it remains significantly worse than fully-populated arrays. Sparse arrays do not necessarily require any additional electronics, can be directly connected to available scanners, and do not necessarily require specialized imaging schemes. However, the cables between the elements and the imaging system can cause significant signal loss due to impedance mismatch [60], [63]. To circumvent this, amplifiers can be used close to the elements [63]. A sparse matrix thus achieves higher lateral resolution at the cost of image quality and SNR. A *row-column-addressed array* (RCA) [64]–[67] is a fully-populated matrix, but in transmit, only either each full column or each full row can be addressed separately, while in receive, the other direction can be addressed. This reduces the number of electrical connections from N^2 to $2N$ compared to a fully-populated array. However, an RCA requires more complex acquisition schemes, generally resulting in a reduced frame rate. Furthermore, in general, only the volume directly below the aperture can be imaged. While the volume can be extended by lenses, this introduces artifacts and is still limited compared to other types of arrays [68], [69]. An RCA can thus also achieve higher lateral

resolution but trades off flexibility and frame rate. The final type is an *ASIC-integrated matrix*. The application-specific integrated circuit (ASIC) is used to reduce the number of electrical connections while allowing the matrix to be fully populated. The reduction is achieved through micro-beamforming (μBF), multiplexing, in-probe digitization, on-chip pulsers, or any combination of these, depending on the specific application [70]–[73]. Furthermore, amplifiers can be integrated into the ASIC to amplify the signal and prevent signal loss [71], [74]. While the channel reduction can be achieved in various ways and therefore can be adapted to an application, each method has its own effects on the imaging, e.g. μBF increases the effective element size in receive and therefore increases the number of grating lobes [75], and requires a certain amount of space on the ASIC, which is limited. Therefore, a trade-off is still necessary to satisfy both imaging and ASIC requirements. An additional issue is that an ASIC-integrated matrix has a more costly development process, both in time and money. Each type thus makes the trade-off differently and has its own set of challenges.

1.4 Challenges with matrix transducers for applications

While both applications require a matrix transducer, the requirements for each application differ. This necessitates different trade-offs and potentially different types of matrix transducers. Here, we discuss both applications further and the specific challenges that arise.

1.4.1 Preterm brain monitoring

For preterm brain monitoring, the device must be small to integrate with other modalities, and the imaging volume must be wider than the aperture, which is limited by the fontanel. Therefore, both a fully-populated matrix and RCA are unsuitable. A sparse matrix has a relatively low SNR and a high of side-lobe level. This might be problematic when measuring perfusion because blood signals have a relatively low amplitude compared to the surrounding tissue, i.e., about 40 to 60 dB lower [76], and the high side-lobe level adds to the already increased side-lobe level from high-frame-rate imaging [7], which is beneficial to use when measuring perfusion [9], [10]. Therefore, we do not consider these three types suitable for this application.

We believe an ASIC-integrated matrix would be a good fit for preterm brain monitoring as it can be adapted to the application and could provide the necessary high channel reduction. However, this type of matrix has its own challenges. For this application, the main challenges are the design of the matrix itself and the required data reduction to minimize the number of cables, as discussed below.

Trade-offs in ASIC-integrated matrix design

A device capable of monitoring does not currently exist and therefore must be designed. This requires considering the clinical requirements, the acoustical effects of the matrix parameters, and the effects and space requirements of the electronics in the ASIC. Therefore, a process is necessary to optimize these trade-offs for this specific application while considering all these factors.

Data reduction methods

Monitoring should be done without restricting contact between mother and child, which is highly advantageous for the baby's development. Ideally, this means the device should be wireless, but at the very least, it should minimize the number of cables. The transfer of data between the transducer and imaging system is a bottleneck in an ultrasound system, so a method is necessary to reduce the amount of data in-probe to minimize the number of cables. One method that can achieve this is two-stage beamforming [77]–[79]. In the first stage, the data is reduced in-probe from channel to scanline data, i.e. a single output instead of one output for every element. In the second stage, a high-quality image is reconstructed by combining the scanline data from each pulse-echo. For the second stage of this process, there are two approaches available: a time-of-flight and a wave equation approach. For linear arrays, which scan the imaging volume by translating the transmit beam, the wave equation approach has superior computational efficiency compared to the time-of-flight approach because most steps can be performed using fast Fourier transforms (FFTs) [79]. Although superior image quality might also be expected [80], this has not been shown. For phased arrays, which scan the imaging volume by rotating the transmit beam, a wave equation approach is possible, but not all steps can be performed using FFTs, making this approach computationally inefficient. For perfusion monitoring, beam steering is required, and a wave equation approach that can work with beam steering would be beneficial due to its potential advantages in both computation and image quality, but this currently cannot be achieved. Therefore, developing a computationally efficient method would be beneficial for this application.

1.4.2 Atherosclerosis screening

The carotid artery is easily accessible for ultrasound, making it suitable for various types of matrices. However, we will focus on the ASIC-integrated matrix and sparse matrix, as both types are developed in-house. For the ASIC-integrated matrix, a device specifically designed for imaging the carotid bifurcation has already been developed [71]. However, we identified two issues related to the integration of an ASIC that resulted in image artifacts. Additionally, high-frame-rate imaging is necessary to measure flow, which requires specialized imaging schemes for this matrix. Regarding the sparse array, a common issue is the high side-lobe level. While methods exist to reduce the side-lobe level, aside from modifying the placement of the elements, they face challenges when applied to flow measurements. Thus, there are three separate challenges for these two matrices when applying them to atherosclerosis screening. We will discuss these issues in the following sections.

Sensor-ASIC integration

While an ASIC can provide significant channel reduction and handle a large number of elements, its integration can introduce several visible imaging artifacts. Specifically, we observed that the non-idealities of the electronics in the ASIC can introduce acoustic artifacts, and that integrating an ASIC with PZT as the sensor material in the acoustic stack negatively affects acoustic performance. This is further discussed in the following paragraphs.

High-voltage components require more isolation than their low-voltage counterparts. In an ASIC-integrated matrix, where space is limited, low-voltage components are preferred

whenever possible. There is at least a two orders of magnitude difference between the voltage of the transmit pulse and the received signals, allowing the receive electronics to use more compact components. To achieve this, the receive electronics must be isolated from the transmitted signals, necessitating a Tx/Rx switch. However, the required metal–oxide–semiconductor field-effect transistors (MOSFETs) for this switching operation have non-idealities, leading to clock feedthrough and charge injection [81]. In an ASIC-integrated matrix for the carotid artery [71], this was observed as additional transmitted pulses emitted when switching between Tx and Rx, with amplitudes similar to that of the transmitted pulse. Various techniques exist to counteract these non-idealities [82], [83], but they require additional components. This is not feasible to include in the ASIC, as space is at a premium and the high-voltage MOSFETs required for the switch are considerably larger than their low-voltage counterparts. Therefore, an alternative solution is necessary.

While at the output of an ASIC the amount of electrical connections can be reduced, all individual sensor elements still need to be connected to the input of the ASIC. One solution is integration with a pitch-matched ASIC, where an interconnection layer, such as a flex circuit [84] or a non-conducting buffer layer with gold balls [71], connects the individual elements to an ASIC with input pads spaced according to the element pitch. However, this type of integration has a downside: the ASIC becomes part of the backing of a transducer. The backing is crucial for the transfer efficiency and bandwidth of the transducer [2]. For instance, an air-backed transducer, which effectively has a high impedance mismatch backing, achieves high transfer efficiency as all energy is transmitted forward. Conversely, a high-attenuating backing achieves high bandwidth by damping all incoming waves. An ASIC, however, acts as neither in our matrix transducers, as it has a similar impedance to PZT and low attenuation [85], [86]. This results in reflections from layers beneath the ASIC being visible in the signal and crosstalk between elements due to the propagation of Lamb waves in the ASIC [86]. Together, these effects lead to lower bandwidth and spurious signals. To mitigate these issues, the interconnection layer must either sufficiently attenuate the waves or completely reflect them. Both approaches exist, but they either cannot be applied to a small pitch [87] or require extremely precise manufacturing tolerances [84]. Therefore, another approach would be helpful to reduce the negative effects of an ASIC.

High-frame-rate data acquisition scheme

An ASIC-integrated array might require different data acquisition schemes, depending on the data-reduction methods applied. This also applies to a matrix array designed specifically for measuring various quantities around the carotid bifurcation [71]. The matrix covers an area of 12 mm by 36 mm, subdivided into 80 columns and 120 rows. To address these 9600 elements, 120 transmit and 120 receive channels are connected to the 120 rows. Beneath each element is a set of switches that allow each row to have an arbitrary set of elements connected in transmit and receive modes separately, which can be changed after each pulse-echo. For the best image quality, a full read-out with 80 pulse-echo events is necessary, resulting in a volume rate of 250 volumes per second at a PRF of 20 kHz. However, this frame rate is insufficient for both carotid pulse-wave imaging and blood flow measurements in the carotid, which require at least 1000 volumes per second [88]–[90]. Therefore, an alternative acquisition scheme is necessary that provides both a high frame rate and sufficient image quality for these applications.

Vector flow imaging with a sparse array

Methods exist to reduce the high clutter level of a sparse array, but they have various issues when applied to flow imaging. The most common method is image compounding [7], [91]. This technique involves transmitting a sequence of partially overlapping ultrasound beams and coherently combining the reconstructed lower-quality image data to produce a final image with improved quality, both in terms of resolution and clutter reduction. However, such compounding acts as a moving average over the captured series of lower-quality image data, effectively low-pass filtering the temporal data. Since high axial velocities of blood and tissue correspond to high temporal frequencies, the moving average operation may remove these signals. Therefore, although a longer compounding ensemble of unique beams generally improves image quality, it also suppresses high-velocity signals [92]. An alternative method is needed that effectively reduces clutter while still being capable of measuring high velocities.

1.5 This thesis

1.5.1 Aim

The aim of this thesis is to develop ultrasonic clinical tools that can quantify blood flow to detect abnormalities. Accurate flow measurements need a full flow resolution in space and time, and hence require the use of matrix transducers to capture the full volume of tissue and vasculature, and resolve the flow velocity in three orthogonal directions. Yet, matrix transducers are hampered in their utilization by several challenges depending on the application, and two specific applications were chosen. For preterm-born baby brain monitoring, the main challenges lie in designing an ASIC-integrated matrix that meets all clinical requirements and achieving the necessary data reduction. For atherosclerosis screening, the challenges include sensor-ASIC integration, developing a high-frame-rate data acquisition scheme for the ASIC-integrated matrix including data processing for volumetric flow quantification, and addressing the high side-lobe level of a sparse matrix. Therefore, the objective of this thesis is to address these challenges and develop the necessary technology to enable the use of ultrasound matrix transducers in quantifying blood flow and detecting abnormalities for the two mentioned applications.

1.5.2 Outline

Chapters 2 to 4 focus on the design, characterization, and manufacturing of an ASIC-integrated matrix, thereby tackling the first three challenges. **Chapter 2** provides a simplified and concise overview of the process to design a new ultrasound PZT-on-ASIC matrix for monitoring of the preterm brain. The clinical requirements for this matrix, the effect of acoustical design parameters and various electronic considerations are discussed. Furthermore, a design for this matrix is proposed and the prototypes to verify this design are discussed. **Chapter 3** presents a second generation transceiver ASIC that reduced switching artefacts present in the first generation. The pitch-matched high voltage switches that switch between transmission and reception suffered from charge injection and clock feedthrough causing parasitic transmissions and associated imaging artefacts. In **Chapter 4**, the same matrix is acoustically characterized. Furthermore, this chapter describes an

interconnection layer that reduces the negative effects of an ASIC that is part of the backing.

Chapters 5 and 6 focus on data reduction and data acquisition schemes. In **Chapter 5**, a computationally efficient frequency domain two-stage beamforming approach is presented for a polar geometry. This approach allows for significant data reduction in the first stage, applied in-probe, and then generates a high-quality image by combining the first-stage data. While the approach is verified with a phased array, it can also be applied with matrix arrays. **Chapter 6** evaluates an electronically translatable linear-array imaging scheme in combination with the matrix used in **Chapters 3 and 4** for high-frame-rate carotid pulse wave imaging. The performance is evaluated both in simulations and measurements on a static phantom.

In **Chapters 7 and 8**, the focus is on high-frame-rate volumetric vector flow imaging using matrix arrays, aimed at applying these matrices in population monitoring of the carotid artery. In **Chapter 7**, the same imaging scheme and transducer from **Chapter 6** are applied to this application, which requires an even higher frame rate. The performance is directly evaluated based on the estimated velocities. **Chapter 8** presents an alternative to conventional image compounding and applies it to vector flow imaging. This approach circumvents the drawback of conventional compounding, which involves a trade-off between image quality and the ability to measure high velocities. The performance is evaluated using a sparse array and a simulated flow phantom.

Finally, **Chapter 9** provides an overview of the results of this thesis, discussing how well they addressed the various challenges associated with matrix arrays. Additionally, it offers recommendations for future research to further tackle the remaining challenges.

2

Ultrasound Matrix Transducer Design for Monitoring of the Neonatal Brain

This chapter was written with input from Jorinde Kortenbout and Peng Guo.

2.1 Introduction

Every year, more than 150 million babies are born worldwide. Of these 150 million, about 10% are born preterm [15], [16], which is defined as born before 37 weeks of gestation. Over the years, the survival rates of preterms have improved significantly [16]. However, preterms tend to suffer from health issues. Neuro-developmental problems are not uncommon, especially in preterms born before 32 weeks of gestation [20], and this may lead to further health issues during adulthood [17]. These issues are often connected to inadequate brain perfusion, for example due to hemorrhages [22]. As the percentage of preterm births increases every year worldwide [15], [16], improved care and monitoring to prevent and treat brain injuries becomes of utmost importance.

In order to detect an abnormality in the brain early, it should be monitored via multiple modalities. Standard monitoring includes monitoring of vital parameters and methods like near-infrared spectroscopy (NIRS) and amplitude-integrated electroencephalography (aEEG). However, they are inadequate for brain monitoring. Monitoring vital parameters, e.g., blood pressure and oxygenation level, only provides a global overview of the health of a preterm and therefore does not provide direct readings of changes in the brain. NIRS is a non-invasive modality that can be used to monitor the oxygenation level in the brain for prolonged periods [26]. However, it can only provide localized readings near the sensor of the oxygenation. Furthermore, it is not robust enough to provide quantitative levels and interpretation of the trend in oxygenation level cannot be done without other modalities [26], [27]. aEEG is used to monitor electrical activity in the brain [93], [94]. This approach enables the early detection of encephalopathy and epileptic seizures, which may arise following changes in medication or post-operation [95], [96]. Disadvantages of aEEG include that changes in blood flow are not always mirrored in the aEEG readings [28] and that, similarly to NIRS, it does not provide information about areas not covered by electrodes. Each of the modalities can thus only provide incomplete information about the state of the brain. Furthermore, the readings might be difficult to interpret on their own. Consequently, a solution is needed that integrates all monitoring modalities to provide sufficient information [29]. However, even together, these modalities do not provide sufficient information about the perfusion throughout the brain.

Cranial ultrasound could supplement the other modalities to provide a more complete reading of the brain. It has the capability to monitor haemodynamic changes across the entire brain and offer localized readings [32]. However, while ultrasound is already used to image the brain manually, it is not generally included to constantly monitor the brain. The transducers used for imaging are generally quite large, making integration with other modalities difficult. While they can be made smaller, 3D imaging capabilities are also necessary to image all points of interest and provide resilience against movement of the probe and placement errors. A currently existing ultrasound device that can be used for monitoring is the NeoDoppler [33], but it cannot provide 3D imaging as it consists of a single element. Therefore, the development of a new ultrasound monitoring device is necessary.

The MIFFY project, short for Monitoring Infant brain perFusion by trans-Fontanel echographY, aims to develop a specialized 2D matrix array for monitoring the preterm brain, as depicted in Figure 2.1. The envisioned final system proposes a wireless matrix array designed to monitor the preterm brain through the anterior fontanel, which serves

as an acoustic window to the brain. The matrix would be embedded within a wearable patch together with other monitoring technologies and attached to infant's head. New data would be acquired every 10 minutes without the intervention of a sonographer and transmitted wirelessly to a remote workstation. At the workstation, the volumetric data is provided to facilitate proper diagnosis by clinicians. However, a full implementation of the envisioned system is beyond the scope of the current project. Therefore, the focus is on developing and manufacturing a proof-of-concept wired ultrasound matrix array that meets most of the clinical requirements. In parallel, further research will be conducted into the clinical case for brain monitoring using ultrasound [97].

There are different kinds of matrix arrays, and we decided to design one integrated with an application-specific integrated circuit (ASIC) as it offers the highest level of adaptability for a specific application. An ASIC directly below the elements allows for various ways of channel reduction, such as micro-beamforming, multiplexing schemes, in-probe digitization, on-chip pulsers, or a combination of these, depending on the unique requirements of the application [70], [72]–[74], [98]. Additionally, amplifiers can be integrated into the ASIC to amplify the signal close to the source and prevent signal loss, for example, due to attenuation in the cable in wired systems [74], [98]. The combination of channel reduction schemes employed depends on the clinical requirements, the acoustical effects, and the space requirements of the underlying electronics. Therefore, the matrix must be designed with careful consideration of all these aspects.

This chapter provides a simplified and concise overview of the process to design a new ultrasound matrix array for monitoring of the preterm brain. Section 2.2 discusses the clinical requirements to understand the essential functionalities needed for effective monitoring. Section 2.3 investigates acoustical effects of the matrix parameters, such as pitch, and electronic components that have an acoustical influence. Based on the investigation, we derive values that align with the clinical requirements. Section 2.4 discusses various aspects in the electronics and ASIC design, such as the transmit electronics and programming requirements. Section 2.5 proposes a matrix design that achieves most of the clinical requirements, based on findings from the previous sections, Section 2.6 discusses the two prototypes to verify the proposed design and ASIC components. Finally, Section 2.7 concludes this chapter.

Figure 2.1: Final proposed mode of operation of the MIFFY matrix. On the left, preterm baby with a matrix transducer on top of its head. On the right, a workstation monitored by the nurse. The data is transferred wirelessly between the device and workstation.

2.2 Clinical requirements

The main aim of the MIFFY matrix is to monitor the brain of a very preterm, born before 32 weeks of gestation, for the first 3 days of life. Among the critical concerns during this early period are germinal matrix and/or intraventricular haemorrhages [19]–[21], which are generally common during these 3 days and tends to rapidly escalate in severity. Therefore, the device must at least be able to measure up to the depth of the ventricles and assess the periventricular zone. This is essential to allow for early detection of haemorrhages, enabling timely intervention to prevent further damage, or to prevent them entirely by detecting changes in the brain that could indicate a high risk of haemorrhaging.

While monitoring the preterm brain for haemorrhages is the main aim, the probe could also be used for other monitoring applications. Additional applications in preterms include monitoring the brain after an infection, which is likely after prolonged hospitalization [99], and monitoring treatment effects, for example, to help keep parameters like blood pressure and oxygenation within bounds [100], [101]. For newborns in general, the brain can be monitored after surgery for non-cardiac congenital anomalies as 50% end up with some sort of brain injury [102], [103].

In the rest of this section, we will discuss the modalities that we plan to use for monitoring, the required imaging volume, the aperture size, the resolution requirements of the matrix and a small study about the attenuation in the preterm brain. At the end the requirements are summarized in a table.

2.2.1 Modalities

To monitor the brain for changes we aim to use 3 modalities, which are illustrated in Figure 2.2. First, the standard greyscale images to monitor for change in echo density. For example, in Figure 2.3 the infarction causes a noticeable change in echo intensity in the area marked by the circle. Second, Doppler imaging to visualize the vascular tree and track alterations in blood flow. The focus is on smaller vessels with dimensions in the order of 200 µm and with velocities lower than 10 cm/s. There are two main requirements to be able to measure these small vessels. A high frame rate in the order of 1 kHz to be able to distinguish small vessels from surrounding tissue [10] and a high frequency to achieve a sufficient resolution. This modality provides an additional way of identifying and monitoring infarctions, as depicted in Figure 2.3, where the right hemisphere has significantly less perfusion after the infarction. Finally, elastography would allow for measuring changing in stiffness of brain tissue. Dysfunction or changes in blood pressure may give rise to changes in elasticity [105] and, therefore, elasticity measurement could potentially enhance the diagnostic sensitivity [106]. Our aim is to measure the stiffness passively using naturally occurring shear waves, a technique described by Catheline *et al.* [107]. Unlike the other modalities, there is insufficient information about the naturally occurring shear waves in the preterm brain and their associated velocities to arrive at specific requirements for this method. However, based on the paper by Catheline *et al.* [107], it is likely that a frame rate of 1 kHz is sufficient, which is the same as required for Doppler imaging.

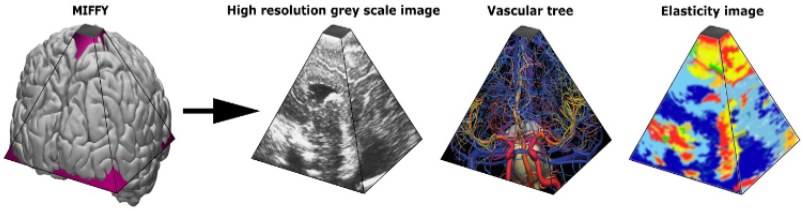

Figure 2.2: Modalities to be used with the MIFFY matrix.

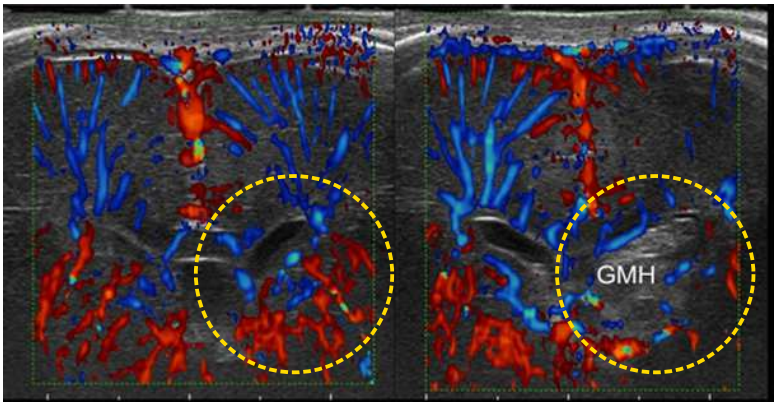

Figure 2.3: Ultrasound image including an colour Doppler overlay of the vessels in the preterm brain before, left, and after, right, a germinal matrix haemorrhage (GMH). The GMH caused a change in grayscale in the area marked by the circle, and significant reduction in blood flow in the right hemisphere. Adapted from [104].

2.2.2 Imaging volume

There are two requirements for the imaging volume. First, the volume has to encompass the periventricular zone. To get an estimate for the position of this zone, we determined the width and depth of this zone in 41 preterms. This is a subset of the data obtained in a study used to develop a novel scoring system to evaluate the quality of neonatal cerebral ultrasound images [97, Chapter 2]. From the data, we estimated that the deepest part of the ventricles extended to a depth of 3.0 ± 0.6 cm, while the width of the ventricles was 2.6 ± 0.5 cm achieved at a shallower depth of about 2 cm. We decided that the matrix should be able to measure the majority of all preterms and decided that the mean plus standard deviation was a good measure for this. The second requirement is to have a clear advantage over 2D and cross-plane imaging. Therefore, we decided that the imaging volume has to be pyramidal, like in Figure 2.2, with the same width in both lateral dimensions. Therefore, the imaging volume will be pyramidal, extending up to a depth of 3.5 cm, and the required width in both lateral dimensions is 3 cm at a depth of 2 cm.

2.2.3 Aperture size

The fontanelles of neonates provide an ideal acoustic window for ultrasound imaging, since imaging through the skull introduces aberrations and reflects most of the signal [30], [31].

We plan to use the anterior fontanel and therefore, the maximum size of the aperture is limited by its size. The data in literature [108]–[110] shows that the fontanel size, defined as the average of the length and width of the fontanel, varies widely between infants, ranging from less than 1 cm to more than 6 cm. The width and length of the fontanel appear to be similar at term [108]. We saw a similar result in the dataset used to estimate the imaging volume, where the measured width was 1.8 ± 0.9 cm. We decided that we should have an aperture size on the lower end of the measured sizes as imaging through bone is difficult and to keep the number of elements limited. Furthermore, as there is no clear difference between the length and width of the fontanel and there is no clear reason to have a better image quality in one of the lateral dimensions, we decided that the aperture can be a square. Therefore, we decided that the aperture should be a square with sides of 1.5 cm.

2.2.4 Resolution requirement

To determine the resolution requirements for our probe, we qualitatively investigated Doppler images made with different centre frequencies using standard-of-care transducers in the Neonatal Intensive Care Unit (NICU) in Utrecht. All images were acquired using line-by-line imaging. In general, images made with a low frequency showed blood flow deeper into the brain, but also only in the larger vessels. This aligns with the common trade-off in ultrasound imaging: penetration depth versus resolution. Based on these comparisons, we concluded that higher frequencies are preferable in general, but a centre frequency of 8 MHz using line-by-line imaging is sufficient for the intended purpose.

2.2.5 Preterm brain attenuation

Limited research exists on the attenuation in the preterm brain. A study by Kremkau *et al.* [111] suggests that the attenuation in the brain of an infant is approximately 0.33 dB/cm/MHz$^{1.1}$, which is roughly three times lower than the attenuation observed in an adult brain in the same study. However, as there was only one infant measured and there is an absence of additional information on the attenuation in preterm or term babies, a small clinical study was conducted to verify the previously mentioned value [112]. In this study we used a clinical ultrasound machine, the Zonare ZS3 (Mindray Medical International, Hoevelaken, Netherlands), with a high frequency linear probe (L20-5) to image the brain of 3 preterms. The estimated attenuation ranged from 0.09 to 0.22 dB/(cm MHz). Although the number of estimates is limited, the investigation suggested that the value determined by Kremkau *et al.* serves as a reasonable upper limit for the attenuation in the preterm brain. Therefore, the attenuation value of the preterm brain was assumed to be 0.33 dB/cm/MHz$^{1.1}$.

2.3 Acoustical Design

To design a PZT-on-ASIC matrix transducer, there are various parameters to consider. Some of these can be directly derived from the clinical requirements and limitations, which are listed in Table 2.1. For other parameters, the effects they have on the image need to be taken into account. These include the pitch, channel reduction, delay quantization, and the transmit voltage. Additionally, the effect of high-frame-rate imaging should be considered,

as it affects the resolution and, in turn, the required centre frequency. In this section, these effects will be investigated.

Regarding the channel reduction, there are various ways to achieve it. In this section, we will only discuss time-division multiplexing (TDM) and micro-beamforming (μBF) as they affect the image quality. The other methods will be discussed in Section 2.4.2.

Table 2.1: Parameters derived from clinical requirements

Parameter	Value	Determined by
Aperture size	1.5 cm × 1.5 cm	Fontanel size
Imaging volume	Pyramid shape	Germinal matrix
Maximum depth	3.5 cm	Germinal matrix
Maximum width	3 cm at 2 cm depth	Germinal matrix
Doppler velocity	10 cm/s	Velocity in smaller vessels
Frame rate	> 1 kHz	Tissue Filtering
Attenuation	0.33 dB/cm/MHz$^{1.1}$	[111] and own research
Resolution target	Line-by-line imaging at 8 MHz	Image comparisons
Monitoring interval	10 minutes	-

2.3.1 Simulation Environment

Table 2.2: Simulation parameters

Parameter	Value
Aperture size	1.5 cm
Centre frequency	10 MHz
Transmit pulse	Sine modulated with a 3 cycle Hann
Tx apodization	Tukey - 0.1 cosine fraction
Rx apodization	Hamming
Kerf	20 μm
Angles	5: 0°, ±12° and ±24°
Simulation Dimension	2D

To investigate the effect of the acoustical parameters, simulations were done using Field II [113], [114] with the settings listed in Table 2.2.

While a matrix array can make 3D images, it is not necessary to do 3D simulations to investigate the effect of the parameters. There are two reasons for this. First, the clinical requirements allow for a square matrix with the same parameters in each lateral direction. Second, we assume that if a certain trend or threshold is visible in 2D simulations, it will be similar or worse in 3D. Therefore, our simulations were done in 2D instead of 3D.

Matrix

The width of the 1D array used in the simulations was always about 1.5 cm. The pitch was one of the parameters to be varied, so the value used is mentioned along with the results. The kerf was always kept at 20 μm, the minimum that we are able to manufacture.

The transmit pulse is a sine modulated with a 3-cycle Hann. The centre frequency is a parameter under consideration. However, the centre frequency is fixed at 10 MHz in the simulations. This is done as most other parameters affected by the centre frequency can be scaled with the centre frequency if necessary.

In transmit, a Tukey window with a cosine fraction of 0.1 was used to reduce the effect of edge waves while keeping the beam-width as wide as possible. In receive, a Hamming window was used as apodization.

Phantom and metrics

In order to investigate the impact of different parameters on image quality, it is essential to employ a standardized method for retrieving one or more metrics. Two commonly used metrics are resolution and contrast-to-noise ratio (CNR). Both these metrics can be investigated using a phantom such as the CIRS-040GSE (CIRS, Norfolk, VA, USA), which is shown in Figure 2.4a. One issue with such a phantom is that the metrics can only be retrieved at a limited number of locations that are not well spread. For instance, in this phantom the CNR can be assessed at different depths using the hypoechoic cysts, but not at different lateral locations. This issue could be circumvented by extracting the CNR in different images taken at different positions, but we wanted a simpler process.

Therefore, to investigate the image quality we utilized the phantom shown in Figure 2.4b. This phantom consists of an array of point scatterers, spaced at 1 mm intervals. To extract image quality metrics, we initially subdivide the image into 1 mm × 1 mm squares, each centred around a point scatterer. Now, the image quality metrics can be obtained using a single image and at 1 mm intervals.

In this chapter, the only image metric that we consider is the signal-to-clutter ratio (SCR). This metric is similar to the CNR, i.e. a high SCR implies a high CNR. However, due to lack of hypo-echoic cysts in the phantom, calculating the CNR is not possible. The SCR is defined as

$$SCR = \frac{S_p}{S_m}, \tag{2.1}$$

where S_p is the peak amplitude and S_m the mean in a rectangular region around the point scatterer. A higher value for the SCR is better, but otherwise interpreting the value on its own is difficult. Therefore, we compare the SCR values to a baseline or look at the trend.

For the SCR numbers that we present, we always only calculate the SCR within the region illuminated by the transmitted plane waves, between a depth of 5 mm and 40 mm, within ±15 mm lateral and within ±24° as defined from the outer edges of the transducer.

Measuring resolution is also possible. However, in general, (lateral) resolution and the SCR tend to worsen in tandem. Furthermore, in the image reconstruction, the amount of clutter can be a trade-off against the achievable resolution. Therefore, to simplify the investigation, we ignore this metric.

Compounding angles

To image a 2D slice of the volume determined in the clinical requirements, at least 3 angles are required: 0° and ±∠21. In 3D this translates to a minimum of 9 angles. Ideally, as many transmit angles as possible are wanted to achieve the highest resolution and image quality. However, as will become clear during Section 2.3.5, there is not much time available for compounding at all. Therefore, we minimized the number of angles.

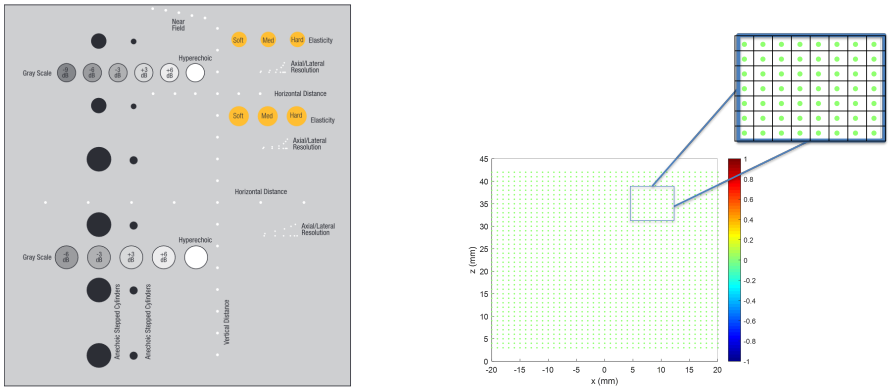

(a) (b)

Figure 2.4: (a) Layout of the CIRS 040-GSE tissue phantom [115]. (b) Phantom with point scatterers spaced by 1 mm in both directions. In the squares centred at each scatterer the local resolution and Signal-to-Clutter ratio (SCR) can be calculated

For the results in this chapter we increased the number of angles to 5 per direction: $\angle 0$, $\pm\angle 12$ and $\pm\angle 24$. The maximum angle has been increased as a limited size matrix will not transmit a perfect plane wave. The width of the plane wave becomes narrower deeper into the medium due to the natural focusing of the transducer. A slightly wider angle compensates this. Because of this however, the same problem that we wanted to prevent now appears between the 0° and 24° plane waves as well, so we also added $\pm\angle 12$.

Beamforming

Beamforming was performed using Delay-And-Sum (DAS). In every simulation, all elements were used in reception. This choice worsens the amount of clutter but generally results in the highest lateral resolution.

2.3.2 Centre frequency

The target lateral resolution for our matrix was achieved at 8 MHz and line-by-line imaging. However, with high-frame rate imaging the focusing in transmit is absent and, therefore, the lateral resolution is lower. Table 2.3 shows the lateral resolution achieved with and without transmit focusing for different frequencies. To achieve the same lateral resolution as with line-by-line imaging at 8 MHz, the plane wave image would have to be made with a centre frequency of 11 MHz. Such a high frequency would also imply a small pitch, and whether that can be achieved will be further investigated in the next subsection.

Table 2.3: Resolution in degrees for different frequencies derived from the array directivity.

	8 MHz	9 MHz	10 MHz	11 MHz	12 MHz
Focused	**0.59**	0.53	0.47	0.43	0.39
Plane Wave	0.82	0.73	0.65	**0.59**	0.54

2.3.3 Pitch

Introduction

An element pitch larger than half a wavelength introduces grating lobes [1]. In general, the pitch is compared to a wavelength (λ_c) corresponding to the centre frequency. While with a 0.5 λ_c pitch, there are no grating lobes for the centre frequency, there might be grating lobes for the higher frequencies present in the signal. For example, for a 10 MHz sine modulated with a 3 cycle Hann, the −6 dB bandwidth reaches 13 MHz, which corresponds to a pitch of 0.65 λ. However, whether those grating lobes significantly degrade the image quality depends on the signal bandwidth, the maximum steering angle used and the imaging method, e.g. line-by-line or plane wave.

Two types of commonly used 1D arrays are the phased and linear array [1], [2]. A phased array has a relatively small footprint so that it, for example, can image the heart through the space between the ribs. The pitch is generally 0.5 λ_c so that it can achieve high steering angles without having grating lobes severely degrading the image quality. A linear array has a larger footprint and generally has an array pitch around λ_c. A linear array is generally only used to image the region in front of the transducer. This allows the steering angle to be kept small and limits the effect of grating lobes. Therefore, as the required imaging volume extends beyond the array, we require something akin to a phased array pitch.

Ideally, our array would thus have a pitch of 0.5 λ_c. However, a 0.5 λ_c pitch at 11 MHz equals 70 µm and that is significantly smaller than the pitch of any matrix that we have constructed before. We think it is feasible to manufacture an array with a pitch of 100 µm, but for a centre frequency of 11 MHz, which is required to hit our resolution target array, the pitch would correspond to about 0.7 λ_c. With this pitch we can expect grating lobes to affect the image, but we are not certain how much. Therefore, here we will investigate the effect of pitch on image quality and determine what we think is the maximum pitch possible.

Effect on image

As the effect of a large pitch is most easily seen at large steering angles, we first look at the resulting images using 0.5 λ_c and λ_c pitch probes, with the transmit beam steered at an angle of 30°. In Figure 2.5 the beamformed image (a) and the corresponding SCR (b) using a 0.5 λ_c pitch probe are shown. Within the transmit beam, indicated by the white lines, the SCR starts off high close to the probe and then slowly drops off further away. The main contributing factor is the lower lateral resolution further away from the probe. Additionally, at the edges the SCR degrades faster as the width of the transmitted plane wave decreases due to the natural focus of the probe. Outside the transmit beam, the scatterers are mostly invisible and the SCR is low as they are not illuminated. As mentioned before, even a probe with a 0.5 λ pitch has some grating lobes due to the higher frequencies within the signal. These are visible in the top left of Figure 2.5a.

When the pitch is doubled to λ_c the situation changes significantly as can be seen in Figure 2.6. While the resolution has not changed, the clutter has increased to a level that obscures the point scatterers to the eye due to the higher grating lobe level. The resulting SCR is about 15 dB to 20 dB lower as compared to the 0.5 λ_c pitch probe, as is visible in Figure 2.6b. The largest difference is at the rightmost side of the image where the receive

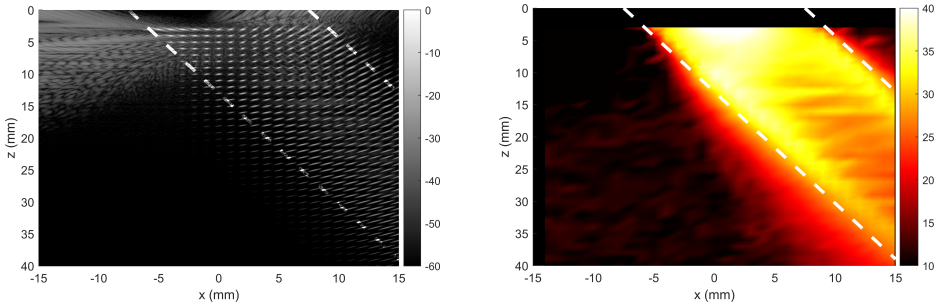

(a) (b)

Figure 2.5: Gray scale, in (a), and the SCR, in (b), image of a 0.5 λ probe with a plane wave transmitted at 30°. The white lines indicate the width of a plane wave steered at 30°

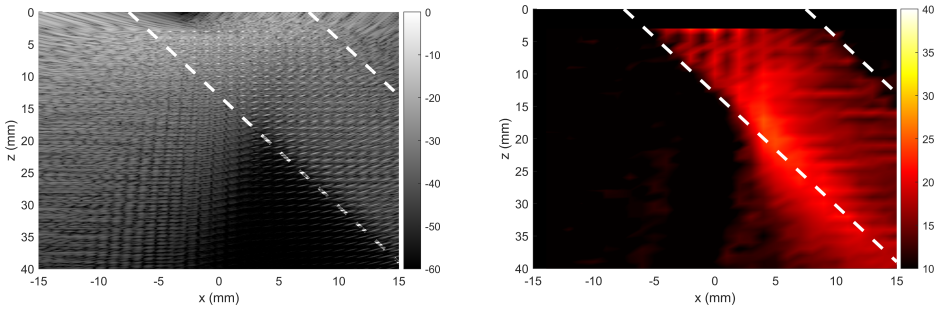

(a) (b)

Figure 2.6: Gray scale, in (a), and the SCR, in (b), image of a 1 λ probe with a plane wave transmitted at 30°. The white lines indicate the width of a plane wave steered at 30°

steering angle is largest. Additionally, the grating lobes also clearly show up on the left side of Figure 2.6a. Even though this area will not be used for imaging, it clearly shows the effect that increasing the pitch has on the image.

Effect on SCR

In Figure 2.7a the SCR is plotted for a pitch ranging between 0.5 and λ_c. Instead of a single transmit angle, as in the cases before, we used $\angle 0$, $\pm\angle 12$ and $\pm\angle 24$ to image the whole region of interest and calculate the SCR there. For a pitch of 0.5 λ_c and lower there is hardly any difference. There is a very minor decrease with increasing pitch that is caused by grating lobes of frequencies higher than the centre frequency. For a pitch larger than 0.5 λ_c the SCR drops considerably with each step. Even when the maximum required steering angle is only $\pm\angle 24$, a pitch of 0.6 λ_c already causes a visible worsening in all metrics.

To show that the maximum steering angle affects the drop-off point, we also calculated the SCR with the angles $\angle 0$ and $\pm\angle 12$ in the region illuminated by those angles. The result in Figure 2.7b shows that the drop-off starts at 0.7 λ_c instead of 0.6 λ_c. As expected, if smaller steering angles are required, the pitch could be made larger.

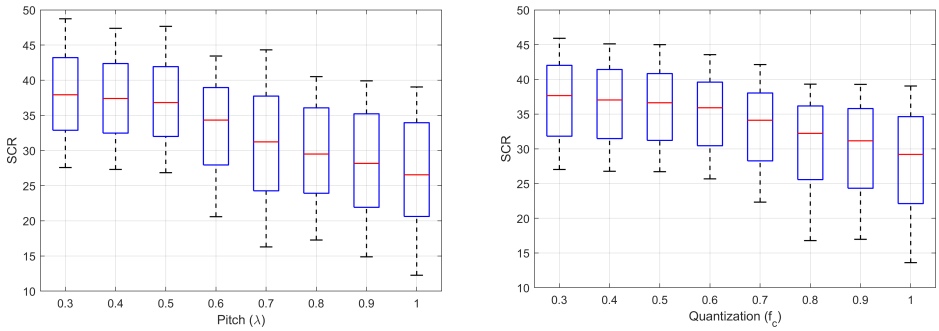

(a) (b)

Figure 2.7: A boxplot of the SCR for a varying pitch. In (a) the used angles are 0, ±12° and ±24°, and in (b) only 0 and ±12° are used.

As mentioned before, to achieve a 100 µm pitch at 11 MHz a pitch of 0.7 λ_c is required, but a pitch larger than 0.5 λ_c worsens the image quality. Therefore, we decided to compromise on resolution and image quality by selecting a pitch of 0.6 λ_c and a centre frequency of 9.2 MHz.

2.3.4 Micro-beamforming

Introduction

Micro-beamforming (µBF) [70], [75], [116], [117] modifies the DAS receive beamforming process, as shown in Figure 2.8a, to reduce the number of channels. This is achieved by splitting the beamforming delays into two parts: a fine delay applied at the transducer and a coarser delay applied within the ultrasound system, as illustrated in Figure 2.8b. This method allows the signals from a µBF sub-array to be combined into a single signal. In the figure, the sub-array size is 4, resulting in a fourfold reduction in the number of channels. However, it is important to note that µBF impacts the image quality.

Investigation

The situation illustrated in Figure 2.8 depicts an ideal scenario where there is no difference in the final result. The delays are exact, resulting in no variation in the final signal. However, this is not always the case, as shown in Figure 2.9, which presents the SCR for no µBF , µBF 2, and µBF 3. Further from the transducer and closer to the center, the differences in SCR are minimal, but otherwise, the SCR is significantly worse. There are two main reasons for this. First, the flat wavefront shown in Figure 2.8 is only valid for regions further from the probe. The closer the region is to the probe, the greater the curvature. Therefore, the combined delays of the on-chip and off-chip beamformers are not exact for all regions. Second, the combined signals from the sub-arrays effectively form an array with larger elements in receive. These larger elements are more directive and provide worse performance when large steering angles are used, as discussed in Section 2.3.3. These two effects combined result in lower SCR near the probe and towards the lateral edges of the domain. The increased clutter from using µBF could be mitigated by limiting the number of elements used for image reconstruction. However, this would lead to a reduction in

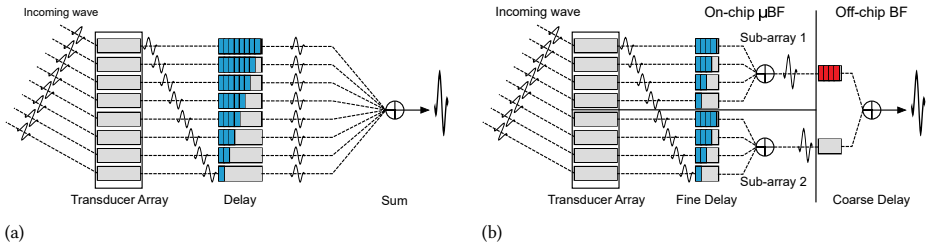

Figure 2.8: Illustration of the μBF concept. (a) Beamforming process employing DAS. (b) μBF process employing two-step DAS. Adapted from [73]

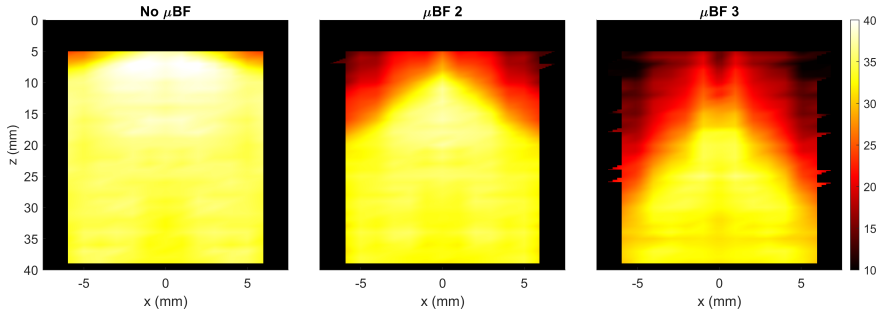

Figure 2.9: SCR for no μBF (left), μBF 2 (middle) and μBF 3 (right). The transducer has a 0.6 λ_c pitch.

resolution due to the smaller aperture. Consequently, μBF will worsen the image quality regardless.

For the monitoring application, imaging near the probe is essential, and a wide imaging volume per pulse-echo is preferred to reduce the number of shots needed to reconstruct the entire imaging volume, thereby limiting the amount of data. Therefore, these results indicate that the extent of μBF should be minimized.

2.3.5 Time division multiplexing

Introduction

Another way to achieve a channel reduction is by time division multiplexing (TDM) [118]. There are two ways to apply TDM. By applying it at the input, only a subset of the elements is read out each pulse-echo event, thereby requiring multiple shots to read out all elements and reducing frame rate. By applying TDM at the output, i.e., after the Rx electronics, it allows multiple channels to share a single output by dedicating a separate time slot at the cost of a reduced SNR due to interference [119]. We will apply TDM at the input as we plan to digitize the signals at the output of the Rx electronics.

The maximum possible amount of time multiplexing depends on two factors: The maximum imaging depth sets the maximum possible pulse repetition frequency (PRF), and the blood and tissue velocities together with the centre frequency of the transducer determine the minimum required PRF. The maximum possible time multiplexing is simply the PRF divided by the required frame rate.

Investigation

As described in Section 2.2, the maximum imaging depth for the MIFFY project is 3.5 cm. This results in a maximum possible pulse repetition frequency of 22 kHz.

To derive the minimum required frame rate we can rewrite eq. (10.4) from [2] into

$$\mathrm{FR}_{min} = \frac{4 v_{max} \cos\theta f_c}{c_0}, \tag{2.2}$$

where FR is the frame rate, v_{max} the maximum velocity to be measured, θ the angle between the beam and the flow direction, f_c the centre frequency and c_0 the speed of sound. Using our desired 10 cm/s, a centre frequency of 9.2 MHz and a beam-to-flow angle of 0°, a worst-case scenario for the angle, the minimum FR would be about 2.4 kHz.

The maximum PRF of 22 kHz and the minimum required frame rate of 2.4 kHz result in a maximum time multiplexing factor of 9 to make a single image.

Doppler De-Aliasing

If the maximum multiplexing factor would be necessary to achieve the required channel reduction, there is no room for any compounding. However, there are methods that allow to increase the maximum measurable velocity. For example, the method by Posada *et al.* [120] varies the PRF to achieve velocity estimates with a different aliasing limit and combines them to de-alias the final estimate. Another method by Porée *et al.* [121] does something similar, but instead of varying the PRF, the estimates are made from a different frequency band in the same data. These methods could at least double the aliasing velocity, and possibly even triple it. This would then allow using 2 or 3 compounding angles to improve the image quality.

Motion Artefacts

A possible issue with TDM is the appearance of motion artefacts as a single image is constructed from several pulse-echo events at different time. They could severely impact the resulting image and flow estimation, but motion compensation methods also exist to mitigate this. An example of such a method is the one by Porée *et al.* [122]. They use a specialized transmit sequence where multiple images acquired with different transmit angles are used to compensate for motion. Because that effectively reduces the frame rate, it is not an option for us. However, another method by Jorgensen *et al.* [123] uses an iterative scheme where the estimated velocities of the previous estimate are used to compensate for the motion. This iterative scheme quickly converges and reduces the estimation errors significantly. Motion artefacts are thus not expected to be a problem.

2.3.6 Delay quantization

Introduction

A channel reduction in transmit is necessary as well, just as it is in receive. This can be achieved by employing on-chip pulsers to generate the transmit wave for each element. However, space constraints pose a challenge in providing the same functionality as 1D arrays in transmission, such as arbitrary waveform generation and independent delays for each channel. Specifically, achieving arbitrary transmit delays within the confines of on-chip space may be unfeasible. Here, our focus will be on the transmit delays.

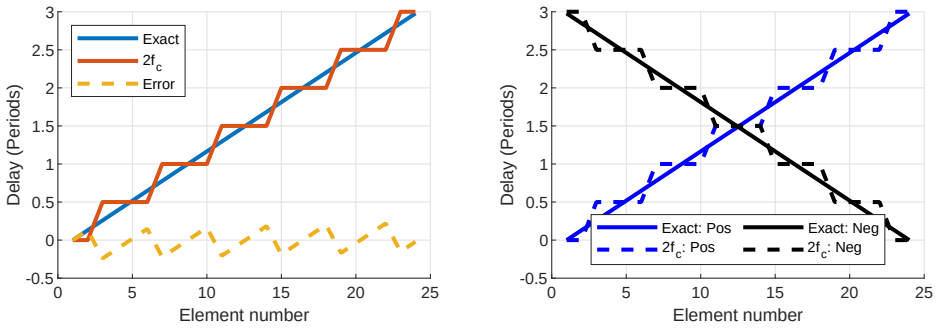

Figure 2.10: (a) The exact delay and a delay quantized at $2f_c$, together with the delay error for the quantized delay for a steered plane wave. (b) A comparison of the exact and quantized delays for a positive and negative angled plane wave.

On-chip pulsers still offer the possibility of creating an arbitrary delay profile, albeit potentially with coarser quantization. Early research in the 1980s already investigated the effects of delay quantization for pulsed waves due to hardware limitations at the time [124], [125]. Although technological capabilities improved subsequently, the issue resurfaced with the demand for miniaturization in ASIC design [126] and the development of low-cost ultrasound devices [75], [127], [128].

Studies indicate that quantization errors have a lesser impact on pulsed signals compared to continuous ones, owing to the short overlap between pulses from different elements [125]. Moreover, research suggests that relatively coarse quantization already yields comparable results [127], [129], albeit with performance clearly varying depending on the specific scenario. Therefore, we will analyze the effect of delay quantization for our situation.

Setup

We will quantize the delays as an integer multiple of the centre frequency. A delay quantization of Nf_c, where f_c is the centre frequency, would allow for delays every $1/N$ periods. An example of this quantization level is shown in Figure 2.10a for a steered plane wave. By defining the quantization with respect to the centre frequency, the results in this subsection are also applicable to transducers with a different centre frequency.

In this section, we will not use any delay quantization in receive. While the delays in a µBF group might also be quantized, the negative effects of quantization are expected to be significantly lower due to the small number of elements in a µBF group.

Transmit beam

The effect on a 30° plane wave for two different quantization levels is shown in Figure 2.11 where the peak amplitude, in (a), and the energy, in (b), at each position are plotted. There are two main differences between the exact delays and the $2f_c$ quantization.

First, there is less energy transmitted into the wanted direction. The peak amplitude is lower in Figure 2.11a for $2f_c$ quantization and in Figure 2.11b it is visible that more energy is transmitted into the opposite direction. While for the exact delays there are some grating lobes, for $2f_c$ quantization there also appears to be a transmission at −30°

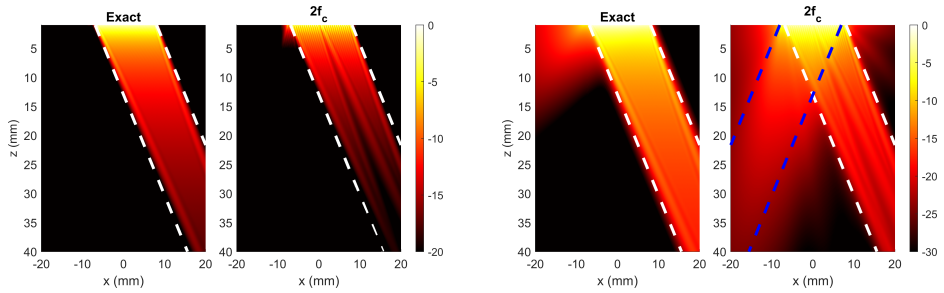

Figure 2.11: (a) Peak amplitude and (b) energy at each position for a transducer of 0.6 λ pitch transmitting a plane wave at 30° for two different quantization levels. The white dashed lines indicate the width of a plane wave at 30° and the blue dashed lines indicate one at −30°. Every sub-figure is separately normalized.

with more or less the same width of the array. This can be seen as an additional grating lobe as the quantized delays effectively create larger elements, i.e. all elements with the same delay in Figure 2.10a can be seen as a single element. However, this does not explain why this grating lobe appears at −30°. That specific angle can be explained by considering Figure 2.10b, where the delays for a positive and negatively angled plane wave are shown, and noting that for a continuous wave half and whole period delays are equal to a delay of 0 and 0.5 periods, respectively. Therefore, the delays for a continuous plane wave at ±30° and all other angles are equal. However, because we use pulsed waves, only parts of the transmitted pulse interfere at −30° and the effect is just an increased amount of energy transmitted in that direction. For the image, this will reduce the maximum imaging depth and increase the amount of clutter.

The second main difference is a larger variability in amplitude, especially near the probe. This is because subsequent groups of elements have a delay that is out-of-phase by a half period, which causes destructive interference. Further away the effect is less pronounced, but still visible. This effect on its own will mainly be visible as additional amplitude variations in the image.

SCR

The results in Figure 2.12 show the effect of the SCR for quantization between 0, i.e. no quantization, and 16, and an element pitch of 0.5 λ and 0.6 λ. For both, the SCR with $2f_c$ is significantly lower than without quantization with a 7 dB and 8 dB lower median for a pitch of 0.5 λ and 0.6 λ respectively. However, there are two main differences. First, the highest achieved SCR is different as with 0.6 λ there are additional grating lobes. Second, the SCR appears to recover more slowly with increasing quantization for 0.5 λ. We are not sure why, but it does indicate that the effects of the quantization are very situation dependent as is also seen in literature.

The results thus show that the exact performance is very situation dependent and there can be still some visible effects up to a quantization of $16f_c$. Choosing a specific minimum requirement is therefore difficult. However, the difference between subsequent levels becomes progressively smaller with increasing quantization level while the system

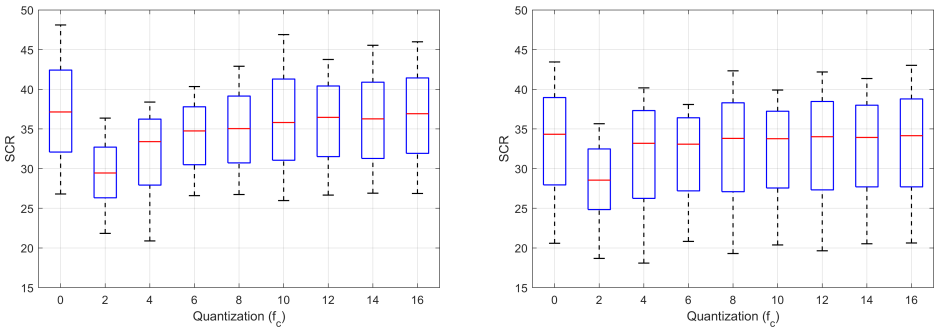

(a) (b)

Figure 2.12: SCR for quantizations between 0, i.e. no quantization, and 16 levels. In (a) for a transducer with a 0.5 λ pitch and in (b) with a pitch of 0.6 λ.

complexity becomes progressively larger. Therefore, we decided that the quantization level should be $6f_c$.

2.3.7 Maximum Tx Voltage

The maximum achievable transmit voltage depends upon both the piezo material and the accompanying electronics. Here, we primarily address the former aspect. A very safe upper limit for the electric field strength is 300 V/mm [130], but the exact value varies depending on the specific materials employed and whether the pulse is uni- or bi-polar. Considering this limit, and assuming a $\lambda/4$ oscillation mode for the PZT (i.e., utilizing a hard backing material), a speed of sound of approximately 3500 m/s [131], and a centre frequency of 9.2 MHz, we can estimate a maximum voltage of about 28 V.

This estimation falls below voltages achieved in our previous work with other matrices [132], [133], albeit those matrices feature larger pitch and varying functionality. Consequently, achieving the desired voltage level should be feasible for our current application.

2.4 Electronics and ASIC Design

With the clinical requirements set and the investigation into the acoustical effects of various parameters completed, it is now time to dive into the Electronics and ASIC Design. In this section, the transmit electronics, the required channel reduction, requirements for wirelessness, ASIC tiling, programming requirements, and time-gain compensation will be discussed.

2.4.1 Transmit Electronics

In general, the transmit electronics of an ASIC are typically bulkier compared to the receive electronics due to the need for sufficient isolation to handle high voltages. The exact space requirements depend on the transmit capabilities. Based on clinical requirements and acoustical design considerations, the necessary transmit capabilities are as follows: A delay quantization of at least 6 fcfc to keep the clutter low, a fully functional delay profile to image the whole pyramidal region, a small footprint to fit below the 100 μm^2 pitch elements,

and a maximum transmit voltage of 28 V. While an arbitrary waveform is not mandatory, the ability to vary the pulse length will aid in optimizing axial resolution and penetration depth.

In the event that achieving all requirements for a prototype within a 100 µm × 100 µm pitch is not feasible, the prototypes at least have to show that the design fits the clinical requirements. Therefore, achieving the delay requirements, i.e., a fully functional delay profile with sufficient quantization, is strictly necessary. If this cannot be accomplished with the desired pitch, we determined that the pitch should be increased.

2.4.2 Channel reduction requirements

With our target centre frequency of 9.2 MHz and a pitch of 0.6 λ_c, a square matrix with sides of 1.5 cm would require more than 20 000 elements, which is impractical to handle with existing technology. To address this, various methods for channel reduction can be used. We plan to employ a combination of on-chip digitization, time-division multiplexing (TDM), and µBF to achieve a reduction of 128 channels, thereby bringing the total number of Rx channels below 200.

On-chip digitization is anticipated to achieve a fourfold channel reduction, similar to designs as reported in previous works [133], [134]. The remaining 32-fold reduction should thus be achieved through a combination of TDM and µBF . The analysis indicated that minimizing the number of µBF units is crucial and that the maximum TDM achievable is 9. Therefore, we have opted for a 2 × 2 µBF and an 8-fold TDM strategy.

2.4.3 Wirelessness

To enable implementation in a wearable cap, the matrix ideally needs to operate wirelessly, necessitating additional components alongside the ASIC integrated matrix itself [135]. Apart from the matrix, the system architecture of the envisioned wearable ultrasound patch would include an FPGA to control all components and potentially post-process the measured data, a power management module to regulate and control the power supply in the system, a WIFI module for wireless data transfer, memory units for temporary storage of measured data before transfer, and, of course, a battery. The challenge of incorporating all these components within a compact wearable cap imposes strict requirements on the entire device, which have been deemed unattainable within the scope of this project. Hence, our focus has been on meeting clinical requirements with minimal cabling between the probe and mainframe, as well as reducing space and power requirements for all components on the ASIC. Subsequent development efforts could then concentrate on realizing a fully wireless solution.

2.4.4 Tiling

Manufacturing a single large ASIC can be very expensive [136]. To mitigate this, a tiled approach can be employed, wherein multiple smaller ASICs are positioned adjacent to each other to form a larger aperture. This approach has been utilized, for instance, by dos Santos *et al.* [98], where the full matrix comprises 10 identical ASIC tiles. A similar strategy could also be applied to the MIFFY matrix. However, at present, this is a consideration to be addressed later, as the prototypes we plan to develop during this project are sufficiently small.

2.4.5 Programming requirements

For high-frame-rate imaging, either the chip has to be quickly re-programmed during or in between the pulse-echo events, or have sufficient pre-programming capability. Re-programming the chip every time requires a sufficiently high clock frequency, while pre-programming requires extra space on-chip. As space is at a premium, we deemed having sufficient pre-programming capabilities out of reach and opted for quick re-programming. Here we discuss the requirements for that.

For the delays in both transmit and receive, the amount of required memory per element is determined by the relative delay times between neighbouring elements [133]. Using relative delays instead of absolute delays can reduce the memory bits required by an order of magnitude. Assuming a maximum plane wave steering angle of 24°, a 100 µm pitch, a quantization frequency of 6 times 9.2 MHz, which is the centre frequency, 2 bits would be sufficient to program the delays in transmit. Therefore, 2 bits per element would be sufficient to program the delays in transmit and receive.

In receive, in addition to the 2 bits to program the delays, the TDM sub-group also has to be selected. As there are 8, 3 bits per group are sufficient. Therefore, each element would effectively require 2.375 bits to program the chip in receive.

Combining both, if a 15 mm × 15 mm aperture is used, 98 438 bits are required for programming. These bits would need to be re-programmed within 50 µs at most, which is the time for a single pulse-echo event. Therefore, a 2 GHz clock would be needed to program all bits within a pulse-echo event, assuming all elements are programmed via a single data channel. Clock speeds in the order of 1 GHz are not uncommon [137], and if necessary, parts of the matrix could be programmed in parallel. Re-programming the chip each pulse-echo event would therefore be feasible, even if additional bits are required.

2.4.6 Time-gain compensation

Direct connection of the matrix elements to the imaging system would result in a large loss of signal [60], [63]. Therefore, the signals have to be amplified on the ASIC itself. This poses a challenge as there is a high difference between the lowest and highest amplitude of the received signals, also referred to as the dynamic range (DR). This has two main reasons. First, the signal from blood is approximately 40 to 60 dB [76] lower than tissue. Second, the signals are attenuated depending on the depth and frequency. In our case, the expected attenuation value is about 0.33 dB/cm/MHz$^{1.1}$ [111], which results in an attenuation of about 28 dB. This means that the overall dynamic range requirement for the receiver is at least 88 dB to capture all signals.

Achieving a high dynamic range for a wideband signal results in challenges to the circuit design and leads to a power-hungry ADC. The requirements can be reduced by applying time-gain compensation (TGC) to adjust the gain as a function of time to counteract the depth dependant attenuation as illustrated in Figure 2.13. This would reduce the DR for the ADC to 40 dB.

In previous designs from our group, the TGC was implemented as discrete gain steps [71], [98], [139]. However, this leads to artefacts when switching gain levels [139, Fig. 15]. Therefore, our aim is to implement a continuously variable TGC.

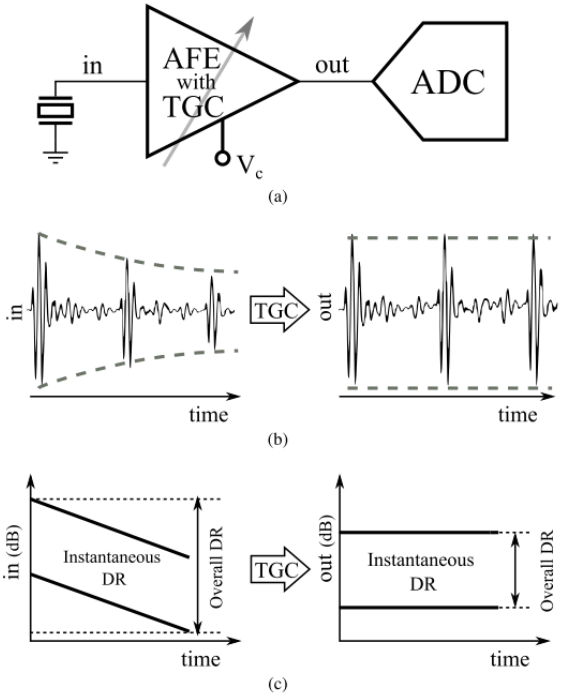

Figure 2.13: (a) Block diagram of the AFE with TGC function followed by an ADC. (b) Input and output signals of the AFE with TGC function. (c) Evolution of DR as a function of time with TGC function. From [138]

2.5 MIFFY Matrix Proposal

In Table 2.4 we list the "ideal" matrix parameters, which describe the values necessary to strictly adhere to the clinical requirements or the best possible value that can be achieved, and the parameters we think are feasible to achieve after our investigation. As these parameters were decided before any prototypes have been built and tested, they are still subject to change depending on the results obtained with the prototypes.

The main difference between the ideal and proposed parameters is the achieved pitch and centre frequency. An element size of 70 µm would represent 0.5 λ_c at 11 MHz, but it is smaller than that we can currently manufacture in-house. Additionally, this pitch would also not provide enough space for the pitch-matched electronics. Therefore, a larger pitch is necessary.

We decided that the minimum feasible pitch to manufacture would be 100 µm based on the yield of previous manufactured prototypes with a larger pitch. As a pitch larger than 0.5 λ_c would result in increased clutter due to grating lobes, as shown in Section 2.3.3, we also lowered the centre frequency to 9.2 MHz. This is a compromise between resolution and artefacts as this corresponds to 0.6 λ_c.

Table 2.4: Ideal and proposed parameters for the MIFFY matrix

	"Ideal"	Proposed	Comment
Aperture	15 mm × 15 mm	15 mm × 15 mm	Limited by fontanel area
Pitch	70 µm	100 µm	Minimum manufacturing
Centre frequency	11 MHz	9.2 MHz	Trade-off resolution/artefacts
Pitch (λ)	0.5	0.6	Trade-off resolution/artefacts
Elements	46000	22300	
Required channel reduction	256	128	Final channel count <256
µBF	None	2 × 2	Minimize
Time-multiplexing	1	8	Maximum possible
Rx output	Digital	PAM 16 - 4-fold reduction	
Tx voltage	28 V	28 V	Breakdown voltage of PZT
Tx pulse	Arbitrary	Multiple uni-polar pulses	Space requirements
Tx strategy	Element-wise	Element-wise	Imaging volume
Tx/Rx Delay quantization	None	$8\,f_c$	Minimum of $6\,f_c$
Imaging strategy	Sub-volumes & Compounding	Sub-volumes & Compounding	
Imaging Depth	0.5 cm to 3.5 cm	0.5 cm to 3.5 cm	Clinical requirement
Maximum angle	±24°	±24°	Clinical requirement
Frame rate	2.4 kHz	2.75 kHz	Clinical requirement

2.6 Prototypes

To verify the design as proposed in the last section, we have realized two prototypes during the project. They are summarized in Table 2.5 and are discussed further below.

Table 2.5: Parameters of the realized prototypes

	MIFFY0	MIFFY1
Centre Frequency	10 MHz	9 MHz
Pitch	100 µm / 0.65 λ	125 µm / 0.73 λ
Elements	8x8	16x16
Tileable	No	No
µBF	2 × 2	2 × 2
Time-multiplexing	8	8
Rx output	Direct - No reduction	PAM-16 - 4-fold reduction
TX voltage	36 V	20 V
Tx strategy	Rows	Element level
Delay Quantization	8 f_c	8 f_c

2.6.1 Prototype 1

The aim of the first prototype was to test the analog front-end [138], which includes a low noise amplifier with a continuously variable gain level of 36 dB, and a novel µBF architecture [73], which has a smaller footprint than other architectures. The prototype only allowed for separate transmit signals on each row. An overview of this prototype is shown in Figure 2.14.

Acoustic Measurements

Figure 2.15 compares the received signal with and without TGC enabled. The input was a pulse train with a decay rate of 0.4 dB/(cm MHz), resulting in a 36 dB amplitude difference over 60 µs. As shown, without TGC the signal visibly decays and drops below noise level, while with TGC enabled the output is more or less constant, with variations smaller than ±0.36 dB. This indicates that the TGC is working as expected. In Figure 2.16 the imaging setup and B-mode image in elevation plane of 3 needles at 6, 8 and 10 mm depth are shown. Even with the small aperture of 0.8 mm × 0.8 mm and no image compounding the needle positions are clearly visible. As expected, the needles have visible grating lobes due to the relatively large pitch as compared to the wavelength.

Manufacturing and ASIC design issues

During manufacturing of the acoustic stack of this prototype we ran into various issues due to the small pitch. We therefore initially decided to increase the pitch further to 115 µm. After further design of the next prototype, another increase in pitch to 125 µm was necessary to allow for the wanted transmit capabilities. With the current manufacturing process of the ASIC, a 180 nm BCD process, it was deemed impossible to achieve all design targets. For the future, this implies that further ASIC development is required and/or the design has to be modified to achieve the current clinical requirements.

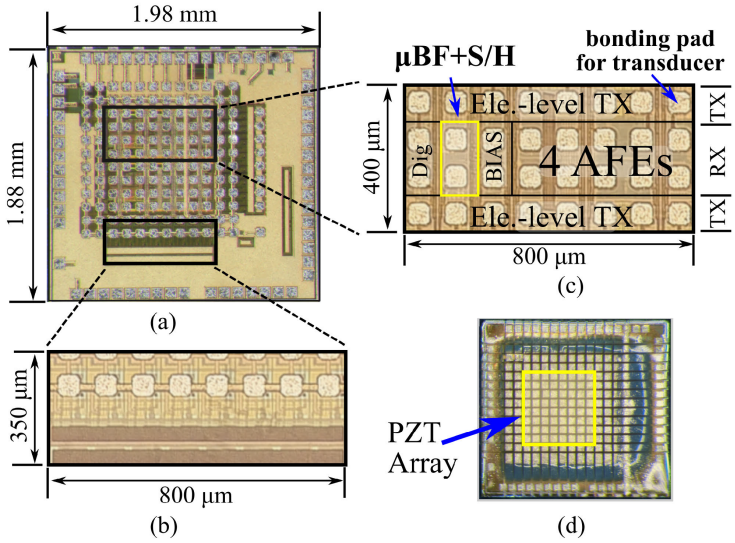

Figure 2.14: (a) Micrograph of the first prototype ASIC. (b) Inset showing the peripheral TX circuitry. (c) Inset showing the element-level TX/RX circuitry. (d) ASIC with PZT array built on top. From [73]

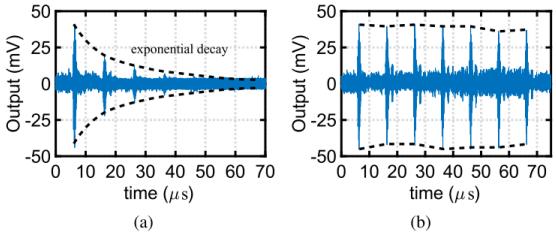

Figure 2.15: (a) Uncompensated ASIC output with the TGC function disabled. (b) Compensated ASIC output with the TGC function enabled. From [138]

2.6.2 Prototype 2

The second prototype [140] contains more elements, includes full transmit capabilities, has an analog-to-digital converter (ADC) and concatenates the output of 4 ADCs into 1 digital output channel. The pitch was also increased to 125 µm, to ensure enough space for all pitch-matched components, and the centre frequency has been reduced from 10 to 9 MHz. An overview of this prototype is shown in Figure 2.17.

Acoustic Results

With the new prototype a similar imaging experiment was done. The resulting image and imaging setup can be seen in Figure 2.18. Unlike the image in Figure 2.16, this image was created by combining 25 different steering angles.

There are three notable differences between Figure 2.16 and Figure 2.18. First, the resolution is better due to the wider aperture and the use of compounding. Second, the

side-lobes are absent, even with the higher dynamic range of the newer image. This is also caused by the use of compounding. Finally, there is a significant amount of reverberations visible behind the needles that were absent before. The acoustic stack used for this probe was not adapted to the used centre frequency, causing severe ringing.

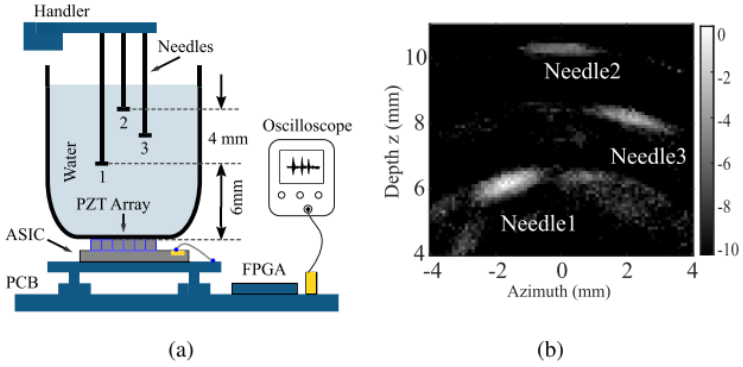

Figure 2.16: (a) Setup for imaging experiment. (b) B-mode image using the first prototype showing the position of the needles. From [138]

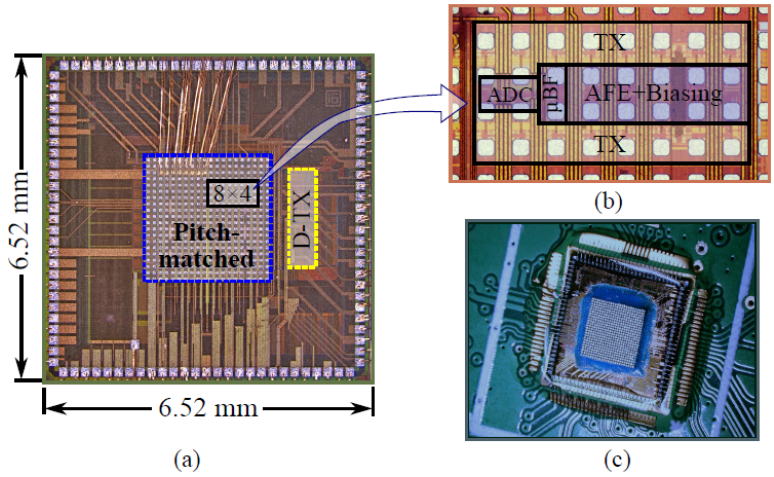

Figure 2.17: (a) Micrograph of the second prototype ASIC. A pitch-matched and a peripheral region are indicated. (b) Inset showing the pitch-matched TX/RX circuitry of 8 µBF sub-arrays of 2 × 2 elements. (c) ASIC with PZT array built on top. From [140]

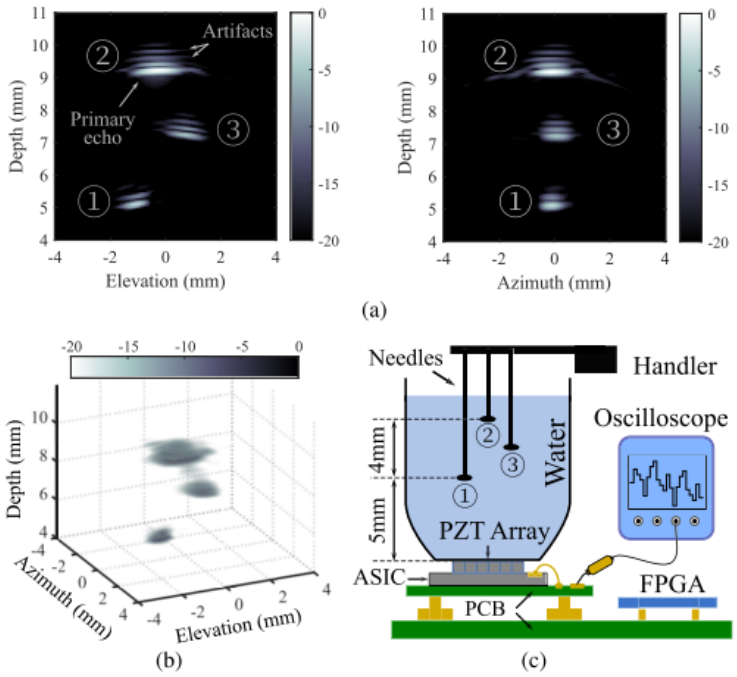

Figure 2.18: (a) B-mode images using the second prototype in elevation and azimuth planes. The primary echo and artefacts behind are indicated for the second needle. (b) Rendered 3-D image. (c) B-mode imaging experiment setup. From [140].

2.7 Conclusion

In this chapter we described a process to design a new ASIC integrated ultrasound matrix array specifically for monitoring of the preterm brain. We presented the clinical requirements, investigated the acoustical effects of the matrix parameters discussed a part of the electronics and ASIC design, proposed a design that fits most of the clinical requirements, and, finally, presented and discussed two prototypes to verify the proposed design and ASIC components are discussed. While the two prototypes do partly validate key concepts crucial for the eventual implementation of the final matrix, they also showed that achieving the proposed design will require further development or changes to the design itself. Therefore, the presented research is a good starting point for further research and development towards a novel ultrasound monitoring device of the preterm brain.

3

Design of an Ultrasound Transceiver ASIC with a Switching-Artifact Reduction Technique for 3D Carotid Artery Imaging

This paper presents an ultrasound transceiver application-specific integrated circuit (ASIC) directly integrated with an array of 12x80 piezoelectric transducer elements to enable next-generation ultrasound probes for 3D carotid artery imaging. The ASIC, implemented in a 0.18 µm high-voltage Bipolar-CMOS-DMOS (HV BCD) process, adopted a programmable switch matrix that allowed selected transducer elements in each row to be connected to a transmit and receive channel of an imaging system. This made the probe operate like an electronically translatable linear array, allowing large-aperture matrix arrays to be interfaced with a manageable number of system channels. This paper presents a second-generation ASIC that employed an improved switch design to minimize clock feedthrough and charge-injection effects of high-voltage metal–oxide–semiconductor field-effect transistors (HV MOSFETs), which in the first-generation ASIC caused parasitic transmissions and associated imaging artifacts. The proposed switch controller, implemented with cascaded non-overlapping clock generators, generated control signals with improved timing to mitigate the effects of these non-idealities. Both simulation results and electrical measurements showed a 20 dB reduction of the switching artifacts. In addition, an acoustic pulse-echo measurement successfully demonstrated a 20 dB reduction of imaging artifacts.

This chapter has been published as:
T. Kim, **F. Fool**, D. S. dos Santos, Z.-Y. Chang, E. Noothout, H. J. Vos, J. G. Bosch, M. D. Verweij, N. de Jong, and M. A. P. Pertijs, "Design of an ultrasound transceiver asic with a switching-artifact reduction technique for 3D carotid artery imaging," *Sensors*, 2021, DOI: 10.3390/s21010150

3.1 Introduction

Real-time 3D ultrasound imaging is an essential technique for the accurate assessment of carotid artery disease by measuring blood flow, plaque deformation, and pulse wave velocity [59], [88], [89], [141]. To realize this, the next generation of ultrasound probes require matrix transducer arrays with thousands of elements to cover a sufficiently large aperture (>400 mm^2). It is possible to build a matrix array with such a high number of elements, but making electrical connections to all the elements is highly challenging since conventional imaging systems have a limited number of channels. This issue can be addressed by integrating application-specific integrated circuits (ASICs) into the probe to reduce the number of electrical connections via cables to the imaging system. Various approaches to interface such large-aperture matrix transducer arrays using a reduced number of cables have been reported, such as receive sub-array beamforming [70], [74], [142], [143], programmable high-voltage (HV) pulsers [144]–[149], switch matrices [150], [151], row-by-row scanning schemes [146], [148], and row- or column-parallel connection schemes [147].

We previously reported a first-generation transceiver ASIC with a row-level architecture for both receive (RX) and transmit (TX) channels [71]. This ASIC consists of 24x40 element-level HV switches and control logic that allows selected transducer elements in each row to be connected to a TX and RX channel of an imaging system. The element-level circuits are laid out in a pitch-matched fashion and connect directly via bondpads to transducer elements stacked on top of the chip. Although the functionality of this ASIC has been successfully demonstrated in a 3D imaging experiment, noticeable imaging artifacts associated with parasitic transmissions generated by HV switch actuation at the TX to RX transition and vice versa were found. In particular, thousands of switches actuate simultaneously in a full-aperture selection for plane wave transmission, making this problem more serious. The parasitic transmissions originate from non-idealities of the HV MOSFETs in the switch circuits, i.e., clock feedthrough and charge injection, generating switching transients on the transducer elements.

Charge injection and clock feedthrough in low-voltage analog complementary metal–oxide–semiconductor (CMOS) circuits have been discussed extensively in the literature [81], and several techniques to cancel their effects have been reported, such as dummy transistor compensation [82], [152] and differential clock feedthrough attenuation [83]. However, these techniques are not directly applicable in this design because the HV laterally diffused metal oxide semiconductor (LDMOS) transistors used for HV switches are much larger than low-voltage transistors. As a result, these solutions, which rely on additional transistors, would make die area occupied by the element-level switch circuit too large in comparison to the size of the transducer elements. Recently, one approach, linearized control of the gate voltage of a HV MOSFET, has been reported to address this issue in an ASIC design with large aperture transducer arrays for ultrasound imaging applications [153].

In this work, as an alternative, we propose a second-generation transceiver ASIC focusing on minimizing the effects due to non-idealities of the HV MOSFETs, the root cause of the mentioned imaging artifacts. To achieve this, we propose a new HV switch controller that generates control signals for the HV switches with improved timing to alleviate the effects of their non-idealities. In this design, a current discharging path from

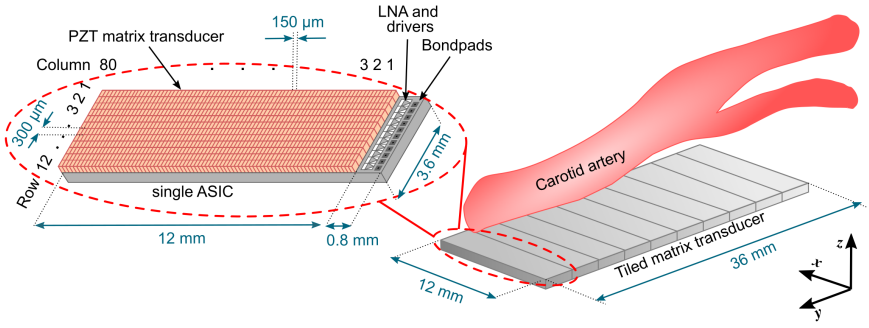

Figure 3.1: Overview of the proposed matrix transducer on tiled application-specific integrated circuits (ASICs) (right). Overview of a single tile consisting of 12 × 80 transducer elements on top of an ASIC with 12 × 80 element-level switches and row-level circuits (left).

the transducer element to the ground is created at the TX and RX switching moments. Consequently, this leads to significantly reduced peak-to-peak amplitudes of the switching transients.

This paper is structured as follows. Section 3.2 describes the materials and methods of this work, which comprise a system overview in Section 3.2.1, the architecture of the designed ASIC in Section 3.2.2, the implementation of the element-level switch circuit and an analysis of the associated switching transients due to non-idealities of the HV MOSFETs in Section 3.2.3, the design of a switch controller with a switching-artifact reduction technique in Section 3.2.4, and its validation in simulation in Section 3.2.5. Section 3.3 describes the measurement results and discussion, explaining the experimental prototype used to validate the design in Section 3.3.1, presenting its electrical verification in Section 3.3.2, and showing reduced imaging artifacts in Section 3.3.3. Finally, the paper is concluded in Section 3.4.

3.2 Materials and Methods

3.2.1 System overview

The size of the matrix transducer to cover an aperture sufficiently large enough for carotid artery imaging is 36 mm × 12 mm. To facilitate the realization of a full-sized array, we designed the second-generation ASIC via a MLM (multi-layer mask) full-wafer fabrication process. Compared to our previous work [71], the row pitch was increased from 150 to 300 µm while keeping the center frequency as it was. Thus, the number of rows in the ASIC was reduced from 24 to 12 so that the density of the wire bonds that electrically connect the ASIC to a printed circuit board (PCB) was also significantly reduced. This modification of physical dimensions enabled us to wire bond more reliably, which is one of the main challenges of the first-generation ASIC. On the other hand, the number of columns per ASIC increased from 40 to 80, which allowed us to implement the targeted aperture by tiling 1 × 10 ASICs, as shown on the right of Figure 3.1. This increased number of columns provided an important additional advantage compared to the previous work with 2 × 10

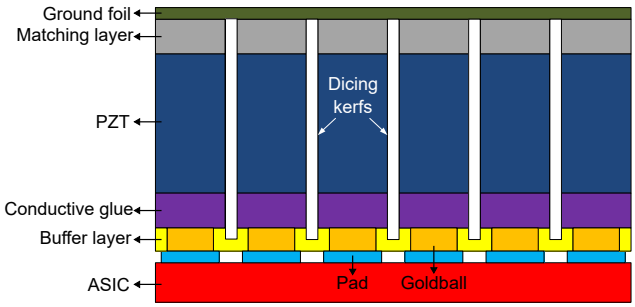

Figure 3.2: Cross-sectional view of the transducer array mounted on top of the ASIC.

ASICs tiled, since wire-bond connections only have to be made on one side of the tiled array.

As shown on the left of Figure 3.1, each of the ASICs had a die size of 3.6 mm × 12.8 mm, and interfaced with an array of 12 × 80 (rows × columns) transducer elements through element-level and row-level circuits. Each pitch-matched element-level circuit was connected to the corresponding transducer element via a bondpad. Bondpads on the periphery of each ASIC were arranged in two columns. The inner column connected row-level TX and RX signals to an imaging system. Bondpads of the outer column made connections for digital control signals as well as analog and digital power supplies.

In the same way as the first-generation ASIC, the piezoelectric layer (PZT)-on-CMOS integration scheme illustrated in Figure 3.2 [154] was adopted to build the transducer array on top of the ASICs. To electrically connect the circuitry on the ASIC to the transducer elements, we formed gold bumps on top of the ASIC bondpads using a wire-bonding tool. This was done in a matrix pattern with the same pitch as the transducer array. A nonconductive epoxy buffer layer was then deposited, filling the gaps between the gold. After this, the buffer layer was ground down to expose the gold, thus providing reliable electrical contacts for the transducer elements. On top of the epoxy layer, the acoustic stack consisting of a PZT and a matching layer was constructed. The conductive glue layer created the electrical connection between contacts and the electrode on the back-side of the piezoelectric ceramic. After that, the stack was diced into the desired 150 µm × 300 µm pitch array pattern using a diamond saw. The dicing kerfs were air-filled to minimize the crosstalk between elements. Finally, the array was covered with an aluminum foil that formed the elements' common ground electrode.

3.2.2 ASIC architecture

Figure 3.3 shows the top-level architecture of the second-generation ASIC. The 80 elements in each row of the matrix shared a row-level RX and TX bus to reduce channel count by a factor of 80. Even with 1x10 tiled ASICs, the total number of RX and TX channels was 240, which could be managed by an imaging system. Each transducer element was connected to the RX bus or the TX bus through a programmable element-level circuit. The RX bus was associated with a shared row-level circuit, which amplified the received echo signals, filtered out-of-band noise, and drove the connection to the imaging system.

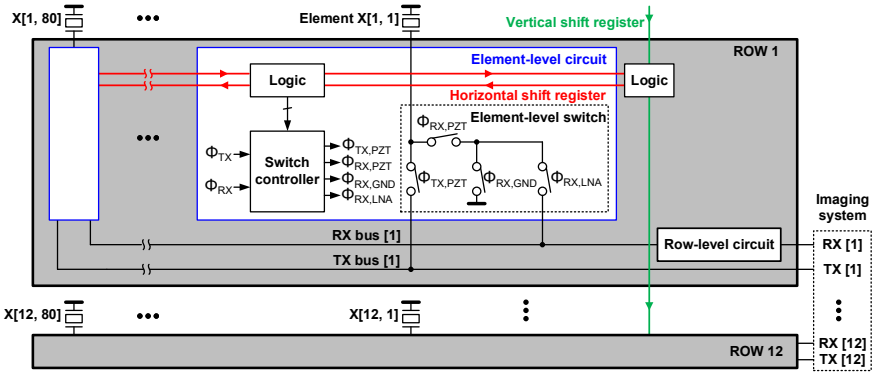

Figure 3.3: Block diagram of the second-generation ASIC.

Ahead of starting successive transmit/receive cycles, we needed to program the ASIC. Row-level logic was used to select one of the various element-selection modes supported by the ASIC to implement a specific imaging scheme and set the gain of the row-level circuit. This logic was programmed through a vertical shift registers (VSR) that was loaded during the programming phase. Each element was associated with logic allowing us to change rapidly between transmit/receive cycles the selection of active elements for a specific transmit and/or receive cycle. This element-level logic was pre-loaded through a horizontal shift register (HSR) during the programming phase. The switch controller received low-voltage digital signals (ϕ_{TX} and ϕ_{RX}) from a field-programmable gain array (FPGA) and generated 5 V control signals ($\phi_{TX,PZT}$, $\phi_{RX,PZT}$, $\phi_{RX,GND}$, and $\phi_{RX,LNA}$), according to the pre-loaded data, to drive the element-level switch circuit. In this design, the switch controller was implemented using a non-overlapping clock generator to minimize the non-idealities of HV devices introduced above in the switch circuit.

3.2.3 Element-Level Switch Circuit and Non-Idealities

Figure 3.4 shows the circuit diagram of the element-level switches implemented in the first-generation ASIC. The HV switches were needed to enable HV pulse transmission while keeping a more compact implementation and less power consumption. The control signals were generated by simple combinational logic from the TX/RX phases (ϕ_{TX} and ϕ_{RX}) and three enable bits (ELE_EN[i, j], TX_EN[i, j], and RX_EN[i, j]), which were pre-loaded via the HSR in the programming phase. The ELE_EN bit determined whether an element was enabled (high) or disabled (low). If a certain element was disabled, it was excluded from participating in imaging and connected to the ground via transistors M5 and M6. This helped to prevent the signal of disabled elements from coupling to the RX bus and capacitive coupling from the TX bus to the disabled elements in the TX phase ϕ_{TX}. For the enabled elements, the remaining two bits, TX_EN and RX_EN, determined whether they participate in transmission and/or reception.

During the TX phase ϕ_{TX}, the row-level TX bus, TX[i] was connected to the element if ELE_EN[i, j] and TX_EN[i, j] were high. Two back-to-back n-type HV LDMOS transistors (M1 and M2), driven by $\phi_{TX,PZT}$, allowed an external imaging system to send a unipolar

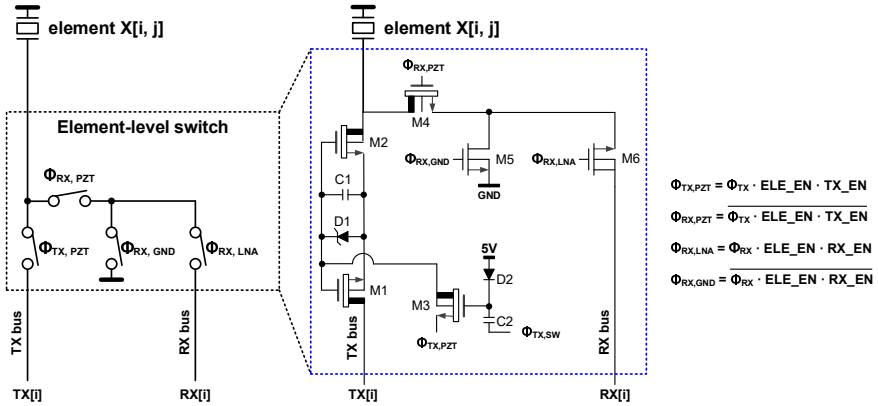

Figure 3.4: Simplified circuit diagram of the element-level switch and the combinational logic equation, implemented as the switch controller, proposed in [71].

pulse with a peak value up to 65 V. To turn on M1 and M2, we charged a bootstrap capacitor C1 connected between their source and gate through M3 by making $\phi_{TX,SW}$ high at the beginning of ϕ_{TX}. Soon after that, $\phi_{TX,SW}$ went low to turn off M3, keeping M1 and M2 on and allowing them to swing up with the transmit HV pulses on the TX bus. To provide a sufficiently high gate voltage to turn on M1 and M2, we gave the bootstrap capacitor C1 a relatively large value of 7.2 pF in this design. At the end of ϕ_{TX}, C1 was discharged by pulling down the source of M3 so that M1 and M2 were turned off. During the RX phase ϕ_{RX}, transistors M4 and M6 connected the element to the RX bus if ELE_EN[i, j] and RX_EN[i, j] were high.

As described earlier in Section 3.1, an important consideration in this design is minimizing the impact of non-idealities, clock feedthrough, and charge injection of the HV switches, which generate switching glitches on the transducer element at the TX to RX transition and vice versa. This problem eventually leads to visible imaging artifacts. Figure 3.5a shows simulated waveforms of the control signals driving the element-level switch transistors. Even without a transmitted pulse, noticeable switching glitches appear on the element, as shown in Figure 3.5b. The peak amplitudes of these undesired glitches at the RX to TX transition and vice versa were 2.19 V and −0.64 V, respectively. This amplitude, in the volt range, led to visible imaging artifacts, even when applying a high-voltage transmit pulse with an amplitude of tens of volts.

3.2.4 Proposed Switch Controller

To minimize the switching transients discussed in the previous section, we proposed a new timing diagram, shown in Figure 3.6a, of the switch control signals. At the transition from RX to TX, the RX bus was first disconnected from the element by making $\phi_{RX,LNA}$ low while $\phi_{RX,PZT}$ remained high. Subsequently, M5 was turned on by making $\phi_{RX,GND}$ high; thus, a low-impedance discharging path from the element to ground was created before actuating M1 and M2 associated with the HV TX switch. Thus, when $\phi_{TX,PZT}$ was made high, the clock feedthrough-induced current could flow to the ground through transistor

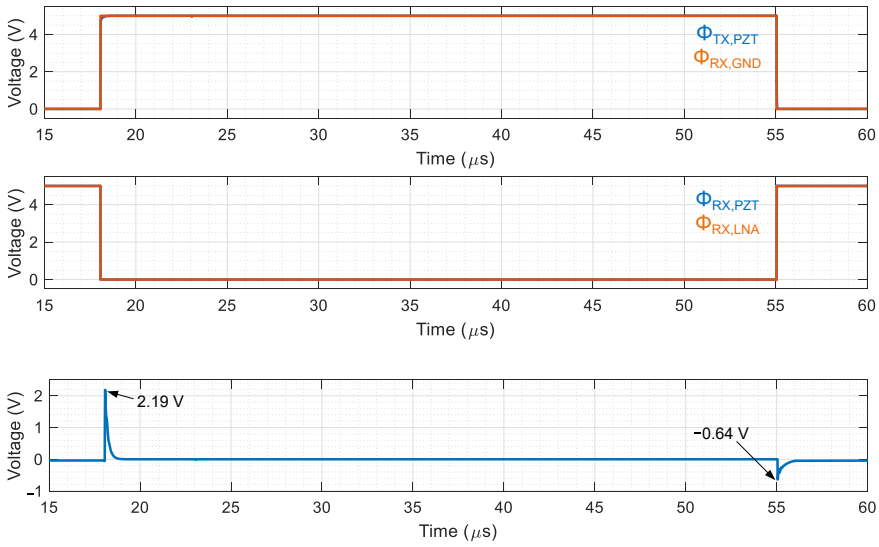

(a)

(b)

Figure 3.5: Simulated waveforms of the element-level circuit implemented in the first-generation ASIC (Figure 3.4): (a) control signals driving the element-level switch circuit and (b) the switching transients on the transducer element.

M5 instead of to the element. Finally, when $\phi_{RX,PZT}$ was made low, the charge injection error from M4 could be absorbed to both ground and the low-impedance output of the pulser. This switching sequence reduced the peak amplitude of the switching transients significantly at the transition of RX to TX. Although M6, a 5 V device, was switching without a discharging path to the ground, the associated transient was not critical because M6 was much smaller than the high-voltage devices.

Conversely, at the transition of TX to RX, transistor M4 was activated first to create a discharging path again from the element to the ground. At the transition of $\phi_{TX,PZT}$, a significant error could be generated due to charge injection related to M1 and M2. However, the resulting voltage transient on the element was minimized because the associated charge could flow via M4 and M5 to the ground. Figure 3.6b shows the switch controller's design with cascaded non-overlapping clock generators to generate the control signals presented in Figure 3.6a. Each stage employed delay unit cells in which metal–oxide–semiconductor (MOS) capacitors were used to make sufficient delay (>100 ns) between the signals.

3.2.5 Validation in Simulation

The proposed switch controller was simulated to validate the reduction of the switching transients. Figure 3.7 shows the simulation results of the control signals generated by the controller, the voltage on the element, and the current flowing through M5 in Figure 3.4 at the switching moments for the TX to RX transition and vice versa. Figure 3.7a shows the transition of the signals at the switching moment from RX to TX, with the peak-to-peak amplitude of switching transients being 139.2 mV, as shown in Figure 3.7b.

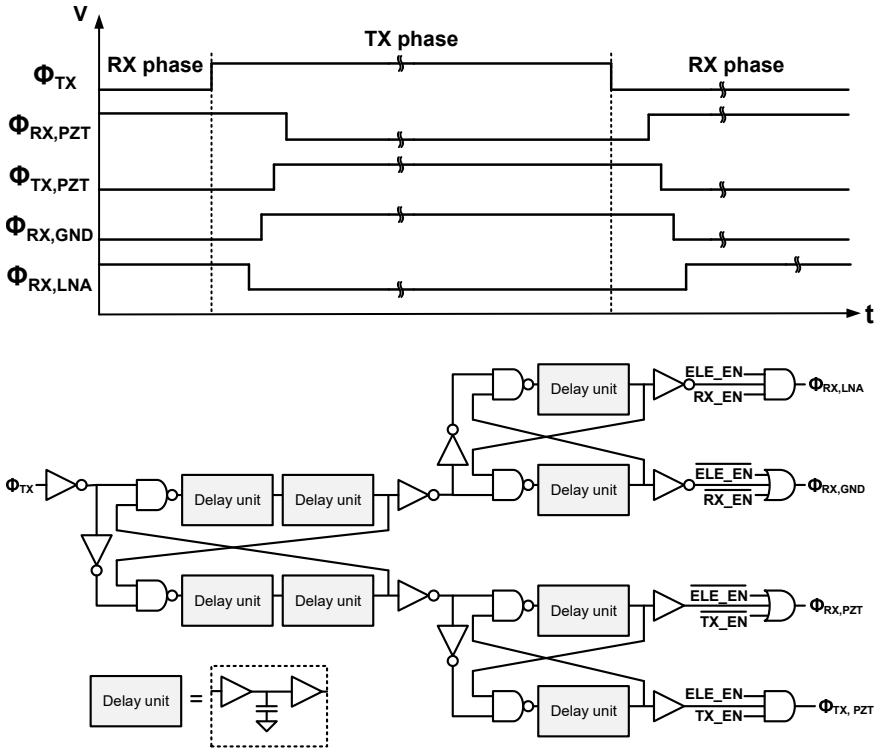

Figure 3.6: (a) The proposed timing diagram of the control signals to minimize the switching transients and (b) implementation of the switch controller to generate such signals.

Figure 3.7c shows that the current flows through M5 at the switching moments of high-voltage transistors M1, M2, and M4, resulting in the reduction of the switching transients. Figure 3.7d shows waveforms of the control signals at the transition from TX to RX, with the peak-to-peak amplitude being 207.3 mV, as shown in Figure 3.7e. In particular, the largest peak value of −118.8 mV, associated with the falling edge of $\phi_{TX,PZT}$, was caused by the charge injection effect of M1 and M2. This amplitude was significantly reduced because the charge-injection-induced current was also absorbed into the ground via M5, as is confirmed in Figure 3.7f. Consequently, compared to 2.19 V in the first-generation ASIC simulation, the peak-to-peak amplitude of the switching transients with the newly designed switch controller was reduced by around 20 dB.

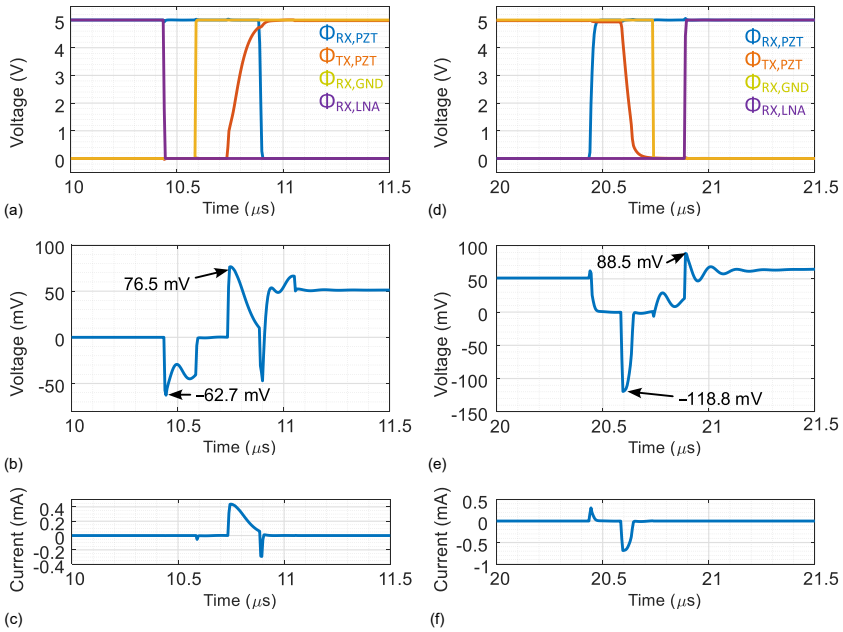

Figure 3.7: Simulated waveforms with the proposed switch controller at the transition of RX to TX (a-c) and vice versa (d-f). (a,d) Control signals driving the element-level switch circuit, (b,e) the switching transients on the transducer element, and (c,f) the drain current flowing via M5.

3.3 Results and Discussion

3.3.1 Experimental Prototype

The ASIC was fabricated in a 0.18 µm HVBCD process. Figure 3.8a,b shows a photograph of a bare die and a plot of the layout of the element-level TX and RX circuits, respectively. The area of the element-level circuit was matched to the 150 µm × 300 µm transducer element size. In the prototype shown in Figure 3.8c, four ASICs were mounted on a test PCB and wire-bonded for RX and TX channels as well as for power and control signals. A piezo-electric transducer array was built on top of the ASICs using the process described in [154]. The prototype was covered by a ground foil, the common ground electrode of the transducer elements, and by a moisture protection layer.

3.3.2 Electrical Verification

In the electrical characterization, an ASIC die without transducer array was used, on which selected transducer pads were wire-bonded to the test board to observe the switching transients. Without applying a high-voltage TX pulse, residual switching transients were visible, as shown in Figure 3.9. Their peak-to-peak amplitudes at the TX to RX transition and vice versa were 100 mVPP and 30 mVPP, respectively. Compared to the simulation results with the first-generation ASIC shown in Figure 3.5, the peak-to-peak values were reduced by factors of 6 and 70. Compared to the simulation results shown in Figure 3.7,

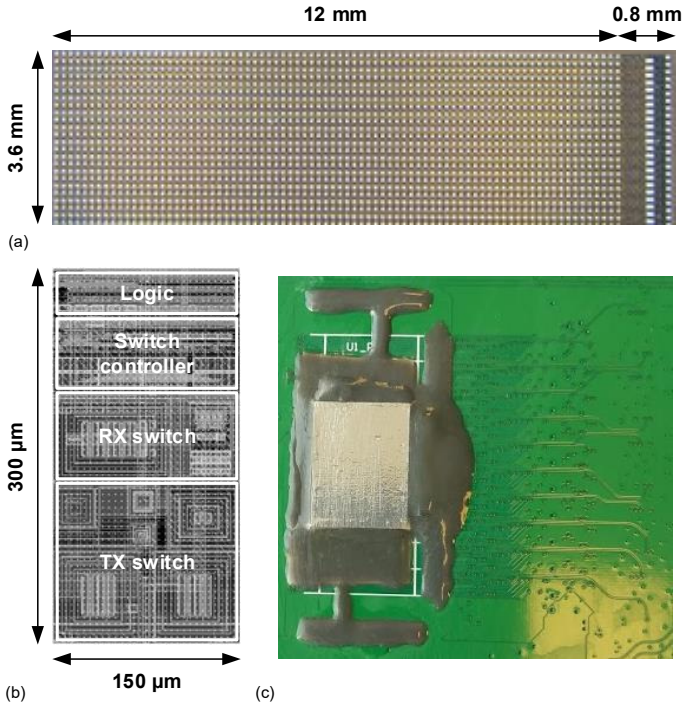

Figure 3.8: (a) Chip photograph of the ASIC, (b) layout of the pitch-matched element-level circuit, and (c) the test printed circuit board (PCB) with transducer array on top of the ASICs.

the measured peak-to-peak amplitudes were a factor of 2 and 5 lower. This was likely due to the effects of the wire-bonded connection, the bondpad on the PCB, and the probe capacitance in the test setup, which resulted in a higher capacitance, and hence a smaller transient voltage than in the simulation. Taking this loading effect into account, the results were consistent with the expected reduction of 20 dB derived in Section 3.2.5.

3.3.3 Improvement in Clock Feedthrough and Charge Injection-Induced Imaging Artifact

The test-bench for acoustic experiments to validate the reduced switching artifacts is shown in Figure 3.10. A Verasonics V1 imaging system (Verasonics, Kirkland, WA, USA) was used to generate the HV TX signals. To interface the TX and RX signals between the Verasonics and the test PCB, we designed a motherboard PCB. On the transmit paths, a matching circuit was implemented to guarantee a unipolar excitation pulse. The received signals were buffered with unity-gain operational amplifiers on the motherboard before being fed into the Verasonics. The motherboard also included low-dropout regulators (LDOs) to generate supply voltages for analog, digital, and 5 V circuitry. Moreover, the board contained digital buffers to transfer the signals from the field-programmable gate array (FPGA) board. These digital signals consisted of clock and data for programming the ASICs and their control signals.

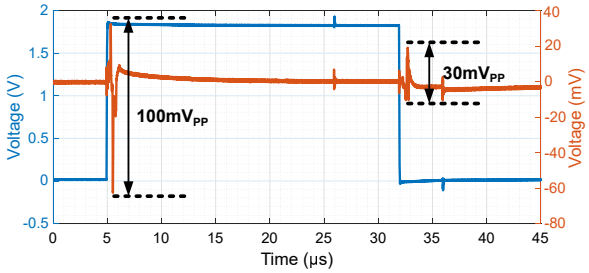

Figure 3.9: Measured waveforms of the RX phase (blue) and the switching transient observed on the element X [6, 41] (orange).

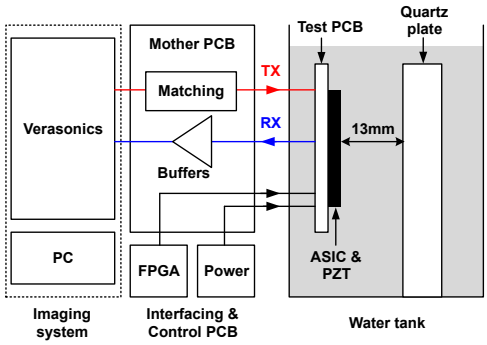

Figure 3.10: Overview of the measurement setup used for demonstrating the effect of the switching transients for the first- and the second-generation ASICs.

Pulse-echo measurements were performed to obtain imaging results using a quartz plate as a reflector located at a depth of 13 mm. The TX signal was a unipolar half-cycle 7.5 MHz pulse with a peak value of 1 V. All elements were enabled to send a plane wave on the full-aperture in TX, and echo signals were received in a column-by-column fashion. The reason for using a relatively small 1 V pulse was to better bring out the switching artifacts compared to the 60 V pulse used in normal operation. To record the switching glitches at the transitions of both TX to RX and vice versa, we applied two successive RX phases, as shown in Figure 3.11. During the first RX phase, the echo signal from the transmitted 1 V pulse and the switching transients from the first transition from TX to RX (the first rising edge) can be recorded. In the second cycle, the switching transients from the first transition from RX to TX (the first falling edge) and from the second transition from TX to RX (the second rising edge) were recorded.

Figure 3.12 demonstrates how the switching transients affected the image and how much imaging artifacts were improved with the proposed switch controller circuit. Figure Figure 3.12a,b show the RF signal for a single channel captured by the Verasonics and the imaging result, respectively, with the first-generation ASIC. As can be seen in Figure 3.12a, the peak-to-peak amplitude of the RX to TX switching transients located at a depth of 38 mm was considerably larger than the echo signal from the transmitted 1 V pulse. Even if the largest pulse amplitude supported by the ASIC of 65 V would be used, these switching

transients would give significant artifacts in the image. On the other hand, the amplitude of the RX to TX switching transients was reduced by a factor of 20 dB in Figure 3.12c,d for the second-generation ASIC. This reduced amplitude corresponded to a parasitic transmitted pulse with an amplitude of only 0.3 V. If the maximum pulse amplitude of 65 V were to be used, the echo signals from the switching would be 46.7 dB smaller than the echoes from the intended pulse, making their impact on the image much less significant compared to the 20 dB difference between pulse and switching artifacts in the first generation ASIC. This result demonstrated that the switching artifact reduction scheme with the proposed switch controller improved image quality significantly.

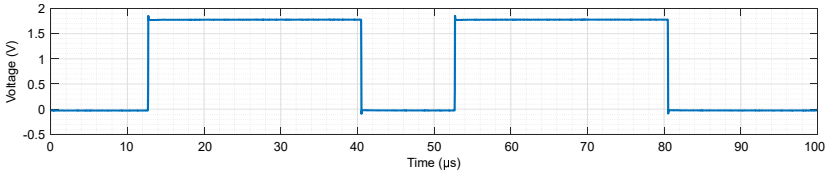

Figure 3.11: The waveform of the RX phase with two cycles used in the pulse-echo measurement to record the switching glitches at both TX to RX transition and vice versa.

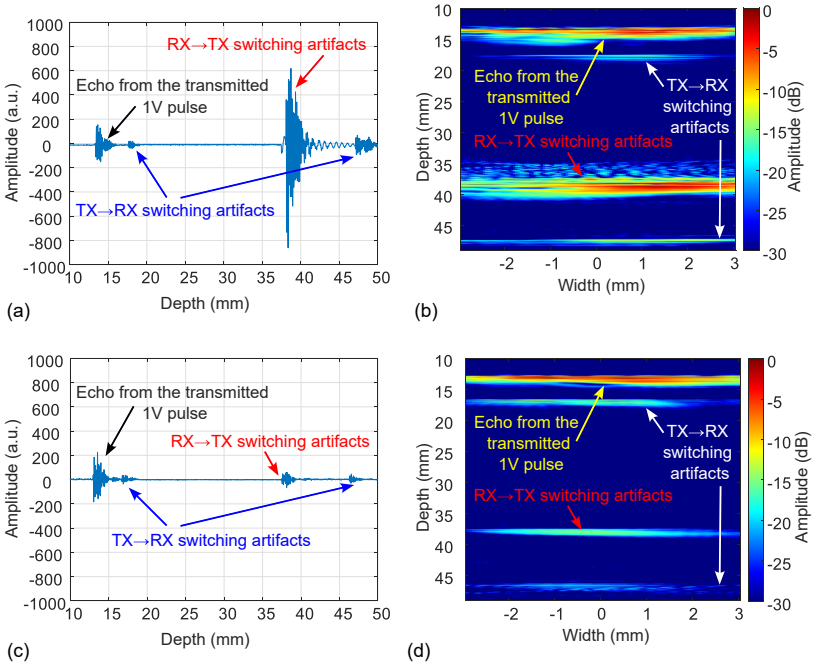

Figure 3.12: Comparison of switching transients for the first- and second-generation ASICs. (a) Time-domain plot of the received RX output data for a single channel and (b) B-Mode imaging result with the first-generation ASIC. (c) Time-domain plot for the second-generation ASIC with the same test conditions and (d) its imaging result.

3.4 Conclusions

We present an ultrasound transceiver ASIC design with a switching artifact reduction technique, designed for 3D volumetric imaging of the carotid artery. We have previously reported a first-generation ASIC design [71] that demonstrated the 3D imaging capability; however, we observed noticeable ghost echoes in the experiment. We have identified that this issue originates from clock feedthrough and charge injection of the HV MOSFETs in the element-level switch circuits, generating switching transients on the transducer elements that lead to parasitic pulse transmission. The improved switch controller proposed in this paper generates control signals of HV switches such that a discharge path to ground is created at the critical switching moments, strongly reducing the transients on the transducer element. Measured results demonstrate a 20 dB reduction in imaging artifacts compared to our previous ASIC.

4

A Tiled Ultrasound Matrix Transducer for Volumetric Imaging of the Carotid Artery

High frame rate three-dimensional (3D) ultrasound imaging would offer excellent possibilities for the accurate assessment of carotid artery diseases. This calls for a matrix transducer with a large aperture and a vast number of elements. Such a matrix transducer should be interfaced with an application-specific integrated circuit (ASIC) for channel reduction. However, the fabrication of such a transducer integrated with one very large ASIC is very challenging and expensive. In this study we develop a prototype matrix transducer mounted on top of multiple identical ASICs in a tiled configuration. The matrix was designed to have 7680 piezoelectric elements with a pitch of 300 µm × 150 µm integrated with an array of 8×1 tiled ASICs. The performance of the prototype is characterized by a series of measurements. The transducer exhibits a uniform behavior with the majority of the elements working within the −6 dB sensitivity range. In transmit, the individual elements show a center frequency of 7.5 MHz, a −6 dB bandwidth of 45%, and a transmit efficiency of 30 Pa/V at 200 mm. In receive, the dynamic range is 81 dB and the mini-mum detectable pressure is 60 Pa per element. To demonstrate the imaging capabilities, we acquired 3D images using a commercial wire phantom.

This chapter has been published as:
F. Fool, D. S. dos Santos, M. Mozaffarzadeh, M. Shabanimotlagh, E. Noothout, T. Kim, N. Rozsa, H. J. Vos, J. G. Bosch, M. A. P. Pertijs, M. D. Verweij, and N. de Jong, "A Tiled Ultrasound Matrix Transducer for Volumetric Imaging of the Carotid Artery," *Sensors*, 2022, DOI: 10.3390/s22249799

4.1 Introduction

Carotid arteries are major blood vessels located on both sides of the neck that supply the head and brain with oxygen and nutrients. Carotid artery disease, which is referred to as atherosclerosis or stenosis, occurs when fatty deposits (plaques) clog the carotid artery [35]. The blockage of the carotid arteries is a frequent source of stroke, a medical emergency that occurs when blood supply to the brain is interrupted or seriously reduced [36]. Assessing the progression of the atherosclerosis in the carotid artery is very useful for risk stratification, evaluation of patient response to medical interventions, evaluation of new risk factors, genetic research, and quantification of the effects of new therapies [155], [156]. The assessment of the carotid plaque state is commonly performed with ultrasound imaging for the purpose of medical diagnosis [157].

With conventional two-dimensional (2D) ultrasound imaging, the assessment of the plaque is based on multiple 2D images, which are mentally combined by the operator to form a subjective impression of the three-dimensional (3D) vessel structure. Using this approach, accurate assessment of the plaque progress is difficult and highly dependent on the skills and experience of the sonographer [52]. This requires reproduction of the same imaging plane at later times, which is difficult and sometimes impossible due to the restrictions imposed by the patient's anatomy or position. Moreover, quantitative estimation of the plaque volume in 2D ultrasound is based on measurements of height, width, and length in different orthogonal views for ideal shapes (e.g. ellipsoidal), which are prone to error [51]. 3D ultrasound has the potential for accurate quantitative monitoring of the changes in plaque volume and might be vital for therapy assessment [36], [156], [158], [159]. In carotid artery diagnosis, measurement of blood flow and plaque surface motion are important parameters [49]. For accurate analysis of the dynamics of the blood flow, 3D vector velocities at a high frame rate are necessary. Two-dimensional methods do not provide a realistic picture of the actual flow and do not provide information about the out-of-plane velocity component [55]. Thus, these 3D phenomena can only be assessed correctly with high frame rate 3D ultrasound imaging.

Going from 2D to 3D high frame rate ultrasound imaging is challenging. While mechanically swept or free-hand scanning techniques using a linear (i.e., one-dimensional) transducer array might suffice for low-frame rate applications, a 2D matrix transducer array is necessary for high frame rate applications [51]. This matrix transducer should cover a sufficiently large aperture (>400 mm^2) and its element pitch should preferably be smaller than half of the wavelength (λ) in both directions to avoid grating lobes. The combination of small elements and a large aperture results in a very large number of transducer elements (in the order of thousands) [59], [160], [161]. It is possible to build a matrix array with such a vast number of elements, but making electrical connections to all the elements is a great challenge [132]. Various techniques have been proposed to reduce the complexity of fully populated matrix arrays, such as sparse matrix arrays and row-column addressed matrix arrays. Sparse arrays can effectively reduce channel count and electronic complexity, and can perform high frame rate volumetric imaging [62], [162]–[164]. However, this type of array has two fundamental limitations which are the lower signal-to-noise ratio (SNR) and higher clutter levels [144], [165], [166]. Row-column addressed arrays, on the other hand, can reduce the number of connections from N^2 to $2N$ in a matrix array consisting of $N \times N$ elements [65], [67], [167]. However, the inherent drawbacks of this transducer are

the more complex read-out sequences and the lower frame rate, which is limited due to switching [165].

As an alternative, Application-Specific Integrated Circuits (ASICs) can be directly integrated with the matrix array to reduce the number of electrical connections, allowing large-element-count transducers to be used with traditional 128 to 256 channel systems and probe cables [84], [168]. With this approach, the channel reduction can be done in multiple ways depending on the intended application, for example by channel multiplexing, sub-aperture beamforming, in-probe-digitization, or time-division multiplexing [70], [72], [134]. Besides channel reduction, an ASIC can also perform amplification of the received signals to prevent attenuation due to the loading of the cables connecting the ASIC to the imaging system [71], [74]. These advantages make matrix arrays with in-probe electronics an attractive technology for 3D high frame rate ultrasound imaging, although this comes at the cost of a more complex and costly developing process. Examples of commercially available matrix array probes with a large element count and integrated ASIC include the xMATRIX technology from Philips [169], the iQ+ technology from Butterfly [170], [171] and the 4G CMUT technology from Fujifilm [172].

We have previously presented a first-generation matrix transducer array made of lead zirconate titanate (PZT) and designed for high frame rate, 3D imaging of the carotid arteries that was built directly on top of an ASIC [71], [161]. Since building one single ASIC large enough to cover the carotid bifurcation is very challenging and expensive, we opted for a tiling approach in which multiple small identical ASICs were tiled together in both the lateral and elevation direction to form a larger array. A single ASIC contained 24x40 element-level circuits that consisted of transmit (TX) switches, receive (RX) switches, and control logic. The ASIC architecture could accommodate nine arbitrary TX/RX patterns in the provided memories. The architecture allowed the matrix to operate like an electronically translatable array and we have previously shown how to achieve a high frame rate with such transducer [173]. The layout of element-level circuits was matched to the element pitch of the matrix array, which was 150 µm in both directions. By using 10x2 tiled ASICs, a probe with an aperture of 36 mm × 12 mm consisting of 19 200 elements (240 rows and 80 columns) could be constructed, however, at that time, we only presented a 4×2 tiled design, which was too small for carotid artery imaging. Although the functionality of this matrix transducer was successfully demonstrated in a 3D imaging experiment [161], the probe had limitations in terms of transmit voltage, cable count, and number of pre-programmed patterns, that needed to be tackled in the next generation of the probe.

In the second generation of the transducer, presented in this paper, we have developed a prototype to resolve the limitations present in the previous design. The new version contains 12x80 elements per ASIC that interface with a PZT matrix array of 300 µm × 150 µm. Due to this, we only need to tile the ASICs in one direction instead of two directions, which makes the alignment during manufacturing much easier. In addition, the larger pitch overcomes electronics space limitations in the pitch-matched configuration, which allows to increase the TX pulse voltage from 30 V to up to 65 V. Also, the number of pre-programmed arbitrary patterns is increased to 20. Finally, undesired transmit signals that originated from the TX-to-RX mode switching (and vice versa) are significantly reduced in the new version of the ASIC [132].

This paper describes the development of the prototype tiled matrix transducer that is based on the second-generation ASIC described above. The goal of this work is to demonstrate the feasibility of using the tiling approach to build a sufficiently large aperture and to evaluate the potential of using the prototype for 3D imaging of the carotid artery. In so doing, we will discuss the design, fabrication process, and extensive characterization of the transducer that was targeted to have 7680 piezo elements built on top of 8x1 tiled ASICs. We also performed volumetric imaging of a wire phantom to demonstrate the imaging capabilities of the prototype.

4.2 Materials and methods

4.2.1 Design choices

Volumetric imaging currently cannot attain the same frame rate, resolution, and image quality as in 2D, at least not all at the same time. The main issue is that with a large fully populated matrix array there are too many elements to control and read out at once. Therefore, trade-offs exist between frame rate, resolution, and image quality, which are different for the various types of matrix arrays discussed in the introduction. We have opted to use an ASIC to have large field of view yet still maintaining high frame rates. In this section, we discuss our design choices.

The matrix transducer is designed for imaging of the carotid bifurcation. We have chosen a center frequency of 7.5 MHz as this is recommended for carotid imaging applications [174]. For the aperture size, we aimed at about 40 mm × 15 mm as the carotid bifurcation is easily accessible and therefore allows for larger apertures. However, manufacturing such a large ASIC in one piece would be very expensive [136]. So, we opted to employ a tiled approach where we place multiple smaller and identical ASICs next to each other to create a larger aperture. The final aperture will be 36 mm × 12 mm, which consists of an array of 10×1 tiled ASICs of 3.6 mm × 12 mm each. A schematic drawing is shown in Figure 4.1.

A large aperture requires a large number of elements, but the number of available channels on an ultrasound system is limited. Research scanners like the ULA-OP [175] and the Verasonics Vantage [176] nowadays contain up to 256 channels. Our ASIC design requires separated TX and RX channels; therefore, we opted to limit ourselves to 128 transmit and 128 receive channels. However, since filling the total aperture with square elements with a pitch of 0.5 λ would require over 40 000 elements and thus also over 40 000, a significant degree of channel reduction is required.

As we are using ASICs, there are various ways to reduce the channel count. In our design, we make use of the fact that the fastest flow velocities in the carotid bifurcation are achieved along the long axis of the vessel, corresponding to the long side of the probe aperture (y-direction in Figure 4.1) and that the velocities in the direction of the short side (x-direction) are in comparison much slower. We can therefore use an asymmetric design where each row of the probe has a single transmit and receive channel and the columns can be enabled or disabled at will. This design represents an electronically translatable 1D array (translatable in x-direction). Using this approach, assuming a pitch of 0.5 λ, the channel count could be reduced to 360 transmit and 360 receive channels, which would still be too high for contemporary research scanners. A way to further reduce the channel count is by increasing the element pitch in the y-direction to 300 µm, which corresponds

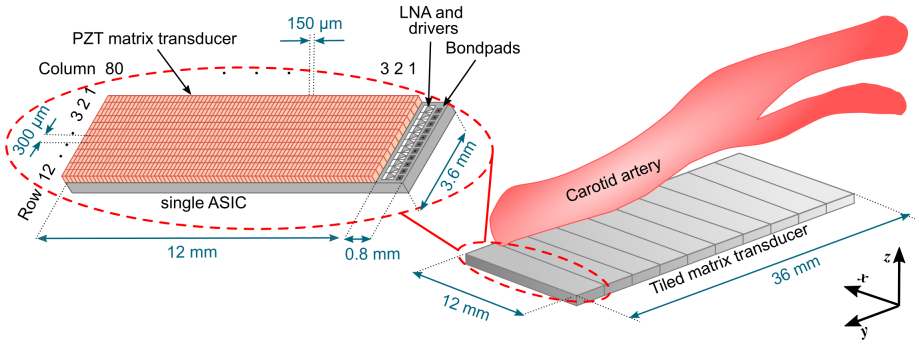

Figure 4.1: Schematic drawing of the envisioned full matrix transducer (right), together with a single ASIC transducer with PZT elements mounted on top (left).

to 1.5 λ. Such a large pitch can result in grating lobes and limited steering capability, yet it could be acceptable as we have chosen to make the aperture very large and therefore high steering angles are not necessary. Another downside of having larger PZT elements is that they will not vibrate like a piston because the element width is much larger than 1.5 λ [177]. Instead, unwanted vibration modes will be generated, which significantly reduce the efficiency of the transducer [177], [178]. Fortunately, the performance of elements having a width greater than 0.7 λ can be improved by subdicing the elements, as we have previously investigated through simulations [178] and experiments [179]. With the proposed pitch of 300 µm in the y-direction, only 120 TX and 120 RX channels are necessary, which satisfies our requirements.

4.2.2 Imaging Scheme

Each imaging modality requires a different trade-off between spatial and temporal resolution: conventional B-mode requires the highest spatial resolution possible, Doppler imaging needs the best temporal resolution [65], [180], and pulse wave imaging (i.e., wall motion imaging during the pulse wave in the blood vessels) requires a bit of both [155]. The designed ASIC allows for an arbitrary element group selection and thus supports different element configurations for different imaging purposes [71]. A few examples are outlined in Figure 4.2. For high-resolution B-mode imaging, the whole aperture can be used for transmission, while reception can take place column by column. For high-frame-rate flow imaging, the transducer can operate like an electronically translatable fully addressable 1-D array where a subset of the columns is used in transmit and receive, and these columns are translated between each TX/RX event. For other purposes, specific patterns or even pseudo-random selection are possible [71], [181].

4.2.3 ASIC design and implementation

Figure 4.3 shows the top-level architecture of the second-generation ASIC. Each row of the matrix has 80 elements that share a row-level TX and RX buses to reduce the channel count by a factor of 80. Each transducer element has a programmable switching circuit that allows the element to be connected to the TX bus, the RX bus, both TX and RX buses

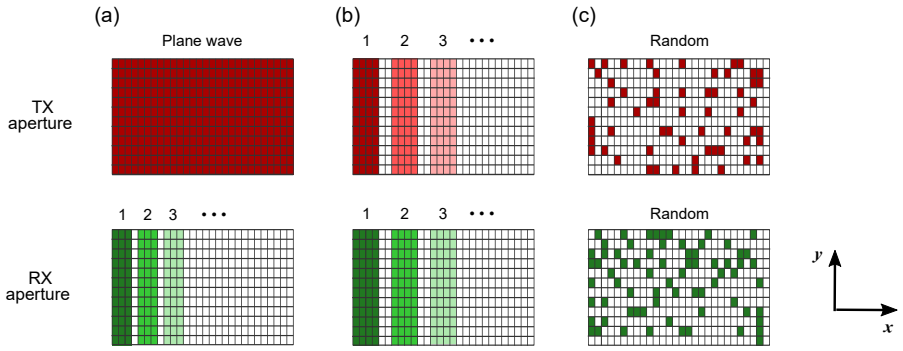

Figure 4.2: Example imaging schemes determined by different transmit and receive element configurations. (a) Plane wave imaging. (b) Dynamic linear array. (c) Random pattern imaging.

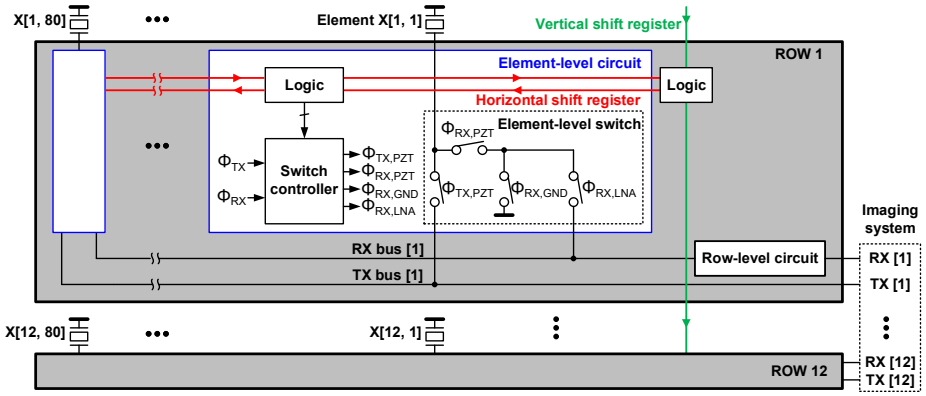

Figure 4.3: Block diagram of the architecture of a single ASIC.

(i.e., pulse-echo operation), or to the ground (i.e., disabled). The element-level circuitry fits in the 300 µm × 150 µm area occupied by the transducer element, allowing the PZT matrix to be integrated directly on top of the ASIC.

Each RX bus is associated with a shared row-level circuit consisting of a low-noise amplifier (LNA), programmable gain amplifier (PGA), and a cable driver, which connects the output signal to a receive channel of the imaging system. The various combinations of LNA/PGA gain settings allow to achieve a programmable gain ranging from −8.6 to 32.7 dB with an average step of 2.75 dB. The gain can be changed during the receive phase to make sure the signal level stays within the dynamic range of the ASIC. Each TX bus receives an externally generated high voltage transmit unipolar pulse with an amplitude of tens of volts. The control logic, which is programmed through horizontal and vertical shift registers, determines whether an element participates in a given TX/RX cycle; selects the element configuration for a specific imaging scheme; and sets the gain of the row-level circuit. More details about the current ASIC design can be found in our previous publication [132].

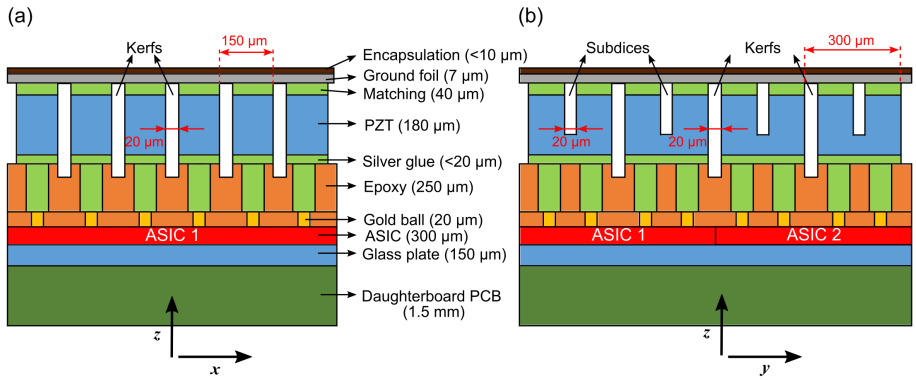

Figure 4.4: Overview of the acoustic stack (not drawn to scale). (a) Front view. (b) Side view. The numbers in parenthesis indicate the dimension in the z-direction (i.e. thickness).

4

4.2.4 Acoustic stack fabrication

Stack design

Our stack design was similar to what we have used previously for matrix transducers in our lab [71], [86], [155], [161], [173] and consisted of a PZT array built on top of an ASIC, a single matching layer, an aluminum ground foil, and a top protective layer. At the bottom of the PZT, there was a buffer layer that allowed for tolerances in dicing depths, and electrically isolated neighboring elements. A major issue in the previous designs was the fact that the acoustic stack was mounted only through thin layers on top of the ASIC. This made fabrication easier, but due to the lack of damping between the PZT and the ASIC, a significant amount of energy was transmitted into the ASIC, which hardly attenuates the waves. This resulted in two effects: reflections from layers beneath the ASIC; and cross-talk between elements due to the propagation of Lamb waves, which can be visible as extra peaks in the directivity pattern [86]. There are various approaches to reduce the effect of the ASIC on acoustic performance. Shabanimothlag et al. proposed to either lap down the thickness of the ASIC and place a standard acoustic backing behind the ASIC, or dice deep cuts into the ASIC [86]. These approaches work in simulation but are difficult to be realized in practice as the ASIC mainly consists of silicon which is brittle and hence hard to process. All alternative methods use an interfacing surface layer such as epoxy between the ASIC and PZT to induce a quarter-wavelength mode and direct most of the acoustic energy from the PZT forward [182]. Wildes *et al.* proposed a high-impedance "dematching" layer that reduced the need for a high-attenuation backing layer [84]. They used anisotropic conductive adhesive and flex circuits to attach the acoustic stack to the ASIC. Wodnicki *et al.* proposed to use an interposer conductive backing of pillars to connect the acoustic stack to the surface of the ASIC [183]. The interposer consisted of a 3D printed acrylic frame that was filled with conducting and acoustically absorbing silver epoxy material. The thickness of the interposer backing was considerably large (4 mm) to ensure great attenuation.

In the current design, we have opted for an interposer layer that consists of pillars of silver glue and an epoxy material with a high attenuation. The composite layer consists of a small channel of silver glue that electrically connects the PZT material to the ASIC and

an epoxy that we previously used as a backing and has high attenuation. The thickness of the interposer was chosen such that it dampens the waves significantly, but not completely as in the work of Wodnicki *et al.* [183]. A schematic drawing of the designed acoustic stack with material information is presented in Figure 4.4.

Stack fabrication

In our previous work [179], in which we investigated the effect of subdicing on a PZT matrix built on top of ASICs, we limited ourselves to the fabrication of a matrix transducer consisting of 4x1 tiled ASICs. The main difficulty lied in maintaining a flat surface of the stack over the whole area. The flatness of the stack surface is crucial for the dicing process because the dicing kerfs should be deep enough to guarantee the electrical and acoustical isolation between the elements, but shallow enough to not cut into the ASICs. Unfortunately, ASIC damage during the dicing process was a recurrent problem encountered in our previous attempts to fabricate the matrix.

In the current work, in order to minimize the risk of ASIC damage when dicing, we opted to manufacture a sample consisting of 8 × 1 tiled ASICs with a gap of one ASIC in the middle, i.e., the acoustic stack consists of two times 4 × 1 tiled ASICs with a gap of one ASIC in between the two. This is not the final version of the matrix transducer, however, this prototype is certainly relevant to verify the reliability of our manufacturing process; and to evaluate the functionality and performance of a prototype twice as large as our previous ones.

The transducer fabrication process starts with gluing the ASIC tiles onto a glass plate, which acts as a flat surface to guide the alignment of the ASICs and ensure that the ASICs have the same surface height. After this, gold balls are deposited on the ASIC pads (two bond pads are available per element to improve the connection stability). The gaps between the gold balls are filled with an electrically isolating epoxy material, which is then grinded down until the gold balls are again exposed. The main role of this layer is to establish a mechanical buffer for dicing the interposer layer, and to electrically isolate neighboring elements from each other. This buffer layer also provides the electrical connections from the ASIC bond pads to the interposer layer.

Next, the interposer is built by first depositing a thick layer of the non-conductive epoxy material. A 50 µm dicing blade is used to dice in one direction to expose the gold balls. These grooves are then filled with conductive glue and afterwards, the excess material is grinded away. Then, the dicing blade is used to dice in the other direction in between the gold balls and these grooves are filled again by the non-conducting buffer material. Excess material is again grinded away so that we end up with a flat top layer.

Next in the process, a matching layer made of conductive glue is applied on top of the piezoelectric material (3203HD, CTS Corporation, Lisle, IL, EUA). Then, the stack consisting of PZT and matching layer is glued on top of the interposer. After this, the acoustical stack is diced. Two types of cuts are used. The through-cuts are made to separate the PZT elements with 300 µm × 150 µm pitch and they may partially extend into the interposer layer (see Figure 4.4). The subdicing cuts, on the other hand, only extend to about 70% of the pillar thickness. All the dicing/subdicing cuts are made using a 20 µm thick diamond blade and the dicing kerfs are not re-filled with any material, to minimize the acoustical crosstalk between the elements.

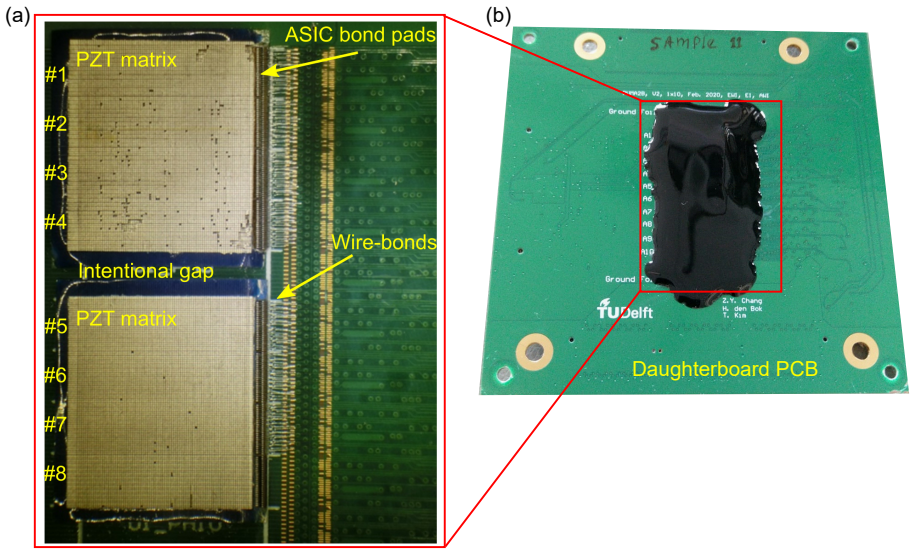

Figure 4.5: Photograph of the prototype transducer. (a) Fabrication of the PZT matrix with 96×80 (rows × columns) elements on top of 8x1 tiled ASICs. (b) Finished transducer on the daughterboard.

To finalize the matrix, a common ground electrode is made by gluing a 7 µm thick aluminum foil on top of the whole matrix array. Afterward, a thin layer of an encapsulation material (AptFlex F7, Precision Acoustics Ltd., Dorchester, UK) is placed on top to prevent moisture from infiltrating the acoustic stack and thereby damaging the array. Photographs taken during and after the fabrication of the matrix transducer are shown in Figure 4.5.

Electrical Connections

A daughterboard (see Figure 4.5b) was designed to hold the matrix transducer, and to provide the transmit, receive, power, and control signals to the ASIC. The electrical connections from the ASIC bond pads to the daughterboard bond pads were made with a bonding machine using 18 µm thick aluminum wire-bonds. Ultraviolet curing glob top epoxy was applied over the bonding wires for protection.

The daughterboard is connected to a motherboard by micro coaxial cable assemblies (Samtec, New Albany, IN, USA) to transfer the TX and RX data. The motherboard interfaces with a Verasonics imaging system (V1, Verasonics, Inc., Kirkland, WA, USA) via two connectors (DLM5-260PW6A, ITT Corporation, White Plains, NY, USA) such that it can be mounted directly on the Verasonics machine. An electronic matching network is provided in the transmit paths to minimize overshoot and undershoot of the transmission signal, to guarantee the unipolar character of the excitation generated from the Verasonics. On the other hand, to compensate for the cable load effect and to minimize the losses of the transmission line, the receive paths are buffered with unity gain operational amplifiers on the motherboard to provide impedance matching between the output of the ASIC and the Verasonics. The power and control signals are transferred via a flat ribbon cable from the motherboard to the daughterboard. An external FPGA (DE2-115, Altera Corp., San

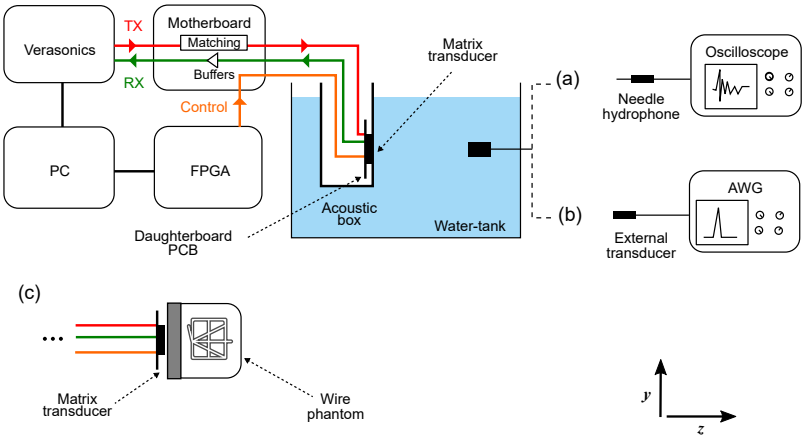

Figure 4.6: Acoustical measurement setup. (a) Transmit characterization. (b) Receive characterization. (c) Imaging using a CIRS phantom.

Jose, CA, USA) generates the control data to program the ASIC, and an external power supply provides the power for the daughterboard and the motherboard. The Verasonics computer controls the overall operation of the whole system through MATLAB (2014b, The MathWorks, Inc., Natick, MA, USA).

4.2.5 Measurement setup

Electrical characterization

The electrical performance of the ASIC and the whole signal chain from the ASIC to the Verasonics, including the cables and the motherboard, was evaluated by a test sample ASIC without the acoustic stack. Randomly selected element bond pads on the ASIC were wirebonded to an externally accessible test pad on the daughterboard. The transmit, receive, power, and control bond pads on the ASIC were wire bonded to the daughterboard in the usual way. After programming the ASIC, we used an arbitrary waveform generator (AWG; 33250A, Agilent Technologies, Santa Clara, CA, USA) to apply a 50-cycle sinusoidal signal of 7.5 MHz to the test bond pad as a test signal. The corresponding output signals were recorded at three different locations: at the input of the buffer on the motherboard; at the output of the buffer on the motherboard (i.e., at the input of the Verasonics); and at the output of the analog-to-digital converter of the Verasonics. We present the electrical performance of the signal chain in Section 4.A.

Acoustical characterization

Figure 4.6 shows a schematic diagram of the setup for the acoustical evaluation of the prototype transducer. For this purpose, the transducer was mounted in a box with an acoustical window made of 25 µm thick polyimide. The whole setup was submerged in a tank filled with deionized water.

For the transmit characterization (see option (a) in Figure 4.6), each element was driven individually with a 20 V unipolar pulse provided by the Verasonics imaging system. The

acoustic pressure generated by the elements was detected by a calibrated 1 mm needle hydrophone (SN2082, Precision Acoustics Ltd., Dorchester, UK) positioned at a distance of 200 mm away from the transducer in the z-direction. On the xy-plane, the hydrophone was placed in front of the active elements in order to reduce the influence of its directivity, as follows. In the y-direction, we aligned the hydrophone with a central row of the ASIC under test, whereas in the x-direction, the hydrophone was aligned at two different positions: at column 20 for measuring elements located on the left-hand side (i.e., columns 1 to 40) of the matrix shown in Figure 4.5; and at column 60 for measuring elements at the right-hand side (columns 41 to 80). The hydrophone output was amplified by a 60 dB amplifier (AU-1519, Miteq, Inc., Hauppauge, NY, USA), digitized by an oscilloscope (DSO-X 4024A, Agilent Technologies, Santa Clara, CA, USA), and automatically transferred to the Verasonics computer. Lastly, the recorded signals were bandpass filtered with cutoff frequencies of 4 MHz and 12 MHz to eliminate noise from lower and higher frequency sources.

The directivity pattern of nine arbitrarily selected elements was characterized in the x- and y-directions with hydrophone scans. For this purpose, we used a calibrated 0.2 mm needle hydrophone (SN2385, Precision Acoustics Ltd., Dorchester, UK) located 50 mm away from the transducer in the z-direction. The hydrophone output was amplified and recorded as detailed in the previous paragraph. For comparison, we have also simulated the directivity pattern of an equivalent rectangular piston using the ultrasound simulator FOCUS [184]. The relevant simulation parameters are given in Table 4.1.

Table 4.1: Parameters for the directivity pattern simulation

Parameter	Value
Element center frequency	7.5 MHz
Element size	300 µm × 150 µm
Excitation type	Hanning weighted pulse
Number of cycles	1
Sound speed	1480 m/s

To evaluate the receive performance (see option (b) in Figure 4.6), an external transducer was utilized as a transmitter and excited with a 3-cycle sinusoidal burst generated by an AWG. We used a pre-calibrated 1 mm circular single-element transducer (PA865, Precision Acoustics Ltd., Dorchester, UK), which was placed at the center of the matrix's surface (i.e., at the origin of the xy-plane) at a distance z=300 mm. The received signals of each individual element were acquired with the Verasonics.

Using the same setup described in the previous paragraph, we have also measured the overall dynamic range, which is defined as the difference between the highest and the lowest detectable pressures. With input pressures ranging from about 1 to 50 kPa, we recorded the received signals for different gain settings of the Verasonics time-gain-compensation (TGC) and the ASIC gain (i.e., the combinations of LNA/PGA gain settings). For the ASIC gains, we used gain levels of 0, 3, 7, 11, and 15, which in decibels correspond to −8.6, 0, 12.1, 23.5 and 32.7 dB, respectively.

Imaging

To test the imaging capabilities of the transducer prototype (see option (c) in Figure 4.6), we imaged a commercial ultrasound phantom for 3D evaluation (model: 055, CIRS, Inc., Norfolk, VA, USA), which contains wires with a diameter of 100 µm. For this test, only the top ASICs (i.e., ASICs 1 to 4) of the prototype were active, which means about 3800 active elements. All the active elements were excited simultaneously to generate a plane wave. In reception, the echoed wavefronts were recorded column-by-column. This necessitates 80 transmit events for recording the data detected by all elements. The raw echo data was filtered using a 50^{th} order bandpass finite impulse response (FIR) filter with cut-off frequencies of 5 MHz and 9 MHz. The sound speed value used for the reconstruction was 1540 m/s.

A 3D volume with a lateral/elevation size of about 14 mm covering a depth ranging from 5 to 35 mm was discretized with a pixel size of 100 µm and reconstructed with a delay-and-sum beamforming technique. The reconstruction was conducted using a GPU code developed based on the direct sampling concept [185], [186]. The beamformed echo data were first normalized, then log-compressed, and finally shown with a dynamic range of 50 dB and 30 dB for 3D and 2D representation, respectively. The 3D volumetric image rendering was performed with MATLAB. For quantitative evaluation, the full-width at half-maximum (FWHM) of the point spread function (PSF) from wire reflections in the lateral and axial directions was calculated in different elevation planes (from −3 to 3 mm, with a spacing of 1 mm) to evaluate the variability of resolution.

4.3 Results

4.3.1 Sensitivity

The normalized sensitivity map across all elements of the matrix transducer in transmit and receive are presented in Figure 4.7a and Figure 4.7b, respectively. The plotted values represent the envelope peak of the time domain signals expressed in decibels (relative to the maximum). Note that some elements (shown in white) have been omitted from the map because they exhibit a considerably higher amplitude (10 dB higher than the mean amplitude over all elements), which hinders the visualization of the variation across the remaining elements. Note also that ASICs 7 and 8 have suffered damages during the fabrication process and have been disconnected from the daughterboard. Due to this, we cannot include these ASICs in the overall evaluation of the prototype transducer, and we have omitted them in all figures presented in this section.

The sensitivity variation is somewhat similar in transmit and receive, but there are noticeable differences between them. In transmit, the elements located at the left bottom corner of the matrix (i.e., near columns 1 to 4 from ASICs 4 to 6) and also the ones located near the vertical centerline (i.e., near column 40 from ASICs 1 to 6) exhibit a lower efficiency, which is below −10 dB. The measurements for these elements were likely affected by the directivity of the hydrophone, as this effect is not seen in the receive map. In total, five rows are not functioning in transmit: rows 1 to 4, and row 48. This means that 400 elements are defective in transmit, which corresponds to 7% of the elements if we consider only elements from ASICs 1 to 6. In receive, however, there are significantly more defective rows: 12 in total. This represents 960 elements, i.e., 17% of the elements from ASICs 1 to 6. Besides the

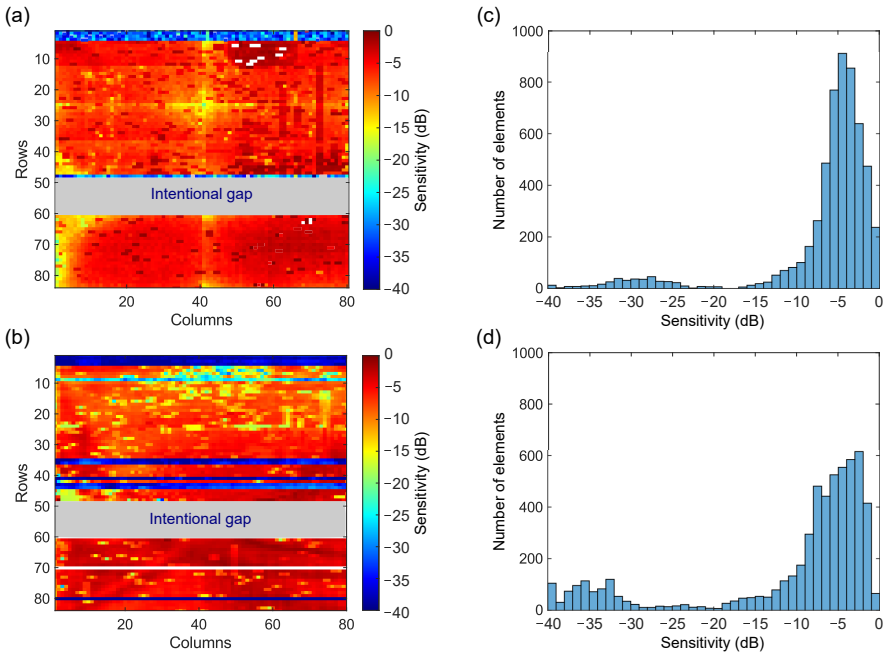

Figure 4.7: Sensitivity variation across the transducer elements. (a) Transmit sensitivity. (b) Receive sensitivity. (c) Transmit sensitivity histogram. (d) Receive sensitivity histogram.

defective rows, many elements in ASICS 1 and 2 show a lower sensitivity (below −10 dB) in receive. Further observations regarding defective elements will be presented later in Section 4.4.

Figure 4.7c shows the histogram of transmit sensitivity. As seen, about 3900 elements are within the 0 dB to -6 dB level. This represents 72% of the elements if we consider only functioning elements (i.e., elements located in defective/missing rows are not counted). In receive, as shown in the histogram in Figure 4.7d, about 2800 elements have a sensitivity above −6 dB. This represents 58% of the functioning elements.

4.3.2 Time and frequency response

Figure 4.8a shows the transmit pressure wave for a single transducer element (blue solid line), recorded with the hydrophone at z=200 mm, together with its fast Fourier transform (red dashed line). Note that there is a second pulse present in the time domain response, with a delay of about 1.5 µs from the main pulse (see black arrow in the figure). This is likely due to reflections from the back side of the ASIC. The second pulse exhibits a peak frequency of about 5 MHz, as seen in the frequency spectrum in Figure 4.8b.

In Figure 4.9, the time and frequency responses for all working elements of the transducer are presented. In the figure, the color of each pixel represents the count of the number of occurrences in that pixel. In the time domain response shown in Figure 4.9a, the time delays between the signals have been corrected using cross-correlation.

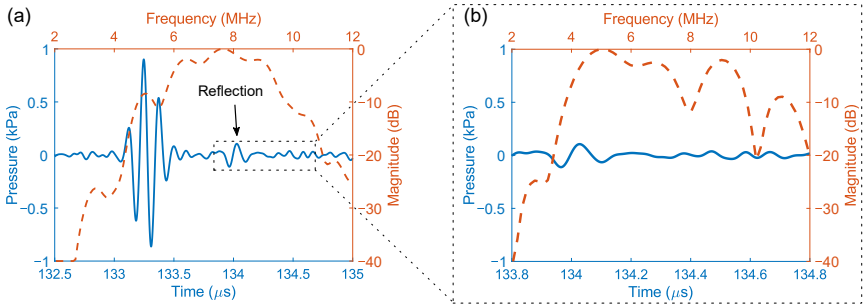

Figure 4.8: (a) Time and frequency domain response for a single element. (b) Close-up look at the second pulse.

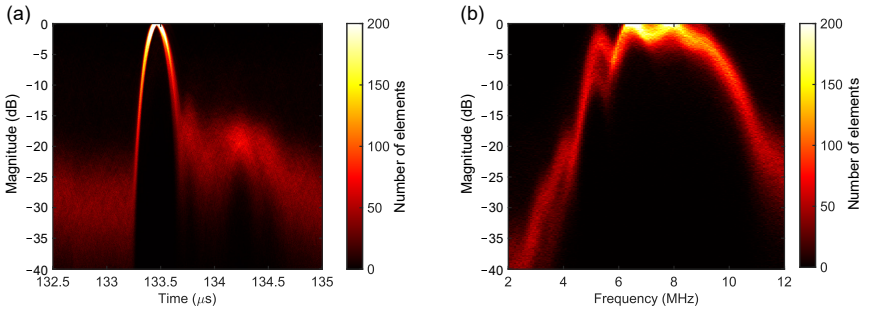

Figure 4.9: Time and frequency domain responses for all elements. (a) Envelope of the time signals. (b) Frequency spectrum.

The transmit performance of the transducer is summarized in Table 4.2 in terms of peak pressure, center frequency, −6 dB bandwidth, and ringing time, which is defined as the time interval for the envelope amplitude to decrease below −20 dB of its corresponding peak. The listed values represent the mean and standard deviation over the working elements (i.e., rows 1-4 and 48 are neglected in the calculations).

Table 4.2: Transmit performance of the prototype transducer.

Parameter	Value
Peak pressure (kPa)	0.6 ± 0.2
Center frequency (MHz)	7.5 ± 0.6
Bandwidth -6 dB (%)	46 ± 14
Ringing time -20 dB (μs)	0.30 ± 0.15

4.3.3 Directivity pattern

Figure 4.10 shows the measured directivity pattern of nine arbitrarily selected elements in transmit together with the corresponding averaged directivity pattern (black solid line) and the simulated result (blue dashed line). The measured directivity pattern differs somewhat

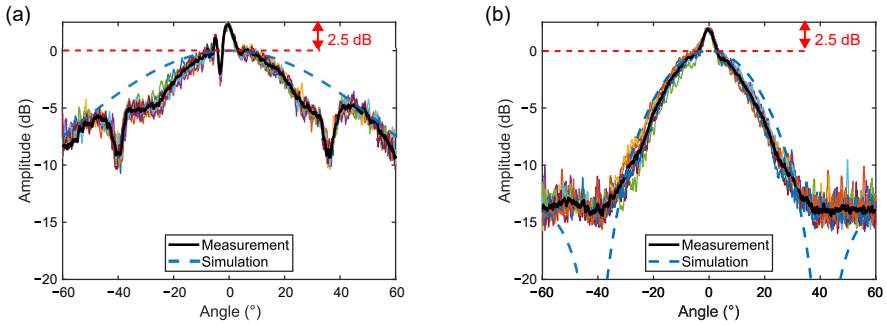

Figure 4.10: Measured and simulated directivity pattern in transmit. (a) Along the x-direction. (b) Along the y-direction.

from the simulated one in both directions. As indicated in the figure, the measurements show a sharp peak with an amplitude of 2.5 dB higher than in simulation at zero degrees. Ignoring this sharp peak, the directivity pattern along the x-direction exhibits a −6 dB beam width of about 70 and 105 degrees in measurements and simulations, respectively. This difference is due to the presence of a dip at ±40 seen in the measurements. In addition, an extra dip at -4 degrees is also present in the measurements. Along the y-direction, the measured directivity pattern shows a −6 dB beam width of about 42 degrees, which agrees well with the simulated one. The dips observed in the simulation at ±40 degrees are not present in the measurements due to the noise floor, which is about −14 dB.

4.3.4 Dynamic range

Figure 4.11 shows the relation between the received pressure at the transducer surface and the corresponding ASIC RX output voltage for different TGC and ASIC gain settings. The plotted values represent the average over all the functioning elements. The received signal amplitudes were converted from Verasonics output units back to millivolts at the Verasonics channel input using the results obtained from the electrical characterization (see Section 4.A). Note that the values ranging from 50 kPa to 1 MPa (gray region in the figure) were extrapolated based on the trend before and the observed saturation limits. This was done because we did not apply pressures above 50 kPa to avoid damage to the transmitting transducer.

It can be seen that the relationship between received pressure and output voltage is characterized by both linear and non-linear regimes. In the mid-range, where the curves are nearly linear, we observed an average difference of about 3 dB between most of the adjacent ASIC gain steps. For the lowest gain, we measured a receive sensitivity of approximately 55 nV/Pa, whereas for the highest gain the receive sensitivity is about 9 µV/Pa. This corresponds to a total gain range of 44 dB.

In the low-range, the curves are dominated by the noise floor of both the Verasonics and the ASIC, as indicated in the figure. It is noticeable that the noise floor varies for different TGC and ASIC gain settings. As seen, the noise floor for higher ASIC gain levels (gains 11 and 15) remains approximately the same regardless of the TGC changes. From this perspective, we can conclude that the noise floor is determined exclusively by the

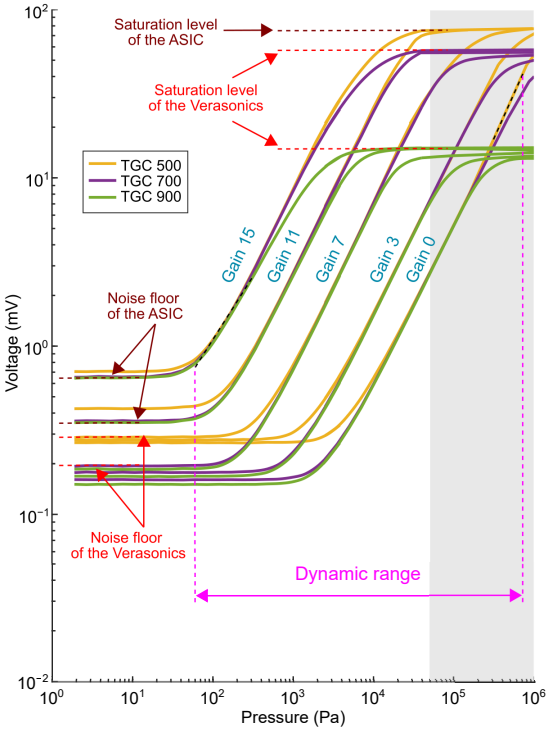

Figure 4.11: The relation between the received pressure and ASIC output voltage for different gain settings.

ASIC gain. On the other hand, for lower ASIC gain levels (gains 0 to 7), the noise floor remains basically the same regardless of the ASIC gain changes. Therefore, we can say that the noise floor for this gain setting is determined by the Verasonics only. Note that TGC 500 exhibits a slightly higher noise floor than TGC 700 and 900 possibly because the noise floor is significantly determined by both the ASIC and the Verasonics.

In the high-range, the curves are dominated by the saturation levels of the Verasonics and the ASIC. As noticed in the figure, the saturation level for TGC 900 is about 15 mV, whereas for TGC 700 it is 60 mV. This is in agreement with the corresponding saturation levels presented in Section 4.A. However, for TGC 500 we did not observe a saturation at about 80 mV in the electrical characterization (see Figure 4.14 in Section 4.A). Therefore, the saturation observed in Figure 4.11 for TGC 500 actually corresponds to the saturation level of the ASIC (note that the saturation level of the ASIC is irrespective of the ASIC gain). Because of the observed saturation values for both the ASIC and Verasonics, we were able to extrapolate the results above 50 kPa.

The receive performance of the prototype transducer for different gain settings is summarized in Table 4.3. Here, the minimum detectable pressure is defined as the pressure level at which the SNR becomes 0 dB, whereas the maximum detectable pressure is defined as the pressure level at which the 1 dB compression is reached.

Table 4.3: Receive performance for different gain settings. The "*" indicates extrapolated values

ASIC gain	Minimum pressure (kPa)	Maximum pressure (kPa)	Receive sensitivity (μV/Pa)
0	30	700*	0.06
3	2	200*	0.15
7	0.3	70*	0.72
11	0.2	20	2.73
15	0.06	4	8.79

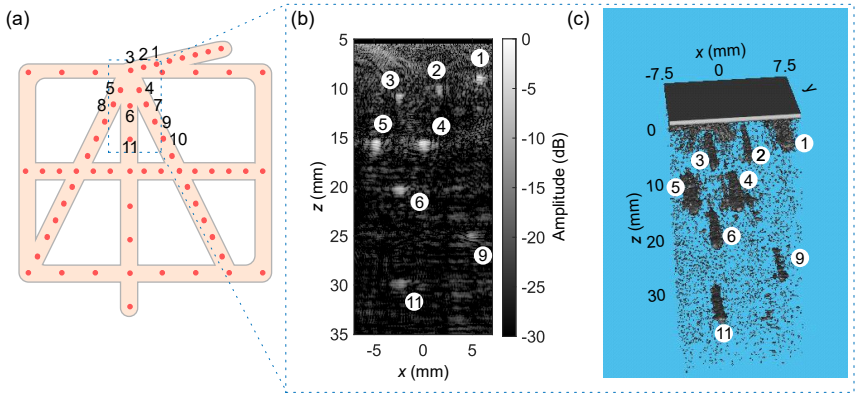

Figure 4.12: (a) Scheme of the wire phantom and numbered wires (the dashed rectangle depicts the field of view of the transducer). The reconstructed (b) 2D and (c) 3D images.

4.3.5 Imaging

Figure 4.12 shows the schematic representation of the wire phantom together with the reconstructed 2D and 3D images (the 2D image is one slice of the 3D image). As seen, the wires numbered 1 to 6 and 11 are well detectable in both the 2D and 3D images. Wires 7, 8, and 10 were not detected though, and wire 9 was barely detectable. This could be due to the small effective aperture (contribution of a low number of elements) in reconstructing the pixels on the edge of the image. The trend of lateral FWHM in Figure 4.13 indicates that the lateral resolution degrades when the imaging depth increases. The range of lateral and axial FWHM is almost the same for all the wires except wires 9 and 11 which are positioned at larger z values. The wide range of FWHM values for each wire mainly comes from the different sensitivity of the elements of the prototype transducer.

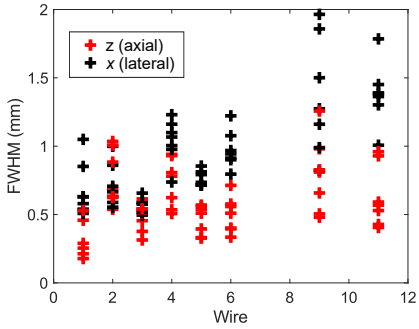

Figure 4.13: The axial and lateral FWHM for different wires in different elevation planes.

4.4 Discussion

In this work, we have presented a 7.5 MHz prototype transducer for 3D imaging of the carotid artery. We have built an array of 8 × 1 tiled ASIC integrated with a PZT matrix consisting of 7680 elements. We have opted to leave a gap in the middle of the array to reduce the risk of mechanical damage to the ASICs during the manufacturing process due to misalignment. The current size of the gap is one full ASIC due to the current design of the daughterboard PCB layout, but if building a large aperture in parts remains necessary a redesigned PCB can reduce the gap to a single row. Unfortunately, two ASICs still were malfunctioning due to electrical issues: in ASIC 8, we observed a short in one of the power supplies to the ASIC during manufacturing and decided not to use this ASIC further. In ASIC 7, we found a short during the final check before finishing the fabrication and decided to remove the bond wires for this ASIC. We are currently investigating ways to minimize damage on the ASICs (both mechanical and electrical) during the fabrication process. One potential approach is to prefabricate the acoustic stack (i.e., the PZT matrix, matching layer, and interposer) separately and attach it to the ASIC pads (or gold balls) at a later time. The procedure of bonding the acoustic stack to the ASIC could be accomplished by using an anisotropic conductive film, as described in [136]. In addition, the risk of electrical damage, such as caused by electrostatic discharge (ESD) events, could be significantly reduced if we are able to effectively ground leakage paths during the assembly of the acoustic stack on the ASICs. We will explore these possibilities in our future work.

The maps presented in Figure 4.7 show that 72% and 58% of the working elements exhibit sensitivity variation within −6 dB range in transmit and receive, respectively. On the one hand, the achieved element yield is sufficient to demonstrate the technology employed in the prototype transducer, allowing us to evaluate features and test the functionality of the current design. On the other hand, for imaging purposes or mass production, the element yield must be improved to avoid defective rows. This is a major problem that needs to be tackled in our manufacturing process. Regarding rows 1 to 4, which do not work in both transmit and receive, we found afterward that this was caused by a damaged cable in our measurement setup. Regarding the rows that do not work only in receive (mostly from ASIC 4), we believe this is due to faulty wire-bonds or damage to the motherboard components. Besides defective rows, many elements in ASICs 1 and 2 show a lower sensitivity (below

−10 dB) in receive. These elements probably suffered damage/degradation during or after the transmit experiments (the transmit and receive measurements were performed in an interval of one week). The degree of degradation might be verified by repeating the transmit characterization and comparing with the previous measurements. Regarding the omitted elements in the map (shown in white), we think that they exhibit a considerably higher amplitude due to a short in the acoustic stack between multiple elements.

Figure 4.8 and Figure 4.9 show that the time and frequency responses of different transducer elements are quite similar (based on the number of overlapped pixels in Figure 4.9) and behave as expected. Based on the measured peak pressure (0.6 kPa) and the transmit voltage (20 V peak amplitude), we estimate an average transmit efficiency of approximately 30 Pa/V at 200 mm. This value is comparable with our previous prototype with subdiced elements [179]. On average, the elements have a center frequency of 7.5 MHz and a −6 dB single way bandwidth of about 45%. However, we have observed that many elements exhibit a sharp peak at 5 MHz and a dip at 6 MHz, which reduces their bandwidth significantly. This is likely caused by the effect of reflections and standing waves from the bottom side of the transducer, i.e., from the ASICs.

The measured directivity pattern shown in Figure 4.10 follows the trend of the simulated one in both directions but deviates significantly in specific points. These deviations can be explained by a combination of both electrical and acoustical crosstalk (see Section 4.B for details). The electrical crosstalk in our case means that all elements of a row are somewhat excited when an electrical pulse is sent to the transmit bus of that row. This is likely the cause of the sharp peak of 2.5 dB at 0 degrees. Since this type of crosstalk only happens in transmit, the sharp peak will be absent in the receive directivity pattern. Furthermore, because we intent to use at least half of the elements on a row in transmit, the peak will not affect the images generated by this probe. Along the x-direction, the dips observed at ±40 degrees are likely caused by acoustical crosstalk. Since the prototype transducer was designed to operate with low steering angles, these dips are not considered to be important. Previously, in the design without an interposer layer, we also observed peaks at ±20 degrees in the directivity pattern. With the interposer, there is now an attenuating medium in between the elements and the ASIC and due to that these peaks do not show up anymore. This suggests that the employed interposer layer helps to reduce the crosstalk due to the propagation of Lamb waves in the ASIC.

As seen in Figure 4.11, the minimum detectable pressure of 60 Pa is limited by the noise floor of the ASIC for gain 15. On the other hand, the maximum detectable pressure is about 700 kPa, which is limited by the saturation level of the ASIC for gain 0 and TGC 500. Therefore, the overall dynamic range of the prototype transducer is about 81 dB, which is sufficient for carotid imaging applications [187].

The performance of the prototype transducer was tested by imaging a commercial wire phantom, as shown in Figure 4.12 and Figure 4.13. The figure proves the applicability of the prototype for plane wave 3D imaging, however further evaluation of beamforming image quality needs to be performed in the future.

4.5 Conclusion

We have demonstrated the design, fabrication, and characterization of a PZT matrix transducer with integrated electronics. The ASIC architecture together with the subdicing of the piezo elements allowed us to effectively reduce the channel count to 120 transmit and 120 receive channels. The prototype transducer was targeted to have 7680 elements built on top of 8 × 1 tiled ASICs, however, two ASICs were damaged during the fabrication process. On average, the individual elements of the transducer exhibited a transmit efficiency of 30 Pa/V at 200 mm and a −6 dB bandwidth of 45%. The receive dynamic range is 81 dB with a minimum and maximum detectable pressure of 60 Pa and 700 kPa, respectively. Overall, the characterization results are promising and encourage us to pursue further up-scaling by fabricating a larger PZT matrix transducer on 10 × 1 tiled ASICs. In this way, we expect to realize a fully populated matrix consisting of about 10 000 elements in the near future.

Appendix

4.A Electrical characterization

Table 4.4 shows the relationship between the output voltage of the ASIC (connected to the Verasonics input channel) and the output of the Verasonics for different TGC settings. The curves show that for TGC levels of 100, 300, and 500, the Verasonics signals are always linear in the range evaluated. However, with TGC levels of 700 and 900, nonlinear deformation of the signal is observed above 5500 units (shown by the dashed lines) due to the saturation of the Verasonics output. Table 4.4 presents the maximum acceptable input voltage (determined using the 1 dB compression point), the corresponding Verasonics output, and the gain in the linear range at each TGC setting. By increasing the TGC, the Verasonics gain is increased, however, the maximum acceptable input voltage in the linear regime is decreased.

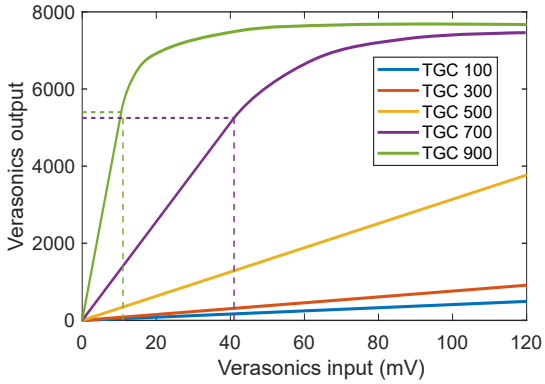

Figure 4.14: Relation between the input and output of the Verasonics V1 system for several TGC gains at 7.5 MHz.

Table 4.4: Characterization of the Verasonics V1 system for different TGC settings.

TGC	Maximum input (mV)	Verasonics output	Slope (1/mV)
100	310	1245	4.1
300	310	2315	7.6
500	185	5497	31.4
700	45	5514	129.3
900	11	5602	543.3

4.B Crosstalk analysis

Herein, we investigate whether the differences observed between the simulated and experimental directivity patterns could be explained by interelement crosstalk present in the prototype transducer. Since our measurement setup and transducer configuration do not allow us to measure the crosstalk directly, we analyzed the possible effects of both electrical and acoustical crosstalk on the directivity pattern via simulations. For this, we used the ultrasound simulator FOCUS, as explained previously (see Table 4.1), to simulate the directivity pattern of the transducer elements excited with different amplitudes and time delays to mimic the crosstalk [188], [189]. In all simulations, we used an array of 31 elements with the active element being the central one.

For the electrical crosstalk simulations, the neighboring passive array elements were excited simultaneously with an equal amplitude between them but lower amplitude as compared to the active element, as shown in Figure 4.15a. With regard to the acoustical crosstalk, we hypothesized that there were two different kinds of acoustical crosstalk happening. First, we assumed that the vibration of the active element will generate wave propagation through the interposer layer that will induce a vibration in the neighboring elements. To simulate this, the passive elements were excited with amplitudes and delays based on the distance from the active element, as shown in Figure 4.15b. Second, we hypothesized that there will also be crosstalk via a non-attenuating medium such as the ASIC. Here the delays are again based on the distance from the active elements, but the amplitude of the passive elements are the same, as shown in Figure 4.15c. The crosstalk analysis was performed only along the x-direction.

Figure 4.16a shows the effect of each simulated crosstalk on the directivity pattern. As can be seen, the electrical crosstalk introduces a sharp peak at zero degrees. We observed that the magnitude of the sharp peak is determined by the amplitude of the passive elements. Regarding the acoustical crosstalk via the interposer, the beam is narrowed and two bumps appear whose position is determined by the velocity of the medium. Finally, the acoustical crosstalk via the non-attenuating material generates two dips or peaks, depending on the phase.

To investigate the combination of electrical and acoustical crosstalk, we swept through different values of amplitudes and time delays in order to fit the simulated data to the experimental one. Figure 4.16b shows the result of the fitting procedure and Table 4.5 lists the values of amplitudes, time delays, and propagation speeds used to fit the curve. As seen, the trend of the simulated directivity pattern with crosstalk follows the experimental curve. This result suggests that the extra peak and dips observed in the measured directivity pattern could be caused by a combination of electrical and the two types of acoustical crosstalks. Note, however, that the value of propagation speed in the non-attenuating medium differs significantly from the propagation speed of Lamb waves in the ASIC [86], which suggest that this kind of crosstalk goes via another layer.

For our purposes, this brief analysis suffices to represent the contribution from different types of crosstalks in the directivity pattern. An in-depth simulation study of crosstalk is left for a later work as this is beyond the scope of this paper.

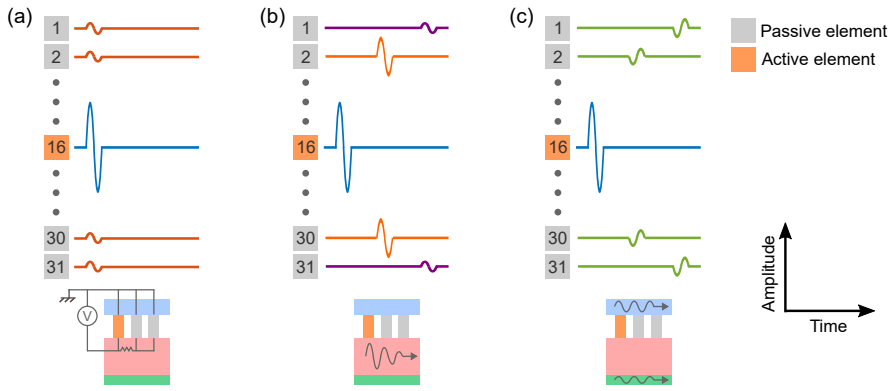

Figure 4.15: Assumptions for crosstalk simulations. (a) Electrical crosstalk. (b) Acoustical crosstalk via an attenuating medium. (c) Acoustical crosstalk via a non-attenuating medium.

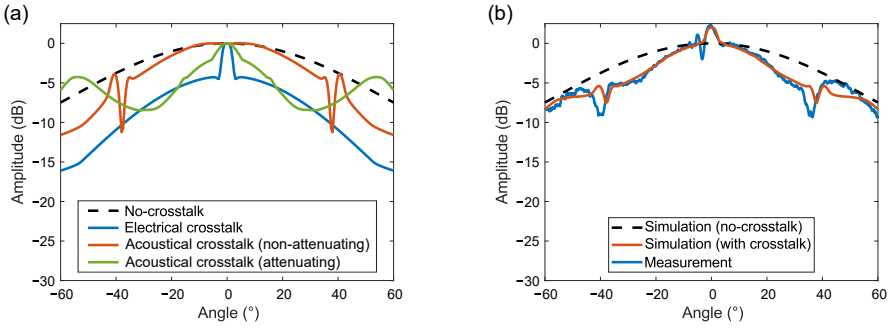

Figure 4.16: Directivity pattern along the x-direction. (a) Effect of individual crosstalks. (b) Effect of the combined crosstalk.

Table 4.5: Parameters for crosstalk simulations. *Between adjacent elements.

	Electrical	Acoustical (non-attenuating)	Acoustical (attenuating)
Amplitude	−30 dB	−20 dB	−3.5 dB*
Time delay*	-	0.0612 µs	0.0833 µs
Propagation speed	-	2450 m/s	1800 m/s

5

Two-Stage Beamforming for Phased Array Imaging using the Fast Hankel Transform

An ultrasound scan generates a huge amount of data. To form an image this data has to be transferred to the imaging system. This is an issue for applications where the data transfer capacity is limited such as hand-held systems, wireless probes and miniaturized array probes. Two-stage beamforming methods can be used to significantly reduce the data transfer requirements. In the first stage, which is applied in-probe, the amount of data is reduced from channel to scanline data. In the imaging system the data is then beamformed to obtain images that are synthetically focused over the entire image. Currently two approaches exist for the second stage. The first approach is a time-of-flight approach called synthetic aperture sequential beamforming (SASB) that has been developed for both linear and phased arrays. SASB does however introduce artefacts in the image that can be reduced by tapering the first stage scan lines at the cost of lateral resolution. The second approach is based on the wave equation, but a computationally efficient method for phased arrays that is producing sector scan data is lacking. Here we propose an algorithm that uses the fast Hankel transform to obtain a fast algorithm. The imaging performance of this method is evaluated with simulations and experiments. Compared with PSASB, which is an adaption of SASB for phased arrays, our method requires a similar amount of operations to construct the entire image and there is no trade-off between resolution and artefacts. These results show the advantage of using the wave equation instead of a time-of-flight approach.

This chapter has been published as:
F. Fool, J. De Wit, H. J. Vos, D. Bera, N. De Jong, and M. D. Verweij, "Two-Stage Beamforming for Phased Array Imaging Using the Fast Hankel Transform," *IEEE Transactions on Ultrasonics, Ferroelectrics, and Frequency Control*, 2019, DOI: 10.1109/TUFFC.2018.2885870

5.1 Introduction

An ultrasound scan generates a huge amount of data. To form an image this data has to be transferred from the probe to the imaging system. For the standard systems found in most hospitals this is not an issue as each element in the probe can be wired out individually. It is an issue for portable hand-held systems, that could for example be used in remote areas, emergency rooms and for use in primary care [190], [191], and probes that are used in size-restricted areas such as Intravascular Ultrasound. As a specific example consider a portable system to be used in remote areas. From a cost perspective smartphones or tablets would be preferred as imaging system. The probe then has to be able to connect via USB or WiFi to the imaging system. The data transfer requirements for a typical phased array configuration is 1.5 GB/s, assuming 30 frames per second, 128 scanlines per frame, 128 channels per scanline, 2048 samples per trace and 12 bit per sample. While the latest USB standard (3.2 Gen 2x2) would just be able to transfer this amount, the current WiFi standards (802.11ac) cannot. Data reduction is thus required.

A first line of thought might be to construct the image in-probe using Dynamic Receive Focusing (DRF). This would compress the channel data to scanline data. This means that instead of 1.5 GB/s the amount of data would be reduced to 12 MB/s, which is well within the limits of current USB and WiFi standards. In-probe DRF will thus significantly reduce the amount of data. However, the current on-chip DRF solutions [192]–[194] are either too large, have a limited frame rate or a decreased resolution. A method with a reduced in-probe complexity is wanted.

Dynamic receive focusing can be combined with Retrospective Transmit Focusing to improve the lateral resolution [195]. However, depending on its implementation this either implies no data reduction or an even more complex first stage.

Two-stage beamforming is an alternative approach for data reduction [77]–[79], [196]–[199]. The first stage consists of a simple single focus Delay-And-Sum (DAS) that reduces the amount of data from channel to scanline data. In the second stage the scanline data is further beamformed in the imaging system to obtain images that are synthetically focused over the entire image. Two-stage beamforming has two main advantages over in-probe DRF. First, the in-probe algorithm has a much lower complexity, allowing for smaller probes and less power dissipation. Second, the lateral resolution is better [77]–[79].

Currently there are two approaches available for the second stage: a time-of-flight (TOF) approach based on geometrical path length and an approach based on the wave equation. The first approach is called synthetic aperture sequential beamforming (SASB) and has been developed for linear and phased array imaging [77], [78] the latter called Phased SASB (PSASB). SASB has already been tested in clinical conditions and found to be at least as good as DRF [196], [197]. Furthermore, the feasibility of a wireless ultrasound probe in combination with consumer-level mobile devices that use SASB for beamforming has been demonstrated by Hemmsen *et al.* [198], [199]. A wave equation approach for linear array imaging has been developed by Vos *et al.* [79], based on Stolt migration [200], [201]. The main advantage of this approach over SASB is the computational efficiency. A better image quality might also be expected because the wave equation is used instead of a TOF approach [80]. However, superior performance in terms of image quality has not been demonstrated with a linear array [79].

A wave equation approach has not yet been developed specifically for the second stage of a two-stage beamforming method for phased array imaging. However, a similar method for a single scanning element on a cylinder does exist [202]. It is possible to adapt this method for phased array imaging, but it is computationally inefficient because one of the integrations cannot be performed using a Fast Fourier Transform (FFT). The latter problem does not arise with Stolt migration used for linear arrays, where after a change of integration variables all integrations can be done using FFTs. Therefore, this specific implementation is not very suitable as a basis for real-time imaging using phased arrays.

In this paper, which is an extension of an earlier proceedings paper, we will develop a computationally efficient two-stage beamforming method for phased array imaging that we will refer to as Phased Array Migration (PAM). The first stage consists of conventional phased array imaging with a single focus in both transmission and reception. The focal points in the first stage can be considered as virtual point sources and point receivers with a limited opening angle doing pulse-echo measurements [77]–[79], [203]. The second stage is based on the wave equation in polar coordinates. To make it computationally efficient a change of variables is introduced after which a Fast Hankel Transform (FHT) can be applied. We will show that our method contrary to PSASB has no trade-off between lateral resolution and artefacts, and that the computational performance of our implementation is very similar to PSASB.

This paper is structured as follows. Section 5.2 describes the general concept and gives the derivation of the migration and the subsequent implementation. In section 5.3 the simulation and experimental setups are described, of which the results are presented in section 5.4. Section 5.5 discusses the developed method and section 5.6 concludes this paper.

5.2 Concept and Theory

5.2.1 Concept

To use the concept of virtual sources/receivers, the time origin of the first stage scan lines, which are made with a fixed focus in transmit and receive, are shifted according to

$$t' = t - 2\frac{r_f}{c}, \tag{5.1}$$

in which t is the original time, t' is the shifted time, r_f is the first stage focal depth and c is the speed of sound in the medium. This time shift splits the dataset in two parts: for $t' < 0$ the data originates from the pre-focal zone ($r < r_f$) and for $t' > 0$ the data originates from the the post-focal zone ($r > r_f$). This is also shown in Figure 5.1. The shifted data is effectively assumed to originate from a pitch-catch configuration of virtual point sources/receivers located at the focal points.

The signal that is received from a scatterer by a virtual receiver has travelled through the medium twice: from the source to the reflector and back to the receiver. Since the source and receiver have the same location, these two paths are identical. Hence, the recorded signal is, apart from the amplitude, similar to a signal originating from a transmission at $t' = 0$ at the scatterer position that has travelled with an effective speed $\hat{c} = c/2$. This approach is called the exploding reflector model (ERM) [201]. Every scattering event can be regarded as a sound emission at $t' = 0$, that propagates with speed $\hat{c}$ and which amplitude

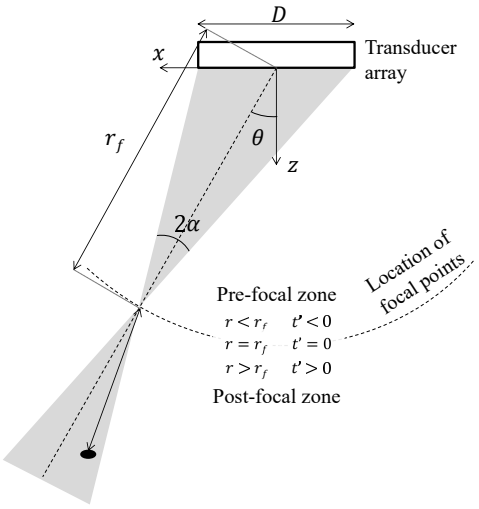

Figure 5.1: Schematic overview of the geometry for phased array migration.

is proportional to the strength of the scattered signal. The position and strength of the scatterers can be determined by back-propagating the recorded field with speed $\hat{c}$ to a certain depth and evaluating the field at $t' = 0$.

5.2.2 Theory

Stolt migration has been derived in Cartesian coordinates for a linear scan with sources/receivers that are located on a straight line [79]. A detailed derivation of this algorithm is given by Margrave [201]. In a sector scan the virtual sources/receivers are located on a semi-circle that is centred at the transducer midpoint as shown in Figure 5.1. Stolt migration is therefore not applicable to this geometry. Hence, we will show the derivation of a similar algorithm for this geometry below.

Phased Array Migration

The Helmholtz equation in polar coordinates reads [204]

$$r^2 \frac{\partial^2 \tilde{p}}{\partial r^2} + r \frac{\partial \tilde{p}}{\partial r} + \frac{\partial^2 \tilde{p}}{\partial \theta^2} + r^2 k^2 \tilde{p}^2 = 0, \tag{5.2}$$

in which

$$\begin{aligned} r &= \sqrt{x^2 + z^2} \\ \theta &= \arctan\left(\frac{x}{z}\right), \end{aligned} \tag{5.3}$$

are the polar coordinates, x and z are the Cartesian coordinates, $\tilde{p}$ is the Fourier transform of the acoustic pressure field and $k = 2\pi f/\hat{c}$ is the wavenumber. This equation can be solved by separation of variables, so we write

$$\tilde{p} = R(r)\Theta(\theta), \tag{5.4}$$

and substitute this in (5.2) to get

$$\frac{r^2}{R}\frac{\partial^2 R}{\partial r^2} + \frac{r}{R}\frac{\partial R}{\partial r} + \frac{1}{\Theta}\frac{\partial^2 \Theta}{\partial \theta^2} + r^2 k^2 = 0. \tag{5.5}$$

We can separate this partial differential equation in two ordinary differential equations for Θ and R

$$\frac{1}{\Theta}\frac{\partial^2 \Theta}{\partial \theta^2} = -m^2, \tag{5.6}$$

$$\frac{r^2}{R}\frac{\partial^2 R}{\partial r^2} + \frac{r}{R}\frac{\partial R}{\partial r} + r^2 k^2 - m^2 = 0, \tag{5.7}$$

where m is a constant. Equation (5.6) has the general solution

$$\Theta(\theta) = a_{1,m} e^{-im\theta} + a_{2,m} e^{im\theta}, \tag{5.8}$$

in which the boundary condition $\Theta(\theta) = \Theta(\theta + 2\pi)$ makes that m can only have real integer values.

After introducing the new radial coordinate $\rho = kr$, (5.7) can be rewritten as

$$\frac{\partial^2 R}{\partial \rho^2} + \frac{1}{\rho}\frac{\partial R}{\partial \rho} + R\left(1 - \frac{m^2}{\rho^2}\right) = 0, \tag{5.9}$$

which is known as Bessel's differential equation [205]. This has the general solution

$$R(\rho) = b_{1,m} H_m^{(1)}(\rho) + b_{2,m} H_m^{(2)}(\rho), \tag{5.10}$$

where $H_m^{(1)}$ and $H_m^{(2)}$ are the m^{th} order Hankel functions of the first and second kind. From their asymptotic expansions [205] it follows that $H_m^{(1)}$ represents a wave that propagates toward the origin and $H_m^{(2)}$ represents a wave that propagates away from the origin. A general solution to the polar wave equation must contain all possible m.

To form an image from the measured wavefield at the virtual receivers, first the recorded field has to be transformed to the frequency and angular Fourier domain using the transformation

$$\tilde{p}(r_f, m, f) = \int_{-\infty}^{\infty}\int_{0}^{2\pi} p(r_f, \theta, t') e^{i(-m\theta + 2\pi f t')} d\theta dt'. \tag{5.11}$$

Next, the data is propagated to a new depth using the effective speed $\hat{c} = c/2$. For the post-focal zone ($r > r_f$) we note that for these depths there are only waves travelling towards the origin that originate from the exploding scatterers. This means that only $H_m^{(1)}$ is of importance. In view of (5.10) we can therefore write

$$\tilde{p}(r, m, f) = \tilde{p}(r_f, m, f)\frac{H_m^{(1)}(\hat{k}r)}{H_m^{(1)}(\hat{k}r_f)}, \tag{5.12}$$

5

in which $\hat{k}$ is the wavenumber containing the effective speed $\hat{c}$. The final step is to take the inverse Fourier Transform over θ and evaluate the field at $t' = 0$, which is the time at which the scatterers exploded in the ERM. The resulting expression is

$$p(r, \theta, t' = 0) = \sum_{m=-\infty}^{\infty} \int_{-\infty}^{\infty} \tilde{p}(r_f, m, f) \frac{H_m^{(1)}(\hat{k}r)}{H_m^{(1)}(\hat{k}r_f)} e^{im\theta} df. \tag{5.13}$$

This solution is valid for a scatterer in the post-focal zone ($r > r_f$). The solution in the pre-focal zone ($r < r_f$) can be obtained by replacing $H_m^{(1)}$ by $H_m^{(2)}$, as for these depths the waves are travelling away from the origin towards the virtual receivers, and reversing the time axis (i.e. $t' \longrightarrow -t'$) before calculating $\tilde{p}$ using (5.11).

Fast Hankel Transform

In its current form (5.13) cannot be completely evaluated using FFTs only. A similar problem in Cartesian coordinates was solved by Stolt, who changed the integration variables after which all integrations could be evaluated using FFTs [200]. Here there is a ratio of two Hankel functions instead of a complex exponential and therefore exactly the same approach is not possible. However, we can look more closely at the parts in (5.13) that contain the frequency

$$\bar{p}(r, m) = \int_{-\infty}^{\infty} \frac{\tilde{p}(r_f, m, f)}{H_m^{(1)}(\hat{k}(f)r_f)} H_m^{(1)}(\hat{k}(f)r) \, \mathrm{d}f, \tag{5.14}$$

in which $\bar{p}$ is the pressure transformed with respect to the angle only. The above equation, which has to be computed separately for each angular frequency, is very similar to a Hankel transform [206]. However, there are two main differences. First of all, the integration is from $-\infty$ to $+\infty$ instead of from 0 to $+\infty$. A solution is to calculate the integral for positive and negative frequencies separately. A better solution is to drop the integration over the negative frequencies. This is similar to computing the discrete time analytic signal by setting the negative frequencies to zero [207]. This will save computation time in the second stage and because the analytic signal can be used to calculate the envelope of the signal, which is done before image display, it can also save time later in the process. The second difference is that the integration kernel is not a Bessel function of the first kind, but a Hankel function. However, it is still possible to apply the same kind of algorithms. We have applied the same approach as used for the Quasi fast Hankel transform algorithm by Siegman [206]. The basic idea is to introduce the following change of variables

$$\begin{aligned} f &= f_0 e^{+\alpha x}, \\ r &= r_0 e^{-\alpha y}. \end{aligned} \tag{5.15}$$

This change will turn (5.14) for the positive frequencies into an equation of the form

$$r_0 e^{-\alpha y} \bar{p}(y, m) = \int_{-\infty}^{\infty} \frac{\bar{p}(x, m)}{H_m^{(1)}(x)} H_m^{(1)}(x - y) \, \mathrm{d}x. \tag{5.16}$$

Equation (5.16) has the form of a convolution integral, except that the argument of the rightmost Hankel function is $x - y$ instead of $y - x$. Still, by using the time-reversal property

the above equation can be computed using Fourier Transforms as

$$r_0 e^{-\alpha y} \tilde{p}(y,m) = \mathscr{F}^{-1}\left[\mathscr{F}\left(\frac{\tilde{p}(x,m)}{H_m^{(1)}(x)}\right)\left[\mathscr{F}\left(H_m^{(1)}(x-y)\right)\right]^*\right]. \tag{5.17}$$

The above equation is significantly more computationally efficient than (5.14) evaluated using a matrix multiplication. However, the requirement of exponentially spaced grids prevent direct application. To solve this nonuniform Fourier Transforms can be used in (5.17) to apply the algorithm on linearly spaced grids. This approach called the nonuniform fast Hankel transform (NUFHT) has been introduced by Liu and Zhang [208].

Required line density and expected angular frequencies

The scan line density is an important parameter in the first stage of the imaging process. This parameter determines the density of the virtual point receivers that sample the wavefield and ultimately determines the maximum frame rate. Spatial aliasing can be avoided by choosing the distance between the virtual receivers less than one half of the effective wavelength. This requirement can be described by [79, eq.12]

$$\Delta\theta \leq \frac{\hat{c}}{2 r_f f_{\max} \sin\alpha} \tag{5.18}$$

in which $\Delta\theta$ is the angle between subsequent ray lines, $f_{\max}$ the highest frequency in the signal and α is the half width opening angle that can be geometrically approximated as [78]

$$\alpha \approx \tan^{-1}\left(\frac{D\cos\theta}{2 r_f}\right), \tag{5.19}$$

in which D is the aperture width and θ is the angle of the ray line as shown in Figure 5.1.

The required line density gives a limit on the expected angular frequencies. The maximum angular frequency m for a frequency f is

$$m_{\max}(f) = \frac{2\pi r_f f \sin\alpha}{\hat{c}}, \tag{5.20}$$

which can be derived from (5.18) using

$$m_{\max} = \frac{\pi}{\Delta\theta} \tag{5.21}$$

and noting that the required spacing is different for each frequency. This limitation on the angular frequency can be used to design a filter that effectively takes into account the limited opening angle of the virtual point sources/receivers. Frequencies that lie outside the maximum expected frequencies are just noise. This filter is due to its form very similar to velocity filters often used in seismic data processing [209].

5.2.3 Implementation

After the single focus scan lines are obtained in the first stage of the imaging process, the second stage beamforming algorithm is applied to the data. The numerical algorithm consists of several subsequent operations:

1. Shift the time origin of the image lines to points on a semi-circle with radius r_f.
2. Expand the sector of scanlines to a full circle by zero-padding in the angular direction.
3. Transform $p(r_f, \theta, t')$ to $\tilde{p}(r_f, m, f)$ by applying a 2D Fast Fourier Transform (FFT).
4. Apply a filter to account for the limited opening angle of the virtual sources/receivers.
5. Transform f to r for each angular frequency m using the NUFHT.
6. Take the Inverse Fast Fourier Transform (IFFT) in the angular direction.
7. Discard the ray lines from outside the scanning region.

By using the entire time domain signal in this calculation, and not separating the signals from pre- and post-focal zones, we obtain two important advantages. As the FFT assumes periodic time, circularly connecting the high intensity signal from the focal region to the tapered signal at the domain will result in Gibbs phenomena. Using the entire time signal provides continuity at the boundary between the zones, thereby avoiding Gibbs phenomena that would disturb the final image in the focal region. A second and even greater advantage is that by using the entire time domain signal the far field and the near field region can be reconstructed with the same calculation. Originally, for the calculation of the image in the pre-focal zone the time axis is reversed (i.e. $t' \longrightarrow -t'$) before applying the Fourier transform and the Hankel function of the second kind is used instead of the first kind. Instead of reversing the time axis, we can make use of the time reversal property of the Fourier transform and thus replace f by $-f$. By substituting $f' = -f$ (which implies $\hat{k}' = -\hat{k}$), we get

$$\tilde{p}(r_f, m, -f)\frac{H_m^{(2)}(\hat{k}r)}{H_m^{(2)}(\hat{k}r_f)} \longrightarrow \tilde{p}(r_f, m, f')\frac{H_m^{(1)}(\hat{k}'r)}{H_m^{(1)}(\hat{k}'r_f)}, \tag{5.22}$$

in which we used that $H_m^{(2)}$ is the complex conjugate of $H_m^{(1)}$ for real arguments [205, eq. 9.1.40], which results in $H_m^{(2)}(\hat{k}r_f)$ being equal to $H_m^{(1)}(-\hat{k}r_f)$. So the replacement of f by $-f$ and the change of the Hankel function mutually cancel and the same expression is used for the far field. Hence, the entire image can be reconstructed with the same calculation.

The expansion to a full circle in step 2 is needed to let the periodic boundary condition in angular direction coincide with the periodicity of the FFT. For this step, it is necessary that $\Delta\theta = 2\pi/n$ with n an integer value. Otherwise, m is no longer an integer value when we perform the Fourier expansion with a FFT.

The filter in step 4 is implemented as a filter with a hard cut-off based on (5.20) for an unsteered beam (i.e. $\theta = 0$). This means that all $|m| > m_{\max}(f)$ are set to zero. Usually, this kind of filter produces distortions [210], but there are two reasons why this filter can be used with no problem in our case. First, the maximum angular frequency decreases for higher steering angles and therefore the end of the domain is already slightly tapered. More importantly, due to the use of apodization the effective aperture decreases and therefore also the maximum angular frequency. Due to this the hard cut-off of the filter is already separated from the actual angular frequencies in the signal.

For the nonuniform Fast Fourier Transform (NUFFT) used in step 5 we used the implementation by Fessler and Sutton [211]. This NUFFT uses an upsampled FFT in combination with a frequency domain interpolation. This particular implementation has a proven low error count [212], [213].

5.2.4 Comparison with Phased Synthetic Aperture Sequential Beamforming and Dynamic Receive Focusing

We will compare our method with Phased Synthetic Aperture Sequential Beamforming (PSASB) method, an adaption of SASB for phased array imaging. This first stage of PSASB is the same as in our method, but in the second stage the image is beamformed using DAS [77], [78]. The delays for the contributing sources/receivers are calculated from the geometrical path length to the image point. The scan lines that contribute to an image point are selected based on the opening angle. For the comparison we use the implementation for phased array data as used by Bera *et al.* [78]. The contributions of each scan line are weighted using two different windows:

- PSASB 1: a boxcar window, i.e. no weighting of contributing lines.
- PSASB 2: a Hann window, as is done in literature [78].

By using an equal weight for all first stage scan lines in the second stage the lateral resolution will be better as effectively a larger virtual aperture size is used compared to the case where the outer lines have a lower weight. However, the sidelobe level is higher [203], which might appear in the final image as artefacts.

We will also compare our method with Dynamic Receive Focusing (DRF) as SASB is often compared with this method in literature [77], [78].

5.2.5 Beamwidth and lateral resolution

One of the quality criteria of an ultrasound imaging system is the lateral resolution, which is often defined as the full-width-at-half-maximum (FWHM) or −6 dB width of the pulse-echo point spread function. In most literature, the theoretical beam width is calculated for continuous waves at the centre frequency of the pulse and in the far field approximation. In case broad-band pulses and apodization are used, the PSF width differs significantly from that theoretical value. To correctly account for the broad-band pulse and apodization the far field theoretical beamwidth is determined using the Fraunhofer approximation of the Rayleigh-Sommerfeld integral. A more detailed explanation of how the beamwidth is calculated can be found in the appendix.

5.3 Methods and Materials

5.3.1 Experimental setup

Experiments were conducted to investigate the performance of our technique. We used a phased array transducer (ATL P4-1, Phillips Ultrasound, Bothel, Washington, USA) connected to a Verasonics Vantage system (Verasonics Inc., Kirkland, Washington, USA). The system was programmed for a phased array scan with 256 scan lines in a 90° arc, which gives a line density that is more than sufficient according to (5.18). The received data of each element was filtered using a fourth-order Butterworth bandpass filter with −6 dB cut-off points at 1 and 4 MHz, and stored for further processing. This data is used as basis for all imaging methods.

Two different phantoms have been used in the measurements: a phantom with thin copper wires in a water bin and a tissue mimicking phantom. The wire phantom is custom built from two boards with holes, between which thin copper wires with a diameter of

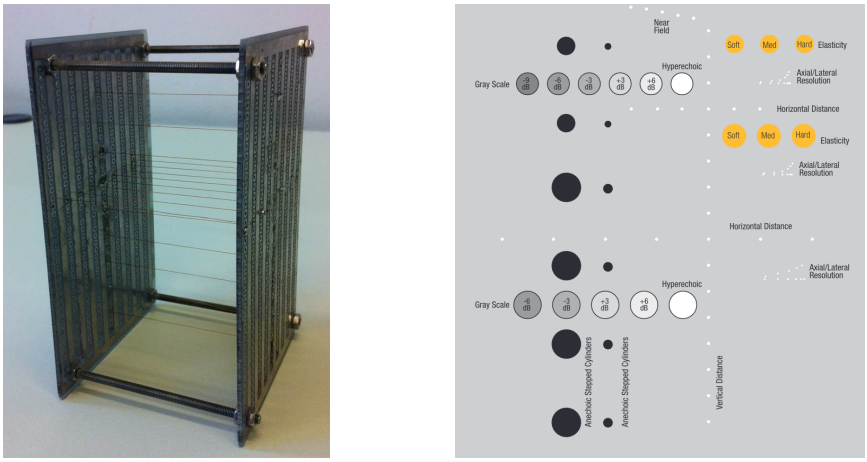

(a) (b)

Figure 5.2: (a) The phantom with copper wires and (b) the layout of the tissue phantom.

120 µm are attached as line scatterers, as shown in Figure 5.2a. The vertical distance between the wires is about 10 mm and the horizontal distance about 8 mm. Other experiments are performed on a commercial tissue mimicking phantom (040-GSE, CIRS, Norfolk, Virginia, USA) with nylon wires and cysts with varying scattering properties. For the measurements on both phantoms, a Hamming window apodization was applied in both transmission and reception for all methods. The experimental settings are summarized in Table 5.1.

For the first stage beamforming a straightforward single focus delay-and-sum (DAS) algorithm was used. In order to avoid discretization errors, the time delays between the elements were applied as phase shifts in the frequency domain. The radial grid spacing for the two-stage beamforming methods was chosen to be 1/4 of the wavelength corresponding to the centre frequency, which is the same spacing as used for DRF. For DRF and the second stage of PSASB the data were first upsampled using Matlab's resample function from 10 to 100 MHz to avoid discretization errors. The greyscale images were made by first applying a time gain compensation such that the amplitudes of the central row of scatterers were close to 0 dB. After this the envelope of the time domain signal for each radial image line is calculated. Finally, the amplitude is log compressed and displayed on a Cartesian grid.

5.3.2 Simulations

Simulations have been performed using FieldII [113], [114] only for the wire phantom. To obtain results similar to the measurements, the pulse-echo response of one central element of the probe has been measured and used as excitation pulse in the simulations. The data has been simulated with a sampling rate of 100 MHz, but before further processing the data was downsampled to 10 MHz. After this, the data were processed equally to the measurement data.

Table 5.1: Parameters used in the experiments.

	Parameter	Value
Transducer	Center frequency	2.5 MHz
	Number of elements	96
	Pitch	295 µm
	Element width	245 µm
Scan settings	Excitation	1 cycle with equalization
	Apodization	Hamming
	Sampling frequency	10 MHz
	Number of scanlines	256
	Scan angle	±45°
	Focal depth	30 mm
Wire phantom	Wire material	Copper
	Wire diameter	120 µm
	Medium speed of sound	1487 m/s
	Medium attenuation	Negligible
Tissue phantom	Model	CIRS 040GSE
	Imaging depth	170 mm
	Medium attenuation	0.5 dB/(MHz cm)

5.3.3 Measures of image quality

The quality of the images was evaluated on the basis of the −6 dB lateral PSF width and the contrast-to-noise-ratio (CNR). The lateral PSF width was determined from the vertical row of line scatterers in both phantoms. All data was linearly interpolated in the angular direction before determining the lateral width. The −6 dB lateral width is compared with the width obtained from the Rayleigh-Sommerfeld integral.

The effect of the f-number on the −6 dB lateral resolution was investigated for f-numbers between 0.25 and 4. The f-numbers were varied by changing the focal depth for a constant aperture. Measurements on the wire phantom with apodization were used for this evaluation.

The imaging performance for a anechoic cyst is evaluated using the CNR that is defined as [214]

$$\mathrm{CNR} = \frac{\left|\mu_s - \mu_c\right|}{\sqrt{(\sigma_s^2 + \sigma_c^2)}}, \tag{5.23}$$

in which μ_c and μ_s are the mean amplitudes in the cyst region and the speckle region before log compression, and σ_c and σ_s are the corresponding variances. These values are calculated for 2 anechoic cylinders of 6.7 mm diameter that are present in the tissue phantom at a depth of 15 and 45 mm and 4 cylinders of 10 mm diameter at depths of 70, 100, 130 and 160 mm. The background region is chosen to be a ring around the cyst with the same area as the region where the cyst statistics are calculated. This ensures that for the calculation of the statistics approximately the same amount of points are used for the cyst and background region. The edges of the cysts are excluded from the calculation so

that changes in resolution do not affect the contrast [215]. Here we used 0.6 or 0.8 of the cyst diameter for the small and large cysts respectively as statistics region. To limit the effect of probe placement and the exact areas that are used to calculate the CNR, eleven measurements have been done on the same cysts and the calculated CNRs have been averaged. Between the measurements the probe was shifted or rotated.

5.4 Results

5.4.1 Wire phantom

Figure 5.3 shows the images obtained with the four methods using simulation data. The wires appear at the same position in each image, but the lateral width differs between the images. With DRF the largest lateral width is obtained, while PAM and PSASB 1 appear to obtain the smallest lateral width. There is however a distinct difference between PAM and PSASB 1. In the image of PSASB 1 artefacts appear around the point scatterers that become wider further away from the focus. The artefacts are at a level of about −35 dB compared to the point scatterers. The artefacts vanish with PSASB 2, which in contrast to PSASB 1 applies a Hann window before summation. The remaining artefacts are at a level of −55 dB or lower, which is 20 dB lower compared to the artefacts that appear in the image made with PSASB 1. The cost of the reduction in artefacts is a worse lateral resolution. With PAM the lateral resolution is as good as in the image obtained with PSASB 1, but without any extra artefacts as compared to PSASB 2. This indicates a clear advantage of using the wave equation over a time of flight approach as with the wave equation there is no trade-off between artefacts and resolution.

The differences between the methods as discussed before can also be observed in the measurement images visible in Figure 5.4. The main difference with the simulated images is the appearance of extra artefacts. For example, there are reverberations visible below the wires. However, these extra artefacts appear in all measurement images and are therefore caused by the measurement setup and not by the different imaging methods.

The −6 dB lateral PSF width of the previously discussed images is shown in Figure 5.5. This figure also shows that the simulation and measurement results correspond very well to each other. Moreover, it is also visible that PAM and PSASB 1 obtain the best lateral resolution over the whole depth range. Compared to PSASB 2, the lateral width is on average 17% smaller while the difference with DRF is on average even 31%. Only around the transmit focus, the lateral resolution of each method is similar as expected.

PSASB and PAM obtain a lateral width that increases linearly with depth, which was also observed for PSASB by Bera *et al.* [78]. This indicates a constant angular resolution over depth. The theoretical far field lateral width calculated using the method described in Appendix 5.A also shows a linearly increasing width. Furthermore, both PSASB 1 and PAM match the theoretical far field width. Because the theoretical width indicates a focus in transmit and receive, this shows that both PAM and PSASB 1 manage to completely focus the image at all depths.

The −20 dB PSF width, which is not shown, has the same trend as the −6 dB width. Around the transmit focus all methods perform similarly, but the best overall resolution is achieved by PSASB 1 and PAM.

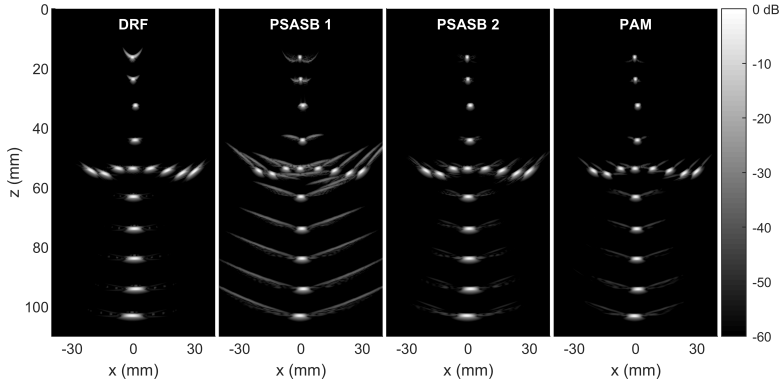

Figure 5.3: Simulation results for the wire phantom. The scatterers in the simulation were positioned at equal positions as in the measurement for best comparison.

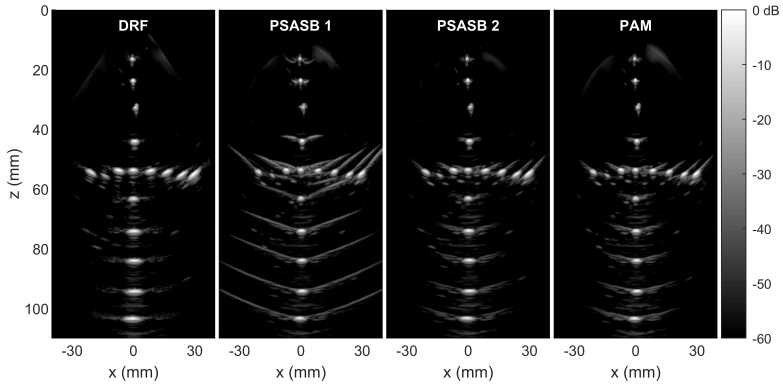

Figure 5.4: Measurement results for the wire phantom.

5.4.2 Tissue phantom

Figure 5.6 shows the result of the measurements on the tissue phantom. The different objects in the phantom are clearly visible in all the images, except for the deepest parts where noise starts to play a significant role. The artefacts that were visible in Figure 5.3 and 5.4 for PSASB 1 are now hidden beneath the speckle pattern.

The obtained lateral resolution is again the narrowest with PAM and PSASB 1. This can for example be observed at the lower left cyst and at the resolution wires, which appear on the right side at a depth of 60 mm and 100 mm. The resolution is quantified in Figure 5.7. On average the resolution obtained with PSASB 1 and PAM is 17% narrows than PSASB 2 and even 32% narrower than DRF, which is very similar to the values obtained in the wire phantom. For depths lower than approximately 120 mm the lateral resolution increases linearly with depth. Deep in the medium however the lateral resolution quickly deteriorates. There are two main causes. First of all, the signal-to-noise ratio in this area is low, which for example also results in the non-black appearing hypoechoic cyst in the lower

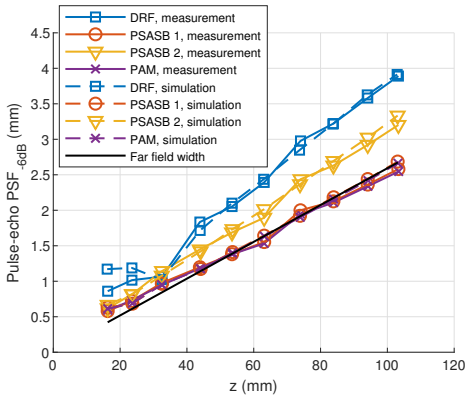

Figure 5.5: The −6 dB lateral width of the PSF for the wire phantom, corresponding to the images in Figures 5.3 and 5.4

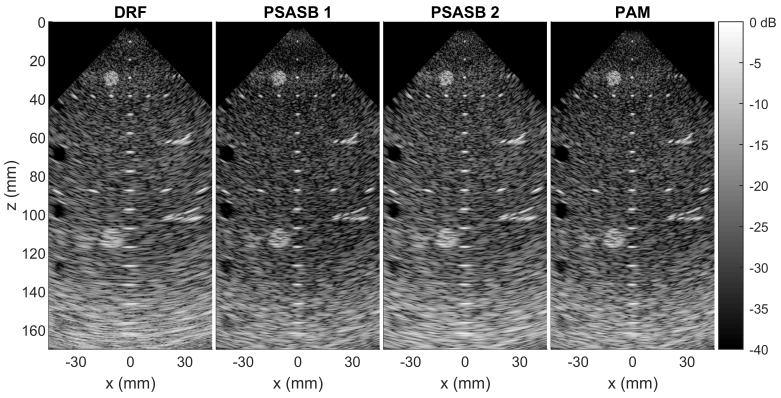

Figure 5.6: Measurement results for the tissue phantom.

left of Figure 5.6. Also, the attenuation lowers both the bandwidth and central frequency of the returned signal, and hence reduces the resolution.

5.4.3 Contrast-to-Noise Ratio

The contrast-to-noise ratio is calculated from two cysts with a diameter of 6.7 mm and four cysts of 10 mm. A subset of the cysts is shown in Figure 5.8, where the resulting image of one of the measurements used for calculating the CNR is shown together with the areas that are used to calculate the statistics of the cysts and background. The averaged CNR over all eleven measurements together with the standard error can be found in Figure 5.9. The CNR obtained with each method decreases with depth. For the two smaller cysts there is hardly any distinction between DRF, PSASB 2 and PAM, but PSASB 1 performs slightly worse. This is most likely caused by the artefacts visible in Figures 5.3 and 5.4. For the four deeper lying cysts, PSASB 1 continues to produce a systematically lower mean CNR compared to PSASB 2 and PAM due to these artefacts. Also for these four cysts, the

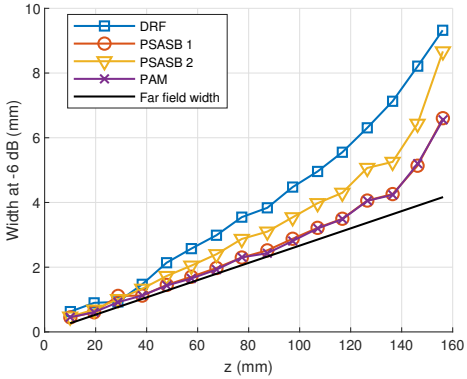

Figure 5.7: The −6 dB lateral width of the PSF for the tissue phantom, corresponding to the image in Figure 5.6

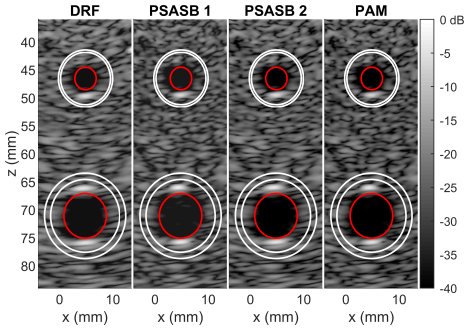

Figure 5.8: The images obtained with one of the measurements that has been used to calculate the CNR. The area within the red line is used for calculating the cyst statistics, while the area between the white lines is used as background.

mean CNR obtained with PAM is initially better, but the performance deteriorates with depth as compared to the other methods. It seems therefore that PAM suffers most from a low signal-to-noise ratio (SNR). The low SNR deep in the medium could be observed in Figure 5.6.

5.4.4 Variation of f-number

Figure 5.10 shows the lateral resolution that is obtained with PAM for different f-numbers in the first stage. For the smallest f-number the lateral resolution is worst, but for the larger f-numbers the width is always close to the theoretical far field width. While the opening angle decreases for increasing f-numbers, and therefore the number of contributing scan lines also decreases, the aperture of the virtual array at the focal depth increases. These effects cancel each other out and therefore the f-number has a limited effect on the lateral resolution. Only for very close focal distances this does not apply. The independence of the lateral resolution from the focal depth for large f-number can also be derived from (5.19) and (5.21). For a large focal distance, the opening angle can be approximated using

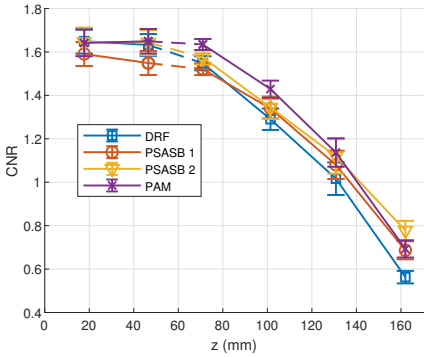

Figure 5.9: Mean CNR together with the standard error from the measurements on the anechoic cysts in the CIRS Phantom. The two shallowest cysts have a diameter of 6.7 mm, while the deepest four have a diameter of 10 mm.

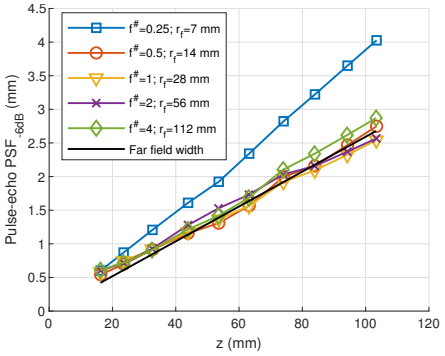

Figure 5.10: The obtained resolution in the wire phantom for different first stage f-numbers.

5

the first term of its Taylor series and this reduces (5.21) for an unsteered beam to

$$m_{\max}(f) = \frac{\pi f D}{\hat{c}}. \tag{5.24}$$

The above equation indicates that $m_{\max}$, and thus also the lateral resolution, becomes independent of the focal distance for large f-numbers.

For the current setup the results indicate that any f-number larger than 0.5 is sufficient to obtain the best possible resolution. This also applies to PSASB 1 and 2, which also show that the resolution is independent of f-numbers for large focal distances. The artefacts do however change for each two-stage method if the f-number changes. A focus near the probe result in more artefacts deep in the medium, while a deeper focus results in the opposite. Besides this, in setups where attenuation plays a significant role, the resolution deep in the medium might deteriorate due to the low SNR as could be observed in Figure 5.7. It might thus be necessary to tune the f-number for a specific situation, but the differences between DRF, PSASB and PAM do not disappear.

5.5 Discussion

In this paper we developed a computationally efficient two-stage beamforming method for phased arrays that reduces the required data flow using a simple front-end algorithm. In the second stage the scan data is further beamformed to obtain images that are synthetically focused over the entire image. Contrary to the time of flight approach in PSASB, we use a method based on the wave equation in the second stage.

The main advantage of Stolt migration for a linear array was the computation time reduction compared to SASB [79]. The computational efficiency of Stolt migration was achieved by a change of variables, after which all integrations could be evaluated using FFTs. For the method presented in this paper we also applied a change of variables, after which the algorithm also could be done using Fourier Transforms. The required frequency

domain interpolation was taken care of by the nonuniform Fourier Transform. In Table 5.2 a comparison is made between the number of operations required after pre-computation for PSASB, our migration algorithm which employs the FHT and the migration algorithm which calculates (5.14) using a matrix multiplication. Constant factors are neglected. In this table N_s is the number of depth samples, N_θ is the number of angles, N_m is the number of angular frequencies, J is the number of neighbours used in the NUFFT and S is the upsampling factor. When inserting regular values of $N_s = 1024$, $N_\theta = 256$, $N_m = 1024$, $S = 4$ and $J = 5$ the numbers in the rightmost column are obtained. First of all, it can be seen that using a NUFHT severely reduces the number of operations required compared to the matrix multiplication algorithm. The matrix multiplication scales with N_s^3, while the FHT approximately scales with $N_s \log(N_s)$. This reduces the total amount of operations by about four orders of magnitude.

The amount of memory required to store the pre-calculated values is also significantly lower for the FHT method. In both cases order N_m different matrices containing the pre-calculated Hankel functions have to be stored, but these matrices contain N_s^2 values in case of the matrix multiplication scheme is used and only $N_s \times S$ in case of the FHT algorithm. This means that about 256 times less memory is required for the FHT algorithm.

This amount of operations required for the migration algorithm presented is very similar to the amount required for PSASB. This similarity was also observed in the computation time of the Matlab implementations of PSASB and our migration algorithm. The time on an Intel I5-6500 (Intel Corp., Santa Clara, California, USA) for both algorithms was about half a second, but these times are of course strongly related to the program efficiency and measurement setup. It should be noted that it is possible to start building the final image in (P)SASB while the data is still being captured, while for PAM the forward transform over the angles can only be done after all first stage lines are made. Still, we believe that for both algorithms real-time implementation should be achievable. The difference in amount of operations between PSASB and PAM is smaller than between SASB and Stolt migration [79]. This is mainly because after pre-computation 2 NUFFTs required to compute the Hankel transform, while in Stolt migration there was only a single FFT required for the same kind of operation.

In the NUFHT the exponential grid depends on the parameters f_0, α and r_0, as can be seen in (5.15), and the upsampling factor S. The exact choice of parameters depends on both the signal bandwidth and the imaging depth. In our situation, the parameters are mainly determined by the imaging depths and in this case the following choice of the other parameters can be used: The parameter r_0 is set to the maximum imaging depth, while α is set such that the complete radial grid encompasses all imaging depths. The minimum frequency f_0 is then set such that the maximum frequency is twice the centre frequency. Finally, an upsampling factor of 4 is enough to prevent any visible artefacts.

The results that were obtained with the PAM match very well with the theoretical limit for the −6 dB PSF width, which represents focusing in both transmission and reception. This is visible in Figures 5.5 and 5.7. This implies that the entire image is completely focused in transmit and receive. Therefore, a better resolution cannot be obtained using conventional imaging techniques.

The resolution obtained with PSASB 1 also matches the theoretical limit, but there are additional artefacts in the image. These artefacts appear because PSASB just uses a

Table 5.2: The amount of operations required for the different algorithms. For PAM the amount required for the individual steps is also shown. The following values were used $N_s = 1024$, $N_\theta = 256$, $N_m = 1024$, $S = 4$ and $J = 5$.

Method	Operations	Amount
PSASB	$N_s N_\theta^2 S$	2.68×10^8
PAM - FHT		1.24×10^8
- 2D-FFT	$N_m N_s \log(N_m N_s)$	2.10×10^7
- FHT		9.23×10^7
* Division	$N_m N_s$	1.05×10^6
* NUFFT	$N_m(N_s \log(N_s) + JSN_s)$	3.15×10^7
* Multiplication	$N_m S N_s$	4.19×10^6
* NUFFT	$N_m(SN_s \log(SN_s) + JN_s)$	5.56×10^7
- Inverse FFT	$N_s N_m \log(N_m)$	1.05×10^7
PAM - Matrix multiplication		1.10×10^{12}
- 2D-FFT	$N_m N_s \log(N_m N_s)$	2.10×10^7
- Matrix multiplication	$N_m N_s^3$	1.10×10^{12}
- Inverse FFT	$N_s N_m \log(N_m)$	1.05×10^7

simple time of flight approach to calculate the delays for each contributing scanline before summation. In case there is a high amplitude scatterer present and nothing else, there is nothing preventing the scatterer to appear on every neighbouring image line. This is clearly visible in Figures 5.3 and 5.4. In the tissue phantom these artefacts are not visible, but it does seem to result in a lower CNR. To prevent these artefacts, PSASB 2 weighs the scanlines before summation. This does however negatively affect the lateral resolution. PAM does not have this trade-off between artefacts and resolution. The wave equation does not only take into account the geometrical travel times of the wavefront, but it applies different complex weighing factors to all the wave components in the wavenumber-frequency domain. As a result, the field that is scattered by each point is approximated as close as physics allows. The effect of this is that the artefacts do not appear and that the lateral resolution is at the theoretical limit. This clearly shows the advantage of using the wave equation over a time-of-flight approach.

To account for the limited opening angle of the virtual sources/receivers we have employed a filter based on (5.20), which gives the highest expected angular frequency m for a certain frequency f. The filter mainly affected the CNR. Without the filter, the mean CNR obtained with PAM was lower at all cysts with the largest difference obtained at the deepest two cysts. Without the filter the mean CNR was equal to mean CNR obtained with DRF at these two cysts, which is worse than PSASB 1 and 2. In the images the effect of the filter was most easily observed in low SNR conditions. For example, deep in the tissue phantom a white noise pattern could be observed in the images without the filter. In the wire phantom no visible difference was observed with and without the filter. The lateral resolution was not affected at all, showing that the improvement in lateral resolution is not due to the applied filter.

Equation (5.18) gives a criterion for the angle between subsequent scanlines to avoid aliasing. This criterion shows that at least 205 scanlines within a 90° sector are required.

In practice, some aliasing for the highest frequencies may be acceptable, especially when apodization is applied in transmit and receive. Apodization dampens the edges of the beamprofile, which give rise to the highest spatial frequencies in the angular direction. This corresponds to the effect that apodization leads to a broader PSF. It turns out that even with half the line density that was used for the images in this paper (i.e. 128 lines within a 90° sector), there were still no additional artefacts visible above −60 dB in the experimental images (not shown) of the wire phantom and tissue phantom. This shows in this case that at least a 65% higher framerate is possible than follows from the criterion. Note that the discussion in this paragraph also applies to PSASB.

In principle our algorithm could be extended from 2D to 3D, that is from a circular geometry to a cylindrical or spherical one. The derivation for the cylindrical geometry can for example be found in the paper by Skjelvareid *et al.* [202]. However, a large field-of-view without aliasing artefacts will result in a very low frame rate. This indicates that two stage beamforming methods using focused beams in 3D may not be suitable for real-time imaging.

5.6 Conclusion

In this paper we have developed a computationally efficient two stage beamforming method for phased arrays that is based on the wave equation. In the first stage a simple single focus DAS is used that reduces the amount of data from channel to scanline data. The second is based on the wave equation and is computationally efficient due to the application of the fast Hankel transform. Compared to PSASB in both simulations and measurements, our method requires a similar amount of operations to construct the image and does not have a trade-off between resolution and artefacts. These results show the advantage of using the wave equation in the second stage instead of a time of flight method in a two-stage approach.

Appendix

5.A Theoretical far field beamwidth

The pressure generated by an array can be calculated using the Rayleigh-Sommerfeld integral. In the far field it turns out that the pressure as function of the angle θ is proportional to [2, eq. 7.6, 7.9]

$$\hat{p}(\theta, f) \sim if\hat{v}(f)\,\mathrm{sinc}\left(\frac{fW\sin(\theta)}{c}\right)\sum_{m=1}^{N} a_m e^{im\Delta\phi} e^{\frac{2\pi i f x_m}{c}\sin\theta}. \tag{5.25}$$

In this equation $\hat{v}(f)$ is temporal Fourier transform of the normal velocity, W is the width of an element, a_m describes the apodization and $\Delta\phi$ is the change in phase for successive elements. The constants of proportionality and the dependence on r have been neglected as we are interested in the beam profile only. To calculate the beam directivity for an arbitrary excitation pulse, first $\hat{v}(f)$ is determined by taking the temporal Fourier transform of the pulse. Next, the above equation is evaluated for a dense grid of frequencies within the pulse bandwidth. After that, the calculated field is transformed back to the time domain and the maximum value of the envelope is taken as pressure amplitude. From the pressure amplitude the angular −3 dB width can be determined, which is equal to the pulse-echo −6 dB width. Finally, the angular width can be converted to the lateral width by using trigonometry.

6

Receive/Transmit Aperture Selection for 3D Ultrasound Imaging with a 2D Matrix Transducer

Recently, we realized a prototype matrix transducer consisting of 48 rows of 80 elements on top of a tiled set of Application Specific Integrated Circuits (ASICs) implementing a row-level control connecting one transmit/receive channel to an arbitrary subset of elements per row. A fully sampled array data acquisition is implemented by a column-by-column (CBC) imaging scheme (80 transmit-receive shots) which achieves 250 volumes/second (V/s) at a pulse repetition frequency of 20 kHz. However, for several clinical applications such as carotid pulse wave imaging (CPWI) 1000 V/s are needed. This allows only 20 transmit-receive shots per 3D image. In this study, we propose a shifting aperture scheme and investigate the effects of receive/transmit aperture size and aperture shifting step in the elevation direction. An angular weighting method is used to suppress the grating lobes caused by the enlargement of the effective elevation pitch of the array. The effective aperture size, level of grating lobes, and resolution/sidelobes are used to select suitable reception/transmission parameters. Based on our assessment, the proposed imaging sequence is a full aperture transmission, a receive aperture size of 5 and an aperture shifting step of 3. Numerical results show that, compared to the fully sampled array, the 1000 V/s is achieved at the expense of, on average, about two times wider point spread function and 4 dB higher clutter level. The resulting grating lobes were at −27 dB. The proposed imaging sequence can be used for carotid pulse wave imaging to generate an informative 3D arterial stiffness map, for cardiovascular disease assessment.

This chapter has been published as:
M. Mozaffarzadeh, M. Soozande, **F. Fool**, M. A. P. Pertijs, H. J. Vos, M. D. Verweij, J. G. Bosch, and N. de Jong, "Receive/Transmit Aperture Selection for 3D Ultrasound Imaging with a 2D Matrix Transducer," *Applied Sciences*, 2020, DOI: 10.3390/app10155300

6.1 Introduction

Arteriosclerosis is a very common cause of death worldwide, caused by deposition of lipids in the vessel wall in the form of plaques [216]. The relation between arterial stiffness and cardiovascular risk has been investigated in several studies as advanced arteriosclerosis can occlude arteries and involve changes of the vessel wall that reduce its elasticity and flexibility [217]–[219]. Estimation of the arterial stiffness would be of significant interest because it provides valuable information for diagnosis, prognosis, and therapy of a patient [48]. Among all the methods to quantify arterial stiffness, the European Society of Cardiology has recommended to use the carotid-femoral pulse wave velocity (PWV) as a favored measure of aortic stiffness [48]. However, this is a global measure of arterial stiffness, in which local plaque stiffness plays no role. Assessment of arterial stiffness by imaging the local propagation of pulse waves can identify plaque characteristics, especially in the carotid arteries [90], [220], [221], which are prone to plaque development associated with stroke [222].

Pulse wave imaging (PWI) is usually conducted based on two-dimensional (2D) images of the pulse wave propagation [223]–[225]. However, it is a 3D phenomenon, and elasticity of the carotid artery varies in different locations [56], [220]. Consequently, 2D images impose limitations. First, 2D elastography is sensitive to out-of-plane motion of the object, which can occur in carotid imaging [57]. Moreover, with conventional 2D ultrasound imaging, it is assumed that the propagation of the pulse wave is parallel to the imaging plane, which results in inaccuracies in PWV estimation [56]. A 3D assessment could be based on multiple cross-sectional 2D images of the 3D vessel structure, but it requires reproduction of the same imaging planes at later times, which is difficult [52]. Thus, it would be of great importance to have a comprehensive view of the arterial walls and generate a 3D elasticity map [56].

Going from 2D to 3D ultrasound imaging is challenging, and specific limitations are imposed, depending on the application [49], [55]. One approach is to mechanically sweep the conventional one-dimensional (1D) linear or phased array probes (used in 2D imaging) by a motorized system to acquire a 3D dataset [58], [226], [227]. With this approach, a low volume rate along with large errors due to motion artifacts is obtained. Free-hand scanning techniques, in which a position and orientation sensor is added to the conventional 1D array transducer to record the trajectory and orientation, can be used to address the motion artifacts [58], [228], [229]. Still, a poor out-of-plane spatial resolution and a low volume rate limit the use of the mechanical scanning approach for applications such as echocardiography, where motion needs to be accurately tracked [52].

Another approach for 3D imaging is to make a 2D matrix array [230]. With a 2D array, the transducer can remain stationary, and electronic scanning can be used to sweep the ultrasound beam over the entire volume under examination [52], which can overcome the frame rate limitation. However, the fabrication and implementation of 2D matrix transducers are challenging. A large 2D transducer is required to obtain a high elevation and azimuth resolution. On the other hand, the element pitch should preferably be kept below half a wavelength (λ) in both directions to avoid grating lobes [1]. The combination of small elements and a large aperture results in a very large number of transducer elements. It is fairly possible to make a matrix array with >1000 elements, but making electrical connections to all the elements is challenging [60].

To realize a fully populated matrix transducer that uses a reduced number of channels, different approaches have been proposed. The signals from the elements in an aperture can be locally beamformed to obtain one output receive signal [74], [144], [231], [232]. With the row-column addressed arra y approach, the number of channels required is reduced from N^2 to 2N, where N is the number of elements in each direction of a square matrix array, at the cost of image contrast and resolution [65], [67], [233]. Channel multiplexing is another approach to combine the data from several receive elements into one output line, at the cost of frame rate reduction [70].

We previously designed and manufactured a matrix transducer by fabricating an array of piezoelectric elements directly on top of an Application Specific Integrated Circuit (ASIC) [71]. A single tile of 12 × 40 (rows × columns) elements was developed as a building block for a larger transducer. The ASIC provides element-level switches and control logic which allow us to connect each individual element in a row (elevation direction) to a corresponding row-level transmit/receive bus. In this study, we use a 4 × 2 tiles configuration to form a large transducer consisting of 48 × 80 (azimuth × elevation) elements. Based on the transducer architecture, 80 transmit/receive shots are required to fully read out the element data for a single plane wave imaging. Considering a pulse repetition frequency (PRF) of 20 kHz (for a depth of 37.5 mm deep enough for carotid PWI (CPWI) [90]), a volume rate of 250 per second can be achieved. However, for CPWI, 1000 V/s are needed [88]–[90]. Therefore, we are obligated to limit the number of receive/transmit shots to 20. To do so, in this paper, we propose to interconnect elements into non-delayed apertures which can be shifted in the elevation direction. We investigate the effects of receive and transmit aperture sizes and aperture shifting step in numerical simulations and in an in vitro experimental setup. An angular weighting (AW) method (based on the directivity pattern of the receive apertures) is used in the image reconstruction procedure to reduce the effects of grating lobes (caused by the increased effective pitch in elevation direction). The goal is to find a trade-off to form good-quality B-mode images, providing suitable inputs for motion estimation methods used in wall velocity measurement [56], [90].

6.2 Materials and Methods

6.2.1 Imaging Schemes

For CPWI, the lateral direction in our 2D assessment (the elevation direction in 3D imaging) lies perpendicular to the carotid artery. For people of age over 60 years, the carotid diameter is 7.4 ± 0.7 mm and 8.2 ± 0.8 mm and over 70, it is 7.6 ± 0.8 mm and 8.0 ± 0.7 mm, for females and males, respectively [234]. The effective covered aperture size is calculated as (Nr + 19Ns) × Pitch, where Nr is the receive aperture size, Ns is the shift of the receiving aperture between sequential shots, and Nt is transmit aperture size. With Ns 1 and 2 and with a small Nr, the obtained effective aperture is much less than what is needed to cover the whole carotid artery. As we aim to have an effective covered aperture size big enough for all ages, we neglect Ns of 1 and 2 in our study.

A tile of 12 × 40 elements (rows × columns) requires 12 channels for transmission and 12 channels for data reception (Figure 6.1a). The row-level circuitry allows us to put two tiles head-to-head in a row to form an array of 12 × 80 elements without increasing the channel count [70]. In this study, the array is fabricated using 4 × 2 (rows × columns) tiles

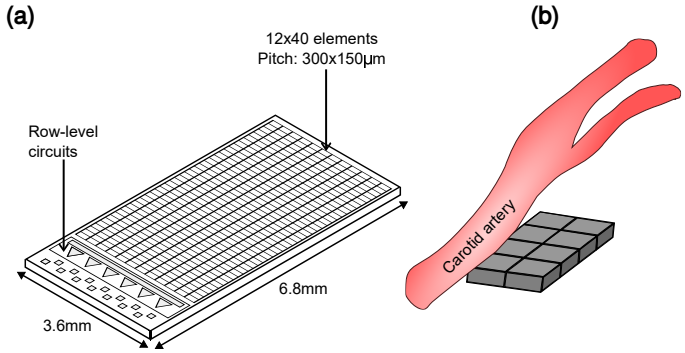

Figure 6.1: (a) Schematic of a single tile consisting of 12 × 40 acoustic elements on top of an Application Specific Integrated Circuit (ASIC) with element-level switches and row-level circuits. (b) The proposed transducer consisting of 4 × 2 tiles with respect to the carotid artery (carotid has a diameter of 6 to 9 mm; the array is 12 mm × 14 mm).

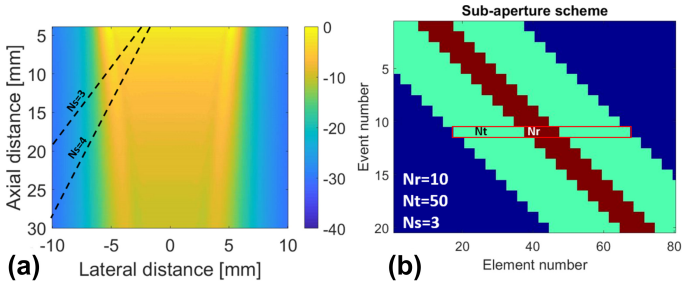

Figure 6.2: (a) The generated pressure field with a full transmission approach (all the elements are excited together); the dashed lines show the direction of grating lobes with different Ns. (b) A schematic of the aperture definition procedure; Ns=3, Nr=10, and Nt=50. Receive and transmit apertures have the same center.

providing 48 × 80 (azimuth × elevation) elements (Figure 6.1b; the carotid has a diameter of 6 to 9 mm [234]; the array is 14 mm × 12 mm). A single plane wave imaging with full data acquisition can be implemented using a column-by-column (CBC) data acquisition approach which requires 80 transmit/receive shots. In this approach, all the 80 elements are connected to the transmit bus, and only a single element in the elevation direction is connected to the receive bus. For CPWI, we need 1000 V/s which restricts the number of transmit-receive shots to 20 for one volume. These 20 shots can be implemented in different manners; an example is shown in Figure 6.2b where the transmit aperture of 50 elements is shifted over three elements for each step, co-aligned with the receive aperture of 10 elements.

Applying dynamic focusing to the received data having an effective element pitch larger than half of a wave length introduces grating lobes [1]. In our study, the 2D matrix transducer has an elevation pitch of 150 μm, and the operating frequency ranges from 6 to 9 MHz, i.e., the shortest wavelength is 170 μm in tissue. Therefore, grating lobes in the elevation direction will appear.

The current ASIC architecture can accommodate 20 arbitrary transmit/receive patterns in the provided memories, which can be used to define sparse patterns (out of the scope of this paper) [71]. In addition to these element level memories, elements can be grouped into a set of transmit/receive apertures with an arbitrary size and shifted along elevation direction with one element per clock cycle [71]. In this study, we use this feature to define regular aperture patterns (see Figure 6.1b for example). The elements contributing in a receive aperture are interconnected (switched in parallel without further inter-element delays) in practice, and one time series is achieved for the receive aperture.

6.2.2 Numerical Studies on the Beam Profile

As element interconnection only happens in the elevation direction, our numerical evaluation was only conducted in the elevation direction. Simulations were conducted in Field II [113], [114] to investigate the beam profile of the different transmit/receive sequences. The image reconstruction in azimuthal direction is unaffected and therefore neglected. We varied the settings provided in Table 6.1.

Table 6.1: The variables used in the numerical study.

Parameter	Value
Number of Shots	20
Receive aperture (Nr)	1 to 20 elements
Element size	130 µm
Pitch	150 µm
Transmit aperture	1 to 80 elements
Shift between sequential shots of the receive aperture (Ns)	3 and 4 (unit is Pitch)
Transmit pulse length	1.5 cycles
Central frequency	7.5 MHz, λ =0.2 mm
Scatterer position	10, 15 and 20 mm
Speed of sound	1500 m/s
Sampling frequency	100 MHz

The impulse response consisted of a Gaussian-modulated sinusoidal waveform (central frequency of 7.5 MHz, bandwidth of 80%). Normalization and log-compression were used to form final images. The response of receive aperture size (Nr), the shift of the receiving aperture between sequential shots (Ns) and the transmit aperture size (Nt) were evaluated using point scatterers positioned at depths of 10, 15 and 20 mm, as we expect the carotid artery in this range [90]. Figure 6.2b illustrates the way that the Nr, Nt, and Ns parameters were defined and implemented in 20 transmit-receive shots. The receive and transmit apertures were concentric and shifted over the same distance.

The level of grating lobes, lateral width of point spread function (PSF) at −6 dB called full-width-half-maximum (FWHM) and level of sidelobes were used to evaluate the image quality as result of the different settings [90]. The finalized imaging sequence was evaluated with a numerical tissue mimicking phantom in which an anechoic cyst having a radius of 3 mm was positioned at the depth of 15 mm. The phantom contained scatterers from −15 to 15 mm in the lateral direction to visualize the off beam energy including the grating lobes.

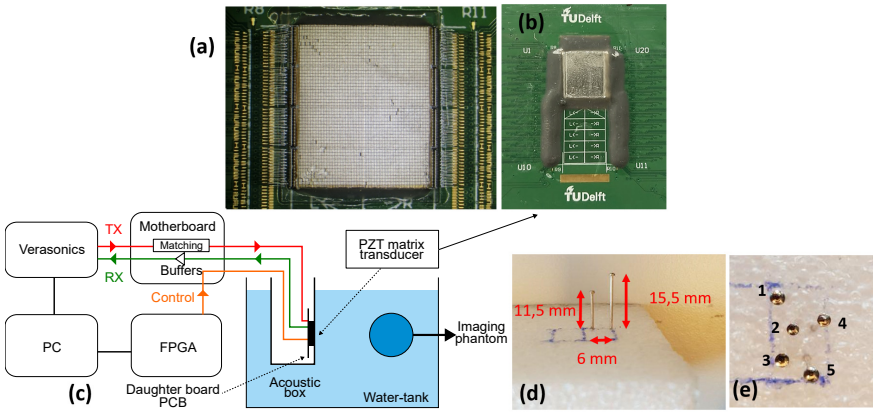

Figure 6.3: (a) The daughterboard with the transducer array before applying the ground foil. (b) The finalized 4 × 2 matrix array. (c) Schematic of the measurement setup. (d) The imaging phantom: a foam pad with two needles. The distance between the foam and the transducer surface is about 26 mm. (e) The imaging phantom: a foam pad with five needles, positioned in different depths (from 10 to 20 mm). The distance between the foam and the transducer surface is about 28 mm. The numbers next to the needles are used for target localization in Section 6.2.3.

6

Multi-scatterer and multi-cyst phantoms were also imaged. We use column-by-column imaging scheme as the ground truth (GT) in our study.

6.2.3 Experimental Study

The 2D matrix array was mounted in a box with an acoustically transparent window (25 µm thick polyimide) and the whole setup was submerged in a tank filled with water (see Figure 3a). The transducer was excited by a custom-programmed experimental ultrasound system (Vantage 256, Verasonics, Kirkland, WA, USA). A picture of the two-needle phantom used in our experiments is provided in Figure 3d. The axial distance between the plastic foam, that acts as base to the needles, and the surface of our 2D transducer was about 26 mm. Matlab 2018b and MeVisLab (MeVis Medical Solutions AG, Fraunhofer MEVIS, Bremen, Germany) software was used to process the data and show 3D images, respectively.

6.3 Results

6.3.1 Numerical Results: Point Scatterer

Receive Aperture

Figure 6.4a,b shows the PSF for varying receive aperture (Nr) between 1 and 20 elements and shifting steps (Ns) of 3 and 4. A full-aperture transmission (transmission with all the elements) is used (Nt=80) and 20 shots are given. For a receive aperture equal to one element (Nr=1) and step size of three elements (Ns=3), the total covered aperture is 8.7 mm resulting in a main beam width of about 2 mm at 10 mm distance. The grating lobe level is −20 dB as expected from the 1.5 cycle excitation and 20 shots and positioned at a lateral distance of −5 mm caused by the large step (Ns=3, effective pitch=450 µm, λ=200 µm). The mean beam width remains about the same for larger Nr up to 5 (see Figure 6.4e) since two

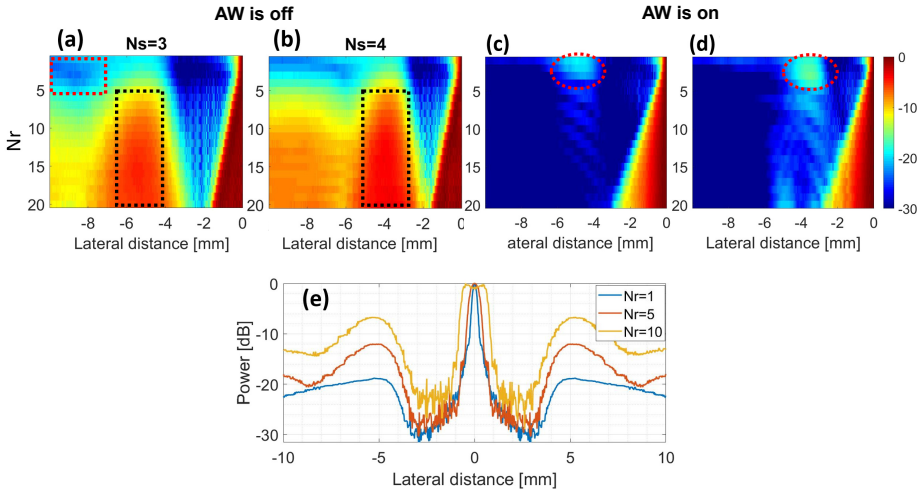

Figure 6.4: (a–d) The point spread functions (PSFs) obtained for different Nr and Ns when a full-aperture transmission is used. A point scatterer was positioned at the depth of 10 mm and the lateral distance of 0 mm. The angular weighting (AW) technique was used in the bottom row. The black and red rectangular regions were used to calculate the clutter level (Figure 6.5a) and effects of grating lobes (Figure 6.5b). The red circles show the effects of grating lobes. (e) The lateral variation for Ns=3 when the AW is on.

6

opposite effects play a role. The first one is the slowly increasing covered aperture (e.g., for Nr=5, the covered aperture is 9.3 mm). The opposite one is the increasing directivity of the receiving apertures (for Nr=5 the directivity is about 10°), which makes the contribution of the outer elements less. For larger receive apertures, Nr=10 the main beam width is increased to about 3 mm and it further increases to 4.2 mm for Nr=20. For Nr=20, the covered aperture is admittedly the largest, but very directive (2°), and therefore only the middle part of the covered aperture is contributing in image reconstruction. For Ns=4 (see Figure 6.4b), the grating becomes stronger, making the grating lobes appear closer to the mainlobe, at −4 mm lateral distance (see the rectangles in Figure 6.4a,b).

Since the effective aperture can be very large and directive, angular weighting, as described in [235], can be applied in reception. This results in reduced grating lobes (compare the first and second rows in Figure 6.4) and about 16 and 13 dB lower clutter level for Ns of 3 and 4, respectively (see Figure 6.5a where the pixel intensities within the red rectangular regions shown in Figure 6.4a were used for statistical analysis). The level of grating lobes (for different Nr) obtained with the AW technique is presented in Figure 6.5b. The AW technique hardly works for Nr of 1 up to 5 due to the large angular view of the receive aperture.

Figure 6.6 shows the FWHM as function of aperture settings. It indicates that the smaller the Nr, the lower the FWHM (i.e., better lateral resolution). This is mainly because we use the dynamic focusing technique in reception, and increment in Nr results in a narrower directivity in each receive aperture, which reduces the effective number of elements (i.e., aperture size) contributing in the reconstruction of a given pixel (voxel in 3D).

An analysis of Figure 6.4 and Figure 6.6 shows that the AW technique helps with suppression of the grating lobes at the expense of resolution. With an AW, a higher

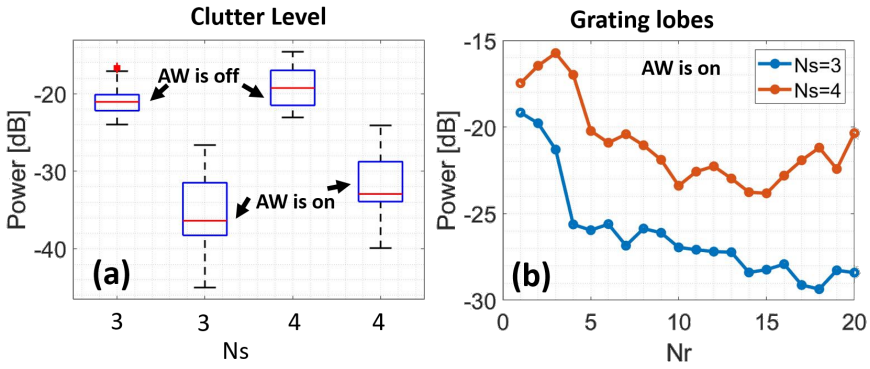

Figure 6.5: (a) Distribution of clutter level measured within the red rectangular region shown in Figure 6.4a. The same area was used in other images. On each box, the central mark indicates the median of the clutter level inside the corresponding region. The bottom and top edges of the box indicate the 25th and 75th percentiles, respectively. The whiskers extend to the most extreme data points not considered outliers. Outliers were plotted individually using the '+' symbol. (b) The level of grating lobes, measured within the black rectangular regions indicated in Figure 6.4.

6

contrast can be expected [235], helping the motion estimation methods used to estimate the wall velocities in CPWI [90]. Thus, we use AW technique in the reconstruction through rest of the paper.

As seen in Figure 6.4c,d, grating lobes are not well-suppressed for Nr=1 (see the red circles). For Ns=3, these effects reduce about 6 dB from Nr=1 to Nr=5 and then reduce with a lower rate along with oscillation (see Figure 6.4c and Figure 6.5b). Almost the same pattern happens for Ns=4 from Nr=1 to Nr=5. We also noticed the same trend happening at depths of 15 and 20 mm (depths of interest for CPWI [90])—results are not provided here. Based on the lower grating lobes for Ns=3 than Ns=4 (Figure 6.5b), the reduction of grating lobes from Nr of 1 to 5 for Ns=3 (Figure 6.5b), and the same resolution in Nr=5 for Ns of 3 and 4 (see zoomed version in Figure 6.6), we proceed with Ns=3 and Nr=5. It is true that Nr=5 increases the FWHM more than a smaller Nr (see Figure 6.6), but lower grating lobes are more beneficial/needed in CPWI than a higher resolution due to motion estimation algorithms used in CPWI [56], [90]. Although even lower grating lobes can be achieved by a Nr larger than 5 (Figure 6.5b), the rate of FWHM increment is much larger than the rate of grating lobes decrement (see Figure 6.6) when Nr increases. It is expected to have 7 dB higher signal-to-noise ratio (SNR) with Nr=5 than Nr=1. Moreover, with Ns=3 and Nr=5, an effective covered aperture of 9.3 mm can be obtained, which is large enough to cover the carotid artery in all ages [234].

We conducted the same assessment for scatterers positioned at depths of 15 and 20 mm (results not shown). For different Ns, almost the same difference in the mean of the level of grating lobes (red lines in Figure 6.6a) is achieved. The same effects indicated by the red circles Figure 6.4c,d occur, but with lower power. Following the same procedure Ns=3 and Nr=5 can be selected for receive aperture in these depths as well.

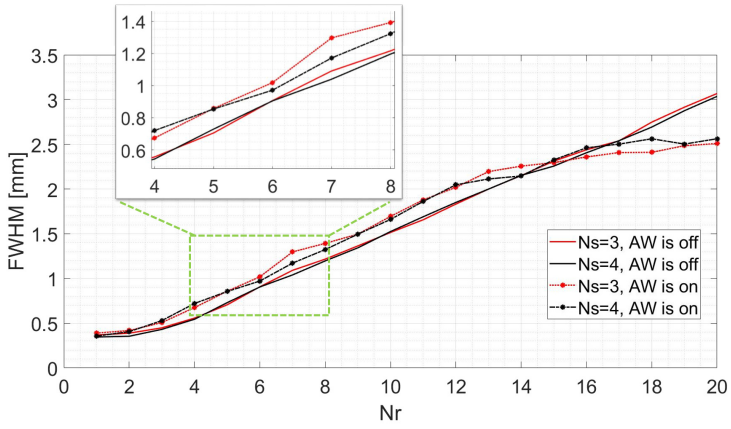

Figure 6.6: Full-width-half-maximum (FWHM) measurements for different Nr and Ns; a full-aperture transmission was used.

Transmit Aperture

So far, we used a full-aperture transmission. In this section, we evaluate the effects of the transmit aperture size (Nt) on the PSFs obtained with the selected reception parameters (Nr=5 and Ns=3). Figure 6.7a–c shows the PSFs obtained with different Nt while a scatterer is positioned at the depths of 10, 15, and 20 mm, respectively. A small Nt leads to strong artifacts caused by the grating lobes. This is due to the omnidirectional pressure field in transmission which causes excitation in the direction of the grating lobes with the same energy as that of main lobe. As the Nt gets larger, the transmission pressure field gets more directional toward the front side of the array and becomes like what is shown in Figure 6.2a. In higher depths, the effects of grating lobes are lower since a lower pressure is transmitted in the direction of the grating lobes (see Figure 6.2a).

The effects of grating lobes are lower when Nt is larger than 20 (see Figure 6.7a–c). From Nt of 1 to 50 the FWHM decreases, and reaches an asymptotic minimum for Nt larger than 50. However, around a Nt of 50, the effects of sidelobes are still more powerful than larger Nt (compare the regions shown by the red and green dashed rectangles in Figure 6.7a–c). Since the larger the Nt, the lower the effects of sidelobes, we proceed with a full-aperture transmission (Nt=80).

Lateral Shift Variance

In Figure 6.7d,e point scatterers positioned at the depths of 10 and 20 mm, respectively, are laterally shifted from −6.5 to 6.5 mm. This image is normalized to its maximum to fairly track the effects of grating lobes (see the green arrows)[236]. Figure 6.7d,e indicates that if a scatterer is positioned in the direction of the grating lobes, its effect is much lower than that of a scattering target in the middle of the array. This is mainly because of the AW technique in reception and the fact that the direct transmitted pressure field excites targets in the lateral center of the array with a higher power, compared to those in the grating lobes angles (see Figure 6.2a). The best resolution is also obtained when the scatterer is at the lateral center.

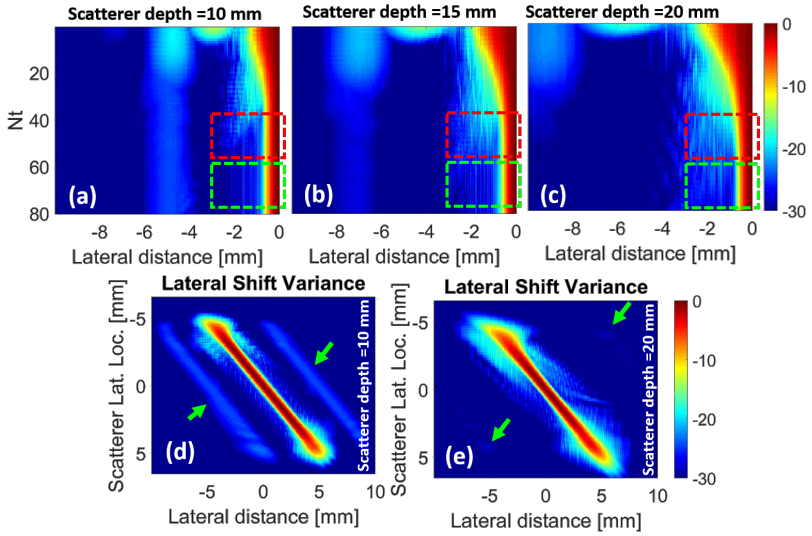

Figure 6.7: (a–c) The PSFs obtained for different Nt; Nr=5, Ns=3. The green rectangular regions show a reduction of sidelobes with respect to the red rectangles. (d,e) The lateral shift variance for full-aperture transmission, Nr=5 and Ns=3, for a scatter at a depth of (d) 10 mm and (e) 20 mm. Green arrows: location of grating lobes.

6

Comparison with Ground Truth

A comparison between the reconstructed images by the proposed imaging sequence (full-aperture transmission, Nr=5 and Ns=3) and the CBC imaging sequence (ground truth, GT) at three depths of interest is provided in Figure 6.8a,b, along with their corresponding PSFs in Figure 6.8c. The AW is applied to the GT to have a fair comparison. By the proposed imaging sequence, the FWHM is almost doubled due to the larger receiving aperture, and the mean clutter level, on average, is 4 dB higher than GT, with a level of grating lobes of about −24, −27, and −29 dB, at the depths of 10 mm, 15 mm, and 20 mm, respectively. See the Supplementary Materials (Figure 6.12) for the results obtained using the multi-scatterer phantom.

6.3.2 Numerical Results: Cysts Phantom

The results obtained with the cyst phantom are shown in Figure 6.9. The images are laterally limited due to the narrow transmission beam profile (see Figure 6.2a). The proposed scheme (Figure 6.9a) is more laterally limited because of the smaller effective aperture size than the CBC GT (Figure 6.9b). The red arrows in Figure 6.9a show the effects of grating lobes. To statistically compare these images, pixel intensities within two regions of interest (ROI1 and ROI2, the red and yellow circles in Figure 6.9b) are used. For the proposed imaging sequence, the mean of ROI1 is 6 dB higher than GT (see Figure 6.9c) due to the effects of the grating lobes and sidelobes (see Figure 6.8c). The 3 dB higher mean in ROI2 provided by the proposed imaging sequence (Figure 6.9c) is also due to the larger FWHM and more constructive interferences of the point scatterers. See the Supplementary Materials (Figure 6.13) for the results obtained using the multi-cyst phantom.

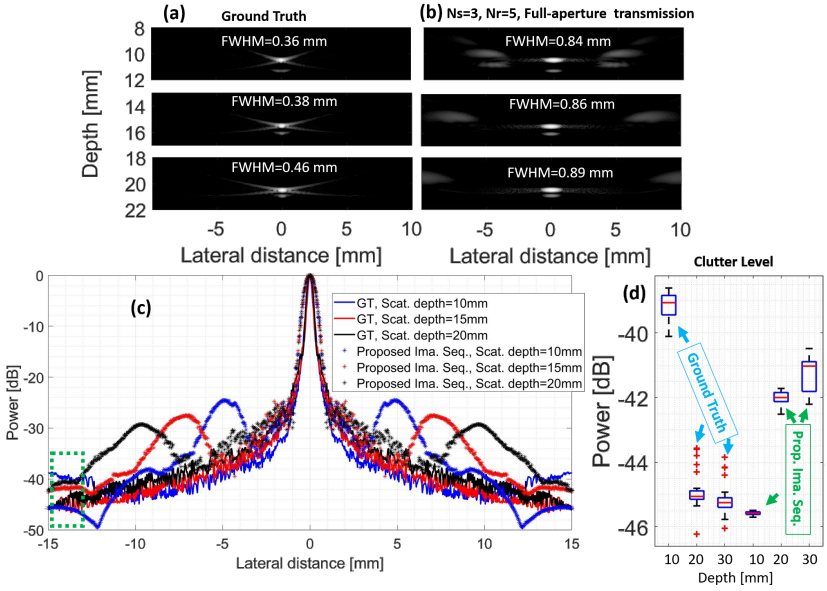

Figure 6.8: The reconstructed images using (a) the column-by-column (CBC) imaging sequence (ground truth—GT) and (b) the proposed imaging sequence (full-aperture transmission, Nr=5 and Ns=3), along with (c) their corresponding lateral variations. The AW is applied on the GT to have a fair comparison. (d) The clutter level using the green rectangular region in (c).

6.3.3 Experimental Results

Figure 6.10 presents the experimental results of the 3D reconstructed images using the GT and the proposed imaging sequence (full-aperture transmission, Nr=5 and Ns=3). The AW is applied on the GT to have a fair comparison. The red, yellow, green, and blue arrows show the foam, the two needles, the grating lobes, and the clutter in the azimuth direction, respectively. The smaller size of foam in Figure 6.10b,e is due to a smaller effective aperture size in the elevation direction. A better visualization on the needles is achieved in Figure 6.10e compared to Figure 6.10d due to the AW technique.

The maximum intensity projection (MIP) over a depth of 1 to 23 mm of the 3D experimental images obtained with the two-needle phantom is shown in Figure 6.11a–c. The difference (a) and (b) is the lack of AW in (b), which causes the grating lobes indicated by the yellow arrows to appear. The elevation FWHM obtained with the proposed imaging sequence at the depth of about 10 mm is doubled, in accordance with the results provided in Figure 6.8a,b. This is the reason that the targets look stretched in the elevation direction, as seen in Figure 6.11a and Figure 6.10b. The azimuth FWHM for different receive parameters stays the same (about 620 µm) as the proposed imaging sequence does not significantly affect the performance of the 2D transducer in the azimuth direction. The same clutter patterns for different Ns, but the same Nr, also prove this matter (see Figure 6.11d). The clutter level in azimuth direction is higher than elevation direction due to the larger pitch (300 µm) and lower number of elements (48).

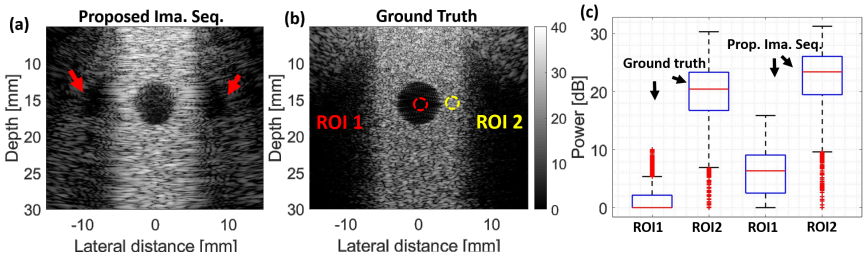

Figure 6.9: The reconstructed images using (a) the proposed imaging sequence (full-aperture transmission, Nr=5 and Ns=3) and (b) the CBC imaging sequence (GT). (c) Statistical analysis of the image intensities indicated by two regions of interest (ROI1 and ROI2) which are the red and yellow circles, respectively.

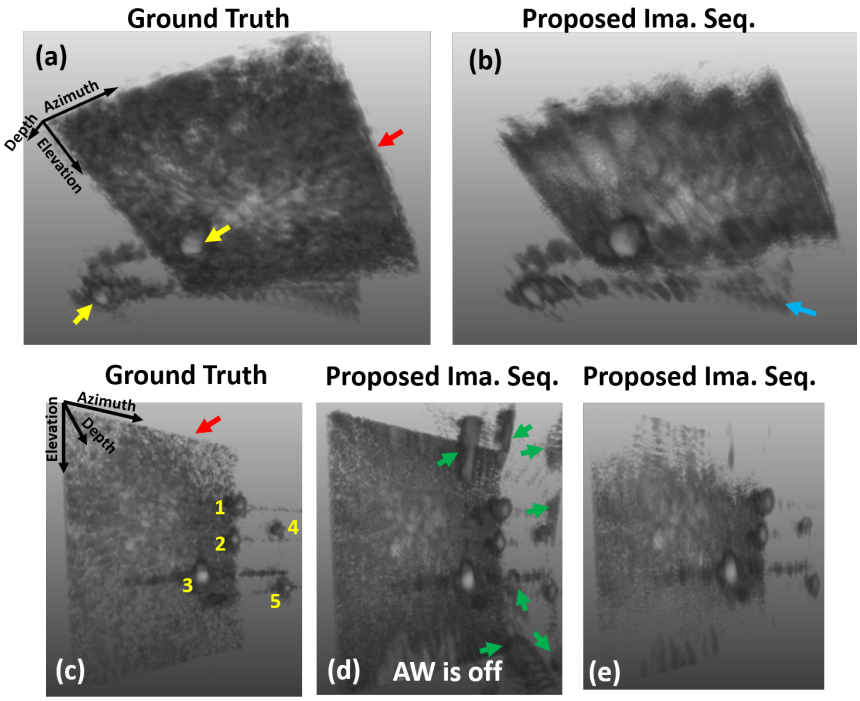

Figure 6.10: The 3D images obtained with (a,c) the CBC imaging sequence (GT) and (b,d,e) the proposed imaging sequence (full-aperture transmission, Nr=5 and Ns=3). The red, yellow, green, and blue arrows show the foam, the two needles, the grating lobes, and the clutter in the azimuth direction, respectively. The dynamic range was 40 dB. The numbers in (c) are related to those shown in Figure 6.3e.

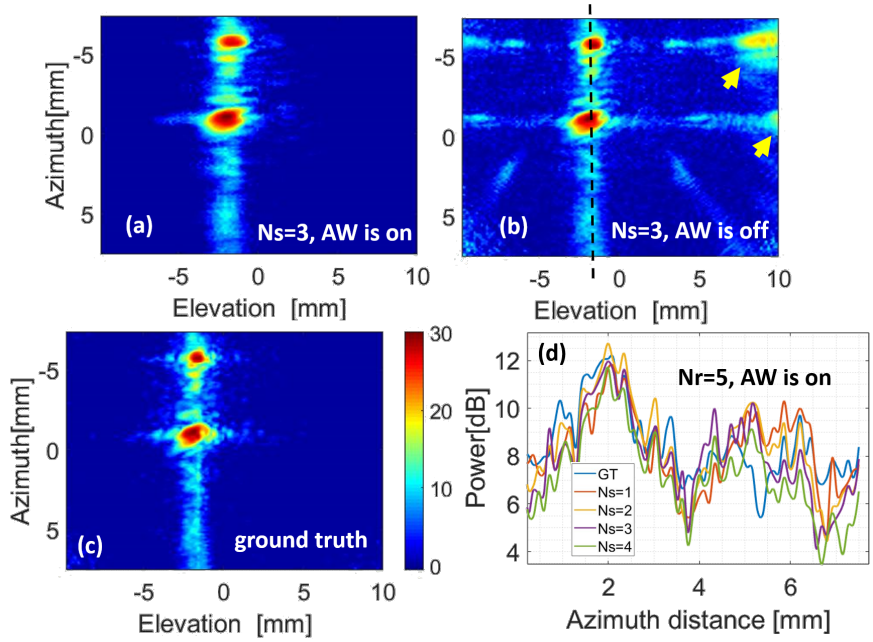

Figure 6.11: (a–c) The maximum intensity projection (MIP) of the reconstructed 3D images of Figure 6.10 using the data obtained with the two-needle phantom. (d) The clutter pattern in azimuth direction measured on the dashed black line in (b). The yellow arrows in (b) point to the grating lobes that appear if the AW is off.

6.4 Discussion

The aim of this study was to find a set of imaging parameters that provides a good image quality using an aperture-shifting matrix array, within the boundary condition of a limited number of transmissions (20), such that a volume frame rate of 1000 per second could be reached. We aimed for such high volume rate to facilitate CPWI (seeing the 4.5 m/s pulse wave pass laterally within a few volumes [90]). Depths of evaluation were 10, 15 and 20 mm as the anterior and posterior walls are expected at these depths [90]. The effects of receive aperture size (Nr), the aperture shifting distance per pitch (Ns), and transmit aperture size (Nt) were studied.

Improving the quality of B-mode images helps in CPWI as it facilitates the motion estimation algorithms to track the axial displacement of the arterial walls [56], [90]. This is essential for accurate local pulse wave velocity estimation required to generate an elasticity map. Our assessment and parameters selection priority were as follows: (1) the size of effective aperture; as it indicates whether we can have a comprehensive view on the carotid artery or not [234], (2) suppression of grating lobes; the lower the level of grating lobes, the higher the contrast, which is important for motion estimation algorithms to better estimate the axial displacement of carotid walls [90], and (3) resolution/sidelobes. Both Ns of 3 and 4 could provide sufficiently large effective aperture. Due to the lower grating lobes achieved with Ns=3, compared to Ns=4, Ns=3 was selected. Selection of Nr imposed a trade-off between FWHM and grating lobes. The rate of decrement of grating lobes and increment of FWHM in Ns=3 led to a Nr of 5. Almost the same trends happened in all the three depths of interest for CPWI [90], which led us to Ns=3 and Nr=5. The finalized imaging sequence, with a boundary condition of 20 transmit-receive shots, consists of a full-aperture transmission (Nt=80), Nr=5, Ns=3 and using the angular weighting (AW) technique in the image reconstruction procedure.

Signal-to-noise ratio (SNR) is also an important criterion in the performance of motion estimation techniques. However, it is not included in our study since in previous studies, an acceptable SNR in CPWI was achievable with both 1D or 2D arrays [56], [90], and it is expected that this is the case with our 2D matrix array as well [88]. If SNR is not good enough (either for CPWI or other applications which need the same effective aperture size) to perform a reliable motion estimation, a larger Nr can be used. However, it would cause a larger FWHM as a consequence of relatively more direct receive apertures and applying the dynamic focusing in reception. Therefore, in the case of using a large Nr (i.e., 20), a more sophisticated image reconstruction method, which takes the narrow directivity of a large Nr into account, should be used in the elevation direction to form a 3D volume [237].

The final version of our 2D transducer will have 10 tiles in the azimuth (row) direction and two tiles in the elevation (column) direction, making 120 × 80 (row × column) elements available to form a 3D image. Having an azimuth pitch of 300 µm, the size of our 2D transducer in azimuth direction will be 36 mm, thus providing an aperture size big enough to track the carotid pulse wave velocity (estimated to be around 4.5 m/s [90]). All the evaluations and decisions in this paper were conducted using static imaging phantoms while in CPWI, there are several types of motion, i.e., carotid wall movement caused by pulse wave propagation, overall movement by breathing, and patient/transducer movement. Motion of the object might lead to unwanted decorrelation of the signals recorded by the sequentially switched apertures, leading to lower image quality. To calculate the risk of

such decorrelation, we performed the following calculation. The wall velocity is, estimated from the interframe axial displacement, reported to be about 5 mm/s [56], [90]. Considering the 1 ms needed for data acquisition by the proposed imaging sequence for a 3D volume, the target moves 5 µm in the axial direction. In this scenario, the PSF obtained with a dynamic scatterer, moving 5 µm in 20 transmit-receive shots, well overlaps with a static scatterer, which is mainly because the motion is lower than 10% of the wavelength (200 µm) during the time needed to acquire the data of a 3D volume [238]. Therefore, we can assume that the coherent compounding from the 20 acquisitions is not negatively affected. In addition, the global movement is slow, will not interfere with the coherent image reconstruction, and can be removed by subtraction of displacement of the tissues and that of carotid artery [90].

With 20 kHz pulse repetition frequency, reflection artifacts come from depths higher than 37.5 mm. In this study, these reflection artifacts are ignored due to tissue attenuation (≈0.4 to 0.6 dB/(MHz cm)) as a scatterer at a higher depth (e.g., 50 mm) is attenuated by 28 dB compared to the reflection coming from 12 mm depth. A more advanced beamforming algorithm might be helpful with suppression of these artifacts as well [77], [239]–[241], taking the change of speckle patterns into account [242].

Finally, although the reported results are linked to the specifications of the matrix transducer reported in our previous publication (see [71]), we would like to stress that the procedure taken in this study to select receive/transmit parameters can be used for other array transducers (either 1D or 2D) to obtain a higher frame/volume rate at a given number of data acquisition channels.

As a future study, we will use the proposed imaging sequence to conduct clinical 3D carotid pulse wave imaging and generate 3D elasticity maps.

6.5 Conclusions

In this paper, we evaluated the effects of receive/transmit parameters on the image quality provided by a linear array in which elements are mutually interconnected, which mimics the elevation direction of our prototype 2D matrix transducer. The parameter selection procedure was based on the effective covered aperture size, level of grating lobes, and resolution/sidelobes. To achieve 1000 volumes/second, only 20 transmit-receive shots were available, considering a pulse repetition frequency of 20 kHz and imaging depth of 37.5 mm. To suppress the effects of grating lobes, an angular weighting technique was used. The proposed imaging sequence consisted of a full-aperture transmission (all 80 elements), receive aperture size of 5, and aperture shifting distance of three elements. For depths of 10 and 20 mm, the results show that, on average, about two times wider point spread function at −6 dB dB and marginally (4 dB) higher clutter level were obtained, compared to the ground truth, and grating lobes level of about −27 dB lower than the main lobe. Having a proper imaging sequence based on 1000 V/s could be beneficial to generate 3D maps of carotid artery stiffness, providing valuable information regarding the cardiovascular risk.

Appendix

6.A Supplementary Materials

Comparing the first and second rows of Figure 6.12 indicates that the AW technique increases the visibility of the scatterers in the region of interest (ROI: −5 to 5 mm in the lateral direction). Artifacts are reduced between the targets (compare Figure 6.12b and d) and a higher contrast is achieved (compare Figure 6.13c and Figure 6.13d) due to the lower sidelobes. The images generated with the proposed sequence get disturbed at the corners due to the lower number of apertures contributing in the reconstruction of those regions.

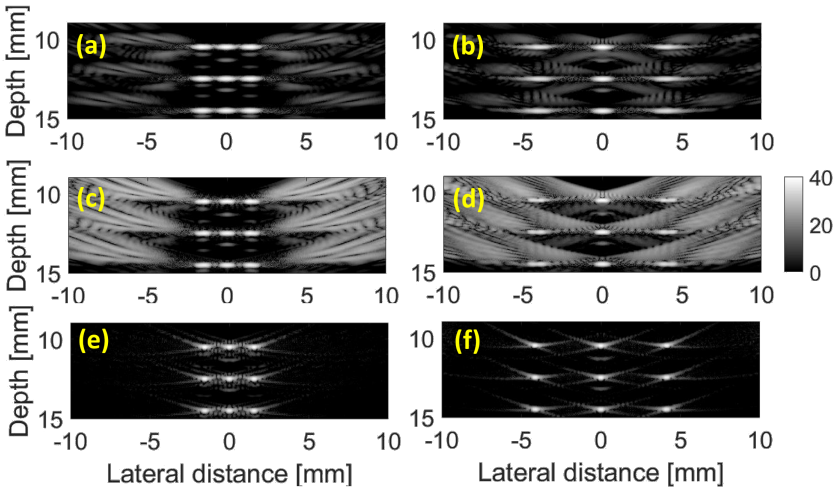

Figure 6.12: The reconstructed images using (a-d) the proposed imaging sequence (full-aperture transmission , Nr=5 and Ns=3), when the AW is (a,b) on and (c,d) off, and (e,f) CBC imaging sequence (GT). The scatterers have a lateral distance of 1.5mm and 4mm in first and second column, respectively.

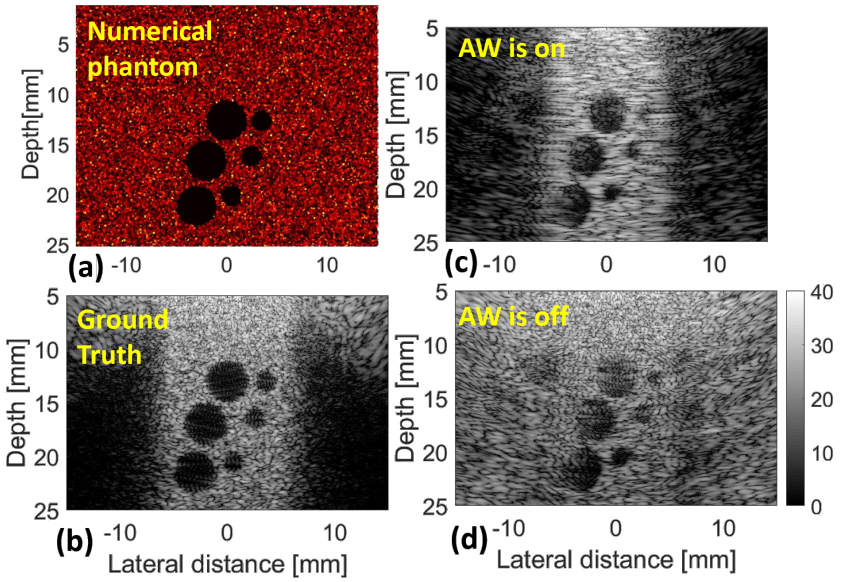

Figure 6.13: (a) The numerical phantom containing multiple cysts. The reconstructed images using (b) the CBC imaging sequence (GT), (c,d) the proposed imaging sequence (full-aperture transmission , Nr=5 and Ns=3) when the AW is on and off, respectively.

7

3D High-Frame-Rate Vector Flow Imaging with an Electronically Translatable Linear Array

This chapter is to be submitted as:
F. Fool, H. J. Vos, J. G. Bosch, N. de Jong, and M. D. Verweij, "3D High-Frame-Rate Vector Flow Imaging with an Electronically Translatable Linear Array,"

7.1 Introduction

Medical three-dimensional (3D) echography is superior to two-dimensional (2D) echography in various applications. For example, 3D echography reduces operator dependency, improves measurement accuracy, and increases repeatability when assessing anatomic structures, disease progression and therapy effectiveness [51], [52], [243]. These advantages have already been shown in the early 2000s in the analysis of carotid plaque volume [244], [245] and the degree of stenosis [246]. Combined with other measurements, the progression of atherosclerosis, the risk for complications and the response of the patient to an intervention can be measured [155], [156]. For these applications, a low frame rate is sufficient and 3D images can be made with mechanically swept linear array transducers or freehand scanning techniques, which both effectively stitch together 2D images to from a 3D image [51], [52].

There are applications where a low frame rate would be insufficient. Focusing on the carotid artery, applications that require high-frame-rate imaging include the measurement of arterial stiffness, blood haemodynamics and plaque surface motion. These three measurements can be used in the diagnosis of carotid artery conditions [48], [49]. Here, we focus on the measurement of blood flow. To quantify blood flow, vector flow imaging (VFI) can be used. A high frame rate is necessary as the peak blood velocity in the carotid artery can reach up to 125 cm/s in normal patients and in excess of 230 cm/s in patients with a significant degree of stenosis [49], [247]. For accurate blood flow measurements in the carotid artery, 3D measurements are beneficial for two main reasons. First, helical flow patterns are present around the carotid bifurcation [53] and therefore the velocity would always have an out-of-plane component with 2D measurements. Since out-of-plane motion cannot be accurately measured, it may lead to inaccurate and inconsistent velocity estimations [54], [55]. Second, with 3D measurements the estimation of volume flow does not require any assumptions about the flow profile, such as the velocity profile and the beam-to-flow angle. Failure to correctly estimate these parameters can introduce a significant bias [248]–[250]. 3D high-frame-rate measurements would thus be beneficial in the diagnosis of carotid artery condition.

To achieve high-frame-rate 3D measurements, the use of a transducer with a 2D element topology is essential [51]. However, fabricating a matrix that is fully populated and addressed is challenging. The number of elements for a matrix will scale quadratically for increasing aperture, instead of linearly with a linear array. For example, covering an area of just 10 mm by 10 mm will already require more than 1000 elements for a 3 MHz matrix [59]. While constructing a transducer with that many or even more elements is in itself not an insurmountable issue, making electrical connections to each element is a formidable challenge [60]. Additionally, ultrasound systems have a limited number of channels available to send and receive data. So, while a fully-populated matrix can provide the same flexibility as an array, the difficulty in operating numerous elements severely limits the aperture and thus also the lateral resolution as compared to an array. To get around this limitation a different kind of matrix transducer is required.

Currently, there are three types of matrix transducers, besides the fully-populated matrix described before. They also cannot match the performance of a linear array, but they each offer a distinct trade-off between side-lobe level, lateral resolution, frame rate, and signal-to-noise ratio (SNR). The first type is the sparse matrix with elements that sparsely

populate a large aperture [61]. Compared to the fully-populated matrix with the same number of elements, the larger aperture results in a higher resolution, but the sparsity results in a high side-lobe level. Sparse matrices do not necessarily require any additional electronics, can be directly connected to available scanners, and do not necessarily require specialized imaging schemes. However, the cables between the elements and the imaging system can cause a significant loss of signal due to an impedance mismatch [60], [63]. To circumvent this, amplifiers can be used close to the elements [63]. The second type is the row–column-addressed array (RCA) [64]–[67]. This matrix has a fully-populated aperture, but in transmit only either each full column or each full row can be addressed separately, while in receive the other direction can be addressed. This reduces the number of electrical connections from N^2 to $2N$ compared to a fully-populated matrix. However, an RCA requires more complex acquisition schemes, resulting in a reduced frame rate. Furthermore, only the volume directly below the aperture can be imaged. The last type is a matrix transducer integrated with an application specific integrated circuit (ASIC). It also has a fully-populated aperture, but the number of electrical connections is reduced in the ASIC through micro-beamforming, multiplexing, in-probe digitization, on-chip pulsers, or any combination of these, depending on the specific application [70]–[73]. Furthermore, amplifiers can be integrated in the ASIC to amplify the signal and prevent signal loss [71], [74]. While this kind of matrix could potentially offer the best adaptation for a specific application, the downside is that the development process is more costly, both in money and time. All of the above types, including the fully-populated matrix, have shown promising results in measuring flow velocities in various applications [251]–[256].

Because a matrix integrated with an ASIC has the highest potential for adaption to a specific application, we have designed a matrix transducer made of lead zirconate titanate (PZT) built on top of an ASIC [71], [98]. This matrix is tailored for measuring various quantities around the carotid bifurcation. The aperture covers an area of 12 mm × 36 mm, subdivided in 80 columns and 120 rows. The 9600 elements can be addressed to operate like an electronically translatable linear array. With this imaging scheme, an arbitrary transmit and receive sub-aperture is translated in one direction between each pulse-echo, and the obtained data is combined into a single image. To minimize the amount of motion artefacts that occur, the translation is perpendicular to the direction in which the highest flow velocities are achieved in the carotid artery.

In a previous work, we optimized the imaging scheme for Carotid Pulse Wave Imaging (CPWI) [161]. While the transmission and reception parameters proposed in that paper could provide satisfactory results in CPWI, these specific parameters are not suitable for measuring the blood flow in the carotid artery because blood peak velocity is much higher than the wall motion during the cardiac cycle [53], [257]. Moreover, although there is an overlap in the requirements for achieving a high-quality B-Mode image and accurate displacement estimation, this does not ensure that a sequence optimized for B-Mode quality also results in accurate flow measurements. Therefore, the imaging scheme should be re-evaluated for high-frame-rate VFI in the carotid artery.

In this paper, our objective is to demonstrate the feasibility of measuring high blood velocities in a large volume using an electronically translatable linear array, with the aim of applying this to measuring the haemodynamics around the carotid bifurcation using the mentioned PZT-on-ASIC matrix. To achieve this, we will study how the parameters of

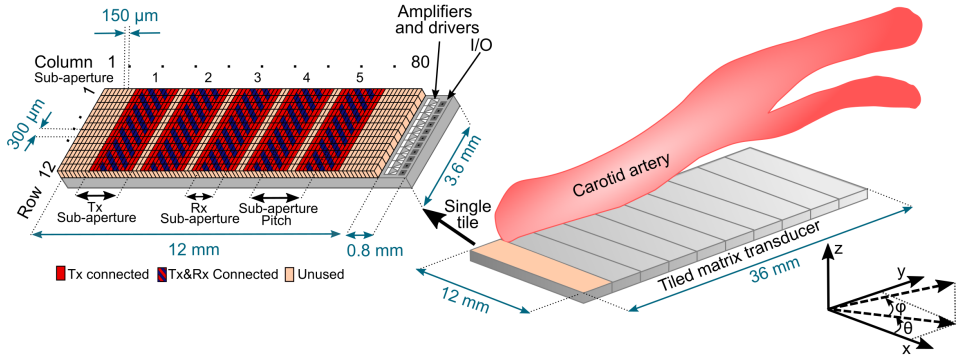

Figure 7.1: Schematic drawing of the envisioned full matrix transducer (right), together with a single ASIC tile with PZT elements mounted on top (left). On the single ASIC tile, the imaging scheme is illustrated together with its four electronically changeable parameters: transmit (Tx) sub-aperture width, receive (Rx) sub-aperture width, sub-aperture pitch and number of sub-apertures per image.

the imaging scheme affect the velocity estimation accuracy and precision obtained from a simulated straight-tube containing a parabolic flow profile.

7.2 Methods and materials

7.2.1 Matrix transducer

The transducer used in our simulation study is based on a PZT-on-ASIC matrix that is designed for imaging the carotid bifurcation [71], [98]. The matrix consists of 10 ASIC tiles placed next to each other. A schematic drawing of a single ASIC tile and the proposed orientation of the complete transducer are shown in Figure 7.1. The full-size transducer will consist of 80 columns and 120 rows with an element pitch of 150 µm × 300 µm and a centre frequency of 7.5 MHz. A total of 9600 elements are addressed by 120 transmit and 120 receive channels that are assigned to the 120 rows. For each row, the connected elements can be chosen arbitrarily and changed between each transmit and receive event. This connection strategy is implemented in the ASIC and allows the matrix to use various imaging schemes as described in the next section.

7.2.2 Imaging Scheme

There are multiple modes of operation possible with this probe. One example is plane wave imaging with column-by-column read-out. However, while a high lateral resolution and low side-lobe level can be achieved using this scheme, the resulting frame rate using this scheme would be relatively low because only a single column is read-out every pulse-echo cycle, which is detrimental to the ability to measure high velocities. Alternatively, the matrix can be operated like an electronically translatable linear array, as illustrated in Figure 7.1. The scheme has four electronically changeable parameters: transmit (Tx) sub-aperture width, receive (Rx) sub-aperture width, sub-aperture pitch and the number of sub-apertures per image. By modifying the parameters of the scheme, it can be adapted to the application. For example, by using fewer sub-apertures than a column-by-column

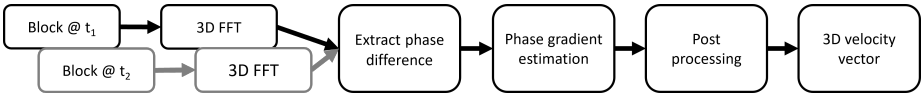

Figure 7.2: The main steps of the algorithm to estimate the 3D velocity in a block. The algorithm is repeated for every block to get estimates over the whole (sub-)volume.

read-out, a higher frame-rate can be achieved because fewer pulse-echo cycles are required. Fewer sub-apertures also reduce the total aperture width used for image reconstruction, which lowers the lateral resolution, but this can be compensated in this scheme by using a larger sub-aperture pitch. Therefore, the parameters can also be optimized to provide the best possible performance for measuring the fast flow in the carotid artery.

Previously, we investigated how to optimize this imaging scheme for use with CPWI [161]. For carotid imaging, a pulse repetition frequency (PRF) of 20 kHz is feasible. For CPWI a volume rate of 1000 volumes per second is sufficient and therefore 20 sub-apertures per volume could be used. However, to measure the fast flow in the carotid artery a higher volume rate is necessary. This means that we have to find the optimum parameters for fewer sub-apertures per volume.

Due to the reduction in the number of sub-apertures, the aperture width in receive is also reduced. To compensate for the limited aperture and improve the lateral resolution, the sub-aperture pitch can be increased. This would however increase the amount of grating lobes because the sub-aperture pitch can be significantly larger than $0.5\,\lambda$. Therefore, we opted to reconstruct the whole imaging volume from multiple sub-volumes, thereby avoiding grating lobes due to the large sub-aperture pitch by limiting the maximum required steering angle in receive.

7.2.3 Motion estimation algorithm

To estimate the flow velocity in a volume, we employed the same algorithm as in an earlier work [173], which is based on the work of Stone *et al.* [258]. The algorithm can work with RF, IQ or envelope data as input.

The first step of the algorithm is to subdivide the volume into smaller sub-volumes, which we will call blocks to distinguish them from the sub-volumes used to reconstruct the whole imaging volume. Blocks can be overlapping, with more overlap resulting in a higher spatial sampling of the estimated velocities. An apodization is applied on the blocks to reduce edge effects. In our case, we employ a Hann window in all three spatial dimensions.

To estimate the velocity within each block, the steps in Figure 7.2 are applied. In essence, the algorithm is similar to a phase-correlation, with a crucial difference: instead of estimating the displacement between two volumes through peak-finding in the spatial domain, this algorithm uses the phase gradient in the frequency domain, as explained below. This saves computation time as it does not require an inverse Fourier Transform and sub-pixel estimation.

After the phase difference has been retrieved, the phase gradient is estimated. This step is based on the Fourier Shift theorem which states that the phase difference between two translated images is

$$\Delta\phi\left(k_x, k_y, k_z\right) = k_x\Delta x + k_y\Delta y + k_z\Delta z, \tag{7.1}$$

where k_x, k_y, k_z are the spatial frequencies and Δx, Δy, Δz the displacements between the images in each spatial dimension. When putting all combinations of spatial frequencies into one expression, Equation (7.1) can be written in matrix form as

$$\Delta\vec{\phi} = K\Delta\vec{r}, \tag{7.2}$$

where $\Delta\vec{\phi}$ is a vector containing the phase differences for all combinations of (k_x, k_y, k_z), K a matrix containing one combination of (k_x, k_y, k_z) per row and $\Delta\vec{r}$ is a vector containing the 3 displacement components. These components can be derived using a least squares estimate as

$$\Delta\vec{r} = K^{+}\Delta\vec{\phi}, \tag{7.3}$$

where K^{+} is the pseudo-inverse of matrix K.

In an ideal case without noise, clutter and aliasing, and where everything moves with the same velocity, only three combinations of spatial frequencies would provide a unique solution to Equation (7.3). In reality more combinations are necessary to provide a good estimation. However, more combinations result in a longer computation time. It is not necessary to take all combinations, as shown by a similar method by Lenge *et al.* [259], where the results do not improve further after using a certain number of spatial frequencies. A simple choice would be to use a subset of equally spaced frequencies within the spatial bandwidth of the received signal. However, this is not optimal for three main reasons.

First, if the displacement is too high, aliasing will occur for the highest frequencies because the phase difference is only unambiguous over the range $\pm\pi$. In 1D, aliasing will occur if the displacement is larger than a grid step. In 2D or 3D, this happens for the highest spatial frequencies if the L^1 norm of the displacements relative to the grid steps exceeds 1. Therefore, to prevent aliasing due to large displacements, the frequencies used for estimating the displacement should satisfy

$$-\pi \leq k_x\Delta x_{\max} + k_y\Delta y_{\max} + k_z\Delta z_{\max} \leq \pi \tag{7.4}$$

where $(\Delta x_{\max}, \Delta y_{\max}, \Delta z_{\max})$ are the maximum displacements in each spatial dimension.

Second, grating lobes can cause spatial aliasing. The matrix described in Section 7.2.1 has a pitch of $0.75\,\lambda \times 1.5\,\lambda$ and thus certainly has grating lobes. Excluding the spatial frequencies of those grating lobes is necessary to prevent their influence.

Third, frequencies that have a low magnitude are more susceptible to noise and clutter. Including frequencies with a low magnitude worsens the bias, as shown by Stone *et al.* [258]. Therefore, frequencies with a low amplitude should be excluded from the estimation.

After the displacement has been estimated using Equation (7.3), post-processing can be applied to remove outliers and smooth the results. For the former, an algorithm like the one presented by Westerweel *et al.* [260] can be used. For the latter, both spatial and temporal smoothing can be used.

7.3 Simulation Setup

To assess the performance of the matrix transducer in combination with the proposed imaging scheme, we have conducted simulations using Field II [113], [114]. A summary of all parameters can be found in Table 7.1. In these simulations, a 3.2 mm radius vessel without

Table 7.1: Parameters used in the simulation.

	Parameter	Value
Numerical Phantom	Vessel radius	3.2 mm
	Centre of vessel	(0 mm,0 mm,15 mm)
	Inclination ϕ	10°
	Rotation θ	80°
	Peak velocity	75 and 150 m/s
	Flow profile	Parabolic
	Speed of sound	1540 m/s
Matrix	# Elements (Columns × rows)	80 × 48
	Element Pitch	150 µm × 300 µm
	Centre frequency	7.5 MHz
	Transmit pulse	5 cycle Hann windowed sinusoid
	Column apodization	None
	Row apodization	Tukey - 0.1
Imaging Scheme	# Sub-apertures per sub-volume	2 to 13
	Tx aperture	Entire matrix aperture
	Rx sub-aperture	5, 7 and 10 columns
	PRF	20 kHz
VFI	# Frequencies ($x \times y \times z$)	5 × 5 × 5
	Frequency range	0 to 0.5 of Nyquist
	Amplitude threshold	−20 dB
	Block size ($x \times y \times z$)	3 mm × 9 mm × 3 mm
	Block apodization	Hann
	Phase averaging	Median of 5 pairs
Sub-volume	Positions	−2, 0 and 2 mm
	Weighting	1 mm STD Gaussian distribution

a wall is initially placed along the x-axis with its centre in the origin. The vessel is then given an inclination by rotating it around the y-axis with angle $\phi = 10^\circ$ and subsequently rotated around the z-axis with an angle $\theta = 80^\circ$. Finally, the centre of the vessel is translated down by 15 mm. The axes and angles are illustrated in Figure 7.1. Within the vessel, scatterers are randomly distributed with a density of 1 scatterer per wavelength at 7.5 MHz, and these particles move in the direction of the axis of the vessel, following a parabolic flow profile with a peak velocity as given in the results.

Instead of emulating the full matrix as described in Section 7.2.1, only 48 rows were used. The transmit pulse used in the simulations is a 7.5 MHz sine modulated with a 5 cycle Hann window. Along the column direction (y) of the matrix, we applied a Tukey window with cosine fraction 0.1 in both transmit and receive to reduce the edge waves. No apodization was applied in the row direction (x).

The numerical phantom is imaged using the scheme described in Section 7.2.2. This scheme has four independent parameters: Tx sub-aperture width, Rx sub-aperture width, sub-aperture pitch and the number of sub-apertures per image. To reduce the number of

parameters, we set the sub-aperture pitch equal to the Rx sub-aperture width, i.e. effectively like a standard array, and refer to it as the Rx sub-aperture. In transmit the entire matrix was used to transmit a plane wave. The effect of the remaining two parameters, the number of sub-apertures and the Rx sub-aperture, is further investigated in this paper.

Images were constructed using a Fourier domain method described by Lu [261]. The grid step for beamforming was the Rx sub-aperture in x, the element pitch in y, and a quarter of the wavelength of the centre frequency in z. After beamforming, the grid spacing was modified to 250 µm in the x-direction, accomplished through zero-padding in the frequency domain and decimation. Upsampling was necessary for larger Rx sub-apertures to ensure sufficient data points for the velocity estimation.

Velocity estimation was carried out at every grid point using the algorithm detailed in Section 7.2.3. Envelope data was used to be able to measure higher flow velocities without phase-wrapping in the VFI algorithm. The dimensions of each block was 3 mm × 9 mm × 3 mm, with the block being wider in the y-direction to account for the higher velocity in that direction. For the estimation, 5 equally spaced spatial frequencies in each direction are used. The upper limit of the spatial frequencies was set to 0.5 of the Nyquist frequency, as a value of either 0.4 or 0.6 turned out to lower the accuracy. This limit was further constrained by Equation (7.4) to prevent velocity aliasing. Also, frequencies with an amplitude lower than −20 dB compared to the maximum amplitude are excluded. In order to improve the accuracy and precision, the median phase difference between 5 image pairs is used in the phase gradient estimation. No post-processing was performed on the velocity estimates.

As the aperture width may not always be sufficient to image the entire vessel, the velocity profile in the whole vessel was estimated from multiple sub-volumes. We used 3 sub-volumes placed at −2, 0 and 2 mm. The final estimates are made by a weighted average of the estimated velocities in each sub-volume with weights based on the distance from the centre of the sub-volume. The weights followed a Gaussian distribution with a standard deviation of 1 mm.

To assess the accuracy and precision of the estimated velocity we used the mean relative error and the mean standard deviation (STD). The mean relative error $\bar{\eta}_v$ for the magnitude v of the velocity $\vec{v}$ is defined as

$$\bar{\eta}_v = \frac{1}{v_{\max} N_s N_t} \sum_{p=1}^{N_s} \sum_{q=1}^{N_t} |v(\vec{r_p}, t_q) - v_r(\vec{r_p})|, \tag{7.5}$$

with $v(\vec{r}, t)$ the speed at a point in space and time, $v_r(\vec{r})$ the ground-truth speed at the same point in space, N_s the total number of spatial points, N_t the total number of time steps and $v_{\max}$ the peak speed of the parabolic flow profile. The mean STD is defined as

$$\bar{\sigma}_v = \frac{1}{v_{\max}} \sqrt{\frac{1}{N_s(N_t - 1)} \sum_{p=1}^{N_s} \sum_{q=1}^{N_t} \left(v(\vec{r_p}, t_q) - \overline{v}(\vec{r_p}) \right)^2}, \tag{7.6}$$

where $\overline{v}(\vec{r})$ is the average speed over all time steps. Both metrics are only evaluated for points within the vessel and between $y = \pm 5$ mm.

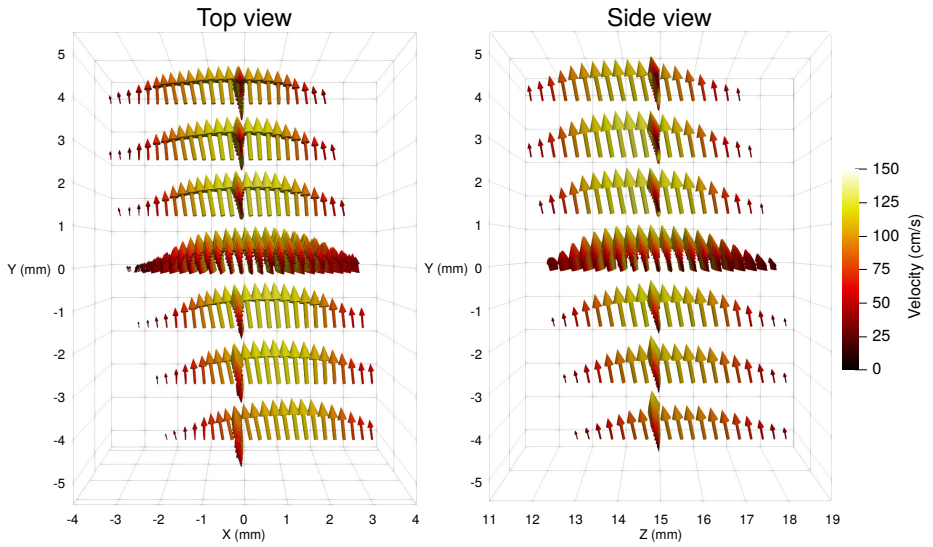

Figure 7.3: Top and side view of the obtained velocity vectors in a simulated parabolic flow phantom. For visualization, the vectors only originate from three orthogonal planes that all cross (0 mm,0 mm,15 mm). Velocities outside the vessel are not displayed.

7.4 Results

7.4.1 3D

In Figure 7.3 a top and side view of the obtained velocity vectors in a volume are shown. To aid visualization, the arrows only originate from three orthogonal planes, but the velocities are estimated in the whole shown volume. From the figure, it can be observed that the vectors consistently point in the same direction, i.e. the direction of the flow, and that the vector lengths are larger in the centre of the vessel as can be expected from a parabolic profile. The figure also shows some inaccuracies, because in the side view the profile appears more symmetric, while this is not the case in the top view where the velocities are generally higher on the right-hand side ($x > 0$). The results are quantified in the next sections.

7.4.2 Number of sub-apertures

In Figure 7.4a the mean relative error and the mean STD are shown as a function of the number of sub-apertures per sub-volume for a peak velocity of 75 and 150 cm/s, and for a Rx sub-aperture of 5 columns. For 150 cm/s the relative error is lowest at 5 sub-apertures with 12.5%, while the STD has a minimum at 6 sub-apertures and is slightly below 9.3%. For 75 cm/s the relative error is lowest at 9 sub-apertures with 9.5%, while the STD is lowest at 10 sub-apertures with 8.6%. No more than 10 sub-apertures are used, because part of the effective elements would otherwise lie outside the emulated matrix with 80 columns. The trend shows that for fewer sub-apertures, the estimation results are limited by the resolution due to the limited aperture size, while for more sub-apertures the frame rate is

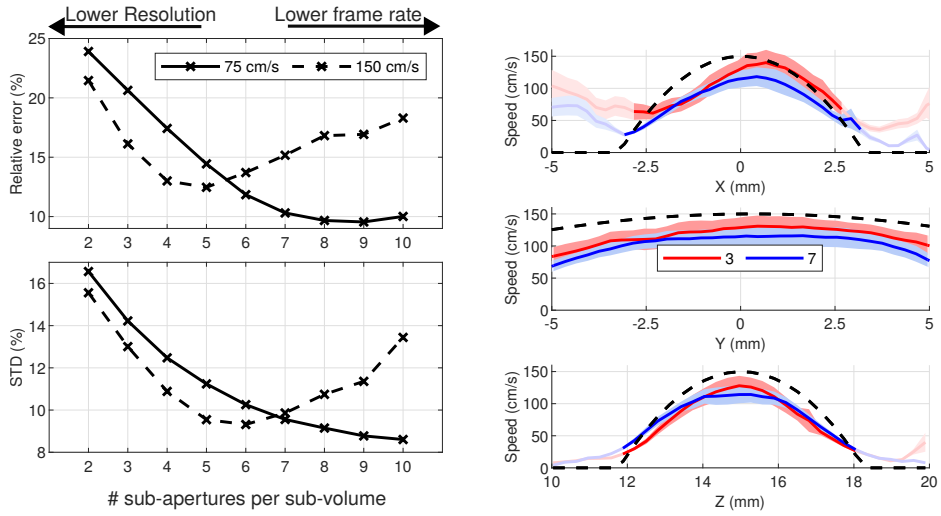

Figure 7.4: (a) Mean relative error and mean STD as a function of the number of sub-apertures for a peak velocity of 75 cm/s (solid line) and 150 cm/s (dashed line), and a Rx sub-aperture of 5 columns. (b) Mean velocity (solid line) and mean STD of the velocity (shaded area) along three different lines, all crossing (0 mm, 0 mm, 15 mm) for a peak velocity if 150 cm/s. In red 3 sub-apertures were used per sub-volume for each image, in blue 7. The transparent parts are outside the vessel and not used for calculating the metrics.

the limiting factor. The STD has a minimum at slightly more sub-apertures because with more sub-apertures, more data is used to form a single image.

Because an image is reconstructed from multiple pulse/echo cycles, motion artefacts can appear. This also affects the estimated velocity, especially in the x-direction where the sub-aperture translation occurs. This is evident at the top of Figure 7.4b, where the estimated profile is asymmetric, with higher velocities estimated on the right side.

For a peak velocity of 150 cm/s, 3 and 7 sub-apertures have a similar performance in terms of absolute error, but the velocity profiles are different. Considering only the top panel of Figure 7.4b, it can be seen that with 7 sub-apertures the velocity is underestimated at all points, except where the velocity comes close to 0. However, with 3 sub-apertures the velocity is mostly overestimated at all positive x. Although for both number of sub-apertures the mean absolute error is similar, the bias with 3 sub-apertures will be lower. Whether this is preferable depends on the circumstances.

In the bottom panel of Figure 7.4b the velocity along the z-axis can be seen. With 7 sub-apertures, the estimated speed around 15 mm is underestimated more and the profile is mostly flat, compared to 3 sub-apertures. This indicates that the estimation accuracy of these higher velocities is limited by frame rate.

7.4.3 Velocity components

Figure 7.5 shows the relative error and the STD of the estimated angles for images created with 5 sub-apertures and a peak velocity of 150 cm/s. The figure shows that the inclination ϕ is estimated with the best accuracy and precision, while the estimation of the rotation

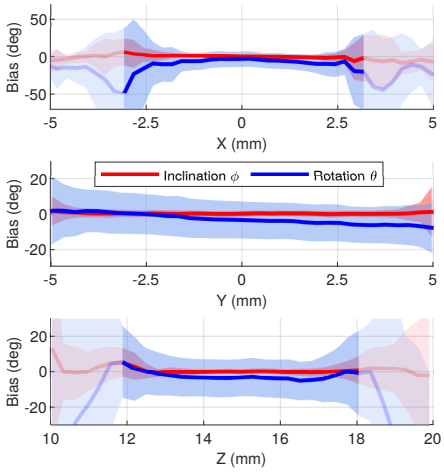

Figure 7.5: The mean bias (solid line) and STD (shaded area) of the estimated angles for 5 sub-apertures per sub-volume, a Rx sub-aperture of 5 elements and a peak velocity of 150 cm/s. Both are shown along three different lines, all crossing (0 mm, 0 mm, 15 mm). The transparent parts are outside the vessel and not used for calculating the metrics.

θ is visibly worse. The results for θ are mainly because of the inability to estimate a consistent x-velocity. If the estimated y-velocity were also inconsistent, the estimation of the inclination ϕ would also be inaccurate, which is not the case.

For both the velocity along the x- and z-axis, the estimation becomes worse towards the edges. There are two main reasons. First, there are no scatterers outside the vessel and therefore the remaining signal is just clutter from side lobes. At some point, part of the block used for estimation includes this region and this clutter causes an increased variance. Second, the velocity gradient is highest at the edges of the vessel. At these points the algorithm is unable to estimate a consistent x-velocity, likely because of the low resolution as the effect is most visible in the top panel of Figure 7.5. Together, this causes a sharp increase in variance and error.

7.4.4 Rx sub-aperture

In Figure 7.6 the mean relative error and mean STD as a function of the Rx aperture width for 7 and 10 sub-apertures per sub-volume are shown. A width of more than 5 columns is not used for 10 sub-apertures as it would require more than 80 columns. The best results are obtained for 7 sub-apertures at 5 columns with an error 10.3 % and an STD of 9.6 %, while for 10 sub-apertures the best results are at 5 columns with an error 9.2 % and an STD of 8.2 %. The high error and STD caused by a small Rx sub-aperture is due to the correspondingly small aperture for imaging reconstruction that results in a low lateral resolution. For a wide Rx sub-aperture the high error and pitch are caused by two effects. First, the large width of each sub-aperture results in more directive sub-apertures that lower the resolution because they contribute less to parts of the image at a large angle. Second, the large pitch results in grating lobes closer to the main lobe and thus increase clutter. Both a too narrow or wide Rx sub-aperture will thus negatively affect the performance.

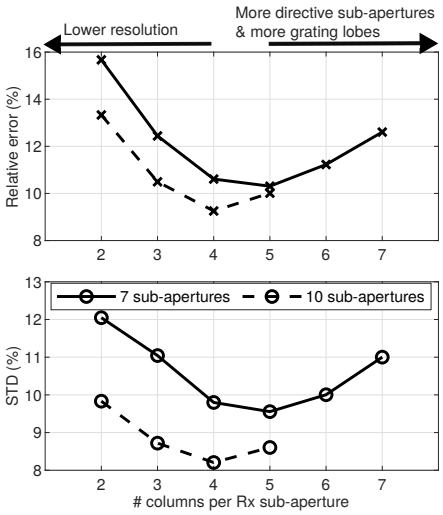

Figure 7.6: Mean relative error and mean STD as a function of the Rx sub-aperture for 7 sub-apertures (solid line) and 10 sub-apertures (dashed line) for a peak velocity of 75 cm/s. A width of more than 5 columns is not used for 10 sub-apertures because it would require more than 80 columns.

Using 10 sub-apertures instead of 7 shifts the optimum width to the left and results in a lower error and STD. The optimum for both number of sub-apertures is more or less at the same total aperture width, but with 10 sub-apertures the spatial sampling of the total aperture for reconstruction is finer. This shows that it is beneficial to use more sub-apertures and a smaller effective receive element whenever possible.

7.5 Discussion

In this paper we numerically investigated the performance of vector flow imaging with an imaging scheme that represents an electronically translatable linear array. The imaging scheme was designed to allow high-frame-rate imaging of the carotid bifurcation with our PZT-on-ASIC matrix. In a previous paper the imaging scheme was investigated for CPWI. Here, we applied it to VFI, which requires a higher frame rate to measure the blood flow in the carotid artery. Additionally, we directly evaluated the performance with the estimated velocities.

7.5.1 Trade-offs of the imaging scheme

The imaging scheme has four parameters that can be varied: Tx sub-aperture width, Rx sub-aperture width, sub-aperture pitch and the number of sub-apertures per image. All these parameters present a trade-off, as we will discuss below.

Number of sub-apertures per sub-volume

The first trade-off is the number of sub-apertures per sub-volume. A low number of sub-apertures yields a high frame rate and a narrow aperture in receive, while the reverse is true for a high number of sub-apertures. A high frame rate results in a higher correlation of

the moving particles between subsequent frames [262]. Furthermore, it prevents velocity aliasing in the VFI algorithm, which for the algorithm in this paper would present itself as phase wrapping at higher spatial frequencies. A wider aperture in general results in a higher lateral resolution, which would allow for more accurate measurements of higher spatial velocity gradients [263]. Consequently, for a specific velocity profile and peak velocity, an optimal number of sub-apertures can be found in terms of error and STD. The result in Figure 7.4a support this, as the trade-off between resolution and frame rate results in a different optimum for different peak velocities.

Purely looking at the effect of the number of sub-apertures on frame rate, it can be expected that halving the velocity would double the optimal number of sub-apertures. This also was more or less observed when comparing the 75 cm/s and 150 cm/s cases in Figure 7.4a. However, this expectation is not always true as the number of sub-apertures also influences the aperture size and, consequently, the lateral resolution. With a low number of sub-apertures, the resulting low lateral resolution hinders accurate measurement of velocity gradients, particularly when they become steeper with higher velocities. Conversely, with a high number of sub-apertures the contribution of outer sub-apertures to the image diminishes. As a result, the anticipated factor of 2 difference is only approximate.

As previously stated, a specific velocity profile and peak velocity would have an optimal number of sub-apertures. In this study, we only varied the peak velocity, but did not study variations in the underlying profile by, for example, changing the vessel width to create different gradients. Higher spatial velocity gradients are expected around the carotid bifurcation as (helical) vortices are present [53]. In such cases, a higher resolution would become more crucial to achieve high accuracy and precision. Consequently, more sub-apertures per sub-volume then become necessary.

Receive sub-aperture

The second trade-off is the Rx sub-aperture. In this paper we have set the sub-aperture pitch equal to the Rx sub-aperture width. The combined effect can be compared to changing the total width of a standard array for a fixed number of elements. Therefore, both a too narrow or too wide Rx sub-aperture will negatively affect the performance, as shown in Figure 7.6. Compared to the number of sub-apertures per sub-volume, the gradient in relative error and STD around the optimum is lower for the Rx sub-aperture. This indicates that the Rx sub-aperture is less critical for performance.

While we kept the sub-aperture width and pitch the same in this paper, the matrix architecture allows them to be decoupled. This was done by Mozaffarzadeh *et al.* [161] in a prior study. For a single scatterer, they observed that a smaller sub-aperture width compared to the pitch led to enhanced resolution, primarily because the increased opening angle caused the outer sub-apertures to play a more substantial role in the reconstruction process, while the grating-lobe level generally worsened. Conversely, a wider sub-aperture width compared to the pitch worsened both the resolution and grating-lobe level, mainly due to the reduced opening angle. However, the effect of this was less pronounced compared to changing the width and pitch simultaneously. Therefore, a smaller sub-aperture width compared to the sub-aperture pitch can at most allow for fine-tuning the trade-off between lateral resolution and clutter.

Transmit sub-aperture

In this paper we transmitted with all elements and we did not further investigate the effect of the transmit sub-aperture width. This parameter was investigated previously by Mozaffarzadeh *et al.* [161]. For a single scatterer and a transmit sub-aperture that is co-centred with the receive sub-aperture, as is illustrated in Figure 7.1, they demonstrated that a larger transmit aperture generally yields improved resolution, along with reduced side- and grating-lobes. This improvement occurred up until a certain sub-aperture width, after which the results did not improve any further. The main reason for the worse performance at smaller sub-apertures was that the scatterer was not consistently illuminated during each pulse-echo and therefore not every receive sub-aperture contributed equally during image reconstruction. This indicates that the transmit aperture should be wide enough to always illuminate the region of interest during all pulse-echo events.

In this paper, we always transmitted with all elements. While this means that the transmit aperture is wide enough, it is also wider than necessary for most situations considered in this paper. If a wider region than necessary is illuminated, signals from remote regions will act as clutter and might therefore deteriorate the performance. Therefore, the best choice for the transmit aperture is thus to make it just wide enough and keep it centred at the region of interest. Due to the simulation environment without tissue and additional clutter, not using this choice has a minimal influence on the results in this paper, but larger effects can be expected in-vivo or on a phantom with more clutter sources.

7.5.2 Number of sub-volumes

To reduce the effect of grating lobes, the velocities in the imaging volume are reconstructed from multiple sub-volumes, as discussed in Section 7.2.2. In our simulations, more, tighter spaced sub-volumes improved the accuracy and precision, but the majority of the improvement was between 1 and 3 sub-volumes (comparison not shown). The reason is that only for a single sub-volume and a sub-aperture pitch of at least 4 columns, grating lobes would influence the results at the edges of the vessel. With multiple sub-volumes, the maximum required steering angle was lower and the effect of grating lobes was thus negligible. Therefore, the number of sub-volumes should be such that the effect of grating lobes remains limited.

It might be possible to further enhance the performance by choosing distinct parameters for each sub-volume. For example, by using more sub-apertures for a sub-volume in areas where the velocity is lower, the performance there could be improved. In this case more sub-volumes might be beneficial, but this needs further investigation.

7.5.3 Limitations of this study

In this study we performed simulations on a phantom with a straight tube vessel with a slight inclination and rotation. We believe this is fine for an initial investigation, but this avoids certain issues that would appear in in-vitro and in-vivo measurements.

Lack of surrounding tissue

In the simulations we did not include a vessel wall and tissue. Ideally, a tissue filter should remove this kind of clutter, and in that case the results from this paper would not change. However, in practice perfectly separating blood and clutter is not always possible. For

example, inadequate separation of the slow blood flow near the vessel walls from the surrounding tissue can cause an under- or overestimation, depending on whether the filter insufficiently attenuates tissue clutter or also removed the low-velocity components of blood flow, respectively [264]. The problem is exacerbated by varying tissue motion that causes the ideal filter parameters to differ depending on the cardiac cycle and breathing. However, this is a general problem with clutter filters and the effects of imperfect filtering on the trends observed in this paper are not expected to be any different. Therefore, by excluding tissue from the simulation, the focus can be on the performance of the estimation with the described matrix and imaging scheme.

Velocity range and gradients

In this paper, a parabolic flow profile with a peak speed of 150 cm/s is considered. The best estimation was achieved with 5 sub-apertures, corresponding to a sub-volume rate of 4000 Hz. Due to the angles used, the peak flow velocities were 26, 145 and 26 cm/s in x, y and z respectively. The peak velocity in yy exceeds the typical range around the bifurcation [247], but higher velocities can occur in zz [265], and possibly in x. Additionally, helical flow patterns around the carotid bifurcation [53] can result in steeper velocity gradients than those used in this paper, which could pose practical issues.

Higher velocities result in more flow in and out of a block between images and can introduce velocity aliasing. The former could be partially alleviated by increasing the block size [266]. Velocity aliasing can be prevented by satisfying Equation (7.4). Higher velocities would then instead limit the number of useable frequencies, which can worsen the estimation results. This is visible in Figure 7.4a, where a slight change in trend for both the error and STD is visible for more than 8 sub-apertures because spatial frequencies in y are excluded to prevent aliasing. Therefore, both a loss of correlation and velocity aliasing can be alleviated, and a higher velocity itself is not an issue.

Steeper gradients, for example due to helical vortices, are a larger problem. Due to the matrix and imaging scheme, the lateral resolution in x is limited, especially for a low number of sub-apertures and a small receive sub-aperture. With a low resolution, the ability to measure high spatial velocity gradients is reduced [263]. This is visible at the top of Figure 7.4b, where the measured velocity at $x = \pm 3.2$ mm has a higher bias with a narrower aperture. Lateral resolution can be improved by using more sub-apertures per sub-volume or widening the Rx sub-aperture to increase the resolution, but this also has its downsides. Therefore, whether the error remains acceptable in regions with a high spatial velocity gradient should be investigated further.

SNR

In this study we did not include any sources of noise and clutter. Therefore, we also did not study the impact of the parameters on signal-to-noise ratio (SNR). A combination of more sub-apertures and narrower sub-aperture could for example increase the SNR. This increase could be crucial for blood flow imaging as the amplitude of the reflected signal is about 40 to 60 dB lower than the surrounding tissue [76]. Therefore, the effect of the parameters on SNR should be further investigated.

7.5.4 Further improvements

To enhance the results obtained in this study, two main changes can be made in addition to addressing the previously discussed limitations: motion compensation and an iterative VFI scheme. Both are discussed below.

Motion compensation

Due to the matrix's architecture and the imaging scheme, a single image is created from multiple pulse-echo events taken at different time instants. Therefore, motion artefacts will appear if anything in the region of interest moves between each pulse-echo, which is the case in this paper. The effect of the artefacts is most evident in the upper part of Figure 7.4b, where the velocity profile is not symmetric around $x = 0$. Here, the motion artefacts cause the velocity on the right side to be estimated higher than on the left. Changing the scanning or flow direction will cause the artefacts to affect the results the other way around, i.e. higher velocities estimated on the left and lower on the right.

These artefacts could be mitigated by applying motion compensation before beamforming. Jorgensen *et al.* [123] has shown that, especially at high velocities, the accuracy of the velocity estimation is improved with an iterative motion compensation scheme, albeit at the cost of lower precision. Implementing this motion compensation scheme will likely resolve the asymmetry in our results and reduce the bias of the velocity estimation.

Iterative VFI

The choice of block size in the VFI algorithm has a profound effect on the results [267]. To achieve a high signal-to-noise ratio, especially at higher velocities, a larger block is required. However, larger block sizes can lead to reduced accuracy, as the estimated velocity is an average of the velocities present in the estimation volume. Moreover, flow patterns can contain shear and rotation, which further worsens the accuracy. To mitigate these issues, the displacement can be estimated in multiple iterations, starting with a larger window size and progressively decreasing it while deforming the images between each pass. Iterations can thus improve the estimation results. However, in our study, we have chosen not to incorporate iterations to limit the number of parameters.

7.6 Conclusion

In this paper we have shown the first step towards measuring 3D velocity vectors in a large volume with an electronically translatable linear array scheme. The imaging scheme has various parameters that affect the accuracy and precision of the estimated velocity. The number of sub-apertures had the largest effect. For a parabolic flow velocity with a peak velocity of 150 cm/s and a receive sub-aperture of 5 columns we achieved a relative error of 13% and an STD of 9% using 5 sub-apertures. With fewer sub-apertures, the results were hampered by a lack of resolution, while for more sub-apertures the lower frame rate caused an underestimation at high velocities. The results in this paper show that it is feasible to measure the high velocities in the carotid artery using an electronically translatable linear array, provided appropriate trade-offs are made.

8

Adaptive Array Clutter Filter for High-Frame-Rate Vector Flow Imaging with a 2-D Sparse Array

This chapter is to be submitted as:
F. Fool, S. Rossi, A. Ramalli, P. Tortoli, N. de Jong, M. D. Verweij, and H. J. Vos, "Adaptive Array Clutter Filter for High-Frame-Rate Vector Flow Imaging with a 2-D Sparse Array,"

8.1 Introduction

Medical volumetric ultrasound imaging has been introduced in past decades in cardiovascular, oncological, and obstetric fields. Originally, the volumetric nature was obtained by mechanically sweeping a 1D array in a dedicated holder, or by manual or automated scanning with positioning sensing [51], [52]. Such techniques can reach up to few volumes per second, which is acceptable if the underlying structure is not moving fast. However, to accurately measure high blood velocities in all three orthogonal components, volume rates in the order of 1 kHz might be necessary.

In the past decade, matrix transducers, also called 2D arrays for 3D or 4D ultrasound, where the fourth dimension is time, have been introduced that can reach the required frame rates. Yet, currently available matrix transducers inherently make a trade-off between resolution, clutter, frame rate and signal-to-noise ratio (SNR), caused by the complexity of signal data capture in such transducers since the number of elements scales quadratically with aperture size instead of linearly compared to the original 1D arrays. The large number of elements poses, among others, a large challenge to the cable count [60], [268], which the various matrix types deal with in different ways [59], [61], [64], [72], [73].

Recently, sparse 2D arrays have been studied in which elements are located or selected sparsely in a larger aperture [61]. They can achieve a similar lateral resolution and field-of-view as fully-sampled matrix transducers with the same aperture width, at the cost of a lower SNR and more clutter. The lower SNR is caused by the reduction in effective transmit/receive apertures. For every halving in the area occupied by the elements, upon further proper design of surrounding electronics, the signal-to-noise ratio is theoretically reduced by 9 dB [166], [269]. This decrease could partly be alleviated by increasing the element size. Normally, the elements in a matrix have typical dimensions of $0.5\,\lambda_c$ in each lateral side, with λ_c being the wavelength of the ultrasound waves in the medium related to the centre frequency. This dimension is a good trade-off between opening angle of the view, area usage, SNR, and grating lobe levels. By increasing the element dimensions the effective area and therefore SNR is increased, at the cost of a reduction in the field of view or an increased clutter level due to the grating lobes [1], [62]. In-probe signal amplification may also increase SNR [63]. The increased amount of clutter is caused by the insufficient spatial sampling of the acoustic field, since the field is sampled at random distances generally larger than half wavelength thus violating the Nyquist criterion. In single-beam transmission and/or single scatter receive experiments, the clutter is visible as relatively high off-beam/off-scatter signal intensity. For example, a recent paper showed clutter levels in the order of −25 dB below the main beam [270], whereas −50 dB is a normal acoustic clutter level for fully-populated arrays. By carefully selecting the placement of the elements in a sparse array, the clutter level can be controlled [61], but not avoided. For example, the elements positions can be based on the Fermat Spiral [62] or optimized based on a cost function [271], which will change the details of the clutter pattern. Notably, this kind of clutter from the insufficient spatial sampling is deterministic and implies that averaging subsequent images will not reduce this. Only changes in transmission fields, or changes in the imaged object, may yield changes. Therefore, while the drawbacks can be partly reduced, the SNR and side-lobe levels will still be worse compared to a fully-sampled array.

Both the lower SNR and higher amount of clutter are detrimental for the ability to accurately measure blood flow. A high SNR is required to be able to measure blood flow, as the signal from blood is approximately 40 to 60 dB [76] lower than tissue, and hence deeper vessels can be detected with higher SNR. The higher side-lobe level causes the signals to become spread out. This causes a mixing of the signals coming from different positions, resulting in a larger bias and variance when estimating velocities. Additionally, high-frame-rate imaging in general has a higher clutter level as a larger volume is illuminated compared to line-by-line imaging [7]. Therefore, SNR and clutter are the main issues reducing the ability to accurately measure blood flow and methods have to be found to improve both.

In this paper our focus is on reducing the amount of clutter to improve velocity estimation performance when measuring blood. There are two kind of clutter sources in blood Doppler. First, tissue clutter is the standard kind of clutter known in Doppler and refers to signals from surrounding tissues that interfere with the ability to measure blood flow. Second, array clutter refers to the side- and grating-lobes that are, among others, affected by the array topology and the transmitted beam. Our focus is on reducing this array clutter.

To reduce array clutter, a number of methods can be employed. For example, more advanced beamforming techniques can be used than delay-and-sum beamforming. Coherence-based beamforming techniques reduced array clutter in multi-line transmission B-Mode imaging [272] and spatial coherence beamforming has shown to significantly reduce clutter in Power Doppler images made with a sparse array and with use of sparsely distributed ultrasound contrast agents [165]. However, the effectiveness of advanced beamforming in improving accuracy and precision when estimating flow velocities has not yet been shown, although initial attempts have been made [273].

An alternative approach might be to apply a filter on the data. In Doppler ultrasound, filters are used to remove tissue clutter from the images. As tissue generally moves at a lower velocity than blood, a temporal high-pass filter on subsequent frames can be used to separate the blood signal from tissue signal [76], [274]. More recent studies show that singular value decomposition (SVD) filters [9], [10] can even further reduce tissue clutter compared to blood signal. The main difference between SVD-based filters and the more traditional spectral filters is that SVD filters also take into account the spatial component of the signals besides the temporal. However, array clutter does not have distinct temporal and spatial components as compared to the point spread function (PSF) peak, which assuming appropriate image reconstruction is performed overlaps with the real position of the point scatter, hence both temporal and spatio-temporal filters fail in separating them.

Alternatively, array clutter can be reduced by using coherent compounding [7], [91], [275]. With this technique, a sequence of partially overlapping ultrasound beams is transmitted and the reconstructed lower-quality image data are then coherently summed in radio-frequency (RF) or in-phase-quadrature (IQ) format. This compounding yields a final image with better image quality, both in terms of resolution and array clutter level, compared to the separate images reconstructed by the single beams. This exploits the fact that for a static point scatterer the array clutter changes based on the transmission field, while the PSF does not, thereby generating a distinct characteristic. However, this approach is problematic if the point scatterer moves between images. The process of compounding is effectively a moving average over the captured series of lower-quality image data, and it thus acts as a temporal low-pass filter. As high axial velocities of blood and tissue corre-

spond to high Doppler frequencies when the series is viewed in the frequency domain, the moving average operation thus attenuates and possibly even removes those signals, thereby resulting in an underestimation of the velocities [92]. Therefore, in practical situations where high velocities are present the ensemble length and array clutter reduction are limited.

In this article, we propose an adaptive array clutter filter that exploits the change in array clutter based on the transmission field, and takes into account the displacement between images to prevent suppression of high velocity signals. To account for different velocities in each part of the image and over time, the algorithm is applied separately on subvolumes and limited temporal windows. We will demonstrate the suitability for flow imaging in a simulation study by applying it to high-frame-rate vector flow imaging with a sparse array, which inherently has higher array clutter.

8.2 Method and materials

The adaptive array clutter filter technique consists of two filter steps. In the first step, tissue clutter is removed based on the different characteristics of tissue as compared to blood. This step also removes array clutter belonging to tissue. The second step employs an adaptive temporal filter to remove array clutter. The temporal filter assumes a range of dominant Doppler frequencies caused by blood flow and adapts the frequency range used for filtering to retain these dominant frequencies while eliminating quasi-random array clutter noise. This approach is different from conventional coherent compounding, which removes high-Doppler-frequency flow signal regardless, whereas the proposed technique can retain such signals as long as a range of dominant frequencies is observed in the measured frequency spectrum. Since we may expect that the velocity is not uniform within the entire volume and measurement period, the adaptive filter is applied on subvolumes and limited temporal windows. The effectiveness of the array clutter filter depends on the sequence of transmitted beams as it affects how the array clutter changes between subsequent images. Therefore, we will discuss the 2 steps, and the transmission sequence, in the next subsections.

We will evaluate the performance of the array clutter filter method in a numerical phantom, which is visualized in Figure 8.1, and compare it to conventional compounding. The parameters for the simulation will be further elaborated in Section 8.2.4.

8.2.1 Transmission sequence

The transmission field partly determines the array clutter, and consequently, the transmission sequence determines the variation in the array clutter in the ensemble of subsequent images. Hence, we will discuss the parameters of the transmission sequence, which are the number of unique beams, the characteristics of each beam, and the order in which they are transmitted. For simplicity, we use collimated beams only in this study, i.e. 'plane waves', and the only beam characteristic that is varied is the transmission direction of each beam.

Beam directions

The transmission beams should always cover the desired imaging volume, constraining the choice of directions. Within this constraint and the given number of beams, the directions must be selected appropriately. We define the beam direction by the normal vector of the

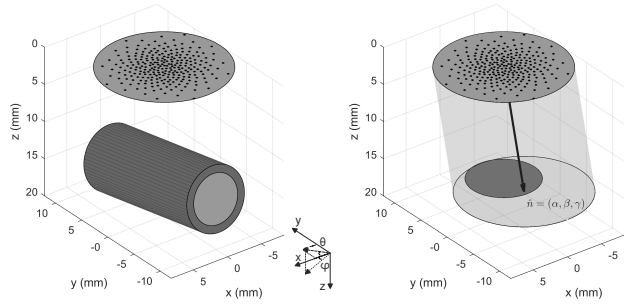

(a) (b)

Figure 8.1: (a) Sparse matrix along with a vessel inclined at 10° and a wall. (b) Sparse matrix with the outline of a steered plane wave and the corresponding normal unit vector. The dark circle at 15 mm depth indicates the region where all plane waves overlap, which decreases in radius with increasing maximum range $r0$ of the transmitted beams.

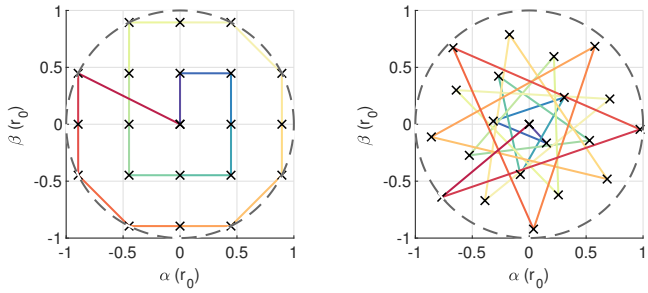

(a) (b)

Figure 8.2: Beam directions represented using the x, y coordinates of the normal vector of the plane wave with a maximum range of r_0. The lines between the coordinates indicate the order in which the angles are traversed. The dashed circle indicates the maximum range r_0. (a) Periodic. (b) Fermat spiral.

plane wave $\hat{n} = (\alpha, \beta, \gamma)$, as illustrated in Figure 8.1b, with $\sqrt{\alpha^2 + \beta^2}$ limited to a maximum range of r_0. The transmission directions can be chosen following either a regular pattern, such as laying on a Cartesian grid as shown in Figure 8.2a, or an irregular pattern, such as based on the Fermat spiral as shown in Figure 8.2b. Similar to the design of sparse arrays, non-periodic sampling reduces the peak array clutter level for the same number of transmissions, as demonstrated by Bae *et al.* [275], [276]. They showed that directions based on the Fermat spiral can provide similar compounded-image quality, in terms of lateral resolution and contrast, as a periodic pattern, yet with 2 to 6 times fewer directions. Therefore, using irregular sampling reduces the number of required directions.

Order of directions

The order of beams in the sequence affects the results if the object is moving. Denarie *et al.* [277] showed that a different order can improve image quality with compounding, and Porée *et al.* [122] demonstrated that different orders affect the performance of their motion compensation scheme. To understand this behaviour, consider Figure 8.3, which shows the

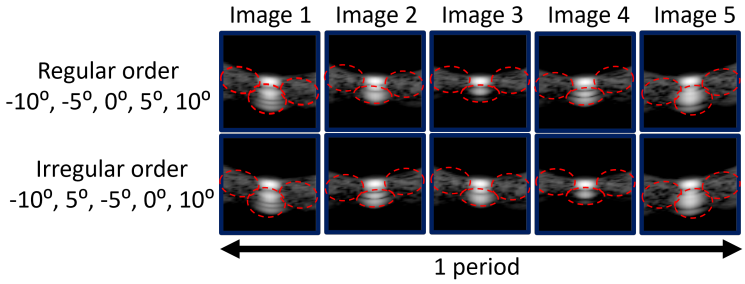

Figure 8.3: Illustration of the resulting image of a single scatterer made with 2 sequences with the same 5 directions, but in a different order. The array clutter is indicated by the red dashed lines.

PSF of a stationary scatterer insonified with 5 beams having varying angle in two different orders The PSF peak is not affected by the change in transmission direction, while the the array clutter, indicated by the red dashed lines, varies strongly with the transmission direction. With the regular order, the rotation is gradual between the subsequent beams, while with the irregular order it is more varied. This implies that the array clutter with the regular order mostly vary with a lower and more consistent velocity and therefore the temporal characteristics of the array clutter will be similar to that of the moving scatterers. On the other hand, the array clutter with the irregular order has a higher and more varied velocity and will hence form temporal 'acoustic noise', that can be removed by an adaptive temporal filter based on the measured dominant Doppler frequency of the moving scatters. Therefore, an irregular order of the directions will result aid in the removal of array clutter.

Considering the two sequences in Figure 8.2, the above reasoning implies that for the periodic sequence, if the directions are traversed in the shown order, it will perform worse than the spiral sequence as the differences between subsequent directions for the Spiral sequence are larger and more varied. It is possible to re-order the periodic sequence to achieve larger differences between subsequent transmissions, but the spiral sequence will still outperform it due to the irregular sampling.

Number of unique beams

The number of unique beams N is limited by the requirements for tissue filtering and this follows from two points. First, the separation of tissue from blood requires different spatial and/or temporal characteristics, which must also be true for their corresponding array clutter. In subsequent images made with different transmission directions, the change in array clutter mostly depends on the change in direction, especially if the change is large between subsequent images, which is important as discussed before. This means that array clutter from tissue and blood will have similar characteristics and not all signals belonging to tissue can be removed. Only between repeated instances of the same direction, the difference is determined by the movement of the PSF peak. Therefore, effective tissue clutter filtering requires a periodic sequence. Second, the length of the periodic sequence is limited due to a limited measurement time and the reduced effective PRF for tissue filtering. The limited measurement time limits the amount of samples available for filtering. Efficient filtering with few samples is a challenge [76], [274]. With few samples available, filters

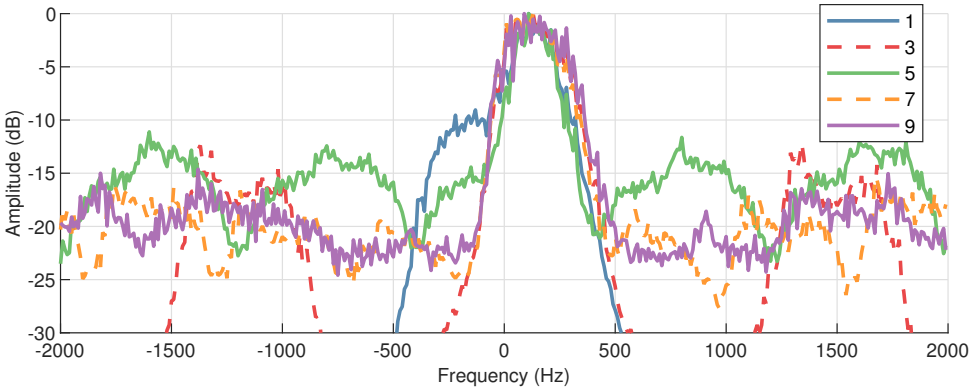

Figure 8.4: Local slow-time frequencies from a 1 mm × 1 mm × 0.2 mm sub-volume centred at (0 mm,0 mm,15 mm) for 1, 3, 5, 7 and 9 unique beams.

generally have a poor transient response or a low attenuation of tissue clutter, which both negatively affect the ability to remove tissue clutter. The effective PRF for tissue filtering is reduced by a factor N, i.e. $PRF_T = PRF/N$, and this can cause temporal aliasing due to the lowered Nyquist frequency. This can be the case for both tissue and blood signals, but only the former presents an issue. Considering an SVD filter, we expect that aliased signals have a lower correlation between the images and thus will appear at a lower rank. Therefore, if only blood signals are aliased, tissue signals will remain a high ranks and can therefore still be separated. If the tissue signals are also aliased, we expect that the ranks containing tissue and blood will not be separated any more and that might make sufficient separation between tissue and blood impossible. Therefore, the number of unique beams N is limited because a periodic sequence of a certain length is necessary for effective tissue filtering.

8.2.2 Tissue filter

The tissue filter separates tissue signals from blood signals by exploiting the differences in the temporal and/or spatial characteristics. These differences are only found in data obtained with the same direction, as discussed in Section 8.2.1. Therefore, the tissue filtering is applied on a sequence formed of each transmission direction separately.

In principle, temporal high-pass filters could be used to remove the tissue signals. However, the application per-direction does increase the sampling interval, possibly leading to aliasing of the blood and tissue signals. In that case, a spatio-temporal filter, like an SVD Filter [9], might be necessary to separate the two as their temporal characteristics overlap.

8.2.3 Array clutter filter

The array clutter filter removes the array clutter corresponding to blood signals using a temporal filter. Compared to conventional compounding, we propose two modifications. First, instead of a 'fixed' moving average, we use an adaptive frequency filter that determines the dominant spectral frequencies in the data and applies a band-pass filter around this band. Second, realizing that the flow velocity will vary spatially and temporally, and thus also the spectral content, this adaptive filter is applied on sub-volumes and temporal

windows. This approach only works if a set of dominant frequencies is present. This is the case in a parabolic flow-phantom with a constant velocity as can be seen in Figure 8.4. The figure shows that with a single transmit beam, all signals are contained within a small part of the spectrum around a centre frequency of about 150 Hz. With 3 to 7 directions, the signals are spread out over 3, 5, and 7 lobes, respectively, although the lobes become less distinguishable, and the spacing between the lobes decreases with an increasing number of directions. With 9 directions, there should be 9 lobes if the same trend continued. However, only a single lobe can be distinguished while the other lobes effectively form an 'acoustic noise' floor as the individual lobes start overlapping. The part around 150 Hz remains relatively unchanged by the change in beams, so it can be assumed that this part of the spectrum that is above the 'acoustic noise' floor mainly contains PSF peaks signals, i.e. dominant spectral frequencies, while the rest is mainly array clutter. Therefore, separating that part from the rest of the spectrum should reduce the amount of array clutter in the image.

Directions for maximum array clutter reduction

From Figure 8.4 it follows that with more directions, more lobes appear that are more tightly spaced, until they effectively form an acoustic noise floor. When this floor has formed, the energy corresponding to array clutter has been maximally spread out within the available frequency spectrum and a higher separation between peak PSF and array clutter signals cannot be achieved. This implies that when using a temporal filter, it is not possible to remove more array clutter without also affecting the main-lobes and therefore the best possible performance is reached, both in B-mode quality and for velocity estimation.

The required amount of directions to form the acoustic noise floor can be estimated from the spacing between the lobes of array clutter and the bandwidth of each lobe. The spacing between the lobes in the spectrum is given by $\frac{\text{PRF}}{N}$, where N is the sequence length. This can be derived by noting that array clutter varies periodically, and only a limited set of frequencies can describe that periodic behaviour, similar to the possible frequencies of the Discrete Fourier Transform (DFT). The bandwidth of each lobe of array clutter is determined by the bandwidth of the PSF peak signals from which they originate. These do not necessarily lie within the same sub-volume. Therefore, for simplicity, we approximate it by the bandwidth of the dominant Doppler frequencies in this sub-volume. Furthermore, we use the bandwidth of the signals above the acoustic noise floor as this can be easily extracted from the spectrum if many directions are used. For the spectrum in Figure 8.4 this would be the −20 dB bandwidth that corresponds to about 600 Hz. If the bandwidth is larger than the spacing, the array clutter is maximally spread out. For the bandwidth derived from Figure 8.4, this would be achieved with 7 directions or more. This does not perfectly match the trend in the figure, but we can expect that at approximately this number of directions, performance will no longer improve.

8.2.4 Simulation Setup

An overview of the setup is visible in Figure 8.1 and a summary of all parameters can be found in Table 8.1.

Phantom

To investigate the algorithm described in the previous section we have done simulations using Field II [113], [114]. The phantom contains a 3.2 mm radius vessel at a depth of 15 mm surrounded with a 1 mm wall mainly running along the y-axis at an inclination of 10°, as also shown in Figure 8.1a. In both the vessel and wall, the scatterers are placed randomly with a density of 2 scatterers per axial-wavelength. The difference in mean amplitude between wall and blood is 30 dB. The particles within the vessel follow a parabolic flow profile with a peak speed of 15 cm/s. In the first simulations the speed is kept constant, but in the second set the speed varies in a sinusoidal pattern at 4 Hz. This split was made to be able to investigate the separate effects of the adaptive filters, the use of sub-volumes and the use of temporal windows.

Array

We emulated a sparse matrix as described by Wei *et al.* [270]. The 256 elements are placed according to a density-tapered spiral geometry as suggested by Ramalli *et al.* [62], but modified so that the elements fall on a 215 µm × 215 µm grid. The dimensions of a single element are 195 µm × 195 µm. The excitation signal is 5 MHz sine modulated with a 4 cycle Hann window. No apodization is used since the density tapering already introduces an apodization window by design.

Transmission Sequence

For the transmission beams we use directions based on a Fermat spiral as discussed in Section 8.2.1. The maximum range r_0 was set to 0.1, which implies that a circle with a radius of 6.5 mm at 15 mm depth was illuminated by every transmitted beam, assuming that the used matrix array is circular with a radius of 8.13 mm, which is the radius at which the outermost element is found.

Beamforming

Images were constructed using a Fourier domain method described by Lu [261]. The used grid had a spacing of 215 µm × 215 µm × 38.5 µm, which corresponds to the pitch of the gridded sparse matrix in x and y, and to a spatial sampling frequency of 4 times the centre frequency in z.

Filters

Tissue signals and array clutter corresponding to blood are removed following a two-step filtering process. For both filters all 400 images were used, unless otherwise mentioned. First, we pixel-wise subtracted the DC component from each sequence formed of a single transmission direction separately to remove the stationary vessel wall and its related array clutter. The second filter is a slow-time frequency filter to separate blood from its array clutter as described in Section 8.2.3. The filter is applied on all images, unless otherwise mentioned, but on each sub-volume with a size of 1 mm × 1 mm × 0.2 mm separately without any overlap. To find the dominant part of the spectrum in each subvolume and temporal window, we first determine the peak frequency in the spectrum. Next, we determine the first points before and after the peak that cross the 'acoustic noise' floor, which we define as the mean amplitude of all spectral frequencies. Within this region, we assumed that the main-lobe signals were in the majority, while in the other part there was mainly

array clutter. By retaining this part the majority of the array clutter is rejected and the main-lobes are retained. The filter was applied in the Fourier domain and its profile is constructed in the following way. First, the filter profile is initialized with a gain of 1 for the dominant Doppler frequencies and a gain of 0 for other frequencies. Then, the gain profile is smoothed by convolving it with Gaussian window having a STD of 5 times the spacing in the frequency domain to reduce temporal ringing.

Velocity estimation

To estimate velocities from the images we used the same algorithm as we used in a previous proceeding [173]. Sub-volumes, denoted as blocks here to distinguish from the sub-volumes used in filtering, of RF data with dimensions of 4 mm × 6.5 mm × 3 mm. The velocity was estimated at intervals of about 0.5 mm in each direction, but no spatial averaging was applied. The other settings of the algorithm are noted in Table 8.1.

Performance metrics

To assess the accuracy and precision of the estimated velocity we calculated the mean relative error and the mean standard deviation(STD) for the speed v. The mean relative error $\bar{\eta}_v$ is defined as

$$\bar{\eta}_v = \frac{1}{v_{max} N_p N_t} \sum_{p=1}^{N_p} \sum_{t=1}^{N_t} |v(\vec{r}, t) - v_r(\vec{r}, t)|, \tag{8.1}$$

with $v(\vec{r}, t)$ the speed at a point in space and time, $v_r(\vec{r}, t)$ the ground truth speed at the same point in space and time, N_p the total number of points, N_t the total time steps and v_{max} the peak speed of the flow. The mean STD is defined as

$$\bar{\sigma}_v = \frac{1}{v_{max}} \sqrt{\frac{1}{N_p(N_t - 1)} \sum_{p=1}^{N_p} \sum_{t=1}^{N_t} (v(\vec{r}, t) - \overline{v}(\vec{r}))^2}, \tag{8.2}$$

where $\overline{v}(\vec{r})$ is the average speed at $\vec{r}$. The metrics were evaluated within the vessel and $y = \pm 5$ mm.

Table 8.1: Parameters used in the simulation.

	Parameter	Value
Phantom	Vessel radius	3.2 mm
	Depth	15 mm
	Inclination ϕ	10°
	Rotation θ	0°
	Peak speed	15 cm/s
	Flow profile	Parabolic
	Speed of sound	1540 m/s
Matrix	Elements	256
	Distribution	Tapered Fermat Spiral
	Pitch	215 µm × 215 µm
	Centre frequency	5 MHz
	Transmit pulse	Sine modulated with a 4 cycle Hann window
	Apodization	None
Transmission sequence	Pattern	Fermat Spiral
	Maximum range r_0	0.1
	PRF	1 to 16 kHz
Filters	Tissue Filter	Mean subtraction per direction
	Sub-volume size	1 mm × 1 mm × 0.2 mm
	Filter profile smoothing	Gaussian window. STD of 5 times the frequency spacing
VFI algorithm	# Frequencies ($x \times y \times z$)	10 × 10 × 10
	Frequency Range	0 - 0.4 of Nyquist
	Block size	4 mm × 6.5 mm × 3 mm
	Estimation interval	0.5 mm × 0.5 mm × 0.5 mm
	Block Apodization	Hann
	Phase Averaging	Median of 5 pairs

8.3 Results

8.3.1 Overview - Slice

In Figure 8.5 the estimated velocity and grayscale image after tissue filtering is shown in a single slice for 3 different methods: single plane wave, conventional compounding and the adaptive filter. For both conventional compounding and the adaptive filter the number of directions is chosen such that the relative error is minimal. The figure shows in two ways the difference in the amount of array clutter between the methods. First, after tissue filtering there should ideally be no signal left in the regions outside the vessel. With each method, some signal is still visible outside the vessel, but the amount differs. The average amplitude in dB with respect to the maximum in the image in the regions above and below the vessel wall together, i.e. above the top white line and below the bottom white line, in the images decreases from -27.5 ± 9.0 dB with a single plane wave to -33.0 ± 8.9 dB with conventional compounding, and to -42.9 ± 7.6 dB with the adaptive filter. Second, the velocity, displayed using the arrows, should follow the green line, which shows the ground truth. The average relative error in this plane is 36.3% for a single plane wave, 20.9% conventional compounding and 13.7% for the adaptive filter. Therefore, the comparison shows the amount of clutter is lowest with the adaptive filter, and that it outperforms conventional compounding in this slice.

While conventional compounding and adaptive filter have a difference in relative error of only 4.7% for the arrows at $y = 0$ mm, the difference is larger at any other shown y, with the largest difference of 9.7% achieved at right-most line of arrows. The reason for this variation is that the Doppler frequencies correspond to a projection of the axial velocity components of the flow. The flow profile is constant in the tube, yet the projection of the axial velocity differs in the image; from axial velocity towards the probe on the left-hand side to almost zero in the middle, and somewhat away on the right hand side. A projected axial velocity of zero means that the Doppler spectral content has maximum amplitude around 0 Hz, and so the adaptive filter will get its pass-band around 0 Hz. This is equal to the conventional compounding, which is moving average filter, i.e., a low-pass filter centered around 0 Hz regardless of the spectral content. Hence, the conventional and the adaptive filter have a similar pass-band for the center part of the vessel and the vectors resulting after these filtering steps indeed show similar direction, magnitude, and errors. Towards the horizontal edges of the images the frequencies are not centred around 0 Hz, and the adaptive filter changes its pass-band to follow the dominant apparent frequency content. This leads to lower estimation error throughout the entire image.

8.3.2 Effect of PRF

Figure 8.6 compares the average relative error and STD achieved in the whole vessel with conventional compounding and the adaptive method as a function of PRF. The single plane wave was excluded from this comparison due to its low-quality. The amount of directions was set such different the relative error is minimal for each method and PRF. At all shown data points a filter adapted to the data outperforms a moving average in both metrics. With the adaptive filter, at least a two times lower PRF can be used to achieve a similar error, while it is at least 4 times for the STD. These results show that a filter adapted to the data outperforms a simple moving average filter.

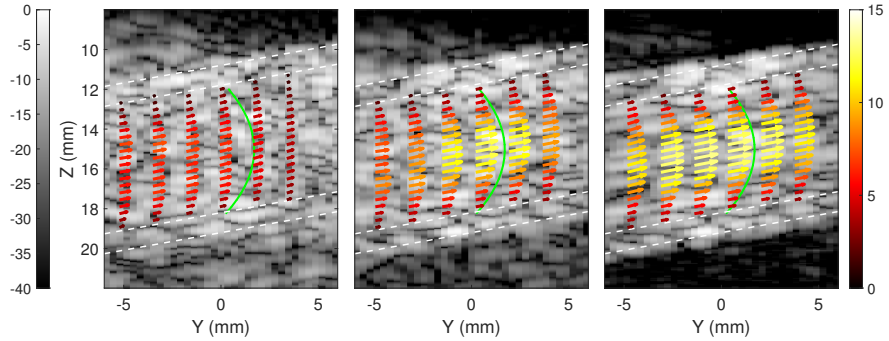

Figure 8.5: Estimated velocity within the vessel in a slice at $x = 0$ mm with a PRF of 4 kHz, shown using the arrows along 6 lines. The green curve indicates the simulated parabolic flow profile for the line at $y = 0$ mm. In the background, the grayscale image after tissue filtering is shown. The white dashed lines indicate where the vessel wall is. The number of directions used for conventional compounding and the adaptive filter is 6 and 10, respectively, which minimizes the relative error. (a) Single plane wave. (b) Conventional Compounding. (c) Adaptive Filter.

For both conventional compounding and the adaptive filter the relative error appears to converge for increasing PRF. From discussion about the directions for maximum array clutter reduction in Section 8.2.3 it could be expected that the error will remain decreasing for larger PRF, as a wider spectrum would allow the array clutter to spread out more. However, the minimum error is also affected by the VFI algorithm, and at high PRF the remaining error is thus mainly affected by the accuracy and precision of the velocity estimation.

8.3.3 Effect of number of directions

In Figure 8.7 the number of directions is varied between 1 and 16 at a PRF of 4 kHz. Similar to the results in Figure 8.6, the adaptive filter outperforms conventional compounding at every data point. Comparing the results at 6 directions where the relative error reaches a minimum with conventional compounding, the error improves by 4.3% with the adaptive method, and the STD improves by 2.0%. With more directions, the performance using the adaptive filter improves even more, until it converges. With 10 directions, the error with the adaptive filter is 5.1% lower than conventional compounding at 6 directions, while the STD is 2.3% lower. Again, this shows that a filter adapted to the data can outperform a simple moving average filter.

With conventional compounding, the relative error reaches a minimum with 6 directions, while the STD remains decreasing. With more directions, and thus a narrower filter with conventional compounding, more high frequencies are attenuated, effectively resulting in slower varying signal and a lower variance in the velocity estimation. At some point, this also means that, beside the array clutter, the frequencies belonging to high velocities are attenuated and thus the relative error increases. Here, this trade-off is illustrated for conventional compounding, but the same trade-off is present with the

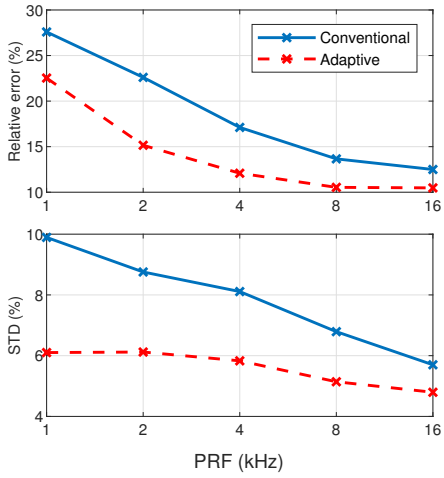

Figure 8.6: Relative error (top) and STD (bottom) of the speed as a function of PRF for conventional compounding and the adaptive filter. The number of beams is set such that the relative error is minimal. Note that the x-axis is logarithmic.

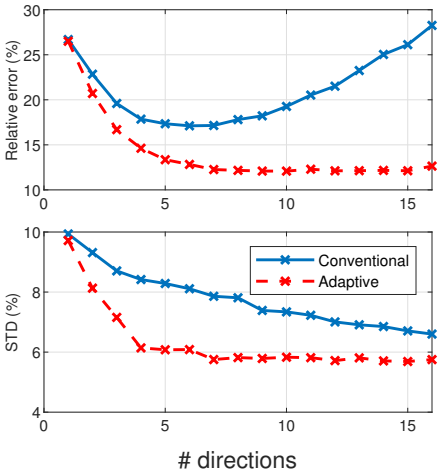

Figure 8.7: Relative error (top) and STD (bottom) of the speed as a function of the number of directions at 4 kHz PRF for conventional compounding and the adaptive filter.

adaptive filter. A narrower filter will thus improve the STD, but also presents a trade-off between retention of main-lobe signals and array clutter reduction.

8.3.4 Oscillating flow

In Figure 8.8a the estimated velocity over time in the centre of the vessel directly below the transducer is shown for a temporal window of 200 ms and 100 ms with 25% overlap between the windows, and a length of 100 ms with no overlap. Focusing on the data with 25% overlap, when the temporal window encompasses all data the highest velocities are underestimated. This indicates the temporal filter is too narrow filter to encompass the higher frequencies. Due to varying velocities, the lower Doppler frequencies corresponding to lower axial velocities are in the majority during this timespan, while there are comparably fewer higher Doppler frequencies. As the method only retains the dominant Doppler frequencies, high frequencies are removed and the velocity is underestimated. With a narrower temporal window, the range of Doppler frequencies in the data is narrower, preventing the removal of main-lobe signal. While the 100 ms window still underestimates the velocity, the same underestimation is present at the highest and lowest velocities, indicating that this is due to the velocity estimation itself, not due to filtering. The lowest error is reached at about 50 ms, as visible in Figure 8.8b. Compared to the 200 ms window, the error drops by more than 3%. With even smaller windows, the error increases again. Here, this is because the attenuation profile of the filter was smoothed to reduce temporal ringing, effectively turning it into an all-pass filter if very few data-points are used. While the smoothing can be reduced, filtering with few samples is challenging in general as discussed in Section 8.2.1. For this data, it follows from Figure 8.8b that a window length in the order of 20% of the oscillation period, i.e. 50 ms appears to be good trade-off. These results show that the

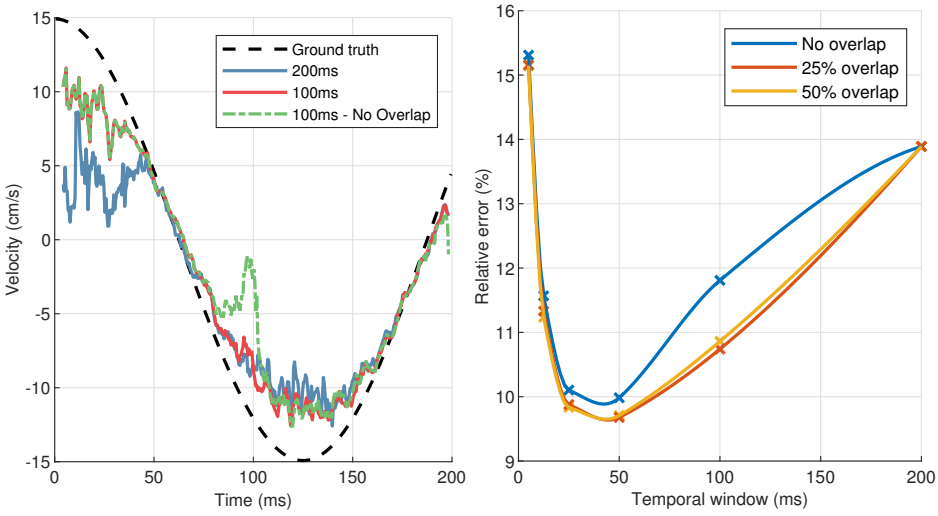

Figure 8.8: (a) Estimated velocity at (0 mm, 0 mm, 15 mm) over time as a function of the temporal window used for the array clutter filter, utilizing 10 directions at 2 kHz PRF. (b) Relative error of the speed as a function of the temporal window used for the array clutter filter, utilizing 10 directions at 2 kHz PRF. The data points are connected using makima interpolation for visualization.

adaptive filter works best if the velocities within its filter samples remain similar, i.e. a short temporal window, but sufficiently long so that the smoothing of filter profile does not cause issues.

Comparing a 100 ms window with and without overlap in Figure 8.8a, the data shows that if no overlap is used, there is a large step in the estimated velocity at 100 ms. This is not unexpected, as in the first 100 ms the velocity is mainly positive, while it is are mainly negative in the second, resulting in vastly different Doppler frequencies in the temporal windows. With an overlap, the transition is smoother resulting in a lower error. The difference between no and a 25% overlap becomes smaller with smaller temporal windows, as shown in Figure 8.8b, proving that the jump in estimated velocity is an effect of the significantly different velocities in subsequent windows. Using a larger overlap than 25% did not seem to have a significant effect, as also shown in Figure 8.8b. Therefore, an overlap is mainly beneficial if the velocities are significantly different between subsequent temporal window, and a 25% overlap seems to work for our data.

8.4 Discussion

In this study we developed an adaptive array clutter filter method to improve performance when estimating blood flow. Array clutter worsens contrast in B-mode images, but also causes a mixing of blood signals originating from multiple locations, thereby potentially causing an inaccurate velocity estimation. The filter consisted of two steps: a tissue filter applied to the data of each transmission direction separately, and an adaptive array clutter filter based on the measured dominant Doppler frequencies applied on sub-volumes and

temporal windows. Velocity estimation is performed on simulated data-sets of which the ground truth velocity profile is known to show the effectiveness of the filtering on the final estimation accuracy and precision. We chose to apply the method on data obtained with a sparse matrix array, which inherently has higher array clutter than a fully populated array. Using the adaptive filter we achieved a relative error and STD of 10.7% and 5.5%, respectively, at a PRF of 16 kHz for a parabolic flow with a peak velocity of 15 cm/s and an inclination of 10°. Compared to conventional compounding, to achieve the same performance the PRF would need be doubled at the least, as follows from Figure 8.6. Furthermore, the adaptive filter reduces array clutter visible in the B-mode images in the regions outside the wall in Figure 8.5 by 15.4 dB at 4 kHz compared to a single plane wave, while conventional compounding only reduces this by 5.5 dB. A lower PRF was used here to more clearly show the differences in the image. The reason for the improvements is that the adaptive filter can apply an arbitrary filter adapted to the data on each sub-volume and temporal window, while conventional compounding uses a fixed low-pass filter for the whole image based on the number of directions. This highlights that the adaptive filter performs better than conventional compounding.

8.4.1 Adaptive filter Parameters

There are several parameters of the adaptive filter that can be modified and have an effect on the performance, i.e. the amount of directions, temporal window, sub-volume and the algorithm to determine the bass-band. We discuss the effects here.

Number of directions

The number of directions has the largest effect on the performance of the adaptive filter as it affects the separation between the array clutter and the peak PSF signals. As discussed in Section 8.2.3, with more directions, the peak PSF signals are unaffected, but the array clutter is spread out more over the frequency spectrum. Because the available bandwidth in the spectrum is limited by the PSF, there is a maximum to how much the array clutter can be spread out. The effect is that with more directions, a lower error and STD are achieved using the adaptive filter until a minimum error and STD are reached at about 7 directions, as shown in Figure 8.7. This corresponds well to the theoretical considerations presented in Section 8.2.3. While this is an approximation using the frequencies of a sub-volume in the center of the vessel directly beneath the probe, it still predicts the results and thus shows that the reasoning is correct. Therefore, more directions will result in a better relative error and STD with the adaptive filter until the array clutter has been maximally spread out over the available spectrum.

While a certain number of directions is needed to achieve the best possible performance, the requirements for effective tissue filtering limit the number, as discussed in Section 8.2.1. We do not think that the number of filter samples will prove an issue due to the use of high frame rates and because relatively few directions are sufficient to reach the best performance. As an example, for a PRF 4 kHz and 7 directions, 57 images for each direction are available within 100 ms. Tissue motion is more likely to limit the number of directions. Using the same PRF and number of directions as before, the aliasing velocity would be 2 cm/s, based on the corresponding slow-time frequency if the tissue motion is purely axial. This is higher than the estimated wall velocities of the carotid, which is about 0.5 cm/s [56],

[90], but lower than the apparent speed of cardiac motion, which is about 10 cm/s in early diastole [1]. In the latter case, the number of directions is thus limited by tissue motion to a number lower than the number required to maximally spread out the array clutter. In conclusion, tissue motion might thus limit the performance of the adaptive filter due to the requirements for effective tissue filtering.

Temporal window

A temporal window for the array clutter filter can be used to adapt the filter to different velocities over time. The results in Section 8.3.4 showed a large temporal window resulted in a high error due the wide range of Doppler frequencies in the window, while for shorter lengths the low number of data points makes filtering difficult. A 50 ms window resulted in the lowest error in this study, which corresponds to about 20% of the oscillation period of the flow. Section 8.3.4 also showed that an overlap between the temporal windows ensured continuity in the data. Without overlap, steps in the estimated velocity were visible when transitioning between windows when the velocity varied over time, as seen in Figure 8.8a. The steps in the data reduced for smaller window lengths, visualized in Figure 8.8b, indicating that the steps mainly appear if the velocities are significantly different in subsequent windows. Therefore, a temporal window length in the order of about 20% of the oscillation period presents a good trade-off between sufficient filter samples and adaptability to the temporal variation, and a small overlap is thus necessary to prevent continuity in the data.

While 20% of the oscillation period works for the setup in this paper, it does not directly translate to other flow profiles, PRFs and arrays. To convert it to other situations, it can be noted that it is the difference in Doppler frequencies over the temporal window that affects the performance, not the velocity difference itself. Furthermore, with a higher PRF larger variations in velocity over time could be measured, and this can be addressed by converting it to a difference within a number of temporal data points. Therefore, by converting the period to a maximum difference in Doppler frequency within a number of data points, the results can also be applied to other situations.

Sub-volume

Sub-volumes are used to adapt the filter to different velocities spatially, and the effect is similar to the temporal window. Therefore, we did not systematically investigate the effect of the sub-volume size in this paper. There are however two notable differences. First, the array clutter does not apply a spatial filter, and therefore small sub-volumes do not affect the filtering performance. However, small sub-volumes will suffer from stochastic noise if present, which is not the case in this paper, and also the stochastic nature of the backscattered signal itself [278]. Both effects will negatively affect the ability to estimate the dominant Doppler frequencies within small sub-volumes, as larger sub-volumes will average out the variation. Second, Doppler frequencies do correspond to a projection of the velocity, as mentioned in Section 8.3.1, and the sub-volume size that achieves the lowest error might thus differ depending on the position of the sub-volume even if the velocities are the same. The effect of both should be investigated in a future study.

Pass-band determination

For the results shown in this study, we choose the cut-off points for the filter at the first frequencies that coincided with the mean amplitude of all frequencies around the peak frequency. This produced good results for this paper, but we expect that this approach is not robust enough. Choosing the first frequency that crosses a threshold is likely severely affected by noise, especially if small sub-volumes or short temporal windows are used. There was no stochastic noise present in this study, but will be present in realistic conditions. Furthermore, by changing the threshold the relative error can be optimized, as implied from the results obtained with conventional compounding in Figure 8.7, and therefore it is possible that the used threshold might not provide the best results in various situations. Therefore, the method for determining the pass-band should be revised in a future study.

8.4.2 Other applications

In this study, we applied the method to measuring blood flow, but the method can also be applied to other applications. For B-mode imaging the method can also provide improvements, as shown in Section 8.3.1, as well as other motion applications. However, the improvement might be less compared to conventional compounding. For example, in Shear Wave Imaging (SWI) shear waves are tracked by measuring the axial velocity of tissue. This motion only lasts a few milliseconds [92], [279]–[281], which is too short to apply any temporal windowing, because filtering is ineffective with few samples. Therefore, the performance difference compared to conventional compounding is smaller than when measuring blood flow. Still, we expect that the application of this adaptive method can improve the trade-off between array clutter reduction and main-lobe retention, as commonly seen with conventional compounding in SWI [92], [279]–[281], due to the use of sub-volumes and an arbitrary filter profile, thereby improving the accuracy and precision of the measurements.

8.4.3 Performance metrics

In this study, our aim was to improve the accuracy and precision of velocity estimation. Therefore, we also directly evaluated the performance on the speed. Whether the settings leading to smallest error and variance in the velocity estimation are equal for those leading to highest contrast and resolution in the B-mode image needs further investigation, but our technique showed a significant improvement of contrast in Figure 8.5 compared to a single plane wave and conventional compounding.

While we did evaluate the speed, we did not show the accuracy and precision of the estimated direction. This was omitted for brevity, but further analysis (not shown) showed that the relative error and STD of the direction had the same trend as in Figure 8.6 and Figure 8.7. The only exceptionto this was the STD using conventional compounding for more than 6 directions in Figure 8.7. Instead of decreasing like the STD of the speed, it went up again as the estimated velocities tended to zero and small errors can then result in vastly different directions. Therefore, for the adaptive filter a low error and STD for the speed implied the same for the direction.

8.4.4 Practical application

For practical application of this adaptive method, the performance in a realistic scenario, the computational performance and the parameters of the algorithm that should be set are important. Here we shortly discuss these three.

Performance in realistic situations

In this study, we have used a parabolic flow profile with a peak velocity of 15 cm/s. This is a relatively low velocity with a low spatial gradient of the velocity. For example in the carotid, velocities could exceed 1 m/s [49], [247], and larger gradients, due to helical flow profiles [53] or vortices [282], can be present as well. We think that the adaptive filter could handle those situations as well, especially after revision of the method to determine pass-band of the filter, albeit at an expectedly reduced due to the larger range of Doppler frequencies. However, this should be further investigated.

Computational performance

The determination of the pass-band and application of a separate filter per sub-volume and temporal window is more computationally expensive than conventional compounding. However, the necessary operations, like a fast Fourier Transform or thresholding, are common in regular Doppler and the method does not require iterations. This limits its expected impact on the computation time.

Parameters

The performance of the adaptive filter is affected by the PRF, the directions and the sizes of each sub-volume and temporal window. These parameters should be set depending on the measurement, but they do not necessarily require extra intervention by the user. The PRF and the maximum range of the directions are set by the measurement area, which is already commonly set by the sonographer during current clinical examinations. The number of directions is limited by tissue motion. This could either be estimated during an examination, or be based on wall filter preselect settings on the ultrasound machine, in line with the implementation of wall filter settings in current clinical systems. The size of each sub-volume can be adaptively determined based on the vessel size and expected velocities, which can be extracted by thresholding, while the temporal window length can be based on the PRF and expected velocities. The parameters could thus either be chosen automatically or based on current common methods of user settings, although it should be verified whether this is robust.

8.4.5 Alternative methods

We proposed an adaptive filter method as alternative to conventional compounding, but there are also alternatives. First, modifications to conventional compounding exist that reduce the amount of directions required for a similar image quality [283]–[285]. For example, with use of an SVD filter Guo *et al.* [283] allowed for a two-fold reduction in the number of angles while keeping the same image quality. However, similar to the advanced beamforming methods, it has not been shown whether these methods work when motion is involved. Second, conventional compounding could be paired with Motion compensation (MoCo) as an alternative to this method [122], [123]. By compensating the underlying

tissue and/or blood motion between the frames used to compound a single image, ideally the peak PSF signals end up at the same positions in each low-quality image and therefore conventional compounding will remove array clutter due to its low-pass nature. How this approach compares to the adaptive method presented in this paper should be further investigated.

8.5 Conclusion

In this article we developed an adaptive filter to reduce array clutter and yield better vector flow velocity estimations, compared to the conventional moving-average coherent compounding. The filter consisted of two steps: a tissue clutter filter applied to the data of each transmission direction separately, and an adaptive array clutter filter based on the measured dominant Doppler frequencies applied on subvolumes and temporal windows. Using the adaptive filter we achieved a relative error and STD of 11.3% and 4.1%, respectively, at 16 kHz for a parabolic flow with a peak velocity of 15 cm/s and an inclination of 10°. Conventional compounding requires at least twice the PRF to achieve a similar performance, and it has been shown that it cannot adapt to spatial and temporal variations in velocities. Furthermore, the adaptive filter reduces array clutter visible in the B-mode images in the regions outside the wall in Figure 8.5 by 15.4 dB compared to a single plane wave, while conventional compounding only reduces this by 5.5 dB. Therefore, this paper shows that the adaptive filter outperforms conventional compounding, and may aid in measuring blood flow velocities using sparse arrays.

9

Discussion and conclusion

This thesis focused on developing ultrasound matrix transducer technology with the final aim of accurately quantifying blood flow, which requires full flow resolution in both space and time. Two specific applications were chosen to benefit from this development. First, perfusion monitoring in the preterm brain would benefit from high-frame-rate volumetric imaging to more effectively distinguish slow-moving blood from tissue and to image the whole brain without moving the transducer, since we foresee a wearable probe that must acquire data autonomously. Second, for screening the carotid artery in adults, matrix transducers allow for measuring high-velocity blood in all three spatial directions, which can exceed 125 cm/s [49], [247]. To satisfy the requirements, matrix transducers are required, but their utilization is hampered by several challenges depending on the application. In this chapter, we first discuss how we addressed these challenges and how effectively they are resolved by the work presented in this thesis. Then, we will discuss the matrix transducers that were specifically developed for these two applications.

9.1 Matrix transducers application challenges

9.1.1 Trade-offs in ASIC-integrated matrix design

The specifications of ultrasound matrix transducers involve a trade-off between resolution, side-lobe level, frame rate, operational flexibility and signal-to-noise ratio (SNR). **Chapter 2** focused on this trade-off, providing a simplified and concise overview of the process to design a new ultrasound PZT-on-ASIC matrix for monitoring the preterm brain. The process involved defining the clinical requirements, examining the acoustical effects using a specialized numerical phantom, and studying the impact of specific electronic components and ASIC design. This investigation led to identifying a set of matrix parameters that should satisfy the clinical requirements, are feasible to manufacture, and fit within the space and power constraints of an ASIC. Although **Chapter 2** focused on a specific application, the approach is applicable to other uses requiring matrix probes. This process allows us to optimize the trade-offs of an ultrasound transducer for any specific application.

Image quality metrics

In the design of a matrix transducer the final image should be judged and quantified. In **Chapter 2** we did that solely using the signal-to-clutter ratio (SCR), that was defined as the peak signal amplitude divided by the mean amplitude in a block that contained a single point scatterer. Other metrics exist that can provide information about the amount of clutter. One such metric is the maximum side-lobe level [162], [286]. It can be a good metric to evaluate sparse matrices, because a low peak implies a low overall level as well, but it does not directly translate to the total clutter level in an image in general since the whole PSF contributes. Another metric is the contrast-to-noise-ratio (CNR) that is somewhat similar to the SCR. High SCR, and thus low clutter levels, will also result in a high CNR. However, as the phantom does not contain cysts, the application of this metric was not possible. The difference between the expected and simulated/measured arrival times can also be used as a metric [287]. While this is not a direct metric of clutter, differences between the expected and actual arrival time can result in extra clutter as the signals are not correctly beamformed. It would therefore be a good addition to use beside the SCR as it can determine one of the possible sources of clutter. Finally, the sensitivity or SNR could have been used. Like the previous metric, it is not direct metric of clutter, but a low

sensitivity for the signal of interest increases the influence of noise on the results. This metric would be especially important when using sparsity as fewer elements reduce the SNR [166], [269], but pitch and the use of μBF can also have an effect on the sensitivity, because larger (effective) elements have a reduced sensitivity to signals from scatterers at an angle. Therefore, beside a lower SCR, as shown in Section 2.3.3 and Section 2.3.4, it would also reduce the sensitivity. We did not use this metric as we did not expect large variations in sensitivity with the investigated parameters, but this kind of metric should be included in future studies to verify this. For our application, we think the SCR works best as a metric of clutter, and that the difference in arrival time and SNR can provide additional information not caught in the SCR.

The resolution is a generally used metric to evaluate the performance, for example by the generally used full width at half maximum. We could have evaluated it in conjunction with the SCR, but we did not use such a metric for two reasons. First, the resolution can be traded off against the amount of clutter in certain situations. For example, excluding elements with a low sensitivity can reduce clutter at the cost of resolution. Whether such a trade-off is beneficial should be further investigated. Second, the SCR metric is affected by the resolution. A wider PSF will result in a more spread out signal, meaning a lower peak and higher mean value and thus a lower SCR. The CNR, used in **Chapter 5**, has a similar issue where the resolution can influence the results. However, in that chapter we did explicitly ignore an area around the edges of the cysts to reduce the influence of resolution, as is visualized in Figure 5.8. We could use something similar for the SCR. For example, we could exclude everything above −6 dB as compared to the peak from the clutter part or only use a region at the edges of the block as a measure for the clutter. Such a modification will reduce the influence of resolution. By taking the above into account, the use of resolution as a metric besides a metric for clutter can be beneficial to investigate the performance.

Another effect of note about the SCR is that on the spacing of the scatterers. Increasing the spacing will decrease the amount of clutter and thus improve the SCR, and a minimum spacing is necessary so that there can be a clear distinction between signal and clutter. This effect should be further investigated, but it is likely that the SCR is best used to investigate trends, as done in **Chapter 2**.

9.1.2 Data reduction methods

To resolve the data transfer bottleneck between the probe and imaging system, a data reduction method is needed that can reduce data in the probe and then recover a high-quality image in the imaging system. Two-stage beamforming is such a method. In **Chapter 5**, we presented a two-stage approach based on the wave equation specifically for phased arrays. While a wave equation method has been shown to be more computationally efficient for a linear array and has the potential for better image quality, it did not exist for the phased array geometry. Our results showed that we successfully developed this method. However, instead of a large gain in computation time, the method achieved both good resolution and low sidelobe levels simultaneously, unlike the time-of-flight alternative. Therefore, we extended the applicability of two-stage beamforming using the wave equation approach.

An additional note should be made though. Unlike the other chapters, the method described in **Chapter 5** uses line-by-line imaging and is therefore not well suited for high-frame-rate imaging of a large field-of-view (FOV). With the settings in **Chapter 5**, a

frame rate of 31 Hz could be achieved for a 2D slice, which is too low for high-frame-rate applications and would be even lower when scanning a volume. While this is for a relatively large FOV and depth range, frame rates in the order of 1 kHz can only be achieved with very few scan lines, resulting in either a small FOV with high image quality or a larger FOV with lower quality. Whether this is suitable for monitoring the preterm brain is currently unknown. However, the data reduction is very simple to implement in a probe [288], [289], and extension of this method to 3D is possible [290]. Therefore, this method is best suited for low-cost, portable systems, or probes that are used in size-restricted areas such as Intravascular Ultrasound.

9.1.3 Sensor-ASIC integration

An ASIC-integrated matrix can be specifically adapted to a specific application and offers the widest variety of data reduction methods. However, integrating an ASIC with a transducer is a complex process, and we observed two specific issues with a PZT matrix designed for imaging the carotid bifurcation. These issues were due to non-idealities in the electronics causing unwanted electronic-switching artefacts and the integration of the ASIC in the acoustic stack. In this thesis, we addressed these problems, as discussed below.

Electronic-switching artefacts

In the matrix designed for carotid imaging, switching is performed between the transmit and receive channels using high-voltage MOSFETs. In an earlier design, these MOSFETs generated parasitic transmissions, causing visible artefacts in the image. The non-ideality causing this issue is a known problem, and solutions exist, but they require additional electronics that demand more footprint on the ASIC, which was not available. An alternative solution was found by changing the switch controller in the new second-generation ASIC such that a path to ground was created at critical switching moments. The method presented in **Chapter 3** reduced the switching transients by 20 dB. Combined with the increase in maximum transmission amplitude by about 6 dB in the new ASIC, the signal strength difference between the transmitted pulse and the parasitic pulses increased to 46.7 dB, from 20 dB at most in the first design. Therefore, the effect of this artefact has been successfully and significantly reduced.

Acoustic stack

Building an ultrasound transducer on top of an ASIC has several major challenges since the ASIC has a high acoustic impedance and very low attenuation. This can cause severe cross talk between the elements by Lamb-waves travelling in the ASIC. To solve this, we developed an attenuating interconnection layer to decouple the ASIC from the elements that can be integrated into our small-pitch manufacturing process. This layer consists of small channels filled with conducting silver glue and a non-conducting epoxy with a high attenuation. The thickness of the interposer was chosen to significantly dampen the waves. This interposer layer has been manufactured using conventional dice-and-fill methods. **Chapter 4** showed that this interposer layer removed cross talk caused by Lamb waves in ASIC since the peaks in the directivity pattern that indicate this, as described by Shabanimotlagh *et al.* [86], were not observed any more. Therefore, this interposer layer successfully resolved this specific issue.

While cross-talk via Lamb waves was resolved with this interposer layer, we still observed irregularities in the directivity pattern. In Section 4.B, we identified three types of cross-talk: (i) electrical cross-talk, (ii) non-attenuating acoustic cross-talk, and (iii) attenuating acoustic cross-talk. However, we did not identify the exact origins of these types of cross-talk. Here, we delve further into these types. (i) The electrical cross-talk resulted in an acoustic pulse from all elements simultaneously, shown in the directivity pattern as a peak at 0° along the x and y directions, with an amplitude approximately 30 dB lower than the original pulse. This type of cross-talk was not observed in the first-generation ASIC. This cross-talk appeared after a change made to resolve an issue we observed in the new ASIC. In the received signal around 7.5 MHz, the center frequency of this matrix, we observed an oscillation due to interaction between neighboring ASIC tiles. This was eliminated using a resistor placed in series with the ground foil, but in turn caused parasitic transmission on the other elements. Therefore, this type of cross-talk is due to an electrical issue. (ii) The non-attenuating acoustical cross-talk is characterized by two dips in the directivity pattern around ±40°. Cross-talk a propagation speed between the elements of 2450 m/s would explain these dips. This velocity falls within the range of common polymers [291]. In the measurement setup, we use a 25 µm polyester layer between the transducer and water. Waves travelling through this layer could generate these dips, as shown by Shabanimotlagh in his thesis [292, Fig 6.11]. Therefore, non-attenuating acoustic cross-talk is due to the measurement setup. (iii) The attenuating acoustic cross-talk narrows the directivity pattern and results in extra peaks around ±55°. This effect can be characterized by a delay between elements corresponding to a speed of 1800 m/s and an attenuation of 3.5 dB between elements. These values correspond to the epoxy materials used in the interposer layer, and this cross-talk is thus due to waves travelling in the interposer. However, this kind of cross-talk can be expected with any kind of backing. Because the materials of the interposer layer can be modified, unlike the material of the ASIC, this kind of cross-talk can be resolved by using materials with a higher attenuation in the interposer. Different materials might also resolve the ringing visible in Figure 4.8, which we believe is caused by the relatively low attenuation of the material in the conductive channel. In summary, the introduction of the interposer resolved the cross-talk via the ASIC but introduced another source of cross-talk. However, this can be resolved by using materials with higher attenuation.

9.1.4 High-frame-rate data acquisition scheme

The matrix designed for imaging the carotid bifurcation, described in **Chapter 4**, can read out the combined signal of a set of elements per row. This channel reduction strategy significantly reduced the number of required channels in receive, making it feasible to handle with current technology. However, reading out the data from all columns separately would result in a too low frame-rate for certain applications. Therefore, we developed a high-frame-rate imaging scheme for this matrix. This imaging scheme is like an electronically translatable linear array, and we evaluated its performance for carotid pulse wave imaging (CPWI) in **Chapter 6** and for vector flow imaging in **Chapter 7**.

Carotid pulse wave imaging

For CPWI, a volume rate of about 1000 volumes per second is necessary. To achieve the required rate, the simulations and experiments in **Chapter 6** showed that with the proposed imaging scheme, the lateral resolution is about two times wider and the clutter level increased by 4 dB compared to an imaging scheme where all columns are read out, which results in too low a frame rate for the application. Having an imaging scheme that can achieve the required frame rates could be beneficial to generate 3D maps of carotid artery stiffness, providing valuable information regarding the cardiovascular risk. However, a limitation with the approach in this chapter is that the performance is only evaluated on B-mode images, in this case using the resolution and CNR. High B-mode quality does not ensure accurate displacement estimation, which is ultimately required to estimate stiffness in CPWI. Further investigation is necessary to evaluate the performance of the imaging scheme for CPWI.

Vector flow imaging

In **Chapter 7**, the same imaging scheme was applied to vector flow imaging in a simulation setup with velocities similar to those in the carotid artery. Compared to CPWI, this requires higher frame rates, necessitating a re-evaluation of the imaging scheme's performance. The results showed that it is feasible to measure the high velocities in the carotid artery using an electronically translatable linear array imaging scheme, provided the appropriate trade-offs are made.

Compared to the previous study for CPWI, the performance was directly evaluated on the estimated velocities and not on B-mode quality. The results in **Chapter 7** indicated that this is important, as higher resolution, e.g., with more shots or a larger sub-aperture pitch, does not necessarily result in better estimation performance. This is mainly because better resolution can also reduce the frame rate or increase the amount of clutter. Furthermore, it was shown that depending on the velocities present, the optimum parameters of the imaging scheme change. Therefore, evaluating performance on metrics relevant to the final applications is important.

The results in **Chapter 7** do not contain experimental results and used a relatively simple phantom. Therefore, there can still be doubts about the feasibility in vivo. However, we have performed initial experiments and presented the results in a proceeding [293]. These showed that the estimated direction, profile, and velocities were feasible, but due to the lack of a constant parabolic flow velocity, the accuracy and precision could not be estimated. While further verification is necessary, the results in **Chapter 7**, combined with those in the proceeding, indicate that it is feasible to measure the high velocities in the carotid artery using an electronically translatable linear array.

9.1.5 Vector flow imaging with a sparse array

Sparse arrays suffer from higher side-lobe levels that can be detrimental to performance in vector flow imaging. Coherent compounding can reduce the side-lobe level, but this method attenuates and possibly even removes high-velocity signals, resulting in an underestimation of the velocities. In **Chapter 8**, we developed a method that applies an adaptive filter based on the velocities present, thereby preventing the loss of high velocities. We demonstrated that the new method achieves a similar error in estimation as coherent compounding with

a twofold lower pulse repetition frequency, significantly lower variance, and that it can adapt to both spatial and temporal velocity variations. Therefore, we have shown that the adaptive filter outperforms conventional compounding and can aid in measuring velocities using sparse arrays.

9.2 Realized matrix arrays

In this thesis we developed an ASIC-integrated matrix for monitoring the brain of preterm babies, and we further developed an ASIC-integrated matrix for imaging the carotid bifurcation. For both, several prototypes have been realized. In the section we will discuss their performance, issues and possible improvements.

9.2.1 Matrix transducer for preterm brain imaging

Chapter 2 showed that with current technology, creating a fully-populated ASIC-integrated matrix for preterm brain monitoring is challenging. The main issue was the need for a small pitch due to the required high frequency for high resolution and sufficiently large steering angles, which we could not achieve within this project. Initially, this was due to expected manufacturing problems with a pitch smaller than 100 µm, but an even larger pitch was necessary in the second prototype as the electronics required a larger footprint on the ASIC. To resolve this, further development on the electronics could help achieve the same functionality within a smaller footprint, or alternatively, further research on the clinical requirements and design could result in a new design that satisfies the updated requirements.

Regarding further research on the clinical requirements, ideally, this would require a matrix to monitor the brain and investigate what is important. As such a matrix does not exist and creating one is challenging, an alternative is necessary. In parallel with the design of the thesis, clinical research was also performed. Kortenbout in her thesis [97] showed that monitoring during surgery using a 1D-array holds significant promise and is likely an effective diagnostic tool. However, those measurements were still performed by hand. The next step would be to transition to constant monitoring by integrating a 1D-array in a probe holder. While this would not provide volumetric information, it can be used to further investigate the effects of medication and surgery, and identify markers that indicate when an intervention is necessary. This could help refine the clinical requirements. Therefore, we think that the next intermediate step towards complete monitoring of the brain is constant monitoring using a 1D-array.

Alternative matrix types

An alternative to modifying the design or further ASIC development could be the use of one of the other array types, as mentioned in Section 1.3.2. However, they all have specific issues that hamper their utilization for this specific application, as mentioned in the introduction. A *fully-populated matrix* is not an option as the enormous number of elements, 22 300 in our design, are too many to handle separately, and a much smaller matrix would not achieve the required resolution. The *RCA* can only interrogate the volume directly in front of the probe, which is insufficient for preterm brain imaging. While lenses can increase the FOV, as shown by Audoin *et al.* [69], they also worsen the SNR and bandwidth, and can introduce additional artefacts, especially for a large FOV. Further

development could possibly resolve these issues, but at this point in time, an RCA with a lens does not fit the clinical requirements. A *sparse matrix* for this application would have very few elements relative to its total aperture. The spiral array used in **Chapter 8** occupies about 5 % of a fully-populated circular matrix with a radius of 8.1 mm, which is the radius where the outermost element of the sparse array is located. This matrix would cover the fontanel, but that is for a frequency of 5 MHz, and for our application, we aimed at a higher frequency. This would require smaller elements compared to a fully-populated matrix, resulting in even more side-lobes and an even lower SNR. We especially think that the SNR would be an issue. While the attenuation is relatively low in the preterm brain, the expected SNR reduction of almost 50 dB is enormous, based on a 9 dB lower SNR for every halving in the number of elements compared to a fully-populated matrix [166], [269] and the reduction in area expected when using a centre frequency of 11 MHz. An increase in the number of elements would help, but that might present problems for the wiring. There are however two main advantages compared to the ASIC-integrated matrix that we designed. First, a sparse matrix can achieve an 8 times higher frame rate due to the lack of TDM, and therefore could at least partially compensate for the high side-lobe level and low SNR with coherent compounding. A full recovery for the SNR is not possible because the SNR increases with the square root of the ensemble length [7], and thus the SNR would increase by only 9 dB using coherent compounding. Second, while a sparse array would still require electronics in-probe so that it can be used wirelessly, the electronics can be placed away from the acoustic stack, unlike the ASIC-integrated matrix. This prevents negative effects on the acoustical performance and allows for the electronics to be made with less stringent space constraints. In summary, a different kind of matrix also likely would not satisfy the requirements.

Hybrid matrix

A combination of the concepts of a sparse and ASIC-integrated matrix could also be an interesting alternative. In **Chapter 2**, it was concluded that not all required electronic functionality fit into the available area dictated by the requirements. Using fewer elements placed further apart results in more available space for the electronics and could therefore resolve this issue. Compared to a sparse array, this hybrid would likely allow for more elements, because other channel reduction methods can also be used, consequently resulting in a lower side-lobe level and higher SNR. Therefore, the use of sparsity could be a good extra channel reduction option for ASICs

To evaluate whether sparsity would be beneficial for the preterm brain monitoring application, we will discuss the advantages and disadvantages of replacing TDM or μBF , which are currently used in the specifications determined in **Chapter 2**, with fewer elements to reduce channel count. Replacing TDM would allow for higher frame rates, enabling the measurement of higher velocities and a possible focus on larger blood vessels. This increase in frame rate could also potentially compensate for the increased side-lobe level and lower SNR by employing coherent compounding. To estimate whether it is feasible to compensate for the higher side-lobe level, we can use the results obtained in other papers. Montaldo *et al.* [7] observed that a 10 dB increase in contrast can be gained by using an ensemble length of 8, while Diarra *et al.* [286] showed that an 8-fold reduction in the number of elements at most resulted in a 10 dB increase in side-lobe beam power. While they use different metrics, they are similar because high contrast also implies low

side-lobe beam power. Therefore, it seems feasible that the higher side-lobe level due to sparsity can be compensated for by coherent compounding. It is even more likely if the method developed in **Chapter 8** is considered, as it was shown that this method outperforms coherent compounding. Compounding can also partially compensate for the loss in SNR, but not completely as discussed in the previous section. The 8-fold reduction in elements and 8-times compounding would result in a net loss of 18 dB in SNR, which is about 20 dB lower than the loss in SNR for the sparse matrix considered in the previous section. Therefore, replacing TDM with sparsity appears to be a valuable option for this application. Replacing µBF would result in effectively smaller receive elements. This allows for larger steering angles in receive without a significant increase in side-lobe level, thereby increasing FOV and requiring fewer images to image a large volume. However, the sparsity would increase the side-lobe level again, also in regions that could be imaged without large steering angles and thus did not suffer from the effectively larger elements with µBF . It thus seems likely that at least part of the image quality will suffer from sparsity, and compared to replacing TDM with sparsity, this seems like a much less beneficial option. The SNR would also be lower, but because it is only a 4-fold reduction if µBF is replaced, this amounts to only 18 dB, which is equal to the loss if TDM is replaced. Comparing the two options, we think that replacing TDM with sparsity is the best, as it results in similar image quality with the advantage of more room for the electronics. Therefore, the use of sparsity is likely a good extra channel reduction option for this application.

Current state

Monitoring brain perfusion using an ultrasound matrix array is challenging because it requires a relatively high frequency to image small vessels, and ideally, the matrix should operate wirelessly to integrate with other monitoring modalities. An ASIC-integrated matrix or a hybrid matrix that combines sparsity with an ASIC are currently the best options, but further research and development are required to create specifications that fit the clinical requirements. In parallel with further developing the matrix, research into the clinical requirements using a 1D-array for monitoring can be performed. While constantly monitoring perfusion in the whole brain is not yet possible, the research presented provides possible next steps towards this goal.

9.2.2 Matrix transducer for Carotid imaging

Chapter 4 describes the design choices, manufacturing process, and acoustic characterization of an 8 × 1 tiled sample of a second generation ASIC for imaging the carotid bifurcation, together with an initial imaging experiment. In **Chapters 6 and 7**, we applied this matrix to carotid pulse wave imaging and blood flow imaging, respectively, using a specifically designed imaging scheme that corresponds to an electronically translatable linear array. Focusing on blood flow, the results in **Chapter 7** indicated that it should be feasible to image the high velocities around the carotid bifurcation, although measuring high spatial velocity gradients might be hampered by the low lateral resolution of the imaging scheme. Initial experiments also pointed towards feasibility [293]. Therefore, we think that measuring the haemodynamics around the carotid bifurcation is possible using this matrix.

Possible improvements to the ASIC

The presented second-generation ASIC contains various improvements over the first generation, which was showcased by Kang *et al.* [71]. Manufacturing has been made easier by increasing the ASIC size, thereby only requiring tiling in a single direction, and the larger pitch in the new version allows for higher transmit voltages and more pre-programmed patterns. Additionally, it resolves a switching artefact, as discussed in **Chapter 3**. However, this new generation ASIC does not contain on-chip pulsers, unlike newer ASICs designed for different applications [133], [140]. If this can be included in a third-generation ASIC, either per row or per element, it would free up 120 channels that can be used for other purposes. We propose two possible modifications that make use of the 120 extra channels. The first modification would be to change the element pitch from 300 µm × 150 µm to 150 µm × 300 µm, and increase the number of rows from 120 to 240. Doing this would not require changes to the pitch-matched electronics, except for some re-routing of current electric connections in the circuit design. From the results in **Chapters 6 and 7**, the extra large elements in the column direction would hardly make a difference. With the high-frame-rate imaging scheme, the elements are already larger, and increasing or decreasing the sub-aperture width by 150 µm does not significantly affect the performance. The smaller row-wise elements could be helpful with steering in transmit and receive in that direction, thereby reducing clutter and increasing resolution. However, solely considering the electronically translatable linear array imaging scheme, there does not seem to be any need for smaller elements in that direction, as the performance is mainly limited column-wise. The second possible modification is to keep the elements the same but split the array into two sides, with each side containing 120 receive channels. This allows for an increase in sub-apertures and/or a decrease in their individual width, thereby allowing higher image quality due to better contrast and lateral resolution. This, in turn, would lead to better estimation of the velocities, as shown in **Chapter 7**. With this modification, the performance achieved at 75 cm/s without the modification can then be achieved at 150 cm/s, which would improve the relative error by 3 % and the STD by 1 %, as derived from Figure 7.4a. The only downside to this modification is that the best performance is only achieved if the imaging volume is centred around the split, causing the performance to be affected by the placement of the probe. However, this might be resolved if the position of the left and right side could be made programmable in the ASIC. Therefore, we deem the second modification the most beneficial for a third generation ASIC.

Alternative matrix types

Unlike for preterm brain monitoring, other matrix types are also an option for this application. For the sparse array, blood volume [294] and Spectral Doppler [295] measurements have already been performed on the carotid in-vivo and the results were promising. Vector flow imaging has also been performed using a sparse matrix and it showed performance comparable to the performance obtained by using a linear array for 2-D velocity measurements [254]. However, as this has only been performed in-vitro, further research is required. The adaptive filter method in **Chapter 8** should prove useful in reducing the negative effects of the sparse array when imaging blood. Therefore, we think that blood flow measurements in the carotid artery are also feasible with a sparse matrix. Jørgensen *et al.* [256] showed that an RCA can accurately measure vector velocities in a phantom with a realistic geometry and velocities. Therefore, using an RCA is feasible as well. Finally,

using a fully-populated matrix, in-vivo measurements on the carotid have been performed by Correia *et al.* [296], thereby showing that it is possible with this kind as well.

9.3 Conclusion

In this thesis, we have advanced the towards the use of ultrasound as a diagnostic tool for quantifying blood flow by developing ultrasound matrix transducer technology, focusing on two applications: perfusion monitoring in the preterm brain and atherosclerosis screening. For preterm brain monitoring, we identified and addressed technological challenges, proposing several directions for further research to enhance ultrasound's capability in monitoring preterm brain perfusion. For atherosclerosis screening, particularly in measuring flow in the carotid bifurcation, we concentrated on an ASIC-integrated matrix approach by developing a high-frame-rate imaging scheme and resolving integration issues. As an alternative to the ASIC-integrated matrix, we also contributed to the advancement of sparse matrices by devising a method to reduce side-lobes especially when measuring velocities. While the focus was on these two applications, the advancements made can also be utilized in other areas. Although ultrasound is not yet capable of quantifying blood flow in all scenarios, it has demonstrated significant potential as a valuable diagnostic tool in these areas.

Bibliography

[1] T. L. Szabo, *Diagnostic Ultrasound Imaging*. Academic Press, 2004, ISBN: 9780126801453, DOI: 10.1016/B978-0-12-396487-8.00001-X.

[2] R. S. C. Cobbold, *Foundations of Biomedical Ultrasound*. Oxford University Press, 2007, ISBN: 0199775125, DOI: 10.1093/oso/9780195168310.001.0001.

[3] S. Campbell, "A short history of sonography in obstetrics and gynaecology.," *Facts, views and vision in ObGyn*, 2013.

[4] K. Graff, "Historical highlights in ultrasonics - 2," in *Proceedings of the 2004 IEEE International Frequency Control Symposium and Exposition, 2004.*, IEEE, 2005, ISBN: 0-7803-8414-8, DOI: 10.1109/FREQ.2004.1418421.

[5] K. Griffiths, "An historical look at ultrasound as an Australian innovation on the occasion of the ultrasound stamp issued by Australia Post – 18 May 2004," *ASUM Ultrasound Bulletin*, 2004.

[6] J. Bercoff, "Ultrafast Ultrasound Imaging," in InTech, Aug. 2011, DOI: 10.5772/19729.

[7] G. Montaldo, M. Tanter, J. Bercoff, N. Benech, and M. Fink, "Coherent plane-wave compounding for very high frame rate ultrasonography and transient elastography," *IEEE Transactions on Ultrasonics, Ferroelectrics and Frequency Control*, Mar. 2009, DOI: 10.1109/TUFFC.2009.1067.

[8] J. Voorneveld *et al.*, "High frame rate ultrasound particle image velocimetry for estimating high velocity flow patterns in the left ventricle," *IEEE Transactions on Ultrasonics, Ferroelectrics, and Frequency Control*, 2018, DOI: 10.1109/TUFFC.2017.2786340.

[9] C. Demené *et al.*, "Spatiotemporal clutter filtering of ultrafast ultrasound data highly increases Doppler and fUltrasound sensitivity," *IEEE transactions on medical imaging*, 2015, DOI: 10.1109/TMI.2015.2428634.

[10] P. Song, A. Manduca, J. D. Trzasko, and S. Chen, "Ultrasound small vessel imaging with block-wise adaptive local clutter filtering," *IEEE Transactions on Medical Imaging*, 2017, DOI: 10.1109/TMI.2016.2605819.

[11] R. Gill, "Medical ultrasound in Australia: A short history," *Australasian Journal of Ultrasound in Medicine*, Feb. 2018, DOI: 10.1002/ajum.12085.

[12] Mindray, *Resona I9 Ultrasound Machine*, 2024, Accessed: Sep. 14, 2022. [Online]. Available: https://www.mindray.com/na/products/ultrasound/general-imaging/resona-i9/.

[13] J. Cleve and M. L. McCulloch, "Conducting a Cardiac Ultrasound Examination," in P. Nihoyannopoulos and J. Kisslo, Eds. Springer International Publishing, 2018, ISBN: 9783319716176, DOI: 10.1007/978-3-319-71617-6_2.

[14] C. J. Harvey and T. Albrecht, "Ultrasound of focal liver lesions," *European Radiology*, 2001, DOI: 10.1007/s003300101002.

[15] H. Blencowe *et al.*, "National, regional, and worldwide estimates of preterm birth rates in the year 2010 with time trends since 1990 for selected countries: A systematic analysis and implications," *The Lancet*, 2012, DOI: 10.1016/S0140-6736(12)60820-4.

[16] S. Chawanpaiboon *et al.*, "Global, regional, and national estimates of levels of preterm birth in 2014: a systematic review and modelling analysis," *The Lancet Global Health*, Jan. 2019, DOI: 10.1016/S2214-109X(18)30451-0.

[17] J. Baranger *et al.*, "Brain perfusion imaging in neonates," *NeuroImage: Clinical*, 2021, DOI: 10.1016/j.nicl.2021.102756.

[18] C. J. Rhee *et al.*, "Neonatal cerebrovascular autoregulation," *Pediatric Research*, 2018, DOI: 10.1038/s41390-018-0141-6.

[19] S. Bolisetty *et al.*, "Intraventricular Hemorrhage and Neurodevelopmental Outcomes in Extreme Preterm Infants," *Pediatrics*, Jan. 2014, DOI: 10.1542/peds.2013-0372.

[20] J. J. Volpe, "Brain injury in premature infants: a complex amalgam of destructive and developmental disturbances," *The Lancet Neurology*, Jan. 2009, DOI: 10.1016/S1474-4422(08)70294-1.

[21] T. E. Inder, J. M. Perlman, and J. J. Volpe, "Preterm Intraventricular Hemorrhage/Posthemorrhagic Hydrocephalus," in Elsevier, 2018, DOI: 10.1016/B978-0-323-42876-7.00024-7.

[22] T. E. Inder, J. J. Volpe, and P. J. Anderson, "Defining the Neurologic Consequences of Preterm Birth," *New England Journal of Medicine*, J. R. Ingelfinger, Ed., Aug. 2023, DOI: 10.1056/NEJMra2303347.

[23] A. Plaisier *et al.*, "Safety of routine early MRI in preterm infants," *Pediatric Radiology*, Oct. 2012, DOI: 10.1007/s00247-012-2426-y.

[24] Y. Zhao *et al.*, "Whole-body magnetic resonance imaging at 0.05 Tesla," *Science*, no. 6696, May 2024, DOI: 10.1126/science.adm7168.

[25] I. Hyperfine, *Swoop® Portable MR Imaging® System*, Accessed: Nov. 12, 2024. [Online]. Available: https://hyperfine.io/swoop/overview.

[26] F. van Bel, P. Lemmers, and G. Naulaers, "Monitoring neonatal regional cerebral oxygen saturation in clinical practice: Value and pitfalls," *Neonatology*, 2008, DOI: 10.1159/000151642.

[27] T. Alderliesten *et al.*, "Cerebral oxygenation, extraction, and autoregulation in very preterm infants who develop peri-intraventricular hemorrhage," *Journal of Pediatrics*, 2013, DOI: 10.1016/j.jpeds.2012.09.038.

[28] W. Li, Z. Zhang, Z. Li, Z. Gui, and Y. Shang, "Correlation and asynchronization of electroencephalogram and cerebral blood flow in active and passive stimulations," *Journal of Neural Engineering*, Dec. 2023, DOI: 10.1088/1741-2552/ad0a02.

[29] S. A. Costerus *et al.*, "Towards integrative neuromonitoring of the surgical newborn: A systematic review," *European Journal of Anaesthesiology*, 2020, DOI: 10.1097/EJA.0000000000001218.

[30] J. Sun and K. Hynynen, "Focusing of therapeutic ultrasound through a human skull: A numerical study," *The Journal of the Acoustical Society of America*, 1998, DOI: 10.1121/1.424383.

[31] M. Tanter *et al.*, "Compensating for bone interfaces and respiratory motion in high-intensity focused ultrasound," *International Journal of Hyperthermia*, 2007, DOI: 10.1080/02656730701209996.

[32] T. Deffieux, C. Demené, and M. Tanter, "Functional Ultrasound Imaging: A New Imaging Modality for Neuroscience," *Neuroscience*, 2021, DOI: 10.1016/j.neuroscience.2021.03.005.

[33] S. D. Vik, H. Torp, T. Follestad, R. Støen, and S. A. Nyrnes, "NeoDoppler: New ultrasound technology for continous cerebral circulation monitoring in neonates," *Pediatric Research*, 2019, DOI: 10.1038/s41390-019-0535-0.

[34] W. S. Aronow, J. L. Fleg, and M. W. Rich, *Tresch and Aronow's Cardiovascular Disease in the Elderly*. CRC Press, 2013, ISBN: 9781842145449.

[35] K. K. Dakok, M. Z. Matjafri, N. Suardi, A. A. Oglat, and S. E. Nabasu, "A review of carotid artery phantoms for doppler ultrasound applications," *Journal of Medical Ultrasound*, 2021, DOI: 10.4103/JMU.JMU_164_20.

[36] A. Delcker and C. Tegeler, "Influence of ECG-triggered data acquisition on reliability for carotid plaque volume measurements with a magnetic sensor three-dimensional ultrasound system," *Ultrasound in Medicine and Biology*, 1998, DOI: 10.1016/S0301-5629(98)00012-X.

[37] A. Saxena, E. Y. K. Ng, and S. T. Lim, "Imaging modalities to diagnose carotid artery stenosis: Progress and prospect," *BioMedical Engineering Online*, 2019, DOI: 10.1186/s12938-019-0685-7.

[38] M. I. Chimowitz, R. M. Poole, M. R. Starling, M. Schwaiger, and M. D. Gross, "Frequency and Severity of Asymptomatic Coronary Disease in Patients With Different Causes of Stroke," *Stroke*, May 1997, DOI: 10.1161/01.STR.28.5.941.

[39] I. Kallikazaros, C. Tsioufis, S. Sideris, C. Stefanadis, and P. Toutouzas, "Carotid Artery Disease as a Marker for the Presence of Severe Coronary Artery Disease in Patients Evaluated for Chest Pain," *Stroke*, May 1999, DOI: 10.1161/01.STR.30.5.1002.

[40] E. R. Mohler *et al.*, "ACCF/ACR/AIUM/ASE/ASN/ICAVL/SCAI/SCCT/SIR/SVM/SVS 2012 appropriate use criteria for peripheral vascular ultrasound and physiological testing part I: arterial ultrasound and physiological testing: a report of the American College of Cardiology Foundation a," *Journal of the American College of Cardiology*, 2011, DOI: 10.1161/CIR.0b0113e31820d8c98.

[41] T. E. Craven *et al.*, "Evaluation of the associations between carotid artery atherosclerosis and coronary artery stenosis. A case-control study.," *Circulation*, Oct. 1990, DOI: 10.1161/01.CIR.82.4.1230.

[42] B. Schaller, *Imaging of Carotid Artery Stenosis*, B. J. Schaller, Ed. Springer Vienna, 2007, ISBN: 978-3-211-32332-8, DOI: 10.1007/978-3-211-32509-4.

[43] H. C. Stary *et al.*, "A definition of initial, fatty streak, and intermediate lesions of atherosclerosis. A report from the Committee on Vascular Lesions of the Council on Arteriosclerosis, American Heart Association.," *Arteriosclerosis and Thrombosis: A Journal of Vascular Biology*, May 1994, DOI: 10.1161/01.ATV.14.5.840.

[44] M. Rafieian-Kopaei, M. Setorki, M. Doudi, A. Baradaran, and H. Nasri, "Atherosclerosis: Process, Indicators, Risk Factors and New Hopes, International Journal of Preventive Medicine," *International Journal of Preventive Medicine*, 2014.

[45] R. Nakanishi, S. Motoyama, J. Leipsic, and M. J. Budoff, "How accurate is atherosclerosis imaging by coronary computed tomography angiography?" *Journal of Cardiovascular Computed Tomography*, Sep. 2019, DOI: 10.1016/j.jcct.2019.06.005.

[46] R. Corti and V. Fuster, "Imaging of atherosclerosis: magnetic resonance imaging," *European Heart Journal*, Jul. 2011, DOI: 10.1093/eurheartj/ehr068.

[47] T. Leiner *et al.*, "Magnetic resonance imaging of atherosclerosis," *European Radiology*, 2005, DOI: 10.1007/s00330-005-2646-8.

[48] G. Mancia *et al.*, "2007 ESH-ESC Practice Guidelines for the Management of Arterial Hypertension: ESH-ESC Task Force on the Management of Arterial Hypertension," *Journal of Hypertension*, 2007, DOI: 10.1097/HJH.0b013e3282f0580f.

[49] A. Harloff, "Carotid Plaque Hemodynamics," *Interventional Neurology*, 2012, DOI: 10.1159/000338360.

[50] T. Adla and R. Adlova, "Multimodality imaging of carotid stenosis," *International Journal of Angiology*, 2014, DOI: 10.1055/s-0035-1556056.

[51] R. W. Prager, U. Z. Ijaz, A. H. Gee, and G. M. Treece, "Three-dimensional ultrasound imaging," *Proceedings of the Institution of Mechanical Engineers, Part H: Journal of Engineering in Medicine*, 2010, DOI: 10.1243/09544119JEIM586.

[52] A. Fenster, D. B. Downey, and H. N. Cardinal, "Three-dimensional ultrasound imaging," *Physics in Medicine and Biology*, May 2001, DOI: 10.1088/0031-9155/46/5/201.

[53] A. Harloff *et al.*, "3D blood flow characteristics in the carotid artery bifurcation assessed by flow-sensitive 4D MRI at 3T," *Magnetic Resonance in Medicine*, 2009, DOI: 10.1002/mrm.21774.

[54] K. L. Hansen *et al.*, "Analysis of Systolic Backflow and Secondary Helical Blood Flow in the Ascending Aorta Using Vector Flow Imaging," *Ultrasound in Medicine and Biology*, 2016, DOI: 10.1016/j.ultrasmedbio.2015.11.029.

[55] S. Holbek, M. J. Pihl, C. Ewertsen, M. B. Nielsen, and J. A. Jensen, "In vivo 3-D vector velocity estimation with continuous data," *2015 IEEE International Ultrasonics Symposium, IUS 2015*, 2015, DOI: 10.1109/ULTSYM.2015.0235.

[56] I. Z. Apostolakis, P. Nauleau, C. Papadacci, M. D. McGarry, and E. E. Konofagou, "Feasibility and Validation of 4-D Pulse Wave Imaging in Phantoms and In Vivo," *IEEE Transactions on Ultrasonics, Ferroelectrics, and Frequency Control*, 2017, DOI: 10.1109/TUFFC.2017.2735381.

[57] H. Li *et al.*, "Investigation of out-of-plane motion artifacts in 2D noninvasive vascular ultrasound elastography," *Physics in Medicine and Biology*, 2018, DOI: 10.1088/1361-6560/aaf0d3.

[58] Q. Huang and Z. Zeng, "A Review on Real-Time 3D Ultrasound Imaging Technology," *BioMed Research International*, 2017, DOI: 10.1155/2017/6027029.

[59] J. Provost *et al.*, "3D ultrafast ultrasound imaging in vivo," *Physics in Medicine and Biology*, Oct. 2014, DOI: 10.1088/0031-9155/59/19/L1.

[60] K. Erikson, A. Hairston, A. Nicoli, J. Stockwell, and T. White, "A128 X128 (16K) Ultrasonic Transducer Hybrid Array," in 1997, ISBN: 0780341538, DOI: 10.1007/978-1-4419-8588-0_77.

[61] A. Ramalli, E. Boni, E. Roux, H. Liebgott, and P. Tortoli, "Design, Implementation, and Medical Applications of 2-D Ultrasound Sparse Arrays," *IEEE Transactions on Ultrasonics, Ferroelectrics, and Frequency Control*, 2022, DOI: 10.1109/TUFFC.2022.3162419.

[62] A. Ramalli, E. Boni, A. S. Savoia, and P. Tortoli, "Density-tapered spiral arrays for ultrasound 3-D imaging," *IEEE Transactions on Ultrasonics, Ferroelectrics, and Frequency Control*, 2015, DOI: 10.1109/TUFFC.2015.007035.

[63] E. Boni, F. Fool, M. D. Verweij, H. J. Vos, and P. Tortoli, "On the efficacy of in-probe pre-amplifiers for piezoelectric 2D arrays," *IEEE International Ultrasonics Symposium, IUS*, 2020, DOI: 10.1109/IUS46767.2020.9251800.

[64] C. E. Morton and G. R. Lockwood, "Theoretical assessment of a crossed electrode 2-D array for 3-D imaging," *Proceedings of the IEEE Ultrasonics Symposium*, 2003, DOI: 10.1109/ultsym.2003.1293560.

[65] M. Flesch *et al.*, "4D in vivo ultrafast ultrasound imaging using a row-column addressed matrix and coherently-compounded orthogonal plane waves," *Physics in Medicine and Biology*, 2017, DOI: 10.1088/1361-6560/aa63d9.

[66] M. F. Rasmussen and J. A. Jensen, "3-D ultrasound imaging performance of a row-column addressed 2-D array transducer: A measurement study," *IEEE International Ultrasonics Symposium, IUS*, 2013, DOI: 10.1109/ULTSYM.2013.0370.

[67] K. Chen, H. S. Lee, and C. G. Sodini, "A Column-Row-Parallel ASIC Architecture for 3-D Portable Medical Ultrasonic Imaging," *IEEE Journal of Solid-State Circuits*, 2016, DOI: 10.1109/JSSC.2015.2505714.

[68] H. Bouzari *et al.*, "Curvilinear 3-D Imaging Using Row-Column-Addressed 2-D Arrays With a Diverging Lens: Feasibility Study," *IEEE transactions on ultrasonics, ferroelectrics, and frequency control*, 2017.

[69] M. Audoin *et al.*, "Diverging Polymer Acoustic Lens Design for High-Resolution Row-Column Array Ultrasound Transducers," *IEEE Transactions on Ultrasonics, Ferroelectrics, and Frequency Control*, 2024, DOI: 10.1109/TUFFC.2023.3327567.

[70] B. Savord and R. Solomon, "Fully sampled matrix transducer for real time 3D ultrasonic imaging," *Proceedings of the IEEE Ultrasonics Symposium*, 2003, DOI: 10.1109/ultsym.2003.1293556.

[71] E. Kang *et al.*, "A Reconfigurable Ultrasound Transceiver ASIC With 24 × 40 Elements for 3-D Carotid Artery Imaging," *IEEE Journal of Solid-State Circuits*, 2018, DOI: 10.1109/JSSC.2018.2820156.

[72] T. M. Carpenter *et al.*, "Direct digital demultiplexing of analog TDM signals for cable reduction in ultrasound imaging catheters," *IEEE Transactions on Ultrasonics, Ferroelectrics, and Frequency Control*, 2016, DOI: 10.1109/TUFFC.2016.2557622.

[73] P. Guo *et al.*, "A 1.2-mW/Channel Pitch-Matched Transceiver ASIC Employing a Boxcar-Integration-Based RX Micro-Beamformer for High-Resolution 3-D Ultrasound Imaging," *IEEE Journal of Solid-State Circuits*, 2023, DOI: 10.1109/JSSC.2023.3271270.

[74] C. Chen *et al.*, "A Front-End ASIC with Receive Sub-array Beamforming Integrated with a 32 × 32 PZT Matrix Transducer for 3-D Transesophageal Echocardiography," *IEEE Journal of Solid-State Circuits*, 2017, DOI: 10.1109/JSSC.2016.2638433.

[75] K. Q. Zhao, T. G. Bjastad, and K. Kristoffersen, "Error analysis of subaperture processing in 1-D ultrasound arrays," *IEEE Transactions on Ultrasonics, Ferroelectrics, and Frequency Control*, 2015, DOI: 10.1109/TUFFC.2014.006822.

[76] D. H. Evans, "Colour flow and motion imaging," *Proc Inst Mech Eng H*, 2010, DOI: 10.1243/09544119JEIM599.

[77] J. Kortbek, J. A. Jensen, and K. L. Gammelmark, "Sequential beamforming for synthetic aperture imaging," *Ultrasonics*, 2013, DOI: 10.1016/j.ultras.2012.06.006.

[78] D. Bera, J. G. Bosch, N. de Jong, and H. J. Vos, "Synthetic Aperture Sequential Beamforming for phased array imaging," *2015 IEEE International Ultrasonics Symposium, IUS 2015*, 2015, DOI: 10.1109/ULTSYM.2015.0499.

[79] H. J. Vos *et al.*, "F-k domain imaging for synthetic aperture sequential beamforming," *IEEE Transactions on Ultrasonics, Ferroelectrics, and Frequency Control*, 2016, DOI: 10.1109/TUFFC.2015.2499839.

[80] A. J. Hunter, B. W. Drinkwater, and P. D. Wilcox, "The wavenumber algorithm for full-matrix imaging using an ultrasonic array," *IEEE Transactions on Ultrasonics, Ferroelectrics, and Frequency Control*, 2008, DOI: 10.1109/TUFFC.952.

[81] M. D. Levine, "Circuit Techniques for Reducing the Effects of Op-Amp Imperfections: Autozeroing, Correlated Double Sampling, and Chopper Stabilization," *Proceedings of the IEEE*, 1996, DOI: 10.1109/JPROC.1996.542409.

[82] C. Eichenberger and W. Guggenbuhl, "On charge injection in analog MOS switches and dummy switch compensation techniques," *IEEE Transactions on Circuits and Systems*, 1990, DOI: 10.1109/31.45719.

[83] C.-Y. Wu, C.-C. Chen, and J.-J. Cho, "Precise CMOS current sample/hold circuits using differential clock feedthrough attenuation techniques," *IEEE Journal of Solid-State Circuits*, 1995, DOI: 10.1109/4.350189.

[84] D. Wildes *et al.*, "4-D ICE: A 2-D array transducer with integrated ASIC in a 10-Fr catheter for real-time 3-D intracardiac echocardiography," *IEEE transactions on ultrasonics, ferroelectrics, and frequency control*, 2016.

[85] V. Daeichin *et al.*, "Acoustic characterization of a miniature matrix transducer for pediatric 3D transesophageal echocardiography," *Ultrasound in Medicine and Biology*, 2018, DOI: 10.1016/j.ultrasmedbio.2018.06.009.

[86] M. Shabanimotlagh *et al.*, "Optimizing the directivity of piezoelectric matrix transducer elements mounted on an ASIC," in *IEEE International Ultrasonics Symposium, IUS*, IEEE, Sep. 2017, ISBN: 9781538633830, DOI: 10.1109/ULTSYM.2017.8091752.

[87] R. Wodnicki *et al.*, "Co-integrated PIN-PMN-PT 2D Array and Transceiver Electronics by Direct-Assembly Using a 3D Printed Interposer Grid Frame," *IEEE Transactions on Ultrasonics, Ferroelectrics, and Frequency Control*, 2019, DOI: 10.1109/tuffc.2019.2944668.

[88] M. Couade *et al.*, "Ultrafast imaging of the arterial pulse wave," *Irbm*, 2011, DOI: 10.1016/j.irbm.2011.01.012.

[89] H. Hasegawa, K. Hongo, and H. Kanai, "Measurement of regional pulse wave velocity using very high frame rate ultrasound," *Journal of Medical Ultrasonics*, 2013, DOI: 10.1007/s10396-012-0400-9.

[90] J. Luo, R. X. Li, and E. E. Konofagou, "Pulse wave imaging of the human carotid artery: An in vivo feasibility study," *IEEE Transactions on Ultrasonics, Ferroelectrics, and Frequency Control*, 2012, DOI: 10.1109/TUFFC.2012.2170.

[91] C. Papadacci, M. Pernot, M. Couade, M. Fink, and M. Tanter, "High-contrast ultrafast imaging of the heart," *IEEE Transactions on Ultrasonics, Ferroelectrics, and Frequency Control*, 2014, DOI: 10.1109/TUFFC.2014.6722614.

[92] Y. Xiao, J. Jin, Y. Yuan, Y. Zhao, and D. Li, "On the Role of Coherent Plane Wave Compounding in Shear Wave Elasticity Imaging: The Convolution Effect and Its Implications," *Ultrasound in Medicine and Biology*, 2023, DOI: 10.1016/j.ultrasmedbio.2023.09.019.

[93] A. Caicedo *et al.*, "Relation between EEG activity and brain oxygenation in preterm neonates," *Advances in Experimental Medicine and Biology*, 2017, DOI: 10.1007/978-3-319-55231-6_18.

[94] J. W. Britton *et al.*, "Electroencephalography (EEG): An introductory text and atlas of normal and abnormal findings in adults, children, and infants," *American Epilepsy Society, Chicago*, 2016, DOI: 10.5698/978-0-9979756-0-4.

[95] R. E. Spitzmiller, T. Phillips, J. Meinzen-Derr, and S. B. Hoath, "Response to correspondence on "Amplitude-Integrated EEG Is useful in predicting neurodevelopmental outcome in full-term infants with hypoxic-ischemic encephalopathy: A meta-analysis"," *Journal of Child Neurology*, 2008, DOI: 10.1177/0883073808317346.

[96] M. E. McCann *et al.*, "Infantile Postoperative Encephalopathy: Perioperative Factors as a Cause for Concern," *Pediatrics*, 2014, DOI: 10.1542/peds.2012-0973.

[97] A. J. Kortenbout, "Neonatal Cerebral Blood Flow Imaging Using High-Frame-Rate Ultrasound," Erasmus University Rotterdam, 2024.

[98] F. Fool *et al.*, "A Tiled Ultrasound Matrix Transducer for Volumetric Imaging of the Carotid Artery," *Sensors*, 2022, DOI: 10.3390/s22249799.

[99] S. Laing, K. Walker, J. Ungerer, N. Badawi, and K. Spence, "Early development of children with major birth defects requiring newborn surgery," *Journal of Paediatrics and Child Health*, Mar. 2011, DOI: 10.1111/j.1440-1754.2010.01902.x.

[100] M. E. McCann and A. N. Schouten, "Beyond survival; influences of blood pressure, cerebral perfusion and anesthesia on neurodevelopment," *Pediatric Anesthesia*, A. Wolf, Ed., Jan. 2014, DOI: 10.1111/pan.12310.

[101] M. E. McCann, J. K. Lee, and T. Inder, "Beyond Anesthesia Toxicity: Anesthetic Considerations to Lessen the Risk of Neonatal Neurological Injury," *Anesthesia & Analgesia*, Nov. 2019, DOI: 10.1213/ANE.0000000000004271.

[102] L. J. Stolwijk *et al.*, "Neurodevelopmental Outcomes After Neonatal Surgery for Major Noncardiac Anomalies," *Pediatrics*, Feb. 2016, DOI: 10.1542/peds.2015-1728.

[103] L. J. Stolwijk *et al.*, "Neonatal Surgery for Noncardiac Congenital Anomalies: Neonates at Risk of Brain Injury," *The Journal of Pediatrics*, Mar. 2017, DOI: 10.1016/j.jpeds.2016.11.080.

[104] M. Raets *et al.*, "Preterm Cerebral Microcirculation Assessed with Color Doppler: A Pilot Study," *Journal of Pediatric Neuroradiology*, 2014, DOI: 10.3233/PNR-14190.

[105] H. Tzschätzsch *et al.*, "In vivo time-harmonic ultrasound elastography of the human brain detects acute cerebral stiffness changes induced by intracranial pressure variations," *Scientific Reports*, Dec. 2018, DOI: 10.1038/s41598-018-36191-9.

[106] D. deCampo and M. Hwang, "Characterizing the Neonatal Brain With Ultrasound Elastography," *Pediatric Neurology*, Sep. 2018, DOI: 10.1016/j.pediatrneurol.2018.06.005.

[107] S. Catheline *et al.*, "Tomography from diffuse waves: Passive shear wave imaging using low frame rate scanners," *Applied Physics Letters*, 2013, DOI: 10.1063/1.4812515.

[108] G. A. Popich and D. W. Smith, "Fontanels: Range of normal size," *The Journal of Pediatrics*, 1972, DOI: 10.1016/S0022-3476(72)80125-2.

[109] R. G. Faix, "Fontanelle size in black and white term newborn infants," *The Journal of Pediatrics*, 1982, DOI: 10.1016/S0022-3476(82)80661-6.

[110] A. Adeyemo and O. Omotade, "Variation in fontanelle size with gestational age," *Early Human Development*, 1999, DOI: 10.1016/S0378-3782(98)00089-9.

[111] F. W. Kremkau, R. W. Barnes, and C. P. McGraw, "Ultrasonic attenuation and propagation speed in normal human brain," *The Journal of the Acoustical Society of America*, Jul. 1981, DOI: 10.1121/1.386578.

[112] J. Luijsterburg, "Ultrasound attenuation in a preterm brain," 2021.

[113] J. A. Jensen, "Field: A program for simulating ultrasound systems," in *10th Nordic-Baltic Conference on Biomedical Engineering, Vol. 4, Supplement 1, Part 1: 351–353*, Citeseer, 1996.

[114] J. Jensen and N. Svendsen, "Calculation of pressure fields from arbitrarily shaped, apodized, and excited ultrasound transducers," *IEEE Transactions on Ultrasonics, Ferroelectrics and Frequency Control*, Mar. 1992, DOI: 10.1109/58.139123.

[115] Computerized Imaging Reference Systems Inc., *Multi-Purpose, Multi-Tissue Ultrasound Phantom Model 040GSE*, 2013, Accessed: Nov. 6, 2024. [Online]. Available: https://www.cirsinc.com/wp-content/uploads/2021/09/040GSE-DS-093021.pdf.

[116] J. D. Larson III, "2-D phased array ultrasound imaging system with distributed phasing," *US Patent 5,229,933*, 1993.

[117] U. W. Lok and P. C. Li, "Microbeamforming with error compensation," *IEEE Transactions on Ultrasonics, Ferroelectrics, and Frequency Control*, 2018, DOI: 10.1109/TUFFC.2018.2834411.

[118] M. Tan *et al.*, "A front-end ASIC with high-voltage transmit switching and receive digitization for 3-D forward-looking intravascular ultrasound imaging," *IEEE Journal of Solid-State Circuits*, 2018, DOI: 10.1109/JSSC.2018.2828826.

[119] G. Jung *et al.*, "Single-chip reduced-wire active catheter system with programmable transmit beamforming and receive time-division multiplexing for intracardiac echocardiography," *Digest of Technical Papers - IEEE International Solid-State Circuits Conference*, 2018, DOI: 10.1109/ISSCC.2018.8310247.

[120] D. Posada *et al.*, "Staggered Multiple-PRF Ultrafast Color Doppler," *IEEE Transactions on Medical Imaging*, 2016, DOI: 10.1109/TMI.2016.2518638.

[121] J. Poree *et al.*, "De-aliasing High-Frame-Rate Color Doppler using Dual-wavelength processing," *IEEE Transactions on Ultrasonics, Ferroelectrics, and Frequency Control*, 2021, DOI: 10.1109/TUFFC.2021.3056932.

[122] J. Poree *et al.*, "High-Frame-Rate Echocardiography Using Coherent Compounding With Doppler-Based Motion-Compensation," *IEEE Transactions on Medical Imaging*, Jul. 2016, DOI: 10.1109/TMI.2016.2523346.

[123] L. T. Jorgensen, M. Schou, M. B. Stuart, and J. A. Jensen, "Tensor Velocity Imaging with Motion Correction," *IEEE Transactions on Ultrasonics, Ferroelectrics, and Frequency Control*, 2021, DOI: 10.1109/TUFFC.2020.3046101.

[124] D. K. Peterson and G. S. Kino, "Real-Time Digital Image Reconstruction: A Description of Imaging Hardware and an Analysis of Quantization Errors," *IEEE Transactions on Sonics and Ultrasonics*, 1984, DOI: 10.1109/T-SU.1984.31514.

[125] P. A. Magnin, O. T. von Ramm, and F. L. Thurstone, "Delay Quantization Error in Phased Array Images," *IEEE Transactions on Sonics and Ultrasonics*, 1981, DOI: 10.1109/t-su.1981.31268.

[126] M. D. Verweij *et al.*, "A Fresnel-inspired approach for steering and focusing of pulsed transmit beams by matrix array transducers," *The Journal of the Acoustical Society of America*, May 2017, DOI: 10.1121/1.4987739.

[127] M. M. Nguyen, J. Mung, and J. T. Yen, "Fresnel-based beamforming for low-cost portable ultrasound," *IEEE Trans Ultrason Ferroelectr Freq Control*, 2011, DOI: 10.1109/TUFFC.2011.1778.

[128] J. T. Yen *et al.*, "Gated Transmit and Fresnel-based Receive Beamforming with a Phased Array for Low-Cost Ultrasound Imaging," *IEEE Transactions on Ultrasonics, Ferroelectrics, and Frequency Control*, 2021, DOI: 10.1109/TUFFC.2021.3062850.

[129] S. Bae, H. Song, and T. K. Song, "Analysis of the Time and Phase Delay Resolutions in Ultrasound Baseband I/Q Beamformers," *IEEE Transactions on Biomedical Engineering*, 2021, DOI: 10.1109/TBME.2020.3019799.

[130] Physik Instrumente, *Piezotechnology: Fundamentals of Piezoelectricity*, Accessed: Apr. 8, 2024. [Online]. Available: https://www.piezo.ws/piezoelectric_actuator_tutorial/Piezo_Design_part2.php.

[131] CTS Corporation, *PZT Materials, Complete Properties*, 2021, Accessed: Nov. 6, 2024. [Online]. Available: https://www.ctscorp.com/Files/DataSheets/Piezoelectric/Bulk-Piezoceramics/CTS-Piezoelectric-Bulk-Piezoceramics-Ceramic-Material-Properties-Datasheet.pdf.

[132] T. Kim *et al.*, "Design of an ultrasound transceiver asic with a switching-artifact reduction technique for 3D carotid artery imaging," *Sensors*, 2021, DOI: 10.3390/s21010150.

[133] Y. M. Hopf *et al.*, "A Pitch-Matched High-Frame-Rate Ultrasound Imaging ASIC for Catheter-Based 3-D Probes," *IEEE Journal of Solid-State Circuits*, 2023, DOI: 10.1109/JSSC.2023.3299749.

[134] C. Chen *et al.*, "A pitch-matched front-end ASIC with integrated subarray beamforming ADC for miniature 3-d ultrasound probes," *IEEE Journal of Solid-State Circuits*, 2018, DOI: 10.1109/JSSC.2018.2864295.

[135] P. Guo, "Pitch-Matched Integrated Transceiver Circuits for High-Resolution 3-D Neonatal Brain Monitoring," 2023.

[136] H. V. Nguyen, T. Eggen, B. Sten-Nilsen, K. Imenes, and K. E. Aasmundtveit, "Assembly of multiple chips on flexible substrate using anisotropie conductive film for medical imaging applications," *Proceedings - Electronic Components and Technology Conference*, 2014, DOI: 10.1109/ECTC.2014.6897330.

[137] Y. Hopf *et al.*, "A Pitch-Matched ASIC with Integrated 65V TX and Shared Hybrid Beamforming ADC for Catheter-Based High-Frame-Rate 3D Ultrasound Probes," *Digest of Technical Papers - IEEE International Solid-State Circuits Conference*, 2022, DOI: 10.1109/ISSCC42614.2022.9731597.

[138] P. Guo *et al.*, "A Pitch-Matched Low-Noise Analog Front-End With Accurate Continuous Time-Gain Compensation for High-Density Ultrasound Transducer Arrays," *IEEE Journal of Solid-State Circuits*, 2023, DOI: 10.1109/JSSC.2022.3200160.

[139] Y. M. Hopf *et al.*, "A Pitch-Matched Transceiver ASIC With Shared Hybrid Beamforming ADC for High-Frame-Rate 3-D Intracardiac Echocardiography," *IEEE Journal of Solid-State Circuits*, 2022, DOI: 10.1109/JSSC.2022.3201758.

[140] P. Guo *et al.*, "A 125 μm-Pitch-Matched Transceiver ASIC With Micro-Beamforming ADC and Multi-Level Signaling for 3-D Transfontanelle Ultrasonography," *IEEE Journal of Solid-State Circuits*, 2024, DOI: 10.1109/JSSC.2024.3355854.

[141] P. Kruizinga *et al.*, "High-definition imaging of carotid artery wall dynamics," *Ultrasound in Medicine and Biology*, 2014, DOI: 10.1016/j.ultrasmedbio.2014.03.009.

[142] T. Kim, S. Shin, and S. Kim, "An 80.2 dB DR 23.25 mW/Channel 8-Channel Ultrasound Receiver With a Beamforming Embedded SAR ADC," *IEEE Transactions on Circuits and Systems II: Express Briefs*, 2019, DOI: 10.1109/TCSII.2018.2889810.

[143] Y. Igarashi *et al.*, "Single-Chip 3072-Element-Channel Transceiver/128-Subarray-Channel 2-D Array IC with Analog RX and All-Digital TX Beamformer for Echocardiography," *IEEE Journal of Solid-State Circuits*, 2019, DOI: 10.1109/JSSC.2019.2921697.

[144] I. O. Wygant *et al.*, "An integrated circuit with transmit beamforming flip-chip bonded to a 2-D CMUT array for 3-D ultrasound imaging," *IEEE Transactions on Ultrasonics, Ferroelectrics, and Frequency Control*, Oct. 2009, DOI: 10.1109/TUFFC.2009.1297.

[145] A. Bhuyan *et al.*, "Integrated circuits for volumetric ultrasound imaging with 2-D CMUT arrays," *IEEE Transactions on Biomedical Circuits and Systems*, 2013, DOI: 10.1109/TBCAS.2014.2298197.

[146] S. J. Jung, J. K. Song, and O. K. Kwon, "Three-side buttable integrated ultrasound chip with a 16, times16 reconfigurable transceiver and capacitive micromachined ultrasonic transducer array for 3-D ultrasound imaging systems," *IEEE Transactions on Electron Devices*, 2013, DOI: 10.1109/TED.2013.2278441.

[147] K. Chen, H. S. Lee, and C. G. Sodini, "A Column-Row-Parallel ASIC Architecture for 3-D Portable Medical Ultrasonic Imaging," *IEEE Journal of Solid-State Circuits*, 2016, DOI: 10.1109/JSSC.2015.2505714.

[148] B. H. Kim, Y. Kim, S. Lee, K. Cho, and J. Song, "Design and test of a fully controllable 64×128 2-D CMUT array integrated with reconfigurable frontend ASICs for volumetric ultrasound imaging," *IEEE International Ultrasonics Symposium, IUS*, 2012, DOI: 10.1109/ULTSYM.2012.0019.

[149] K. Chen, H. S. Lee, A. P. Chandrakasan, and C. G. Sodini, "Ultrasonic imaging transceiver design for cmut: A three-level 30-vpp pulse-shaping pulser with improved efficiency and a noise-optimized receiver," *IEEE Journal of Solid-State Circuits*, 2013, DOI: 10.1109/JSSC.2013.2274895.

[150] S. Tamano *et al.*, "3D ultrasound imaging system using fresnel ring array & high voltage multiplexer IC," *Proceedings - IEEE Ultrasonics Symposium*, 2004, DOI: 10.1109/ultsym.2004.1417838.

[151] R. Fisher *et al.*, "Reconfigurable arrays for portable ultrasound," *Proceedings - IEEE Ultrasonics Symposium*, 2005, DOI: 10.1109/ULTSYM.2005.1602899.

[152] C. Eichenberger and W. Guggenbuhl, "Dummy transistor compensation of analog MOS switches," *IEEE Journal of Solid-State Circuits*, 1989, DOI: 10.1109/4.34103.

[153] R. Wodnicki *et al.*, "Tiled Large Element 1.75D Aperture with Dual Array Modules by Adjacent Integration of PIN-PMN-PT Transducers and Custom High Voltage Switching ASICs," *IEEE International Ultrasonics Symposium, IUS*, 2019, DOI: 10.1109/ULTSYM.2019.8925552.

[154] C. Chen *et al.*, "A prototype PZT matrix transducer with low-power integrated receive ASIC for 3-D transesophageal echocardiography," *IEEE transactions on ultrasonics, ferroelectrics, and frequency control*, 2016.

[155] P. Kruizinga, F. Mastik, N. de Jong, A. F. W. van der Steen, and G. van Soest, "High frame rate ultrasound imaging of human carotid artery dynamics," in *2012 IEEE International Ultrasonics Symposium*, IEEE, 2012, ISBN: 9781467345613, DOI: 10.1109/ULTSYM.2012.0293.

[156] A. Landry, J. D. Spence, and A. Fenster, "Measurement of Carotid Plaque Volume by 3-Dimensional Ultrasound," *Stroke*, 2004, DOI: 10.1161/01.STR.0000121161.61324.ab.

[157] J. D. Spence *et al.*, "Carotid plaque area: A tool for targeting and evaluating vascular preventive therapy," *Stroke*, 2002, DOI: 10.1161/01.STR.0000042207.16156.B9.

[158] U. Schminke, L. Motsch, B. Griewing, M. Gaull, and C. Kessler, "Three-dimensional power-mode ultrasound for quantification of the progression of carotid artery atherosclerosis," *Journal of Neurology*, 2000, DOI: 10.1007/PL00007790.

[159] A. Delcker and H. C. Diener, "Quantification of atherosclerotic plaques in carotid arteries by three-dimensional ultrasound," *The British Journal of Radiology*, Jul. 1994, DOI: 10.1259/0007-1285-67-799-672.

[160] B. Heiles *et al.*, "Ultrafast 3D Ultrasound Localization Microscopy Using a 32 × 32 Matrix Array," *IEEE transactions on medical imaging*, 2019, DOI: 10.1109/TMI.2018.2890358.

[161] M. Mozaffarzadeh *et al.*, "Receive/Transmit Aperture Selection for 3D Ultrasound Imaging with a 2D Matrix Transducer," *Applied Sciences*, 2020, DOI: 10.3390/app10155300.

[162] E. Roux *et al.*, "Spiral array inspired multi-depth cost function for 2D sparse array optimization," *2015 IEEE International Ultrasonics Symposium, IUS 2015*, 2015, DOI: 10.1109/ULTSYM.2015.0096.

[163] N. Ellens, A. Pulkkinen, J. Song, and K. Hynynen, "The utility of sparse 2D fully electronically steerable focused ultrasound phased arrays for thermal surgery: A simulation study," *Physics in Medicine and Biology*, 2011, DOI: 10.1088/0031-9155/56/15/017.

[164] P. Ramaekers, M. D. Greef, R. Berriet, C. T. Moonen, and M. Ries, "Evaluation of a novel therapeutic focused ultrasound transducer based on Fermat's spiral," *Physics in Medicine and Biology*, 2017, DOI: 10.1088/1361-6560/aa716c.

[165] L. Wei *et al.*, "High Frame Rate Volumetric Imaging of Microbubbles Using a Sparse Array and Spatial Coherence Beamforming," *IEEE Transactions on Ultrasonics, Ferroelectrics, and Frequency Control*, 2021, DOI: 10.1109/TUFFC.2021.3086597.

[166] E. Roux *et al.*, "Experimental 3-D Ultrasound Imaging with 2-D Sparse Arrays using Focused and Diverging Waves," *Scientific Reports*, 2018, DOI: 10.1038/s41598-018-27490-2.

[167] M. F. Rasmussen and J. A. Jensen, "3D ultrasound imaging performance of a row-column addressed 2D array transducer: a simulation study," *Medical Imaging 2013: Ultrasonic Imaging, Tomography, and Therapy*, 2013, DOI: 10.1117/12.2007083.

[168] J. Janjic *et al.*, "A 2-D Ultrasound Transducer With Front-End ASIC and Low Cable Count for 3-D Forward-Looking Intravascular Imaging: Performance and Characterization," *IEEE Transactions on Ultrasonics, Ferroelectrics, and Frequency Control*, 2018, DOI: 10.1109/TUFFC.2018.2859824.

[169] Philips, *The XMATRIX Transducer Technology*, Accessed: Jul. 28, 2022. [Online]. Available: https://www.usa.philips.com/healthcare/resources/feature-862%20detail/xmatrix/.

[170] Butterfly, *New Butterfly IQ+*. Accessed: Sep. 14, 2022. [Online]. Available: https://www.butterflynetwork.eu/.

[171] J. M. Rothberg *et al.*, "Ultrasound-on-chip platform for medical imaging, analysis, and collective intelligence," *Proceedings of the National Academy of Sciences of the United States of America*, 2021, DOI: 10.1073/pnas.2019339118.

[172] Fujifilm, *Technologies*, Accessed: Sep. 14, 2022. [Online]. Available: https://hce.fujifilm.com/products/ultrasound/technologies.html.

[173] F. Fool *et al.*, "Two-Stage Beamforming for Phased Array Imaging Using the Fast Hankel Transform," *IEEE Transactions on Ultrasonics, Ferroelectrics, and Frequency Control*, 2019, DOI: 10.1109/TUFFC.2018.2885870.

[174] H. R. Tahmasebpour, A. R. Buckley, P. L. Cooperberg, and C. H. Fix, "Sonographic examination of the carotid arteries," *Radiographics*, 2005, DOI: 10.1148/rg.256045013.

[175] E. Boni *et al.*, "ULA-OP 256: A 256-Channel Open Scanner for Development and Real-Time Implementation of New Ultrasound Methods," *IEEE Transactions on Ultrasonics, Ferroelectrics, and Frequency Control*, 2016, DOI: 10.1109/TUFFC.2016.2566920.

[176] Verasonics, *The Vantage System*, Accessed: May 5, 2022. [Online]. Available: https://verasonics.com/the-vantage-advantage/.

[177] N. de Jong, N. Bom, J. Souquet, and G. Faber, "Vibration modes, matching layers and grating lobes," *Ultrasonics*, Jul. 1985, DOI: 10.1016/0041-624X(85)90027-7.

[178] J. Janjic *et al.*, "Improving the Performance of a 1-D Ultrasound Transducer Array by Subdicing," *IEEE Transactions on Ultrasonics, Ferroelectrics, and Frequency Control*, Aug. 2016, DOI: 10.1109/TUFFC.2016.2561935.

[179] D. S. dos Santos *et al.*, "Experimental Investigation of the Effect of Subdicing on an Ultrasound Matrix Transducer," *IEEE International Ultrasonics Symposium, IUS*, 2021, DOI: 10.1109/IUS52206.2021.9593315.

[180] P. Tortoli *et al.*, "Comparison of carotid artery blood velocity measurements by vector and standard doppler approaches," *Ultrasound in Medicine and Biology*, 2015, DOI: 10.1016/j.ultrasmedbio.2015.01.008.

[181] P. Kruizinga *et al.*, "Towards 3D ultrasound imaging of the carotid artery using a programmable and tileable matrix array," in *2017 IEEE International Ultrasonics Symposium (IUS)*, IEEE, Sep. 2017, ISBN: 978-1-5386-3383-0, DOI: 10.1109/ULTSYM.2017.8091570.

[182] S. Lee, K. Choi, K. Lee, Y. Kim, and S. Park, "A quarter-wavelength vibration mode transducer using clamped boundary backing layer," *Advances in Civil, Environmental and Materials Research*, 2012.

[183] R. Wodnicki *et al.*, "Co-Integrated PIN-PMN-PT 2-D Array and Transceiver Electronics by Direct Assembly Using a 3-D Printed Interposer Grid Frame," *IEEE Transactions on Ultrasonics, Ferroelectrics, and Frequency Control*, 2020, DOI: 10.1109/TUFFC.2019.2944668.

[184] R. J. McGough, "Rapid calculations of time-harmonic nearfield pressures produced by rectangular pistons," *The Journal of the Acoustical Society of America*, 2004, DOI: 10.1121/1.1694991.

[185] K. Ranganathan, M. K. Santy, T. N. Blalock, J. A. Hossack, and W. F. Walker, "Direct sampled I/Q beamforming for compact and very low-cost ultrasound imaging," *IEEE Transactions on Ultrasonics, Ferroelectrics, and Frequency Control*, 2004, DOI: 10.1109/TUFFC.2004.1334841.

[186] M. Mozaffarzadeh, D. J. E. Verschuur, M. D. Verweij, N. de Jong, and G. Renaud, "Accelerated 2-D Real-Time Refraction-Corrected Transcranial Ultrasound Imaging," *IEEE Transactions on Ultrasonics, Ferroelectrics, and Frequency Control*, 2022, DOI: 10.1109/TUFFC.2022.3189600.

[187] D. Lynser, C. Daniala, A. Y. Khan, E. Marbaniang, and I. Thangkhiew, "Effects of dynamic range variations on the Doppler flow velocities of common carotid arteries," *Artery Research*, 2018, DOI: 10.1016/j.artres.2018.02.001.

[188] A. Bybi *et al.*, "Experimental characterization of a piezoelectric transducer array taking into account crosstalk phenomenon," *International Journal of Engineering and Technology Innovation*, 2020, DOI: 10.46604/ijeti.2020.4348.

[189] M. Celmer and K. J. Opieliński, "Research and Modeling of Mechanical Crosstalk in Linear Arrays of Ultrasonic Transducers," *Archives of Acoustics*, 2016, DOI: 10.1515/aoa-2016-0058.

[190] J. Powers and F. Kremkau, "Medical ultrasound systems," *Interface Focus*, 2011, DOI: 10.1098/rsfs.2011.0027.

[191] B. Hope, *What's next for portable ultrasound?* 2012, Accessed: Jul. 6, 2018. [Online]. Available: https://www.itnonline.com/article/what%E2%80%99s-next-portable-ultrasound.

[192] J. Kang *et al.*, "A system-on-chip solution for point-of-care ultrasound imaging systems: Architecture and ASIC implementation," *IEEE transactions on biomedical circuits and systems*, 2016.

[193] B. Lam, M. Price, and A. P. Chandrakasan, "An ASIC for energy-scalable, low-power digital ultrasound beamforming," in *IEEE Workshop on Signal Processing Systems, SiPS: Design and Implementation*, IEEE, 2016, ISBN: 9781509033614, DOI: 10.1109/SiPS.2016.18.

[194] C. Dusa, S. Kalalii, P. Rajalakshmi, and O. Rao, "Integrated 16-Channel Transmit and Receive Beamforming ASIC for Ultrasound Imaging," in *Proceedings of the IEEE International Conference on VLSI Design*, IEEE, 2015, ISBN: 978-1-4799-6658-5, DOI: 10.1109/VLSID.2015.42.

[195] C. Bradley, *Retrospective transmit beamformation*, 2008, Accessed: Jul. 6, 2018. [Online]. Available: https://www.siemens.com.tr/i/Assets/saglik/Whitepaper_Bradley.pdf.

[196] M. C. Hemmsen *et al.*, "In Vivo Evaluation of Synthetic Aperture Sequential Beamforming," *Ultrasound in Medicine and Biology*, 2012, DOI: 10.1016/j.ultrasmedbio.2011.12.017.

[197] P. M. Hansen *et al.*, "Clinical Evaluation of Synthetic Aperture Sequential Beamforming Ultrasound in Patients with Liver Tumors," *Ultrasound in Medicine and Biology*, 2014, DOI: 10.1016/j.ultrasmedbio.2014.07.008.

[198] M. C. Hemmsen *et al.*, "Implementation of synthetic aperture imaging on a hand-held device," in *2014 IEEE International Ultrasonics Symposium (IUS) Proceedings*, IEEE, 2014, ISBN: 9781479970490, DOI: 10.1109/ULTSYM.2014.0542.

[199] M. C. Hemmsen, L. Lassen, T. Kjeldsen, J. Mosegaard, and J. A. Jensen, "Implementation of real-time duplex synthetic aperture ultrasonography," in *2015 IEEE International Ultrasonics Symposium, IUS 2015*, IEEE, 2015, ISBN: 9781479981823, DOI: 10.1109/ULTSYM.2015.0146.

[200] R. H. Stolt, "Migration By Fourier Transform," *Geophysics*, 1978, DOI: 10.1190/1.1440826.

[201] G. F. Margrave, "Numerical methods of exploration seismology with algorithms in Matlab," *The University of Calgary Publ, 2001*, 2001.

[202] M. H. Skjelvareid, Y. Birkelund, and Y. Larsen, "Synthetic aperture focusing of outwardly directed cylindrical ultrasound scans," *IEEE Transactions on Ultrasonics, Ferroelectrics, and Frequency Control*, Nov. 2012, DOI: 10.1109/TUFFC.2012.2478.

[203] C. H. Frazier and W. D. O'Brien, "Synthetic aperture techniques with a virtual source element," *IEEE Transactions on Ultrasonics, Ferroelectrics, and Frequency Control*, 1998, DOI: 10.1109/58.646925.

[204] P. Moon and D. E. Spencer, *Field Theory Handbook: Including Coordinate Systems, Differential Equations and Their Solutions*. Springer, 1971, ISBN: 3642530605.

[205] M. Abramowitz, I. A. Stegun, and D. Miller, "Handbook of Mathematical Functions," *Journal of Applied Mechanics*, M. Abramowitz and I. Stegun, Eds., Mar. 1965, DOI: 10.1115/1.3625776.

[206] A. E. Siegman, "Quasi fast Hankel transform," *Optics Letters*, 1977, DOI: 10.1364/OL.1.000013.

[207] L. Marple, "Computing the discrete-time "analytic" signal via FFT," *IEEE Transactions on Signal Processing*, 1999, DOI: 10.1109/78.782222.

[208] Q. H. Liu and Z. Q. Zhang, "Nonuniform fast Hankel transform," *Applied Optics*, 1999, DOI: 10.1364/AO.39.001842.

[209] K. Peacock, "On the practical design of discrete velocity filters for seismic data processing," *IEEE Transactions on Acoustics, Speech, and Signal Processing*, Feb. 1982, DOI: 10.1109/TASSP.1982.1163847.

[210] R. Machiraju and R. Yagel, "Reconstruction error characterization and control: A sampling theory approach," *IEEE Transactions on Visualization and Computer Graphics*, 1996, DOI: 10.1109/2945.556504.

[211] J. A. Fessler and B. P. Sutton, "Nonuniform fast Fourier transforms using min-max interpolation," *IEEE Transactions on Signal Processing*, 2003, DOI: 10.1109/TSP.2002.807005.

[212] P. Kruizinga, F. Mastik, N. de Jong, A. F. W. van der Steen, and G. van Soest, "Plane-wave ultrasound beamforming using a nonuniform fast fourier transform," *IEEE Transactions on Ultrasonics, Ferroelectrics, and Frequency Control*, 2012, DOI: 10.1109/TUFFC.2012.2509.

[213] B. P. Sutton, D. C. Noll, and J. A. Fessler, "Fast, iterative image reconstruction for MRI in the presence of field inhomogeneities," *IEEE Transactions on Medical Imaging*, 2003, DOI: 10.1109/TMI.2002.808360.

[214] M. S. Patterson and F. S. Foster, "The improvement and quantitative assessment of B-Mode images produced by an annular array/cone hybrid," *Ultrasonic Imaging*, Jul. 1983, DOI: 10.1177/016173468300500301.

[215] O. M. H. Rindal, J. P. Asen, S. Holm, and A. Austeng, "Understanding contrast improvements from capon beamforming," in *2014 IEEE International Ultrasonics Symposium*, IEEE, Sep. 2014, ISBN: 978-1-4799-7049-0, DOI: 10.1109/ULTSYM.2014.0420.

[216] H. D. Moon and J. F. Rinehart, "Histogenesis of Coronary Arteriosclerosis," *Circulation*, Oct. 1952, DOI: 10.1161/01.CIR.6.4.481.

[217] K. Sutton-Tyrrell *et al.*, "Elevated aortic pulse wave velocity, a marker of arterial stiffness, predicts cardiovascular events in well-functioning older adults," *Circulation*, 2005, DOI: 10.1161/CIRCULATIONAHA.104.483628.

[218] S. Laurent *et al.*, "Aortic stiffness is an independent predictor of all-cause and cardiovascular mortality in hypertensive patients," *Hypertension*, 2001, DOI: 10.1161/01.HYP.37.5.1236.

[219] S. Laurent *et al.*, "Aortic stiffness is an independent predictor of fatal stroke in essential hypertension," *Stroke*, 2003, DOI: 10.1161/01.STR.0000065428.03209.64.

[220] K. V. Ramnarine *et al.*, "Shear wave elastography assessment of carotid plaque stiffness: Invitro reproducibility study," *Ultrasound in Medicine and Biology*, 2014, DOI: 10.1016/j.ultrasmedbio.2013.09.014.

[221] M. Couade *et al.*, "Quantitative Assessment of Arterial Wall Biomechanical Properties Using Shear Wave Imaging," *Ultrasound in Medicine and Biology*, 2010, DOI: 10.1016/j.ultrasmedbio.2010.07.004.

[222] T. G. Brott *et al.*, "2011 ASA/ACCF/AHA/AANN/AANS/ACR/ASNR/CNS/SAIP/SCAI/SIR/SNIS/SVM/SVS Guideline on the Management of Patients With Extracranial Carotid and Vertebral Artery Disease: Executive Summary," *Journal of the American College of Cardiology*, Feb. 2011, DOI: 10.1016/j.jacc.2010.11.005.

[223] J. Vappou, J. Luo, K. Okajima, M. D. Tullio, and E. Konofagou, "Aortic pulse wave velocity measured by pulse wave imaging (PWI): A comparison with applanation tonometry," *Artery Research*, 2011, DOI: 10.1016/j.artres.2011.03.002.

[224] J. Vappou, J. Luo, and E. E. Konofagou, "Pulse wave imaging for noninvasive and quantitative measurement of arterial stiffness in vivo," *American Journal of Hypertension*, 2010, DOI: 10.1038/ajh.2009.272.

[225] J. Luo, K. Fujikura, L. S. Tyrie, M. D. Tilson, and E. E. Konofagou, "Pulse wave imaging of normal and aneurysmal abdominal aortas in vivo," *IEEE Transactions on Medical Imaging*, 2009, DOI: 10.1109/TMI.2008.928179.

[226] D. B. Downey and A. Fenster, "Vascular imaging with a three-dimensional power Doppler system.," *American Journal of Roentgenology*, Sep. 1995, DOI: 10.2214/ajr.165.3.7645492.

[227] P. A. Picot, D. W. Rickey, R. Mitchell, R. N. Rankin, and A. Fenster, "Three-dimensional colour doppler imaging," *Ultrasound in Medicine and Biology*, 1993, DOI: 10.1016/0301-5629(93)90001-5.

[228] H. Gao, Q. Huang, X. Xu, and X. Li, "Wireless and sensorless 3D ultrasound imaging," *Neurocomputing*, 2016, DOI: 10.1016/j.neucom.2015.08.109.

[229] J. Welch, J. Johnson, M. Bax, R. Badr, and R. Shahidi, "A real-time freehand 3D ultrasound system for image-guided surgery," in *2000 IEEE Ultrasonics Symposium. Proceedings. An International Symposium (Cat. No.00CH37121)*, IEEE, 2000, ISBN: 0-7803-6365-5, DOI: 10.1109/ULTSYM.2000.921630.

[230] M. Soozande *et al.*, "Virtually Extended Array Imaging Improves Lateral Resolution in High Frame Rate Volumetric Imaging," in *2018 IEEE International Ultrasonics Symposium (IUS)*, IEEE, Oct. 2018, ISBN: 978-1-5386-3425-7, DOI: 10.1109/ULTSYM.2018.8580018.

[231] H. G. Kang *et al.*, "Column-based micro-beamformer for improved 2D beamforming using a matrix array transducer," in *2015 IEEE Biomedical Circuits and Systems Conference (BioCAS)*, IEEE, Oct. 2015, ISBN: 978-1-4799-7234-0, DOI: 10.1109/BioCAS.2015.7348450.

[232] P. Santos, G. U. Haugen, L. Lovstakken, E. Samset, and J. D'Hooge, "Diverging Wave Volumetric Imaging Using Subaperture Beamforming," *IEEE Transactions on Ultrasonics, Ferroelectrics, and Frequency Control*, 2016, DOI: 10.1109/TUFFC.2016.2616172.

[233] M. F. Rasmussen and J. A. Jensen, "3-D ultrasound imaging performance of a row-column addressed 2-D array transducer: A measurement study," *IEEE International Ultrasonics Symposium, IUS*, 2013, DOI: 10.1109/ULTSYM.2013.0370.

[234] F. Hansen, P. Mangell, B. Sonesson, and T. Länne, "Diameter and compliance in the human common carotid artery — variations with age and sex," *Ultrasound in Medicine & Biology*, Jan. 1995, DOI: 10.1016/0301-5629(94)00090-5.

[235] H. Hasegawa and H. Kanai, "Effect of element directivity on adaptive beamforming applied to high-frame-rate ultrasound," *IEEE Transactions on Ultrasonics, Ferroelectrics, and Frequency Control*, 2015, DOI: 10.1109/TUFFC.2015.006973.

[236] T. Hergum, T. Bjastad, K. Kristoffersen, and H. Torp, "Parallel beamforming using synthetic transmit beams," *IEEE Transactions on Ultrasonics, Ferroelectrics and Frequency Control*, Feb. 2007, DOI: 10.1109/TUFFC.2007.241.

[237] T. Stepinski, "An Implementation of Synthetic Aperture Focusing Technique in Frequency Domain," *IEEE Transactions on Ultrasonics, Ferroelectrics and Frequency Control*, Jul. 2007, DOI: 10.1109/TUFFC.2007.400.

[238] W. Jing and L. Jian-yu, "Motion Artifacts of Extended High Frame Rate Imaging," *IEEE Transactions on Ultrasonics, Ferroelectrics and Frequency Control*, Jul. 2007, DOI: 10.1109/TUFFC.2007.391.

[239] G. Matrone, A. S. Savoia, G. Caliano, and G. Magenes, "The Delay Multiply and Sum Beamforming Algorithm in Ultrasound B-Mode Medical Imaging," *IEEE Transactions on Medical Imaging*, Apr. 2015, DOI: 10.1109/TMI.2014.2371235.

[240] M. Mozaffarzadeh, M. Sadeghi, A. Mahloojifar, and M. Orooji, "Double-Stage Delay Multiply and Sum Beamforming Algorithm Applied to Ultrasound Medical Imaging," *Ultrasound in medicine & biology*, 2017.

[241] M. Mozaffarzadeh, A. Mahloojifar, M. Orooji, S. Adabi, and M. Nasiriavanaki, "Double-Stage Delay Multiply and Sum Beamforming Algorithm: Application to Linear-Array Photoacoustic Imaging," *IEEE Transactions on Biomedical Engineering*, Jan. 2018, DOI: 10.1109/TBME.2017.2690959.

[242] G. Matrone *et al.*, "Effects of Coherence-Based Beamforming on Breast Ultrasound Elastograms," in *IEEE International Ultrasonics Symposium, IUS*, IEEE Computer Society, Oct. 2019, ISBN: 9781728145969, DOI: 10.1109/ULTSYM.2019.8926022.

[243] D. J. Sahn, A. DeMaria, J. Kisslo, and A. Weyman, "Recommendations regarding quantitation in M-mode echocardiography: Results of a survey of echocardiographic measurements," *Circulation*, 1978, DOI: 10.1161/01.CIR.58.6.1072.

[244] A. Fenster, C. Blake, I. Gyacskov, A. Landry, and J. D. Spence, "3D ultrasound analysis of carotid plaque volume and surface morphology," *Ultrasonics*, 2006, DOI: 10.1016/j.ultras.2006.06.027.

[245] C. D. Ainsworth *et al.*, "3D ultrasound measurement of change in carotid plaque volume: A tool for rapid evaluation of new therapies," *Stroke*, 2005, DOI: 10.1161/01.STR.0000178543.19433.20.

[246] M. Kozàkovà *et al.*, "Quantification of extracranial carotid artery stenosis by ultrafast three-dimensional ultrasound," *Journal of the American Society of Echocardiography*, 2001, DOI: 10.1067/mje.2001.115619.

[247] E. G. Grant *et al.*, "Carotid Artery Stenosis: Gray-Scale and Doppler US Diagnosis - Society of Radiologists in Ultrasound Consensus Conference," *Radiology*, 2003, DOI: 10.1148/radiol.2292030516.

[248] R. W. Gill, "Measurement of blood flow by ultrasound: Accuracy and sources of error," *Ultrasound in Medicine and Biology*, 1985, DOI: 10.1016/0301-5629(85)90035-3.

[249] C. A. D. Leguy, E. M. H. Bosboom, A. P. G. Hoeks, and F. N. van de Vosse, "Model-based assessment of dynamic arterial blood volume flow from ultrasound measurements," *Medical and Biological Engineering and Computing*, 2009, DOI: 10.1007/s11517-009-0473-9.

[250] P. Picot and P. Embree, "Quantitative volume flow estimation using velocity profiles," *IEEE Transactions on Ultrasonics, Ferroelectrics and Frequency Control*, May 1994, DOI: 10.1109/58.285468.

[251] C. Papadacci *et al.*, "4D simultaneous tissue and blood flow Doppler imaging: Revisiting cardiac Doppler index with single heart beat 4D ultrafast echocardiography," *Physics in Medicine and Biology*, 2019, DOI: 10.1088/1361-6560/ab1107.

[252] M. S. Wigen *et al.*, "4-D Intracardiac Ultrasound Vector Flow Imaging-Feasibility and Comparison to Phase-Contrast MRI," *IEEE Transactions on Medical Imaging*, 2018, DOI: 10.1109/TMI.2018.2844552.

[253] J. Voorneveld *et al.*, "4-D Echo-Particle Image Velocimetry in a Left Ventricular Phantom," *Ultrasound in Medicine and Biology*, 2020, DOI: 10.1016/j.ultrasmedbio.2019.11.020.

[254] S. Rossi, A. Ramalli, F. Fool, and P. Tortoli, "High-frame-rate 3-D vector flow imaging in the frequency domain," *Applied Sciences (Switzerland)*, 2020, DOI: 10.3390/APP10155365.

[255] J. Sauvage *et al.*, "A large aperture row column addressed probe for in vivo 4D ultrafast doppler ultrasound imaging," *Physics in Medicine and Biology*, Sep. 2018, DOI: 10.1088/1361-6560/aae427.

[256] L. T. Jørgensen, M. B. Stuart, and J. A. Jensen, "Transverse oscillation tensor velocity imaging using a row–column addressed array: Experimental validation," *Ultrasonics*, 2023, DOI: 10.1016/j.ultras.2023.106962.

[257] R. X. Li, J. Luo, T. Khamdaeng, and E. E. Konofagou, "Pulse Wave Imaging (PWI) and arterial stiffness measurement of the human carotid artery: An in vivo feasibility study," *IEEE International Ultrasonics Symposium, IUS*, 2011, DOI: 10.1109/ULTSYM.2011.0444.

[258] H. S. Stone, M. T. Orchard, E. C. Chang, and S. A. Martucci, "A fast direct Fourier-based algorithm for subpixel registration of images," *IEEE Transactions on Geoscience and Remote Sensing*, 2001, DOI: 10.1109/36.957286.

[259] M. Lenge *et al.*, "High-frame-rate 2-D vector blood flow imaging in the frequency domain," *IEEE transactions on ultrasonics, ferroelectrics, and frequency control*, 2014.

[260] J. Westerweel and F. Scarano, "Universal outlier detection for PIV data," *Experiments in Fluids*, 2005, DOI: 10.1007/s00348-005-0016-6.

[261] J. Y. Lu, "2D and 3D High Frame Rate Imaging with Limited Diffraction Beams," *IEEE Transactions on Ultrasonics, Ferroelectrics, and Frequency Control*, 1997, DOI: 10.1109/58.655200.

[262] R. D. Keane and R. J. Adrian, "Optimization of particle image velocimeters. I. Double pulsed systems," *Measurement Science and Technology*, 1990, DOI: 10.1088/0957-0233/1/11/013.

[263] J. Voorneveld and J. G. Bosch, "The Effect of Spatial Velocity Gradients on Block-Matching Accuracy for Ultrasound Velocimetry," *Ultrasound in Medicine and Biology*, 2023, DOI: 10.1016/j.ultrasmedbio.2023.09.002.

[264] I. K. Ekroll, V. Perrot, H. Liebgott, and J. Avdal, "Tapered Vector Doppler for Improved Quantification of Low Velocity Blood Flow," *IEEE Transactions on Ultrasonics, Ferroelectrics, and Frequency Control*, Apr. 2021, DOI: 10.1109/TUFFC.2020.3028874.

[265] A. Goddi *et al.*, "High-frame rate vector flow imaging of the carotid bifurcation," *Insights into Imaging*, 2017, DOI: 10.1007/s13244-017-0554-5.

[266] R. D. Keane, R. J. Adrian, and Y. Zhang, "Super-resolution particle imaging velocimetry," *Measurement Science and Technology*, 1995, DOI: 10.1088/0957-0233/6/6/013.

[267] F. Scarano and M. L. Riethmuller, "Advances in iterative multigrid PIV image processing," in *Experiments in Fluids*, Springer Verlag, 2000, DOI: 10.1007/s003480070007.

[268] S. W. Smith *et al.*, "Two dimensional arrays for 3-D ultrasound imaging," *Proceedings of the IEEE Ultrasonics Symposium*, 2002, DOI: 10.1109/ultsym.2002.1192590.

[269] P. Mattesini *et al.*, "Spectral Doppler Measurements With 2-D Sparse Arrays," *IEEE Transactions on Ultrasonics, Ferroelectrics, and Frequency Control*, Feb. 2020, DOI: 10.1109/TUFFC.2019.2944090.

[270] L. Wei *et al.*, "Sparse 2-D PZT-on-PCB Arrays With Density Tapering," *IEEE Transactions on Ultrasonics, Ferroelectrics, and Frequency Control*, 2022, DOI: 10.1109/TUFFC.2022.3204118.

[271] E. Roux *et al.*, "2-D ultrasound sparse arrays multidepth radiatio optimization using simulated annealing and spiral-array inspired energy functions," *IEEE Transactions on Ultrasonics, Ferroelectrics, and Frequency Control*, 2016, DOI: 10.1109/TUFFC.2016.2602242.

[272] G. Matrone, A. Ramalli, J. d'Hooge, P. Tortoli, and G. Magenes, "A Comparison of Coherence-Based Beamforming Techniques in High Frame-Rate Ultrasound Imaging with Multi-Line Transmission," *IEEE Transactions on Ultrasonics, Ferroelectrics, and Frequency Control*, 2019, DOI: 10.1109/tuffc.2019.2945365.

[273] A. N. Madhavanunni and M. R. Panicker, "A nonlinear beamforming for enhanced spatiotemporal sensitivity in high frame rate ultrasound flow imaging," *Computers in Biology and Medicine*, 2022, DOI: 10.1016/j.compbiomed.2022.105686.

[274] S. Bjærum *et al.*, "Clutter filter design for ultrasound color flow imaging," *IEEE Transactions on Ultrasonics, Ferroelectrics, and Frequency Control*, 2002, DOI: 10.1109/58.985705.

[275] S. Bae, J. Park, and T.-K. Song, "Contrast and Volume Rate Enhancement of 3-D Ultrasound Imaging Using Aperiodic Plane Wave Angles: A Simulation Study," *IEEE Transactions on Ultrasonics, Ferroelectrics, and Frequency Control*, 2019, DOI: 10.1109/TUFFC.2019.2931495.

[276] S. Bae, B. H. Kim, A. Alizad, M. Fatemi, and T. K. Song, "Experimental Study of Aperiodic Plane Wave Imaging for Ultrafast 3-D Ultrasound Imaging," *IEEE Transactions on Biomedical Engineering*, 2022, DOI: 10.1109/TBME.2022.3152212.

[277] B. Denarie *et al.*, "Coherent plane wave compounding for very high frame rate ultrasonography of rapidly moving targets," *IEEE Transactions on Medical Imaging*, 2013, DOI: 10.1109/TMI.2013.2255310.

[278] D. H. Evans, J. A. Jensen, and M. B. Nielsen, "Ultrasonic colour Doppler imaging," *Interface Focus*, 2011, DOI: 10.1098/rsfs.2011.0017.

[279] A. Caenen *et al.*, "Effect of ultrafast imaging on shear wave visualization and characterization: An experimental and computational study in a pediatric ventricular model," *Applied Sciences (Switzerland)*, 2017, DOI: 10.3390/app7080840.

[280] M. Capriotti, J. F. Greenleaf, and M. W. Urban, "Time-Aligned Plane Wave Compounding Methods for High-Frame-Rate Shear Wave Elastography: Experimental Validation and Performance Assessment on Tissue Phantoms," *Ultrasound in Medicine and Biology*, 2021, DOI: 10.1016/j.ultrasmedbio.2021.03.003.

[281] E. Widman *et al.*, "Shear Wave Elastography Quantifies Stiffness in Ex Vivo Porcine Artery with Stiffened Arterial Region," *Ultrasound in Medicine and Biology*, 2016, DOI: 10.1016/j.ultrasmedbio.2016.05.021.

[282] A. E. Saris *et al.*, "In Vivo Blood Velocity Vector Imaging Using Adaptive Velocity Compounding in the Carotid Artery Bifurcation," *Ultrasound in Medicine and Biology*, 2019, DOI: 10.1016/j.ultrasmedbio.2019.03.008.

[283] W. Guo, Y. Wang, and J. Yu, "A sibelobe suppressing beamformer for coherent plane wave compounding," *Applied Sciences (Switzerland)*, 2016, DOI: 10.3390/app6110359.

[284] W. Guo, Y. Wang, G. Wu, and J. Yu, "Sidelobe reduction for plane wave compounding with a limited frame number," *BioMedical Engineering Online*, 2018, DOI: 10.1186/s12938-018-0525-1.

[285] B. D. Lindsey and B. Jing, "Phase modulation beamforming in high frame rate imaging," *IEEE International Ultrasonics Symposium, IUS*, 2019, DOI: 10.1109/ULTSYM.2019.8926007.

[286] B. Diarra, M. Robini, P. Tortoli, C. Cachard, and H. Liebgott, "Design of optimal 2-d nongrid sparse arrays for medical ultrasound," *IEEE Transactions on Biomedical Engineering*, 2013, DOI: 10.1109/TBME.2013.2267742.

[287] R. Maffett *et al.*, "Unfocused Field Analysis of a Density-Tapered Spiral Array for High-Volume-Rate 3-D Ultrasound Imaging," *IEEE Transactions on Ultrasonics, Ferroelectrics, and Frequency Control*, 2022, DOI: 10.1109/TUFFC.2022.3188245.

[288] T. D. Ianni, M. Hemmsen, P. L. Muntal, I. H. H. Jørgensen, and J. Jensen, "System-level Design of an Integrated Receiver Front-end for a Wireless Ultrasound Probe," *IEEE Transactions on Ultrasonics, Ferroelectrics, and Frequency Control*, 2016, DOI: 10.1109/TUFFC.2016.2594769.

[289] J. Zhou *et al.*, "Front-End Architecture Design for Low-Complexity 3-D Ultrasound Imaging Based on Synthetic Aperture Sequential Beamforming," *IEEE Transactions on Very Large Scale Integration (VLSI) Systems*, 2021, DOI: 10.1109/TVLSI.2020.3035698.

[290] F. Fool, "Beamforming for novel matrix arrays - Fresnel Zone Beamforming and Stolt Migration," 2017.

[291] M. Sinha and D. J. Buckley, "Acoustic Properties of Polymers BT - Physical Properties of Polymers Handbook," 2007.

[292] M. Shabanimotlagh, *Ultrasound Matrix Transducers for High Frame Rate 3D Medical Imaging*. 2018, ISBN: 9789461868510, DOI: 10.4233/UUID.

[293] F. Fool *et al.*, "3D high frame rate flow measurement using a prototype matrix transducer for carotid imaging," *IEEE International Ultrasonics Symposium, IUS*, 2019, DOI: 10.1109/ULTSYM.2019.8925780.

[294] C. Giangrossi, A. Ramalli, M. De Cianni, F. Guidi, and P. Tortoli, "Blood-flow volume estimation with bi-plane imaging," *IEEE International Ultrasonics Symposium, IUS*, 2022, DOI: 10.1109/IUS54386.2022.9957268.

[295] A. Ramalli *et al.*, "Real-Time 3-D Spectral Doppler Analysis with a Sparse Spiral Array," *IEEE Transactions on Ultrasonics, Ferroelectrics, and Frequency Control*, 2021, DOI: 10.1109/TUFFC.2021.3051628.

[296] M. Correia, J. Provost, M. Tanter, and M. Pernot, "4D ultrafast ultrasound flow imaging: in vivo quantification of arterial volumetric flow rate in a single heartbeat," *Physics in medicine and biology*, 2016, DOI: 10.1088/0031-9155/61/23/L48.

Acknowledgments

Although this is my dissertation, I could not have completed it without the help of others. Therefore, I would like to thank the people who have supported me throughout these years.

First and foremost, I want to thank my promotors **Martin**, **Nico**, and **Rik** for their continuous support. **Martin**, thank you for your strict and critical view on the results and figures, ensuring they are presented well and clearly every time, and your expertise in dissecting and solving problems. **Nico**, thank you for your out-of-the-box questions that made me consider different perspectives, and your help in debugging the prototypes. **Rik**, thank you for constantly challenging my explanations and engaging in discussions to resolve the flaws, among other things. This certainly led to more robust and comprehensible text.

I also want to thank my colleagues who were directly involved in the various projects I worked on. **Jorinde** and **Peng**, thank you for your collaboration on the MIFFY project. Our discussions helped to further specify the medical requirements and translate them into concrete technical specifications. **Maysam**, I appreciate your help in quickly getting me up to speed with simulating and characterizing our prototype matrix transducers. **Djalma**, thanks for automating the measurement setup, making everything run more smoothly and thereby saving precious time, and for all the problem-solving discussions and your company during the many measurements. **Eunchul** and **Taehoon**, thank you for your assistance with the control of the ASICs and conducting electrical tests on them. **Moein** and **Mehdi**, thank you for your contributions to the development of the high-frame-rate imaging scheme for the PUMA. **Luxi**, thanks for your work and scripts for the Spiral matrix, allowing me to focus on the fun part. **Jos**, your work on the first version of the beamforming paper made the revision process much easier. **Piero**, **Alessandro**, and **Stefano**, thank you, along with the others in the MSDLab, for making my stay in Florence pleasant. Your help in developing the adaptive array clutter filter was invaluable. It was refreshing to leave all the work in Delft behind and focus on one research project. **Chris**, **Anne**, and **Stein**, thank you for allowing me to use the flow setup in Nijmegen and for your help with operating it. I also extend my gratitude to the other PIs involved in the projects, **Michiel**, **Hans**, and **Jeroen**, for their unique and insightful perspectives.

My gratitude also goes to all the support staff. **Angela** and **Annelies**, thank you for handling all the administrative matters, most of which I probably don't even know about, and for organizing the outings and get-togethers. **Edo**, thank you for the IT support and extensive work retrieving data from a "failing" hard-drive. **Ronald**, thank you for keeping the group lively, and your support with the HPC cluster and IT issues. **Emile**, thank you for the extensive work in building the many prototypes and continuously making further improvements. **Henry**, I appreciate your constant willingness to assist with a range of things, including computer problems, measurement setups and even water leaks.

I am also grateful to the many PhDs, Postdocs, office mates, and other colleagues who were around during these seven years: **Alberico**, **Jack**, **Boudewine**, **Elango**, **Sabiju**,

Alina, **Eleonora**, **Moein**, **Mehdi**, **Rick**, **Martijn**, **Chih-Hsien**, **Xiufeng**, **Dion**, **Chiara**, **Masa**, **Paulina**, **Ayda**, **Yidong**, **Ulas**, **Lumen**, **Baptiste**, **Yi**, **Agis**, **Martina**, **Min**, **Hugues**, **Gabrielle**, **Joao**, **Verya**, **Maysam**, **Filippo**, **Andrea**, and **Lorenzo**. Especially of course to those who always responded to the lunch call at exactly 12 o'clock or joined in other activities like table tennis, sjoelen, and foosball.

Lastly, I want to thank my family for their continuous support during this extended PhD journey.

Curriculum Vitæ

Fabian Fool

18-07-1994 Born in Vlaardingen, The Netherlands

Education

2012–2015 Bachelor of Science in Applied Physics
Delft University of Technology
Graduated *Cum Laude* and completed the Honours Programme

2015–2017 Master of Science in Applied Physics
Delft University of Technology
Graduated *Cum Laude*

2017–2024 PhD Applied Physics
Delft University of Technology
Thesis: High-Frame-Rate Ultrasound Matrix Transducers for Quantifying Blood Flow
Promotors: Dr. ir. M.D. Verweij (Delft University of Technology)
Prof. dr. ir. N. de Jong (Delft University of Technology)
Dr. ir. H.J. Vos (*Erasmus MC*)

List of Publications

Journal papers

1. P. Guo, **F. Fool**, Z.-y. Chang, E. Noothout, H. J. Vos, J. G. Bosch, N. de Jong, M. D. Verweij, and M. A. P. Pertijs, "A 125 μm-Pitch-Matched Transceiver ASIC With Micro-Beamforming ADC and Multi-Level Signaling for 3-D Transfontanelle Ultrasonography," *IEEE Journal of Solid-State Circuits*, 2024, DOI: 10.1109/JSSC.2024.3355854
2. P. Guo, **F. Fool**, Z.-y. Chang, E. Noothout, H. J. Vos, J. G. Bosch, N. De Jong, M. D. Verweij, and M. A. P. Pertijs, "A 1.2-mW/Channel Pitch-Matched Transceiver ASIC Employing a Boxcar-Integration-Based RX Micro-Beamformer for High-Resolution 3-D Ultrasound Imaging," *IEEE Journal of Solid-State Circuits*, 2023, DOI: 10.1109/JSSC.2023.3271270
3. L. Wei, E. Boni, A. Ramalli, **F. Fool**, E. Noothout, A. F. W. van der Steen, M. D. Verweij, P. Tortoli, N. De Jong, and H. J. Vos, "Sparse 2-D PZT-on-PCB Arrays With Density Tapering," *IEEE Transactions on Ultrasonics, Ferroelectrics, and Frequency Control*, 2022, DOI: 10.1109/TUFFC.2022.3204118
4. **F. Fool**, D. S. dos Santos, M. Mozaffarzadeh, M. Shabanimotlagh, E. Noothout, T. Kim, N. Rozsa, H. J. Vos, J. G. Bosch, M. A. P. Pertijs, M. D. Verweij, and N. de Jong, "A Tiled Ultrasound Matrix Transducer for Volumetric Imaging of the Carotid Artery," *Sensors*, 2022, DOI: 10.3390/s22249799
5. T. Kim, **F. Fool**, D. S. dos Santos, Z.-Y. Chang, E. Noothout, H. J. Vos, J. G. Bosch, M. D. Verweij, N. de Jong, and M. A. P. Pertijs, "Design of an ultrasound transceiver asic with a switching-artifact reduction technique for 3D carotid artery imaging," *Sensors*, 2021, DOI: 10.3390/s21010150
6. S. Rossi, A. Ramalli, **F. Fool**, and P. Tortoli, "High-frame-rate 3-D vector flow imaging in the frequency domain," *Applied Sciences (Switzerland)*, 2020, DOI: 10.3390/APP10155365
7. M. Mozaffarzadeh, M. Soozande, **F. Fool**, M. A. P. Pertijs, H. J. Vos, M. D. Verweij, J. G. Bosch, and N. de Jong, "Receive/Transmit Aperture Selection for 3D Ultrasound Imaging with a 2D Matrix Transducer," *Applied Sciences*, 2020, DOI: 10.3390/app10155300
8. **F. Fool**, J. De Wit, H. J. Vos, D. Bera, N. De Jong, and M. D. Verweij, "Two-Stage Beamforming for Phased Array Imaging Using the Fast Hankel Transform," *IEEE Transactions on Ultrasonics, Ferroelectrics, and Frequency Control*, 2019, DOI: 10.1109/TUFFC.2018.2885870

Conference papers

1. D. S. Dos Santos, **F. Fool**, T. Kim, E. Noothout, N. Rozsa, H. J. Vos, J. G. Bosch, M. A. P. Pertijs, M. D. Verweij, and N. de Jong, "Automated Characterization of Matrix Transducer Arrays using the Verasonics Imaging System," in *2022 IEEE International Ultrasonics Symposium (IUS)*, IEEE, Oct. 2022, ISBN: 978-1-6654-6657-8, DOI: 10.1109/IUS54386.2022.9957544
2. D. S. dos Santos, **F. Fool**, T. Kim, E. Noothout, H. J. Vos, J. G. Bosch, M. A. Pertijs, M. D. Verweij, and N. De Jong, "Experimental Investigation of the Effect of Subdicing on an Ultrasound Matrix Transducer," *IEEE International Ultrasonics Symposium, IUS*, 2021, DOI: 10.1109/IUS52206.2021.9593315

3. E. Boni, **F. Fool**, M. D. Verweij, H. J. Vos, and P. Tortoli, "On the efficacy of in-probe preamplifiers for piezoelectric 2D arrays," *IEEE International Ultrasonics Symposium, IUS*, 2020, DOI: 10.1109/IUS46767.2020.9251800
4. S. Rossi, F. Fool, A. Ramalli, and P. Tortoli, "Experimental validation of a new method for 3-D vector flow imaging in the frequency domain," *IEEE International Ultrasonics Symposium, IUS*, 2020, DOI: 10.1109/IUS46767.2020.9251341
5. **F. Fool**, M. D. Verweij, H. J. Vos, M. Shabanimotlagh, M. Soozande, M. Mozaffarzadeh, T. Kim, E. Kang, M. Pertijs, and N. D. Jong, "3D high frame rate flow measurement using a prototype matrix transducer for carotid imaging," *IEEE International Ultrasonics Symposium, IUS*, 2019, DOI: 10.1109/ULTSYM.2019.8925780
6. **F. Fool**, J. de Wit, H. J. Vos, D. Bera, N. de Jong, and M. D. Verweij, "Frequency Domain Two-Stage Beamforming for Phased Array Imaging Using the Fast Hankel Transform," in *2018 IEEE International Ultrasonics Symposium (IUS)*, IEEE, 2018, ISBN: 9781538634257, DOI: 10.1109/ULTSYM.2018.8579914
7. M. Soozande, **F. Fool**, M. Shabanimotlagh, M. Pertijs, M. Verweij, H. J. Vos, J. G. Bosch, and N. de Jong, "Virtually Extended Array Imaging Improves Lateral Resolution in High Frame Rate Volumetric Imaging," in *2018 IEEE International Ultrasonics Symposium (IUS)*, IEEE, Oct. 2018, ISBN: 978-1-5386-3425-7, DOI: 10.1109/ULTSYM.2018.8580018